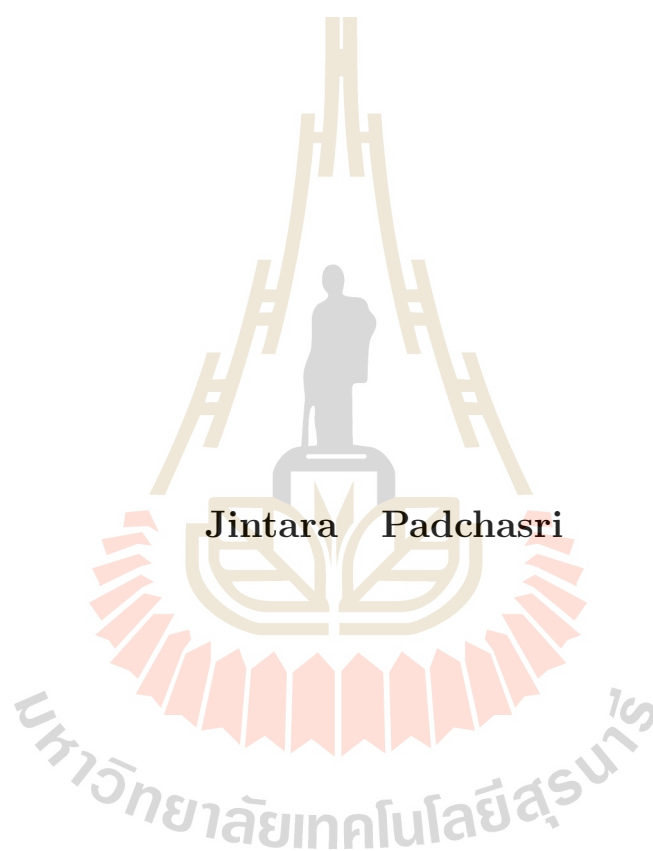


การสังเคราะห์ การหาลักษณะเฉพาะและสมบัติของวัสดุเพอรอฟสไกต์
 $\text{CH}_3\text{NH}_3\text{PbI}_3$ และ $\text{CH}_3\text{NH}_3\text{Pb}_{1-x}(\text{Sn},\text{Ba})_x\text{I}_3$



วิทยานิพนธ์นี้เป็นส่วนหนึ่งของการศึกษาตามหลักสูตรปริญญาวิทยาศาสตรดุษฎีบัณฑิต
สาขาวิชาฟิสิกส์
มหาวิทยาลัยเทคโนโลยีสุรนารี
ปีการศึกษา 2560

**SYNTHESIS, CHARACTERIZATION AND
PROPERTIES OF $\text{CH}_3\text{NH}_3\text{PbI}_3$ AND
 $\text{CH}_3\text{NH}_3\text{Pb}_{1-x}(\text{Sn},\text{Ba})_x\text{I}_3$ PEROVSKITE MATERIALS**



Jintara Padchasri

**A Thesis Submitted in Partial Fullfillment of the Requirements for the
Degree of Doctor of Philosophy in Physics**

Suranaree University of Technology

Academic Year 2017

**SYNTHESIS, CHARACTERIZATION AND PROPERTIES
OF $\text{CH}_3\text{NH}_3\text{PbI}_3$ AND $\text{CH}_3\text{NH}_3\text{Pb}_{1-x}(\text{Sn},\text{Ba})_x\text{I}_3$
PEROVSKITE MATERIALS**

Suranaree University of Technology has approved this thesis submitted in partial fulfillment of the requirements for Doctor of Philosophy in Physics.

Thesis Examining Committee

N. Sanguansak

(Dr. Nuanwan Sanguansak)

Chairperson

Sroj Rujirawat

(Dr. Saroj Rujirawat)

Member (Thesis Advisor)

Rattikorn Yinnirun

(Assoc. Prof. Dr. Rattikorn Yinnirun)

Member

Prayoon Song

(Assoc. Prof. Dr. Prayoon Songsiritthigul)

Member

Pinit Kidkhunthod

(Dr. Pinit Kidkhunthod)

Member

Worawat Meevasana

(Asst. Prof. Dr. Worawat Meevasana)

Dr. Worawat Meevasana
Vice Rector for Academic Affairs
and Internationalization

Dean of Institute of Science

จินตหรา ปัดชาลี : การสังเคราะห์ การหาลักษณะเฉพาะและสมบัติของวัสดุเพอรอฟสไกต์ $\text{CH}_3\text{NH}_3\text{PbI}_3$ และ $\text{CH}_3\text{NH}_3\text{Pb}_{1-x}(\text{Sn},\text{Ba})_x\text{I}_3$ (SYNTHESIS, CHARACTERIZATION AND PROPERTIES OF $\text{CH}_3\text{NH}_3\text{PbI}_3$ AND $\text{CH}_3\text{NH}_3\text{Pb}_{1-x}(\text{Sn},\text{Ba})_x\text{I}_3$ PEROVSKITE MATERIALS) อาจารย์ที่ปรึกษา : อาจารย์ ดร.สาโรช รุจิรวรรณ, 150 หน้า.

เมทิลแอมโมเนียมเลทไอโอไดร์/XANES/EXAFS/FEFF8.2

วิทยานิพนธ์นี้มุ่งศึกษาวัสดุอินทรีย์-อนินทรีย์เพอรอฟสไกต์ไฮไลด์ วัสดุชนิดนี้ได้รับความสนใจเป็นอย่างมากในการนำไปประยุกต์ใช้ในโซลาร์เซลล์ เนื่องจากสามารถเตรียมได้ง่าย ที่อุณหภูมิต่ำ ราคาถูก และที่สำคัญวัสดุยังสามารถหาง่ายอีกด้วย เรามุ่งเน้นไปที่วัสดุ $\text{CH}_3\text{NH}_3\text{PbI}_3$ และ $\text{CH}_3\text{NH}_3\text{Pb}_{1-x}\text{M}_x\text{I}_3$ (เมื่อ M เป็น Sn และ Ba) ผลการตรวจสอบการก่อเกิดผลึกด้วยเทคนิคการเลี้ยวเบนรังสีเอ็กซ์ พบว่าวัสดุที่เตรียมได้นั้นมีความเป็นผลึกสูงซึ่งมีโครงสร้างแบบเตตระโกนอลรวมถึงตัวอย่างที่ทำการแทนที่ด้วย Ba และ Sn ในตำแหน่งของ Pb ซึ่งไม่พบความแตกต่างที่ชัดเจนนัก เพื่อเป็นการยืนยันผลการตรวจสอบจากเทคนิคการเลี้ยวเบนรังสีเอ็กซ์ เราได้ทำการตรวจสอบโครงสร้างผลึกอีกครั้งด้วยเทคนิคการดูดกลืนรังสีเอ็กซ์ (XAS) พบว่าสารตัวอย่างที่ทำการแทนที่ด้วย Ba และ Sn แสดงโครงสร้างเตตระโกนอลจริง ซึ่งผลการทดลองนี้สอดคล้องกับผลการคำนวณทางทฤษฎีโดยใช้โปรแกรม FEFF 8.2 นอกจากนี้การเปลี่ยนแปลงโครงสร้างที่อุณหภูมิต่ำสามารถยืนยันด้วยผลของการวัดสมบัติไดอิเล็กทริกและการตรวจสอบสมบัติทางแสงยังช่วยยืนยันความเป็นไปได้ของประสิทธิภาพทางโซลาร์เซลล์ที่ดีอีกด้วย

สาขาวิชาฟิสิกส์
ปีการศึกษา 2560

ลายมือชื่อนักศึกษา จินตหรา ปัดชาลี
ลายมือชื่ออาจารย์ที่ปรึกษา สาโรช รุจิรวรรณ
ลายมือชื่ออาจารย์ที่ปรึกษาร่วม วิจิตร วัฒนวิจิตร

JINTARA PADCSHASRI : SYNTHESIS, CHARACTERIZATION AND
PROPERTIES OF $\text{CH}_3\text{NH}_3\text{PbI}_3$ AND $\text{CH}_3\text{NH}_3\text{Pb}_{1-x}(\text{Sn},\text{Ba})_x\text{I}_3$
PEROVSKITE MATERIALS. THESIS ADVISOR :
SAROJ RUJIRAWAT, Ph.D. 150 P.

METHYLAMMONIUM LEAD IODIDE/XANES/EXAFS/FEFF8.2

The methylammonium lead iodide ($\text{CH}_3\text{NH}_3\text{PbI}_3$) material is currently investigated as active material in perovskite solar cells. Its stability, high optical band gap, low processing temperature and abundant elemental constituents provide numerous advantages over most powder absorber materials. In this work, $\text{CH}_3\text{NH}_3\text{PbI}_3$ and $\text{CH}_3\text{NH}_3\text{Pb}_{1-x}\text{M}_x\text{I}_3$ (M=Sn and Ba) perovskite powders were studied. The XRD measurement demonstrated that the direct mixing synthesis method was able to produce a highly crystalline $\text{CH}_3\text{NH}_3\text{PbI}_3$ material in a tetragonal phase structure. However, the XANES spectra showed that Sn and Ba substituted in Pb site in $\text{CH}_3\text{NH}_3\text{PbI}_3$ at low substitutes, which corresponded well with the calculated XANES spectra by FEFF8.2 software. The phase transition at low temperature was confirmed by dielectric measurement. In addition, the optical properties were confirmed a direct bandgap of 1.53-1.57 eV in perovskite materials, which in turn will result in a high performance perovskite solar cell.

School of Physics

Academic Year 2017

Student's Signature Jintara Padchasri

Advisor's Signature Saroj Rujirawat

Co-advisor's Signature Pattakorn Yimnirun

ACKNOWLEDGEMENTS

The research involved in the writing of this thesis could not have been done without the assistance and support of many individuals.

First and foremost, I would like to express my gratitude to Prof. Rattikorn Yimnirun, my thesis advisor, for his kindly help during these 4 years, for the scientific discussions as well as in the life and giving me the opportunity to work with him and especially for the key guiding suggestion when nothing was working.

I would like to express my deepest thanks to my thesis advisor Dr. Saroj Rujirawat who has guided and mentored me. His kind patience, pragmatic support, and confidence in me were paramount in providing a smooth and stress-free environment for the successful completion of the final step of this thesis.

I would like to express my thanks to Dr. Taras Kolodiaznyi for suggesting, given me the opportunity to be number of Strongly Correlated Materials Group, NIMs, Japan, and for the providing me an excellent experience research condition. Also, I would like to thank internal NIMs grant PA402 for funding support during research in Japan.

I appreciate the guidance from Dr. Nuanwan Sanguansak and Assoc.Prof. Prayoon Songsiriritthigul as my thesis committee. Especially, Assoc.Prof. Prayoon Songsiriritthigul who gave many useful comments and input during my thesis examination.

I am also grateful to Dr. Pinit Kidkhunthod for his management of beam time in my work at BL5.2, SLRI and for accepting to be a member of the examination committee.

I am deeply grateful to the Science Achievement Scholarship of Thailand (SAST) from Thai Government for financial support.

I would like to thank all of staff at the School of physics, Institute of Science, Suranaree University of Technology for giving me knowledge and inspiring me to do the research. Special thank go to Mrs. Phenkhae Petchmai who helps me doing the documents and always correct some mistakes that I had made.

I appreciate all member of the XAS group which includes Dr. Jaru Jutimoosik, Mr. Chinawat Ekwongsa, Miss. Phitsamai Kamonpha, Mr Thanun Chunjaemsri, Mr. Pattaraphong Nijapal, Mr. Awadol Khejonrak, Mr. Sawawudh Nathabumroong and Miss Wipakorn Rittisut for their comments and discussion on my work. I also appreciate the person who always helps are Miss Thongsuk Srichumsang, Miss Kwunta Siwawongkasem, Miss Ornuma Kalawa, Mr. Kittipong Wangnok, Dr. Benjaporn Yotburut, Dr. Unchista Wongpratrat and Dr. Sumeth Siroroj. I would like to thank all of you from the bottom of my heart.

It is impossible to list all of my fellow graduate students, who were a great support during my Ph.D. study, for all the great times we had together.

Finally, I would like to thank my family who always stand by me and give me inspiration to do many things. You always support me whatever I do. You are in my heart forever.

Jintara Padchasri

CONTENTS

| | Page |
|--|-----------|
| ABSTRACT IN THAI | I |
| ABSTRACT IN ENGLISH | II |
| ACKNOWLEDGEMENTS | III |
| CONTENTS | V |
| LIST OF TABLES | VIII |
| LIST OF FIGURES | X |
| LIST OF ABBREVIATIONS | XI |
| CHAPTER | |
| I INTRODUCTION | 1 |
| 1.1 Background | 1 |
| 1.2 Perovskite | 5 |
| 1.3 Motivation | 12 |
| 1.4 Scope and limitations of the study | 12 |
| II THEORY | 14 |
| 2.1 Lead-free metal based halide perovskite | 14 |
| 2.2 Formability and structural of perovskite | 15 |
| 2.3 Homovalent substitution with divalent cations | 17 |
| III RESEARCH METHODOLOGY | 19 |
| 3.1 Synthetic techniques | 19 |
| 3.1.1 $\text{CH}_3\text{NH}_3\text{I}$ synthesis | 19 |
| 3.1.2 $\text{CH}_3\text{NH}_3\text{PbI}_3$ synthesis | 20 |

CONTENTS (Continued)

| | Page |
|---|-----------|
| 3.1.3 $\text{CH}_3\text{NH}_3\text{Pb}_{1-x}\text{M}_x\text{I}_3$ synthesis | 21 |
| 3.2 Characterization techniques | 22 |
| 3.2.1 Thermal gravimetric analysis | 22 |
| 3.2.2 X-Ray Diffraction | 24 |
| 3.2.3 UV-visible spectroscopy | 27 |
| 3.2.4 Fourier Transform Infrared Spectroscopy Analysis | 28 |
| 3.2.5 X-ray Photoelectrons Spectroscopy | 30 |
| 3.2.6 X-ray absorption spectroscopy | 32 |
| 3.2.7 Low-temperature phase transition | 37 |
| IV RESULT AND DISCUSSION | 42 |
| 4.1 $\text{CH}_3\text{NH}_3\text{I}$ synthesis | 42 |
| 4.1.1 TGA analysis | 43 |
| 4.1.2 XRD spectra | 44 |
| 4.1.3 XPS spectra | 45 |
| 4.2 $\text{CH}_3\text{NH}_3\text{PbI}_3$ perovskite | 47 |
| 4.2.1 TGA analysis | 47 |
| 4.2.2 XRD spectra | 49 |
| 4.2.3 UV-vis spectroscopy | 51 |
| 4.2.4 FT-Raman measurements | 55 |
| 4.2.5 XPS measurement | 59 |
| 4.2.6 XANES analysis | 63 |
| 4.2.7 EXAFS analysis | 64 |
| 4.2.8 Low temperature phase transition | 69 |

CONTENTS (Continued)

| | Page |
|---|------------|
| 4.3 Sn^{2+} doped on $\text{CH}_3\text{NH}_3\text{Pb}_{1-x}\text{Sn}_x\text{I}_3$ perovskite | 75 |
| 4.3.1 XRD spectra | 75 |
| 4.3.2 UV-vis spectroscopy | 79 |
| 4.3.3 FTIR measurement | 81 |
| 4.3.4 XPS measument | 83 |
| 4.3.5 XANES analysis | 92 |
| 4.3.6 EXAFS analysis | 95 |
| 4.3.7 Low temperature phase transition | 98 |
| 4.4 Ba^{2+} doped on $\text{CH}_3\text{NH}_3\text{Pb}_{1-x}\text{Ba}_x\text{I}_3$ perovskite | 102 |
| 4.4.1 XRD spectra | 102 |
| 4.4.2 UV-vis spectroscopy | 105 |
| 4.4.3 FTIR measurement | 107 |
| 4.4.4 XPS measument | 109 |
| 4.4.5 XANES analysis | 117 |
| 4.4.6 EXAFS analysis | 121 |
| 4.4.7 Low temperature phase transition | 123 |
| V CONCLUSIONS | 127 |
| REFERENCES | 129 |
| APPENDIX | 141 |
| CURRICULUM VITAE | 151 |

LIST OF TABLES

| Table | | Page |
|-------|---|------|
| 1.1 | Crystal systems and transition temperatures of $\text{CH}_3\text{NH}_3\text{PbX}_3$. . . | 6 |
| 2.1 | The Goldschmidt tolerance factor (t) values to formed perovskites structure. | 16 |
| 4.1 | Phase formation, lattice parameter and Crystallite size by Rietveld refinement of the XRD pattern. (when AT is annealed temperature, PF is phase formation, LP is lattice parameter and CS is crystallite size). | 51 |
| 4.2 | Measured resonance frequencies of vibrational modes and peak Assignments for perovskites. | 57 |
| 4.3 | The structure parameters coordination numbers N, interatomic distances R and DW factors σ^2 obtained by fitting the EXAFS data for the $\text{CH}_3\text{NH}_3\text{PbI}_3$ | 67 |
| 4.4 | Fitting parameters and goodness of fit (χ^2) for Arrhenius-type thermally-activated model and Vogel-Fulcher-type model of the dielectric relaxation of $\text{CH}_3\text{NH}_3\text{PbI}_3$ sample. The standard deviations of the fitting parameters are given in brackets. | 73 |
| 4.5 | Phase formation, lattice parameter by Rietveld refinement of Sn^{2+} substitution on $\text{MAPb}_{1-x}\text{Sn}_x\text{I}_3$ XRD pattern. | 78 |
| 4.6 | The structure parameters coordination numbers N, interatomic distances R and DW factors σ^2 obtained by fitting the EXAFS data for the $\text{CH}_3\text{NH}_3\text{Pb}_{0.9}\text{Sn}_{0.1}\text{I}_3$ | 96 |

LIST OF TABLES (Continued)

| Table | Page |
|-------|---|
| 4.7 | Fitting parameters and goodness of fit (χ^2) for Arrhenius-type thermally-activated model and Vogel-Fulcher-type model (marked by the asterisk) of the dielectric relaxation of $\text{CH}_3\text{NH}_3\text{Pb}_{0.9}\text{Sn}_{0.1}\text{I}_3$ at low-temperature fit (LT) and high-temperature fit (HT). The standard deviations of the fitting parameters are given in brackets. 100 |
| 4.8 | Phase formation, lattice parameter by Rietveld refinement of Ba^{2+} substitution on $\text{CH}_3\text{NH}_3\text{Pb}_{1-x}\text{Ba}_x\text{I}_3$ XRD pattern. 104 |
| 4.9 | The structure parameters coordination numbers N, interatomic distances R and DW factors σ^2 obtained by fitting the EXAFS data for the $\text{CH}_3\text{NH}_3\text{Pb}_{0.9}\text{Ba}_{0.1}\text{I}_3$ 121 |
| 4.10 | Fitting parameters and goodness of fit (χ^2) for Arrhenius-type thermally-activated model and Vogel-Fulcher-type model of the dielectric relaxation of $\text{CH}_3\text{NH}_3\text{Pb}_{0.9}\text{Ba}_{0.1}\text{I}_3$ materials. The standard deviations of the fitting parameters are given in brackets. 125 |

LIST OF FIGURES

| Figure | | Page |
|--------|---|------|
| 1.1 | crystal structure of $\text{CH}_3\text{NH}_3\text{PbX}_3$ perovskites (X= Cl, Br and I) (Eamesl et al., 2015). | 6 |
| 1.2 | NREL efficiency chart (NREL, 2018). | 9 |
| 1.3 | Overview of the application procedure and the ions calculated (562 organic anion based, 180 halide based) (Kieslich et al., 2015). . . | 11 |
| 2.1 | Calculated t and μ map for different cations (B) in $\text{CH}_3\text{NH}_3\text{BI}_3$ perovskite system for 34 metals to predict novel lead-free perovskite. | 17 |
| 3.1 | Flow chart of the synthesis of $\text{CH}_3\text{NH}_3\text{I}$ powders. | 20 |
| 3.2 | Flow chart of the synthesis of $\text{CH}_3\text{NH}_3\text{PbI}_3$ materials. | 21 |
| 3.3 | Flow chart of the synthesis of $\text{CH}_3\text{NH}_3\text{Pb}_{1-x}\text{Sn}_x\text{I}_3$ and $\text{CH}_3\text{NH}_3\text{Pb}_{1-x}\text{Ba}_x\text{I}_3$ materials. | 22 |
| 3.4 | Heat Flux DSC. | 23 |
| 3.5 | Basic components of X-ray diffractometers. | 25 |
| 3.6 | Schematic representation of diamond ATR accessory. | 29 |
| 3.7 | Schematic of XPS instrument. | 31 |

LIST OF FIGURES (Continued)

| Figure | | Page |
|--------|--|------|
| 3.8 | Schematic of X-ray processes which include photoemission, X-ray fluorescence and Auger electron emission where $h\nu$ is the incident photon, E_{ae} is the energy of the outgoing Auger electron ($E_{ae} = E_K - E_L - E_M$), E_p is the energy of the outgoing photoelectron or relaxation ($E_p = h\nu - E_K - E_M$), E_{erf} is the energy of the outgoing fluorescence photon ($E_{erf} = E_K - E_M$) and E_K , E_L and E_M are the energies of the K, L, and M orbitals respectively. | 33 |
| 3.9 | XAS spectrum of I L3-edge collected in transmission mode. . . . | 34 |
| 3.10 | Detail an atoms.inp input file to generate “feff.inp” for FEFF calculation. | 36 |
| 3.11 | Detail of feff.inp input file of $\text{CH}_3\text{NH}_3\text{PbI}_3$ with Pb as center atom for FEFF calculation. | 38 |
| 3.11 | (Continued) Detail of feff.inp input file of $\text{CH}_3\text{NH}_3\text{PbI}_3$ with Pb as center atom for FEFF calculation. | 39 |
| 3.11 | (Continued) Detail of feff.inp input file of $\text{CH}_3\text{NH}_3\text{PbI}_3$ with Pb as center atom for FEFF calculation. | 40 |
| 3.12 | The alpha Impedance Analyzer in conjunction with the physical property measurement system. | 41 |
| 4.1 | Weight loss curves of powder. | 44 |
| 4.2 | The XRD spectra of $\text{CH}_3\text{NH}_3\text{I}$ powders from mixed precursor solution of HI and CH_3NH_2 | 45 |
| 4.3 | The XPS spectra of a) C 1s, b) N 1s, c) I 3d and O 1s for $\text{CH}_3\text{NH}_3\text{I}$ | 46 |

LIST OF FIGURES (Continued)

| Figure | | Page |
|--------|---|------|
| 4.4 | The weight loss curves of CH ₃ NH ₃ PbI ₃ powder (red) and data from Amalie et al. (black). | 48 |
| 4.5 | a) XRD patterns of CH ₃ NH ₃ PbI ₃ annealed at different temperatures and b) the magnified XRD spectra of (002) and (110) peaks (# PbI ₂). | 53 |
| 4.6 | Rietveld refinement of the powder X-ray diffraction data of the CH ₃ NH ₃ PbI ₃ materials with experimental data are show as • symbols. The solid line is fit, the vertical bars are the expected Bragg reflection position. | 54 |
| 4.7 | The absorption spectra of the CH ₃ NH ₃ PbI ₃ samples. | 54 |
| 4.8 | FTIR spectra of MAPbI powder in the range of 700-4400 cm ⁻¹ | 57 |
| 4.9 | The Raman spectra of MAPbI powder in the range of 50-300 cm ⁻¹ a) and b) comparison between Raman and FTIR spectra in the range of 800-1700 cm ⁻¹ | 58 |
| 4.10 | XPS survey scan of CH ₃ NH ₃ PbI ₃ powders. | 61 |
| 4.11 | XPS spectra of CH ₃ NH ₃ PbI ₃ samples and the Gaussian fitting for Pb 4f of a) MAPbI, b) MAPbI-150°C and c) MAPbI-200°C. | 61 |
| 4.12 | XPS spectra of CH ₃ NH ₃ PbI ₃ samples and the Gaussian fitting for I 3d of a) MAPbI, b) MAPbI-150°C and c) MAPbI-200°C. | 62 |
| 4.13 | XPS spectra of CH ₃ NH ₃ PbI ₃ samples and the Gaussian fitting for C 1s of a) MAPbI, b) MAPbI-150°C and c) MAPbI-200°C. | 62 |
| 4.14 | XPS spectra of CH ₃ NH ₃ PbI ₃ samples and the Gaussian fitting for N 1s of a) MAPbI, b) MAPbI-150°C and c) MAPbI-200°C. | 62 |

LIST OF FIGURES (Continued)

| Figure | Page |
|--|------|
| 4.15 XPS spectra of $\text{CH}_3\text{NH}_3\text{PbI}_3$ samples and the Gaussian fitting for O 1s of a) MAPbI, b) MAPbI-150°C and c) MAPbI-200°C. . . . | 63 |
| 4.16 Measured Pb M5-edge XANES spectra (a) and calculated Pb M5-edge XANES spectra (b). | 65 |
| 4.17 Measured I L3-edge XANES spectra (a) and calculated I L3-edge XANES spectra (b). | 66 |
| 4.18 Comparison of Experiment and fitted magnitude of EXAFS Fourier transform (FT) (a) and (b) comparison of k^2 -weighted spectrum over the k -range of $\text{CH}_3\text{NH}_3\text{PbI}_3$. The k range used in the FT is from $3\text{-}8.7 \text{ \AA}^{-1}$ for data set. | 68 |
| 4.19 Low temperature heat capacity and inset show the C/T^3 of related $\text{CH}_3\text{NH}_3\text{PbI}_3$ material. | 71 |
| 4.20 Temperature dependence of dielectric permittivity and dielectric loss of $\text{CH}_3\text{NH}_3\text{PbI}_3$, $\text{CH}_3\text{NH}_3\text{Pb}_{0.9}\text{Sn}_{0.1}\text{I}_3$ and $\text{CH}_3\text{NH}_3\text{Pb}_{0.9}\text{Ba}_{0.1}\text{I}_3$ | 72 |
| 4.21 Low temperature of permittivity (ϵ_r) and loss tangent ($\tan \delta$) of $\text{CH}_3\text{NH}_3\text{PbI}_3$. Frequency dependent dielectric loss peaks indicating substantial slowing of relaxation dynamics are observed in the sample. | 73 |
| 4.22 Natural logarithm of f as the function of $1/T$ by Arrhenius model a) and b) with the function of T_{max} by Vogel-fulcher fit model for $\text{CH}_3\text{NH}_3\text{PbI}_3$ | 74 |

LIST OF FIGURES (Continued)

| Figure | | Page |
|--------|---|------|
| 4.23 | Rietveld refinement of the powder X-ray diffraction data of the Sn^{2+} doped $\text{CH}_3\text{NH}_3\text{Pb}_{1-x}\text{Sn}_x\text{I}_3$ materials with $x =$ a) 0.02, b) 0.04, c) 0.06, d) 0.08, e) 0.1 and f) 0.2. Experimental data are show as \bullet symbols. The solid line is fit, the vertical bars are the expected Bragg reflection position. | 76 |
| 4.24 | The XRD expanded peak at 2θ of around $13.5\text{-}14.5^\circ$, when a) Sn^{2+} substitution and b) Ba^{2+} substitution. | 77 |
| 4.25 | a) diffuse reflectance UV vis spectra for $\text{CH}_3\text{NH}_3\text{Pb}_{1-x}\text{Sn}_x\text{I}_3$ samples with 0.02-0.2 Sn^{2+} substitutions and b) the plot of the optical bandgap values for each samples. | 80 |
| 4.26 | FTIR spectra of Sn^{2+} substituted in $\text{CH}_3\text{NH}_3\text{PbI}_3$ materials in the range of $500\text{-}1700\text{ cm}^{-1}$ | 82 |
| 4.27 | XPS survey scan of Sn^{2+} substituted in $\text{CH}_3\text{NH}_3\text{Pb}_{1-x}\text{Sn}_x\text{I}_3$ materials. | 84 |
| 4.28 | XPS spectra for C 1s of the samples and the Gaussian fitting, when a) 0.02, b) 0.04, c) 0.06, d) 0.08, e) 0.1 and f) 0.2 Sn^{2+} substituted in $\text{CH}_3\text{NH}_3\text{Pb}_{1-x}\text{Sn}_x\text{I}_3$ materials. | 85 |
| 4.29 | XPS spectra for N 1s of the samples and the Gaussian fitting, when a) 0.02, b) 0.04, c) 0.06, d) 0.08, e) 0.1 and f) 0.2 Sn^{2+} substituted in $\text{CH}_3\text{NH}_3\text{Pb}_{1-x}\text{Sn}_x\text{I}_3$ materials. | 86 |
| 4.30 | XPS spectra for I 3d of the samples and the Gaussian fitting, when a) 0.02, b) 0.04, c) 0.06, d) 0.08, e) 0.1 and f) 0.2 Sn^{2+} substituted in $\text{CH}_3\text{NH}_3\text{Pb}_{1-x}\text{Sn}_x\text{I}_3$ materials. | 87 |

LIST OF FIGURES (Continued)

| Figure | Page |
|--------|---|
| 4.31 | XPS spectra for Pb 4f of the samples and the Gaussian fitting, when a) 0.02, b) 0.04, c) 0.06, d) 0.08, e) 0.1 and f) 0.2 Sn ²⁺ substituted in CH ₃ NH ₃ Pb _{1-x} Sn _x I ₃ materials. 88 |
| 4.32 | XPS spectra for Sn 3d of the samples and the Gaussian fitting, when a) 0.02, b) 0.04, c) 0.06, d) 0.08, e) 0.1 and f) 0.2 Sn ²⁺ substituted in CH ₃ NH ₃ Pb _{1-x} Sn _x I ₃ materials. 89 |
| 4.33 | XPS spectra for O 1s of the samples and the Gaussian fitting, when a) 0.02, b) 0.04, c) 0.06, d) 0.08, e) 0.1 and f) 0.2 Sn ²⁺ substituted in CH ₃ NH ₃ Pb _{1-x} Sn _x I ₃ materials. 90 |
| 4.34 | Measured Pb M5-edge XANES spectra (a) and calculated Pb M5-edge XANES spectra (b) of CH ₃ NH ₃ Pb _{0.9} Sn _{0.1} I ₃ materials. 93 |
| 4.35 | Measured I L3-edge XANES spectra (a) and calculated I L3-edge XANES spectra (b) of CH ₃ NH ₃ Pb _{0.9} Sn _{0.1} I ₃ materials. 94 |
| 4.36 | Calculated Sn L3-edge XANES spectra of CH ₃ NH ₃ Pb _{0.9} Sn _{0.1} I ₃ materials. 95 |
| 4.37 | Comparison of Experiment and fitted magnitude of EXAFS Fourier transform (FT) (a) and (b) comparison of k ² -weighted spectrum over the k-range of CH ₃ NH ₃ Pb _{0.9} Sn _{0.1} I ₃ . The k range used in the FT is from 3-8.7 Å ⁻¹ for data set 97 |

LIST OF FIGURES (Continued)

| Figure | | Page |
|--------|---|------|
| 4.38 | Low temperature of permittivity (ϵ_r) and loss tangent ($\tan \delta$) of $\text{CH}_3\text{NH}_3\text{Pb}_{0.9}\text{Sn}_{0.1}\text{I}_3$ perovskite. Frequency dependent dielectric loss peaks indicating substantial slowing of relaxation dynamics are observed in the sample. | 99 |
| 4.39 | Natural logarithm of f as the function of $1/T$ by Arrhenius model a) and b)with the function of T_{max} by Vogel-fulcher fit model for $\text{CH}_3\text{NH}_3\text{Pb}_{0.09}\text{Sn}_{0.1}\text{I}_3$ | 101 |
| 4.40 | Rietveld refinement of the powder X-ray diffraction data of the Ba^{2+} doped $\text{CH}_3\text{NH}_3\text{Pb}_{1-x}\text{Ba}_x\text{I}_3$ materials with $x =$ a) 0.02, b) 0.04, c) 0.06, d) 0.08, e) 0.1 and f) 0.2. Experimental data are show as \bullet symbols. The solid line is fit, the vertical bars are the expected Bragg reflection position. | 103 |
| 4.41 | a) diffuse reflectance UV vis spectra for $\text{CH}_3\text{NH}_3\text{Pb}_{1-x}\text{Ba}_x\text{I}_3$ samples with 0.02-0.2 Ba^{2+} substitutions and b) the plot of the optical bandgap values for each samples. | 106 |
| 4.42 | FTIR spectra of Ba^{2+} substituted in $\text{CH}_3\text{NH}_3\text{Pb}_{1-x}\text{Ba}_x\text{I}_3$ materials in the range of 500-1700 cm^{-1} | 108 |
| 4.43 | XPS survey scan of Ba^{2+} substituted in $\text{CH}_3\text{NH}_3\text{Pb}_{1-x}\text{Ba}_x\text{I}_3$ materials. | 110 |
| 4.44 | XPS spectra for C 1s of the samples and the Gaussian fitting, when a) 0.02, b) 0.04, c) 0.06, d) 0.08, e) 0.1 and f) 0.2 Ba^{2+} substituted in $\text{CH}_3\text{NH}_3\text{Pb}_{1-x}\text{Ba}_x\text{I}_3$ materials. | 111 |

LIST OF FIGURES (Continued)

| Figure | | Page |
|--------|---|------|
| 4.45 | XPS spectra for N 1s of the samples and the Gaussian fitting, when a) 0.02, b) 0.04, c) 0.06, d) 0.08, e) 0.1 and f) 0.2 Ba ²⁺ substituted in CH ₃ NH ₃ Pb _{1-x} Ba _x I ₃ materials. | 112 |
| 4.46 | XPS spectra for I 3d of the samples and the Gaussian fitting, when a) 0.02, b) 0.04, c) 0.06, d) 0.08, e) 0.1 and f) 0.2 Ba ²⁺ substituted in CH ₃ NH ₃ Pb _{1-x} Ba _x I ₃ materials. | 113 |
| 4.47 | XPS spectra for Pb 4f of the samples and the Gaussian fitting, when a) 0.02, b) 0.04, c) 0.06, d) 0.08, e) 0.1 and f) 0.2 Ba ²⁺ substituted in CH ₃ NH ₃ Pb _{1-x} Ba _x I ₃ materials. | 114 |
| 4.48 | XPS spectra for Ba 3d of the samples and the Gaussian fitting, when a) 0.02, b) 0.04, c) 0.06, d) 0.08, e) 0.1 and f) 0.2 Ba ²⁺ substituted in CH ₃ NH ₃ Pb _{1-x} Ba _x I ₃ materials. | 115 |
| 4.49 | XPS spectra for O 1s of the samples and the Gaussian fitting, when a) 0.02, b) 0.04, c) 0.06, d) 0.08, e) 0.1 and f) 0.2 Ba ²⁺ substituted in CH ₃ NH ₃ Pb _{1-x} Ba _x I ₃ materials. | 116 |
| 4.50 | Measured Pb M5-edge XANES spectra (a) and calculated Pb M5- edge XANES spectra (b) of CH ₃ NH ₃ Pb _{0.9} Ba _{0.1} I ₃ materials. . . . | 118 |
| 4.51 | Measured I L3-edge XANES spectra (a) and calculated I L3-edge XANES spectra (b) of CH ₃ NH ₃ Pb _{0.9} Ba _{0.1} I ₃ materials. | 119 |
| 4.52 | Measured Ba L3-edge XANES spectra (a) and calculated Ba L3- edge XANES spectra (b) of CH ₃ NH ₃ Pb _{0.9} Ba _{0.1} I ₃ materials. . . . | 120 |

LIST OF FIGURES (Continued)

| Figure | | Page |
|--------|---|------|
| 4.53 | Comparison of Experiment and fitted magnitude of EXAFS Fourier transform (FT) (a) and (b) comparison of k^2 -weighted spectrum over the k -range of $\text{CH}_3\text{NH}_3\text{Pb}_{0.9}\text{Ba}_{0.1}\text{I}_3$. The k range used in the FT is from $3\text{--}8\text{ \AA}^{-1}$ for data set. | 122 |
| 4.54 | Low temperature heat capacity of related $\text{CH}_3\text{NH}_3\text{Pb}_{0.9}\text{Ba}_{0.1}\text{I}_3$ material. | 124 |
| 4.55 | Low temperature of permittivity (ϵ_r) and loss tangent ($\tan \delta$) of $\text{CH}_3\text{NH}_3\text{Pb}_{0.9}\text{Ba}_{0.1}\text{I}_3$ Frequency dependent dielectric loss peaks indicating substantial slowing of relaxation dynamics are observed in the sample. | 125 |
| 4.56 | Natural logarithm of f as the function of $1/T$ by Arrhenius model a) and b) with the function of T_{max} by Vogel-fulcher fit model for $\text{CH}_3\text{NH}_3\text{Pb}_{0.9}\text{Ba}_{0.1}\text{I}_3$ | 126 |



LIST OF ABBREVIATIONS

| | |
|--------------|---|
| BE | Binding energy |
| E_a | Activation energy |
| eV | Electron volt |
| EXAFS | Extended X-ray absorption fine edge structure |
| FTIR | Fourier Transform Infrared Spectroscopy |
| f_0 | pre-exponential factor |
| GOF | Goodness of fit |
| MAI | Methylammonium iodide $\text{CH}_3\text{NH}_3\text{I}$ |
| MAPbI | Methylammonium lead iodide $\text{CH}_3\text{NH}_3\text{PbI}_3$ |
| PCE | Power conversion efficiency |
| PPMS | Physical property measurement system |
| r_A | A-site cation |
| r_B | B-site cation |
| r_X | X-site cation |
| t | Goldschmidt tolerance factor |
| $\tan\delta$ | Dielectric loss |
| TGA | Thermal gravimetric analysis |
| T_{VF} | Volgel-Fulcher temperature |
| UV-vis | UV-Visible spectroscopy |
| XANES | X-ray absorption near edge structure |
| XAS | X-ray absorption spectroscopy |
| XPS | X-ray photoelectron spectroscopy |
| XRD | X-ray diffraction |

CHAPTER I

INTRODUCTION

1.1 Background

The silicon-based solar cells have been dominating the photovoltaic market. To achieve good light absorption, relatively thick layers of silicon need to be used. This limits the range of applications where silicon solar cells can be used and hinder the further reduction of their price. In recent years, new materials have been investigated in search of materials that could replace silicon. New solar cell materials have to fulfill a number of demands, including high power conversion efficiencies and low production costs. Moreover, the materials need to be non-toxic, stable over long periods of time and light weight. Especially thin film materials such as CdTe, amorphous silicon and organic molecules are being investigated as promising candidates for a next generation of solar cells.

A new group of materials has emerged as a potential candidate for solar cells production, which is organometal halide perovskite produced in 2009 (Kojima et al., 2009). After that, a rapid increase of the powder conversion efficiencies and the unusual properties of these perovskite materials, have attracted a lot attention and motivated many researchers to focus on this materials group.

In general, perovskites have the structural analogues of the natural crystal of calcium titanium oxide, covering a broad range of versatile materials with applications in many fields such as sensors (Fatih et al., 2015) super conductors (BA, 2003), fuel cell (Vassiliy and Peter, 2003), ferroelectric and thermoelectric (Fatih et al., 2015). The new group of rediscovered members of this family, organo-

lead halide perovskites turned out to be trending component of solar cell (Kojima et al., 2009). Incorporated as a light harvester in solar cell, a remarkable power conversion efficiency of 21.2% was demonstrated in lab-scale device. It can show that apart from the role of the light absorber, the organo-lead halide perovskites can be found both as electron and hole transporting media due to conversions have been reached with three main compounds ($\text{CH}_3\text{NH}_3\text{PbI}_3$:MAPbI₃, $\text{CH}_3\text{NH}_3\text{PbI}_{3-x}\text{Cl}_x$:MAPbI_{3-x}Cl_x and $\text{CH}_3\text{NH}_3\text{PbI}_{3-x}\text{Br}_x$:MAPbI_{3-x}Br_x) showing little modifications in halide content (Nguyen et al., 2016). The direct band gap of semiconductors with a high absorption coefficient, a favorable band gap of 1.48-2.23 eV (Eperon et al., 2014; Noh et al., 2013). However, structural and electronic differences between the three materials, such as the exact role of I, Cl and Br anions have yet to be undoubtedly determined by the community. The scientist observed that incorporation of I or Cl as an dopant can improve the charge transport within the perovskites layer and increase the performance of the photovoltaic and optical properties. The Cl inclusion enhances the granular morphology resulting by electron beam induced current method (EBIC). These findings validate the band gap engineering strategies; the band gap of material might be efficiently adjusted by choosing the halide anion and the organic amide constituent. The key aspects towards a low-coat technology capable of competing with the established silicon technology lies in the material low temperature solution process ability. The current method bare based on both one-step and two-step deposition of a mixture of PbX₂ and CH₃NH₃I (X is halide anion) in a common solvent or sequential deposition of the constituents from a solution onto a mesoscopic scaffold and two-step coating methods. The coverage, pore-filling, and morphology of the deposited perovskite are found to be observed during coating. Both one-step and two step coating methods resulted in reproducible photovoltaic performance, but signifi-

cant difference in especially photovoltage and fill factor. The electron life time was dependent on coating procedure (Jeong-Hyeok et al., 2014). Recent results demonstrated an efficiency of 21.1% on maxing perovskite materials with inorganic cesium. This indicates that it is critical to have fine control over the nucleation and crystal growth of the $\text{CH}_3\text{NH}_3\text{PbI}_3$. The effort to control the morphology of the organometal trihalide perovskite based solar cell by varying processing conditions and the highest photocurrent are attainable only with the highest perovskite surface coverage (Saliba et al., 2016). As well known, despite the success in obtaining excellent photovoltaic performance, the instability of $\text{CH}_3\text{NH}_3\text{PbX}_3$ to water and ambient moisture is still an open problem. Even though perovskite films have to be processed in inert atmosphere and devices cannot survive long in air, which hinder the production and applications of perovskite solar cells (Qidong et al., 2016). In addition, the $\text{CH}_3\text{NH}_3\text{PbX}_3$ perovskite semiconductor has attracted attention because of ease of solution processing and excellent absorption properties. It was often formed from the solution, containing equimolar mixture of MAI ($\text{CH}_3\text{NH}_3\text{I}$ and PbX_2 by co-precipitation method using spin coating technique. Moreover, it has been reported a one-pot solvothermal approach to synthesis the cuboid shaped $\text{CH}_3\text{NH}_3\text{PbI}_3$ single crystal (Yongping et al., 2015).

Today, research in this emerging field is largely driven by the intriguing properties of the hybrid perovskite $\text{CH}_3\text{NH}_3\text{PbI}_3$ in thin film solar cell devices. However, other hybrid perovskites, for example the family of perovskite like metal formats $\text{AB}(\text{HCOO})_3$ (A = protonated amine, B = divalent metal), also show interesting properties such as multiferroic behavior and tunable mechanical properties.

Even then, there are some caveats associated with the various components of the $\text{CH}_3\text{NH}_3\text{PbX}_3$ -based: the stability of the absorber material in ambient conditions and the presence of Pb-toxic to name a couple. Now research addressing

these problems is being conducted worldwide through suitable replacements to both the CH_3NH_3 and Pb cations (Jeong-Hyeok et al., 2014; D B et al., 1995). The properties by changing the constituent elements give this class of material more scope of research and applicability. Such as the bandgap have been observed in the oxide perovskite in only a small variation in bandgap is in ATiO_3 compounds, with A being Sr (3.57 eV), Ba (3.42 eV) and Pb (2.87 eV) (Piskunov et al., 2004). However, there is a large change in bandgap on changing the B cation, e.g. BaTiO_3 (3.72 eV) and BaZrO_3 (5.04 eV) (Wang et al., 2014). The optimization of the absorber material in the case of the lead halide perovskites is also done in a similar manner, albeit via replacement of the halide i.e. I with Br and Cl and the associated changes in the band gap and structure was the subject of many studies (Qingbiao et al., 2004; Wang et al., 2004; Yongping et al., 2015; Nguyen et al., 2016). Similarly, reports on replacing or mixing organic A cation such as CH_3NH_3 with formamidinium have shown that their stability in ambient conditions is increased, albeit its impact on properties of band gap (Noh et al., 2013; Yongping et al., 2015; Nguyen et al., 2016).

Thus, in this work we focus on the synthesis of this particularly promising class of crystalline organic-inorganic lead-free perovskite in form of $\text{CH}_3\text{NH}_3\text{Pb}_{1-x}\text{M}_x\text{I}_3$ (When $\text{M} = \text{Pb}, \text{Sn}$ and Ba) materials powders. The crystalline materials have the advantage that they can be structurally characterized using techniques such as X-ray diffraction; make it possible to correlate structural features with specific materials properties. The crystalline nature and the rigid extended inorganic framework provide opportunities for higher electrical mobility, better thermal stability and template of organic component of the structure. X-ray absorption spectroscopy and X-ray photoelectron spectroscopy; to confirm the presence of some compounds such as metal oxide, and other characterization

techniques to confirm characteristics and properties of materials such as Fourier transform infrared spectroscopy, UV-Vis spectrometer, Raman spectroscopy, and low-temperature permittivity dielectric were also be employed to study the prepared products.

1.2 Perovskite

The name of “Perovskite” has first name of mineral composed of calcium titanate with the formula of CaTiO_3 . The calcium titanium oxide was discovered in 1839 by Gustav Rose and then, the mineralogist use perovskite to describe the crystal with the same as formula ABX_3 . In this structure A and B are cations and X is anion and have valence value ration as 1:2:1 and is derived from the ABX_3 crystal structure of the absorber materials, which is referred to as perovskite structure.

Recently, the most commonly studied perovskite is methylammonium lead trihalide ($\text{CH}_3\text{NH}_3\text{PbX}_3$, where X is a halogen atom such as iodine, bromine or chlorine), with have bandgab between 1.5 and 2.3 eV depending on halide content. The perovskite structure, illustrated in Figure 2.1, is comprised of an extended framework of corner-sharing PbI_6 octahedral with the methylammonium cation ($\text{CH}_3\text{NH}_3\text{I}$) occupying the central A site and surrounded by 12 nearest-neighbor iodide ions.

The methylammonium lead halide perovskites was first used by D. Weber in 1978 (Weber, 1978). His definition referred to methylammonium lead halide perovskites ($\text{CH}_3\text{NH}_3\text{PbX}_3$: X = Cl, Br, I) as cubic perovskite structure and provide structural transition upon heating. The systems and transition temperatures are summarized in Table 1.1, as reported in the previous works (Jung and Park, 2014; Knop et al., 1990).

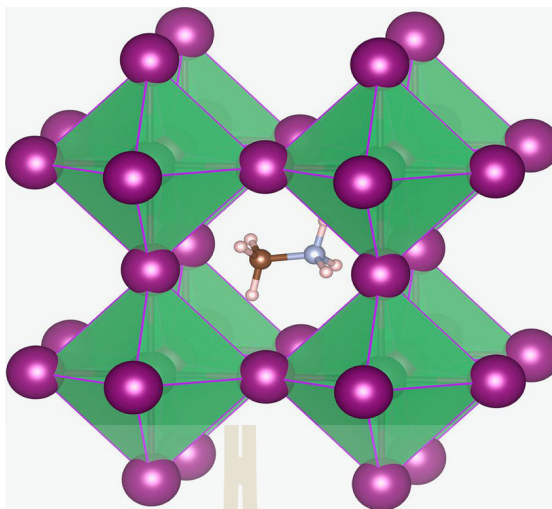


Figure 1.1 crystal structure of $\text{CH}_3\text{NH}_3\text{PbX}_3$ perovskites ($\text{X} = \text{Cl}, \text{Br}$ and I) (Eamesl et al., 2015).

Table 1.1 Crystal systems and transition temperatures of $\text{CH}_3\text{NH}_3\text{PbX}_3$.

| Material | $\text{CH}_3\text{NH}_3\text{PbCl}_3$ | $\text{CH}_3\text{NH}_3\text{PbBr}_3$ | $\text{CH}_3\text{NH}_3\text{PbI}_3$ |
|----------------------------|---------------------------------------|---------------------------------------|--------------------------------------|
| Crystal system | Cubic | Cubic | Cubic |
| Transition Temperature (K) | 177 | 236 | 330 |
| Crystal system | Tetragonal | Tetragonal | Tetragonal |
| Transition Temperature (K) | 172 | 149-154 | 161 |

For $\text{CH}_3\text{NH}_3\text{PbX}_3$ ($\text{X} = \text{Cl}, \text{Br}, \text{I}$) has the cubic perovskite structure with the unit cell parameters $a = 5.68 \text{ \AA}$ ($\text{X} = \text{Cl}$), $a = 5.92 \text{ \AA}$ ($\text{X} = \text{Br}$) and $a = 6.27 \text{ \AA}$ ($\text{X} = \text{I}$). With exception of $\text{CH}_3\text{NH}_3\text{PbCl}_3$ the compounds show intense color, but there is no significant conductivity under normal conditions (Weber, 1978). In addition, his synthesis $\text{CH}_3\text{NH}_3\text{SnBr}_x\text{I}_{3-x}$ ($x = 0-3$) and mixed Sn(II)/Pb(II) compounds of the type $\text{CH}_3\text{NH}_3[\text{Pb}_n\text{Sn}_{1-n}\text{X}_3]$ ($\text{X} = \text{Cl}, \text{Br}, \text{I}$) have the cubic perovskite structure which is established by X-ray powder data. With exception of the chloro system the colored compounds show the increasing of electrical conductivity with increased Sn(II) content. Their physical properties can be interpreted

by means of a “p-resonance bonding”. Replacement of Sn(II) by Pb(II) and I by Br and Cl decreases this bonding effect, which is produced by the interaction of filled X p-orbital with empty p-orbital of Sn(II) or Pb(II) (Weber, 1978, 1979). Knop et al reported that the preparation single-crystal of $\text{CH}_3\text{NH}_3\text{PbX}_3$ and characterized them by single-crystal X-ray diffraction, NMR, adiabatic calorimetry and other methods. To phase of Pm3m symmetry which exists above the upper transition temperature ($T_{\text{tr,u}}$), each of three halides has low-temperature phases. The transition temperatures were determined by heat capacity measurements in the 30 to 350 K range. The cation is inside a cuboctahedral (Oh) cage formed by twelve X atoms undergoing strongly anisotropic thermal motions. XRD has revealed that the cation is positional highly disordered, and evidence from ^2H and ^{14}N nmr spectra show that it reorientates in an isotropic potential at a rate which at 373 K approaches that expected for inertial rotation. In the chloride, the tumbling of the C-N axis ceases on cooling through $T_{\text{tr,u}}$, whereas in the bromide and iodide it continues at a decreasing rate and in an increasingly anisotropic potential. The electrical conductivity of $\text{CH}_3\text{NH}_3\text{PbI}_3$ increases with the increasing of between temperature 0 and 95°C and exhibits no discontinuity at $T_{\text{tr}} = 326.6$ K; the activation energy for the conduction process is estimated at ~ 0.4 eV (Knop et al., 1990; D B et al., 1995).

Since 1996, the heat capacities of $\text{CH}_3\text{NH}_3\text{BF}_4$ and $\text{CD}_3\text{ND}_3\text{BF}_4$ were measured in the temperature ranges 5-300 and 13-300 K, respectively. A large heat capacity peak due to a first-order transition appeared at 251.3 ± 0.1 K for $\text{CH}_3\text{NH}_3\text{BF}_4$ and 251.6 ± 0.1 K for $\text{CD}_3\text{ND}_3\text{BF}_4$. The transition entropies of $\text{CH}_3\text{NH}_3\text{BF}_4$ and $\text{CD}_3\text{ND}_3\text{BF}_4$ were 20.47 ± 0.02 $\text{JK}^{-1}\text{mol}^{-1}$ and were 20.47 ± 0.02 $\text{JK}^{-1}\text{mol}^{-1}$, respectively. These data indicate that the effects of deuterium substitution on both anomalies are minor in this compound (Onoda-Yamamuro

et al., 1996). In the same year, Mitzi et al (D B et al., 1995). studies crystal structure, optical and thermal properties of $(C_4H_9NH_3)_2MI_4$ ($M = Ge, Sn, Pb$) single crystals which have been grown from aqueous hydroiodic acid solutions. For the $(C_4H_9NH_3)_2GeI_4$ melts at $222(2)^\circ C$, significantly below its bulk decomposition temperature, $(C_4H_9NH_3)_2SnI_4$ ($T_m = 256(2)^\circ C$) and $(C_4H_9NH_3)_2PbI_4$ ($T_m = 285(4)^\circ C$) melt/decompose at progressively higher temperature and are less stable as a melt. At room temperature, photoluminescence of a few $(C_4H_9NH_3)_2MI_4$ exhibits a pronounced spectral peak in the visible range, with the peak wavelength varying between $690(5)$, $625(1)$ and $525(1)$ nm for the $M = Ge, Sn$ and Pb compounds, respectively. This materials can be prepared by spin-coated thin film of semiconducting perovskite $(C_4H_9NH_3)_2SnI_4$ from the conducting channel, with field-effect motilities of 0.6 square centimeters per volt-second and current modulation greater than 104. The organic and inorganic components of the hybrids are expected to further improve device performance for low-cost thin-film transistors (D B et al., 1995; Kagan et al., 1999). Other than optical properties of microcrystalline $CH_3NH_3PbX_3$ ($X=$ halogen) are their mixed-halide crystals were fabricated by the spin coating technique and their optical properties were investigated. The $CH_3NH_3PbBr_{3-x}Cl_x$ ($x = 0-3$) were successfully formed on glass substrate self-assembly and oriented with the a-axis. These materials showed clear excitation absorption and free-excitation emission in the visible region at room temperature. Replacing Br and Cl made it possible to control the band structure of materials. The peak position of the excitation band shifted continuously towards blue region with increasing the Cl content in the films (Kitazawa et al., 2002).

Moreover, the human society is depleting fossil energy and increasing energy demands. In order to solve these issues, the construction of efficient and clean energy conversion and storage devices, such as wind turbines, photovoltaic cells,

and lithium-ion (secondary) battery, is essential.

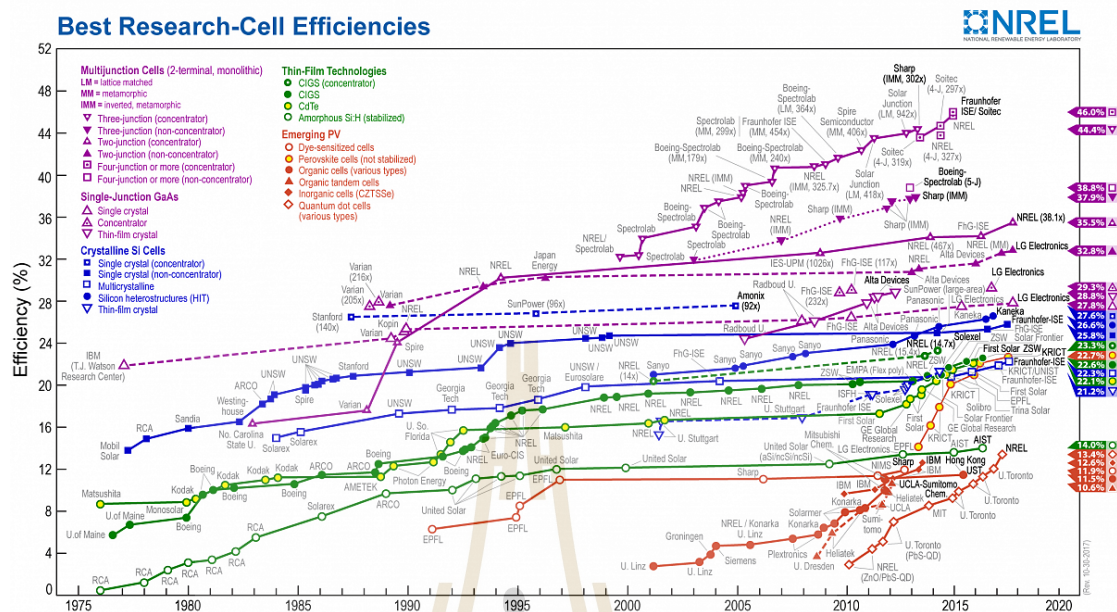


Figure 1.2 NREL efficiency chart (NREL, 2018).

Apart from the above mentioned studies, methylammonium lead halide perovskites materials have been well known for many years, but the first incorporation into a solar cell was reported by Kojima et al. in 2009 (Kojima et al., 2009). This was based on dye-sensitized solar cell architecture and generated only 3.8% power conversion efficiency (PCE) with a thin layer of perovskite on mesoporous TiO_2 as electron-collector. Because a liquid corrosive electrolyte was used, the cell was only stable for a matter of minutes. This was improved upon in 2011, using the same dye-sensitized concept, achieving 6.5% PCE (Jeong-Hyeok et al., 2014). In 2012 success, when Snaith et al. from the University of Oxford realized that the perovskite materials was stable if contacted with a solid-state hole transporter such as spiro-OMeTAD and did not require the mesoporous TiO_2 layer in order to transport electrons (Liu et al., 2013). They showed that efficiencies of almost 9% were achievable using TiO_2 architecture with the solid-state holes transporter, but higher efficiencies, above 10%, were attained by replacing it with TiO_2 scaffold

(Kim et al., 2012). The experiments in replacing the mesoporous TiO_2 with Al_2O_3 resulted in increased open-circuit voltage and a relative improvement in efficiency more than those with TiO_2 (Liu et al., 2013). Which leads to that a scaffold is not needed for electron extraction (Ball et al., 2013). This realization was then closely followed by a demonstration that the perovskite itself could also transport holes, as well as electron. In 2013-2014 both the planar and sensitized by two step solution processing (Burschka et al., 2013) and fabricate planar solar cells by thermal evaporation, which achieving more than 15% efficiency (Liu et al., 2013). In addition, a new deposition technique, nanowire by mean of small quantity of a protic solvent in two-step spin-coating process and synthesis of nanostructure from a novel single-source precursor were reported in 2015 (Jeong-Hyeok et al., 2014; Jin Hyuck et al., 2014; Kollek et al., 2014; Jung and Park, 2014). It was shown that the use of a suitable capping agent enables the control of the shape and the aspect ratio of the perovskite nanocrystals. The same year in December, a research team headed by Prof. M. Grätzel at the Ecole Poly technique Fédérale de Lausanne (EPFL) has established a new world record efficiency for its Perovskite Solar Cells (PSC), with a certified conversion efficiency of 21.7%.

In April 2016, the efficient and stable perovskite solar cells prepared in ambient air irrespective of the humidity was achieved by researchers at The Hong Kong Polytechnic University (Qidong et al., 2016). They reported the use of $\text{Pb}(\text{SCN})_2$ as a precursor for preparing perovskite solar cells in ambient air. It demonstrated by the PCEs up to 15% obtained without humidity control and highlighted by the little efficiency loss ($< 15\%$) upon long-term (> 500 hrs) ageing in humid air without encapsulation.

In addition, during recent years a structurally hybrid perovskite architecture is essentially maintained. Today, this emerging field is largely driven by the

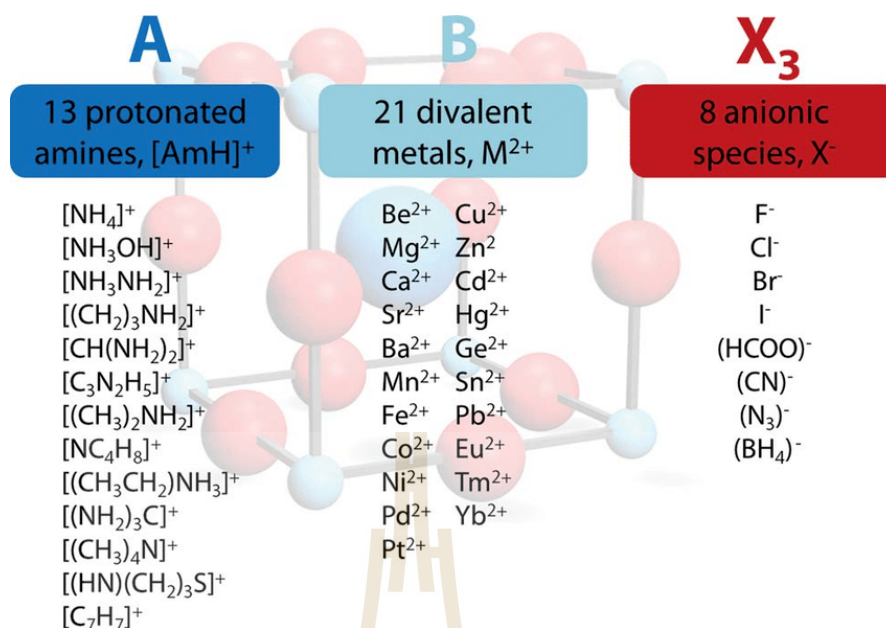


Figure 1.3 Overview of the application procedure and the ions calculated (562 organic anion based, 180 halide based) (Kieslich et al., 2015).

intriguing properties of the hybrid perovskite CH₃NH₃PbI₃ in thin film. However, other hybrid perovskite for example the family of perovskite like metal formats AB(HCOO)₃ (A = protonated amine, B = divalent metal), also show interesting properties such as multiferroic behavior and tunable mechanical properties. From Goldschmidt's initial approach, (effective) ionic radii are used for calculating factors of hybrid perovskite (Kieslich et al., 2015). Goldschmidt's equation, factors are the effective ionic radius of the protonated amine A, the ionic radius of the anion X and the ionic radius of the divalent metal ion B in a perovskite with general formula ABX₃. The effective radii and heights of molecular anions were calculated according to previous publication (Kieslich et al., 2015). Following the recent publication, the applied procedure and the ions used is given in Figure 1.3.

From Figure 1.3, we will consider the effect of a complete replacement of Pb by Ba in CH₃NH₃PbI₃. When ionic radius of cation A (CH₃NH₃) and anion X (I) are taken as 1.8 and 2.06 (Filip et al., 2014). For charge neutrality and

coordination number of 6 in the BX_6 octahedral further reduces the number of possible replacements at B site. Considering the size to be comparable to Pb, Ba and Sr are obvious choices for the Pb replacement at the B site. Sr as a replacement for Pb has already been reported (Jacobsson et al., 2015). And then ionic radii of MA cation (A), Ba and I as 1.8, 1.49 and 2.06, respectively, the Goldschmidt tolerance factor is calculated to be 0.797 for the $CH_3NH_3BaI_3$ crystallizing in the perovskite structure (Jacobsson et al., 2015). Therefore, one can expect the crystal structure and the atom positions of $CH_3NH_3BaI_3$ to be similar to that of the tetragonal distorted perovskite $CH_3NH_3PbI_3$; Goldschmidt tolerance factor = 0.83 (Brivio et al., 2015).

1.3 Motivation

There is a strong need to understand physical, optical, and structural properties of lead-free perovskite material in order to fabricate stable and high performance lead free perovskite solar cells.

1.4 Scope and limitations of the study

This thesis, we shall on basic property with $CH_3NH_3PbI_3$, $CH_3NH_3Pb_{1-x}Sn_xI_3$ and $CH_3NH_3Pb_{1-x}Ba_xI_3$ perovskite materials to understand the dynamics for good performance, including the physical properties on this materials. The standard STA and PXRD will be used to determine the temperature for reaction and confirm global structure of the prepared materials. The chemical state or electronic state of the synthesized will be studied by using FT-IR, UV-Vis, Raman, XPS and XAS technique. In addition, the important properties, such as electrical, solar-cell, and optical properties will also be

investigated.



CHAPTER II

THEORY

2.1 Lead-free metal based halide perovskite

Lead-free (Pb-free) metal perovskite have revolutionized the field of solution-process able photovoltaic. Within a few years, the powder conversion efficiencies of perovskites based solar cells have been improved significantly. The breakthrough in solution based PV, however, has the drawback that these high efficiencies can only be obtained.

The limitations impeding the commercialization of Pb based halide perovskite solar cell are i) the toxicity, lead halides ii) the water solubility of lead that might contaminate water supplies and iii) the chemical instability under ambient conditions, especially in the presence of air, humidity and light. The toxicity issue of lead halide perovskite is still an unsolved drawback. Even though only low amounts are implemented in solar cell, there is a potential risk of harms on humans and environment (Alberto et al., 2015).

Many research groups took up the challenge to substitute lead with other element to find new non-toxic and environmentally benign perovskite materials suitable as efficient solar cell absorbers. Because of the fact that the perovskite crystal structure can be found in many compounds, many different material combinations are possible. However, due to these manifold possibilities, a huge number of materials need to be screened.

2.2 Formability and structural of perovskite

Perovskite are crystalline materials with an ABX_3 structure similar to $CaTiO_3$. In metal halide perovskite, the A-site being larger than B (see Figure 1.3). The B-site are usually divalent metal ions shown in Figure 1.3 and the X-site by a halide counterion (I^- , Br^- , Cl^-). The natures of the ions within the perovskite structure, hybrid organic-inorganic or purely inorganic metal halide perovskite are distinguished. A range of different divalent metal cations such as 21 divalent metal cations (please see Figure 1.3) have already been investigated as B-site cation.

The formability of metal halide perovskite depend on various requirements: a) charge neutrality between cations and anions, $N(A) + N(B) = 3N(X)$, when N represents the valence of A, B and X ions; b) the stability of the BX_6 octahedral, it can be predicted by the octahedral factor μ ; and c) Goldschmidt tolerance factor (t) is an indicator of how much the ions in perovskite could be displaced from the ideal structure (Jingyu et al., 2016; Goldschmidt, 1926).

The μ factor is the ratio of the radii of B site cation (r_B) and X site halide counterion (r_X). It can be used to estimate the stability of BX_6 octahedral by equation 2.1. For μ factor values between 0.442-0.895, it means metal halide perovskites have been found to be stable in perovskite structure (Li et al., 2008).

The t factor calculated as equation 2.1 using ionic radii of A, B and X ions. It can be used to evaluate which mismatches in size of the A, B and X ions are tolerated to form perovskite structure.

$$\mu = \frac{r_B}{r_X}, t = \frac{R_A + R_X}{\sqrt{2}(r_B + r_X)} \quad (2.1)$$

The stability and formability range for ABX_3 structure can be derived for which the tolerance factor was empirically found to be $0.8 \leq t \leq 1.0$ is desired (Li

Table 2.1 The Goldschmidt tolerance factor (t) values to formed perovskites structure.

| t | structure |
|------------|--|
| 1 - 0.9 | cubic |
| 0.89 - 0.8 | orthorhombic, tetragonal or rhombohedral |
| < 0.8 | A cation is too small for formation |
| > 1 | A cation is too large for formation |

et al., 2008). In the cubic phase, the perovskite forms when t in the range 1.0-0.9. If the t is lower 0.8-0.89, the distorted perovskite with orthorhombic, tetragonal or rhombohedral structure are likely to be formed. If $t < 0.8$, the distorted perovskite structure will not be stable because A-site is too small for formation of perovskite structure. In the case of $t > 1$, the A-site is too large for formation of perovskite structure, which can be summary in the Table 2.1 (Kieslich et al., 2015).

The t factor concept was recently adapted for the family of hybrid organics-inorganic metal halide perovskite materials taking organic molecular cations such as $\text{CH}_3\text{NH}_3\text{I}$ into consideration. However, these replacement rules have attracted considerable attention to predict novel lead-free perovskite materials for photovoltaic based on ionic radii of the involved ions (see Figure 2.1). The influence of the size and anisotropy of the linking anion on the t is highlighted for different cations (B) in $\text{CH}_3\text{NH}_3\text{BI}_3$. Anyway, the stability range of the t can be considerable as Figure 2.1.

The class of perovskite that thesis is concerned with the organic-inorganic lead-free perovskite $\text{CH}_3\text{NH}_3\text{PbI}_3$, $\text{CH}_3\text{NH}_3\text{Pb}_{1-x}\text{Sn}_x\text{I}_3$ and $\text{CH}_3\text{NH}_3\text{Pb}_{1-x}\text{Ba}_x\text{I}_3$ (methylammonium lead free). The CH_3NH_3 cation ($r_A = 217$ pm), Pb ($r_B = 119$ pm), Sn ($r_B = 110$ pm), Ba ($r_B = 135$ pm) and I ($r_X = 220$ pm) giving

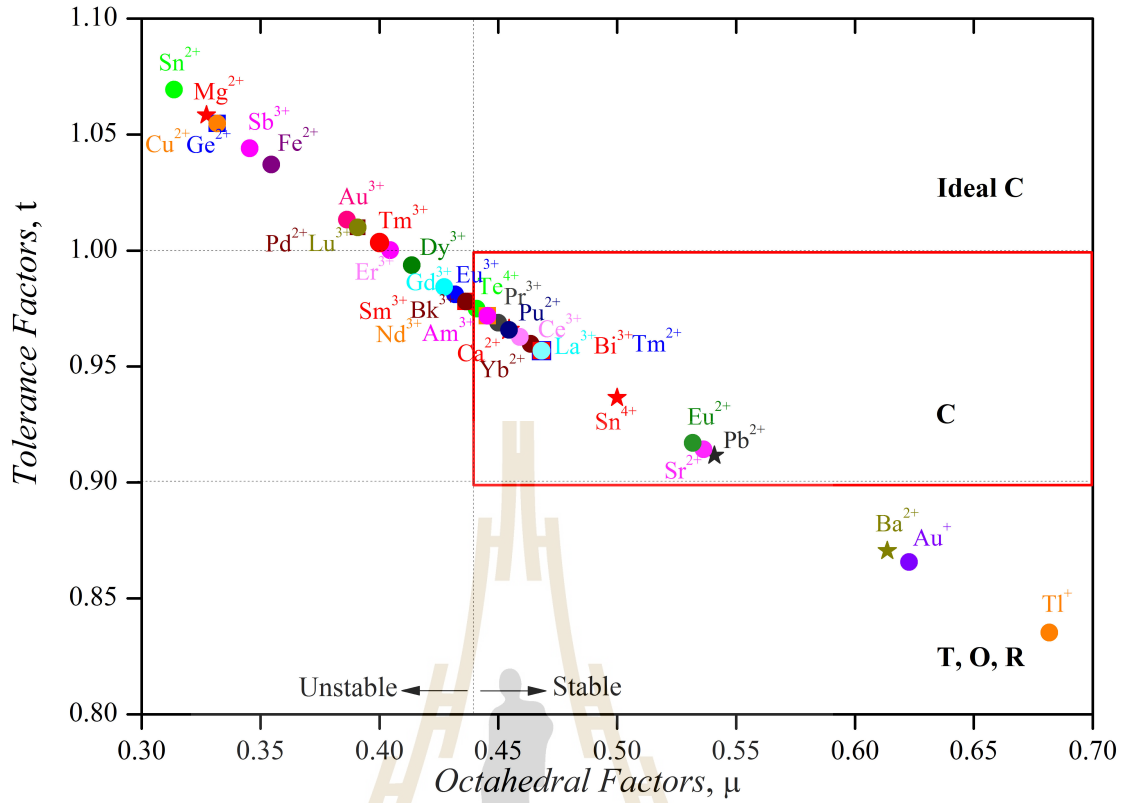


Figure 2.1 Calculated t and μ map for different cations (B) in $\text{CH}_3\text{NH}_3\text{BI}_3$ perovskite system for 34 metals to predict novel lead-free perovskite.

stable perovskite structures t factor of 0.91, 0.93 and 0.87 for t_{Pb} , t_{Sn} and t_{Ba} , respectively. This is one reason to choose the arrangements to reduce Pb replaced by Ba and Sn. The hope that when the transitions from Pb are Ba/Sn, perovskite materials can be stabilized, including well light absorbance. In addition, this approach will also help addressing the toxicity issue of Pb in the compound.

2.3 Homovalent substitution with divalent cations

A replace of lead with non-toxic and environment benign elements form leaf-free metal halide perovskite can be generally achieved via two approaches; 1) homovalent substitution of lead with isovalent cations such as group-14 elements (Ge, Sn), Alkaline-earth metals (Mg, Ca, Sr, Ba), transitions metals (Mn, Fe, Ni,

Pd, Cu, Cd) and lanthanide (Eu, Tm, Yb) and 2) heterovalent substitution with aliovalent metal cations for examples transition metals (Au), lanthanide (La, Ce, Pr, Nd, Sm, Eu, Gd, Dy, Er, Tm, Lu) and actinides (Pu, Am, Bk). However, these substitution approaches cannot be predicted via Goldschmidt replacement rules (see figure 2.1).

The homovalent replacement of lead with isovalent cations such as group-14 elements, Alkaline-earth metals, transitions metals and lanthanide can be considered for alternative lead-free perovskite (Filip et al., 2014; Kieslich et al., 2015). However, some of these candidates have to be excluded due to their limited ability to form perovskite, or not well suited for PV applications because of too high band gaps, their toxicity, radioactivity and instability of the +2 oxidation state.

This work, Tin (Sn) element are the first logical candidate for homovalent substitution of lead. The Sn^{2+} metal cations has a similar S^2 electronic configuration to Pb^{2+} and the not different ionic radius (Pb^{2+} :119 pm and Sn^{2+} :110 pm). It is possible to form a perovskite with a formula ASnX_3 on analogy to lead compound. Tin is often presented as the non-toxic alternative to lead, this toxicity of tin-based perovskite still argued. Even if Tin is good optical properties but Sn^{2+} ions posses a drawback compared to Pb^{2+} because it can be easily oxidized to the oxidation state +4.

More interesting is Barium (Ba) element on perovskite materials. The Ba can be potential homovalent substitutes due to ionic radii (Ba^{2+} : 135 pm) suitable to form perovskite structure, a high abundance in earth's crust, non-toxicity, and stable +2 oxidation state similarly to Pb^{2+} . For applying the t factor replacement rules, t_{Ba} of 0.871 for $\text{CH}_3\text{NH}_3\text{BaI}_3$. Which it is similar to the lead halide perovskite $\text{CH}_3\text{NH}_3\text{PbI}_3$ ($t = 0.911$).

CHAPTER III

RESEARCH METHODOLOGY

3.1 Synthetic techniques

This chapter discusses experimental procedures related to fabrication processing of lead free perovskite materials. Two sets of the samples were investigated. There are two steps to produce metal halide perovskite: (i) synthesis of organic salts and (ii) preparation of perovskite powder materials. The precursor metal halide salts PbI_2 , SnI_2 and BaI_2 are purchased from Sigma-Aldrich Company. For the organic part we synthesized from methylamine solution 33 wt% in ethanol and hydroiodic acid (HI) 57 wt% in water are from Sigma-Aldrich Company. Two sets of the samples were investigated.

3.1.1 $\text{CH}_3\text{NH}_3\text{I}$ synthesis

At first, we need to synthesis the ammonium iodide ($\text{CH}_3\text{NH}_3\text{I}$) salts from the amine by reacting the amine with halogen acid the process could be described by formula: $\text{CH}_3\text{NH}_2 + \text{HI} \rightarrow \text{CH}_3\text{NH}_3\text{I}$. The ammonium salts are methylamine (CH_3NH_2 , 33 wt% in ethanol, Sigma-Aldrich) and hydroiodic acids (HI, 57 wt% in water, Sigma-Aldrich) were stirred in an ice bath for 2 hrs, and controlling the temperature continuously. Then, the solution was stirred at 50°C for 24 hrs and $\text{CH}_3\text{NH}_3\text{I}$ was obtained. Finally, the solid obtained was washed three times with diethyl ether (purity 99.8%, Sigma-Aldrich) and dried at 70°C in vacuum overnight. After the drying procedure, the final salt is stored in the silica gel and

dry place. The procedures are shown in Figure 3.1.

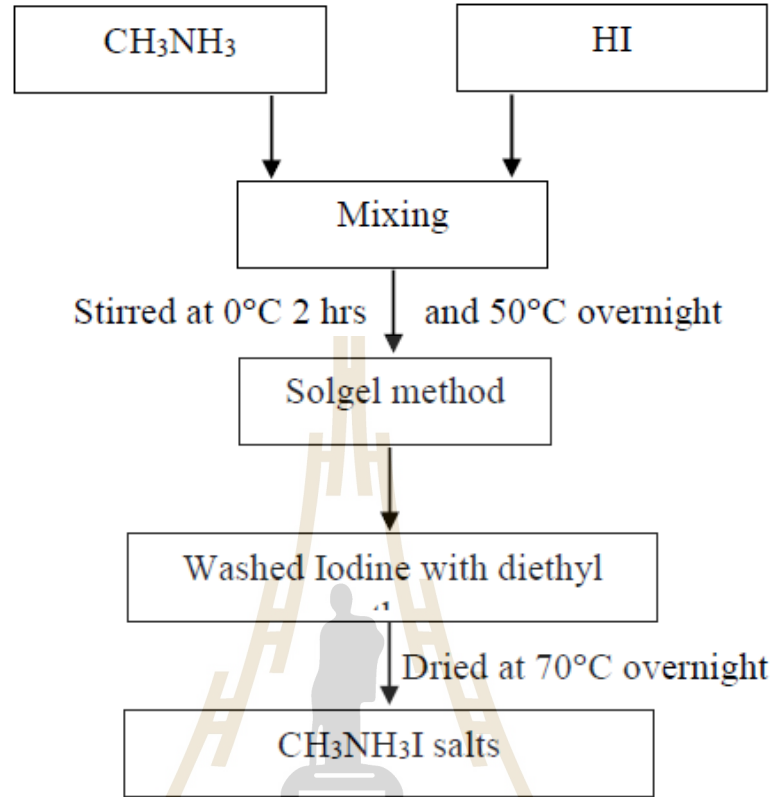


Figure 3.1 Flow chart of the synthesis of $\text{CH}_3\text{NH}_3\text{I}$ powders.

3.1.2 $\text{CH}_3\text{NH}_3\text{PbI}_3$ synthesis

After the synthesis, the dry $\text{CH}_3\text{NH}_3\text{I}$ are used to prepare $\text{CH}_3\text{NH}_3\text{PbI}_3$ perovskite samples powders. In this stage the synthesized $\text{CH}_3\text{NH}_3\text{I}$ and PbI_2 (purity 99%, Sigma-Aldrich) via the direct-mixed method with chemical reaction:



The $\text{CH}_3\text{NH}_3\text{PbI}_3$ powders were pressed into pellets of 11 mm and were heated in Ar-flow at 200°C . The synthesis flowchart is show as figure 3.2.

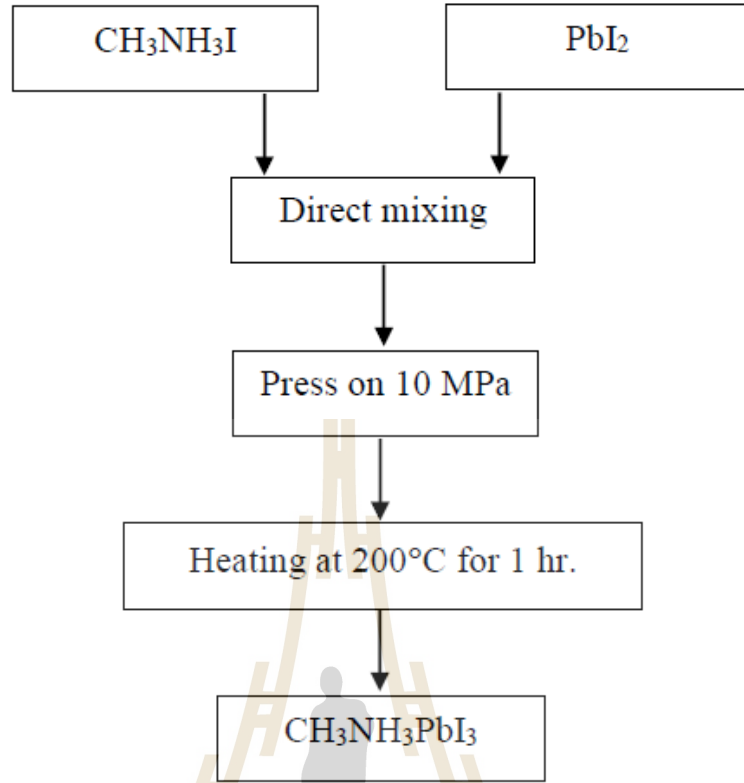
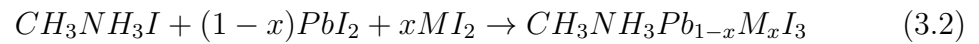


Figure 3.2 Flow chart of the synthesis of $\text{CH}_3\text{NH}_3\text{PbI}_3$ materials.

3.1.3 $\text{CH}_3\text{NH}_3\text{Pb}_{1-x}\text{M}_x\text{I}_3$ synthesis

The samples were prepared in the same way as described in section of $\text{CH}_3\text{NH}_3\text{PbI}_3$ synthesis. In this thesis, the M parts are Sn and Ba. The synthesized $\text{CH}_3\text{NH}_2\text{I}$, PbI_2 , BaI_2 and SnI_2 (purity 99%, Sigma-Aldrich), $x = 0.02, 0.04, 0.06, 0.08, 0.1$ and 0.2 were direct-mixed in mortar. In general, this reaction can be described by the formula:



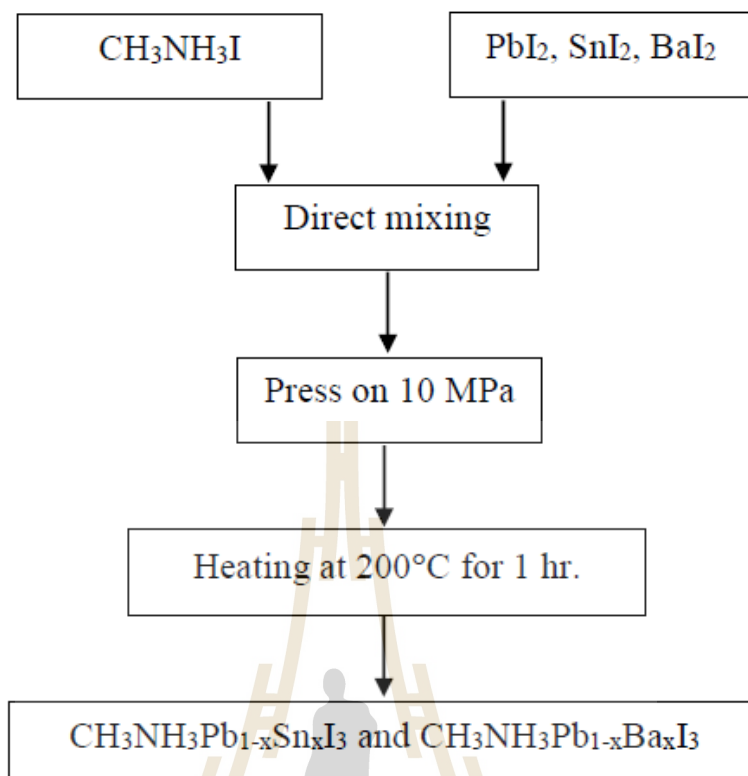


Figure 3.3 Flow chart of the synthesis of $\text{CH}_3\text{NH}_3\text{Pb}_{1-x}\text{Sn}_x\text{I}_3$ and $\text{CH}_3\text{NH}_3\text{Pb}_{1-x}\text{Ba}_x\text{I}_3$ materials.

3.2 Characterization techniques

3.2.1 Thermal gravimetric analysis

Thermal gravimetric analysis (TGA) with differential thermal analysis (DTA) belongs to thermal analysis group of techniques. TGA analysis, change in physical and chemical properties of materials is measured as a weight loss with increasing temperature. This technique a precision balance and programmable furnace is needed. The characteristics of material connected with the mass loss can be examined by this method.

- 1) Determine of the organic and inorganic content in the sample.
- 2) Study of degradation and reaction mechanisms.

3) Characterization by analysis of decomposition patterns.

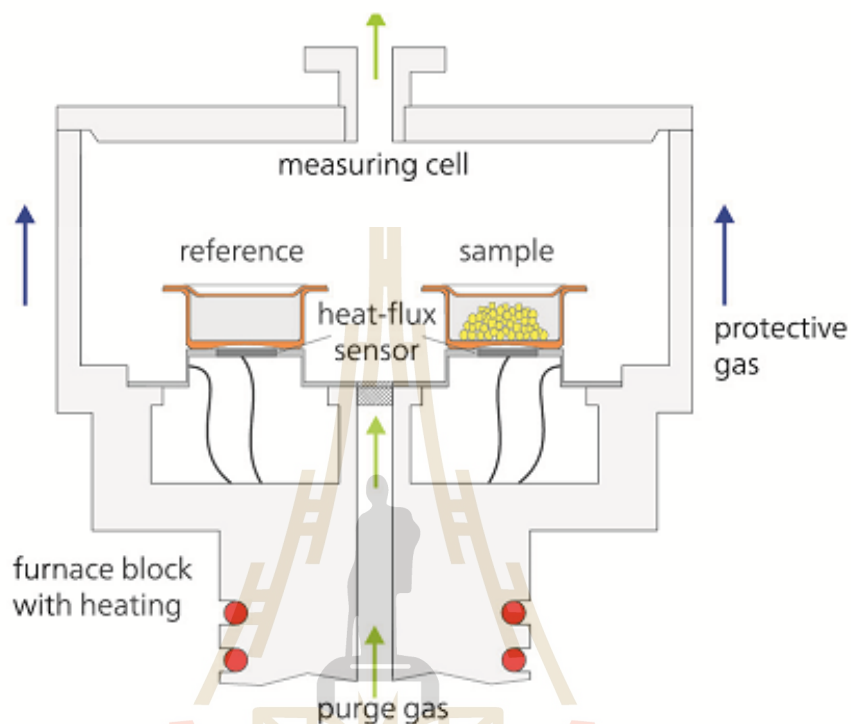


Figure 3.4 Heat Flux DSC.

The curve provides data about physical phenomena such as second order phase transitions, including vaporization, absorptions, adsorption, desorption and sublimation. The chemical phenomena can be traced by TGA, this include dehydration, decomposition, oxidation/reduction reaction and chemisorptions (Coats and Redfern, 1963).

DTA defined formally as a technique for recording the difference in temperature between a substance and reference against either time or temperature as the two specimens are subjected to identical temperature regimes in an environment heated or cooled at a controlled rate. Sampled differential temperature is then plotted against time or temperature, endothermic and exothermic changes

are detected by relation to the inert reference (Bhadeshia, 2002). The DTA curve provides data on the transformation that have occurred such as glass transitions, crystallization, melting and sublimation. The area under peak is the enthalpy change and is not affected by the heat capacity of the sample.

Thermal analysis of the samples were investigated by TGA analysis using a STA NETZSCH STA 449F3 which was performed at a heating rate of 5°C/min from room temperature to 800°C in N₂ atmosphere.

3.2.2 X-Ray Diffraction

X-ray diffraction (XRD) is a technique used for phase identifying the structure of a crystal, which the crystal atoms cause a beam of incident x-ray to diffract into specific directions. Measuring the angles and intensities of diffracted beams, a crystallographer can produce a three-dimensional picture of atoms within the crystal, position, chemical bonds, disorder and various other pieces of information (Richard, 2006). The diffraction can be determined by Bragg's law:

$$2d \sin \theta = n\lambda \quad (3.3)$$

When d is spacing between diffraction of atoms, θ is the incident angle, n is any integer and λ is wavelength of the beam. These specific directions appear as spots on the diffraction pattern called reflections. The XRD patterns were recorded by a Rigaku MiniFlex300/600 for powders with parallel beam and Cu K_α wavelength. Symmetric 2θ scans were obtained using a step size of 0.02° and time per step of 4 s. The crystalline phase identification was carried out by comparison with Crystallographic Information File. The Rietveld refinement of XRD pattern of perovskite materials by JANA2006 software to crystallite size and lattice parameter in this thesis. The Rietveld method uses a least squares

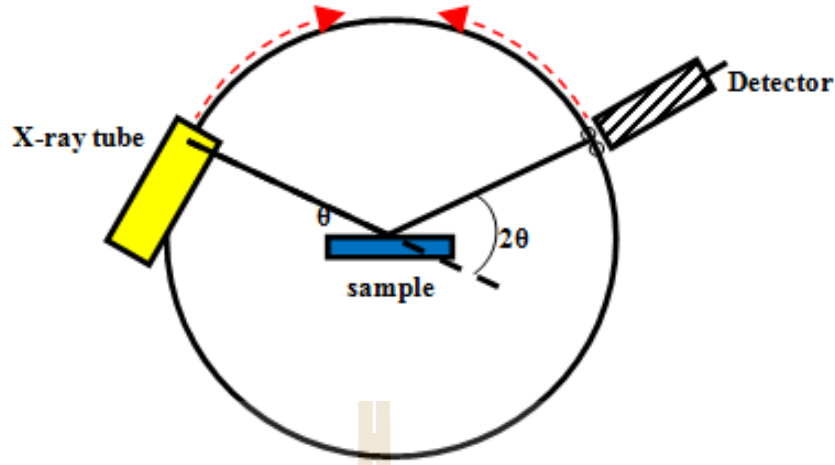


Figure 3.5 Basic components of X-ray diffractometers.

approach to refine a theoretical line profile until it matches the measured profile.

The principle of the Rietveld method is to minimize the sum S of the squares of the difference between the intensity at point i in pattern, y_{i0} , and calculated profile, y_{iC} as:

$$S = \sum_i w_i (y_{i0} - y_{iC})^2 \quad (3.4)$$

where w_i is the statistical weight quality which is equal to $1/y_{i0}$ and y_{iC} is the net intensity at point i . The basic of Rietveld method, determined the calculated intensity at each point of the pattern by

$$y_{iC} = y_{iB} + \sum_p p \sum_{k=k_1^p}^{k_2} {}^pG_{ik} {}^pI_k \quad (3.5)$$

when y_{iB} is the background intensity, G_{ik}^p is the normalized peak profile function and I_k is the intensity of the k bragg reflection contributing intensity at point i and p is the number of phase present. The variation of peak FWHM with θ is defined by

$$H_k = (U \tan^2 \theta + V \tan \theta + W)^{1/2} \quad (3.6)$$

$$I_k = SM_k L_k |F_k|^2 P_k A_k E_k \quad (3.7)$$

where S is the scale factor, M_k is the multiplicity, L_k is the Lorentz polarization factor, A_k and E_k are the adsorption and extinction correction factors, respectively. P_k is used to describe the effect of preferred orientation (no preferred orientation is indicated with $P_k = 1$) and F_k is

$$F_k = \sum_{j=1} f_j \exp[h_r^t r_j - h_k^t B_j h_j] \quad (3.8)$$

where f_j is the scattering factor or scattering length of atom j and h_k , r_j and B_j are matrices representing the miller indices, atomic coordinates and anisotropic thermal vibration parameters, respectively. The superscript t indicates matrix transposition.

The quality of refinement can be confirmed by weighted profile R_{wp} , the profile factor R_p , the profile factor R_{Bragg} , the profile factor R_F , R-expected value (R_{exp}) and Goodness of fit value (GOF) are defined as;

$$R_{wp} = \left| \frac{\sum_{i=1,n} w_i ((y_{i(obs)}) - y_{i(cal)})^2}{\sum_{i=1,n} w_i (y_{i(obs)})^2} \right|^{1/2} \times 100 \quad (3.9)$$

$$R_p = \frac{\sum_{i=1,n} |y_{i(obs)} - y_{i(cal)}|}{\sum_{i=1,n} |y_{i(obs)}|} \times 100 \quad (3.10)$$

$$R_{Bragg} = \frac{\sum_h |I_{(obs,h)} - I_{(cal,h)}|}{\sum_{i=1,n} |I_{(obs,h)}|} \times 100 \quad (3.11)$$

$$R_F = \frac{\sum_h |F_{(obs,h)} - F_{(cal,h)}|}{\sum_{i=1,n} |F_{(obs,h)}|} \times 100 \quad (3.12)$$

$$R_{exp} = \left(\frac{N - P}{\sum_i w_i y_{i0}^2} \right)^2 \quad (3.13)$$

and

$$GOF = \chi^2 = \frac{\sum_{i=1,n} w_i ((y_{i(obs)} - y_{i(cal)})^2}{n - p + c} \times 100 = \left| \frac{R_{wp}}{R_{exp}} \right|^2 \quad (3.14)$$

The GOF is the ratio between R_{wp} and R_{exp} should be not lower than 1, which the good refinement should be give GOF values lower than 2.

In addition, the XRD pattern can be estimated crystallite size of the materials were calculated from diffraction peak by using Scherer's equation as;

$$D = \frac{k\lambda}{FWHM \cos \theta} \quad (3.15)$$

where k is a constant depending on the XRD equipment and has been determined between 0.89-1.39, this work k = 0.89. λ is the wavelength of the X-ray radiation, θ is diffraction angle, FWHM is the full-width at half maximum of XRD peak.

3.2.3 UV-visible spectroscopy

Ultraviolet visible spectroscopy (UV-vis) is method based on the express the refract process, which is the interaction between electromagnetic waves and material. In principle, we can get the band gap from the refraction spectra. For instance, the refraction spectrum can indicate the rotation and vibration information in the molecular. Optical absorption coefficient (α) is calculated using reflectance data according to the Kubelka-Munk equation:

$$F(R) = \alpha = \frac{(1 - R)^2}{2R} \quad (3.16)$$

Transformed Kubelka-Munk function,

$$[F(R)h\nu]^P = A(h\nu - E_g) \quad (3.17)$$

where R is the percentage of refracted data, E_g is band gap energy, A is constant depending on transition property, P is power index: related to the optical absorption process, which is equal to $1/2$, 2 , $3/2$ or 3 for allowed direct, allowed indirect forbidden direct or forbidden indirect and $h\nu$ is incident photon energy.

In this work, the spectra have allowed direct optical reflection and Tauc plot in $[F(R)h\nu]^2$ vs $h\nu$ coordinates allows us to estimate the optical bandgap by dropping a line from the maximum slope of the curve to the x-axis. Room-temperature reflection spectra were recorded using a UV-Vis-NIR spectroscopy (JASCO V-7200 spectrometer).

3.2.4 Fourier Transform Infrared Spectroscopy Analysis

Fourier transform infrared (FT-IR) spectroscopy analysis stands for the preferred method of infrared spectroscopy. In infrared spectroscopy, IR radiation is passed through a sample. Some of infrared radiation is absorbed by the sample and some of it is passed (transmitted). The resulting spectrum represents the molecular absorption and transmission, creating a molecular fingerprint of the samples. Like a fingerprint no two unique molecular structures produce the same infrared spectrum. This makes infrared spectroscopy useful for several types of analysis.

The range of infrared region is $12800 \sim 10 \text{ cm}^{-1}$ and can be divided into near-infrared region ($12800 \sim 4000 \text{ cm}^{-1}$), mid-infrared region ($4000 \sim 200 \text{ cm}^{-1}$) and far-infrared region ($50 \sim 1000 \text{ cm}^{-1}$). Infrared absorption spectroscopy is the method which scientists use to determine the structures of molecules with the molecules' characteristic absorption of infrared radiation. Infrared spectrum is molecular vibrational spectrum. When exposed to infrared radiation, sample molecules selectively absorb radiation of specific wavelengths which causes the

change of dipole moment of sample molecules. Consequently, the vibrational energy levels of sample molecules transfer from ground state to excited state. The frequency of the absorption peak is determined by the vibrational energy gap. The number of absorption peaks is related to the number of vibrational freedom of the molecule. The intensity of absorption peaks is related to the change of dipole moment and the possibility of the transition of energy levels. Therefore, by analysing the infrared spectrum, one can readily obtain abundant structure information of a molecule except for several homonuclear diatomic molecules such as O_2 , N_2 and C_{12} due to the zero dipole change in the vibration and rotation of these molecules. Infrared absorption has useful is capable to analyse all gas, liquid and solid samples. The common used region for infrared absorption spectroscopy is $4000\sim 400\text{ cm}^{-1}$ because the absorption radiation of most organic compounds and inorganic ions is within this region.

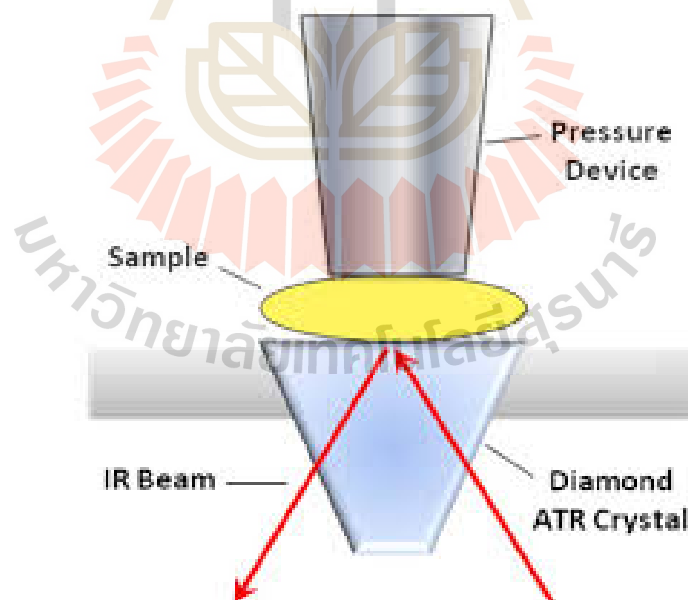


Figure 3.6 Schematic representation of diamond ATR accessory.

This work, we used FTIR by ATR (Attenuated Total Reflectance) is applicable to the same chemical or biological systems as the transmission method.

Figure 3.6 shown infrared beam is directed onto an optically dense crystal with a high refractive index at a certain angle. This internal reflectance creates an evanescent wave that extends beyond the surface of the crystal into the sample held in contact with the crystal. This technique to be successful, sample must be in direct contact with the ATR crystal, because the evanescent wave or bubble only extends beyond the crystal 0.5-5 μm by placing just enough sample to cover the crystal area. The sample height should not be more than a few millimetres. The solid has been placed on the crystal area, the pressure arm should be positioned over the crystal/sample area. When using the ATR accessory, the pressure arm locks into a precise position above the diamond crystal. Force is applied to the sample, pushing it onto the diamond surface. Then the FT-IR software utilizes a Preview Mode for allows the quality of the spectrum to be monitored in real-time while fine-tuning the exerted force. The reflectance examination technique refers to the obtaining an infrared spectrum by passing an IR beam through a sample. FIIR-ATR spectra of the prepared samples were measured using a Bruker Vertex 70 spectrophotometer. FTIR-ATR spectra were recored in the $4000\text{-}400\text{ cm}^{-1}$ at room temperature. The evaluation of the FTIR spectra was performed by OPUS software.

3.2.5 X-ray Photoelectrons Spectroscopy

X-ray Photoelectrons Spectroscopy (XPS) is the surface analysis technique used for studying the elemental, electronic and chemical state of a material. XPS is widely used for studying surface physics and chemistry of a material because of its high sensitivity to the surface (about 5-100 \AA). XPS provides information about the surface of the material being studied: elemental composition, stoichiometry and the empirical formula of the material, and the chemical and electronic state of

the elements on the surface. The basic components of XPS instrument are shown in Figure 3.7. It mainly consists of a Photon source, ultrahigh vacuum (UHV), detector and an electron energy analyzer. The choice of X-ray source is determined by the energy resolution desired and X-rays (about > 1000 eV) are to be used in the case of inorganic or organic samples.

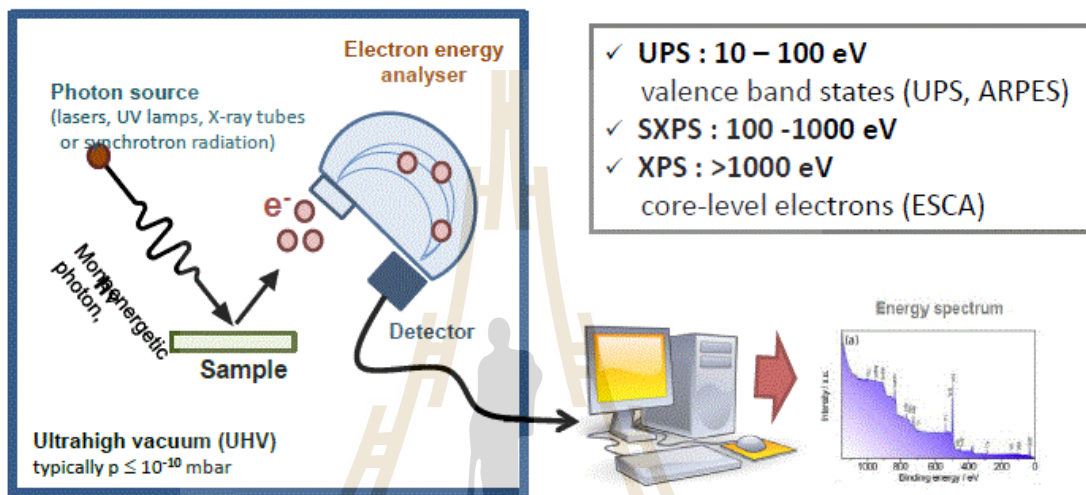


Figure 3.7 Schematic of XPS instrument.

From Figure 3.7 shown the X-ray beam energy is irradiated on sample surface, the energy of the X-ray photon is absorbed completely by the core electron of an atom. If the photon energy $h\nu$ is large enough, the core electron will then escape from the atom and emit out of the surface. The emitted electron with the kinetic energy of E_k is referred to as the photo-electron. The binding energy of the core electron is given by the Einstein relationship:

$$h\nu = E_b + E_k + \phi \quad (3.18)$$

$$E_b = h\nu - E_k - \phi \quad (3.19)$$

where $h\nu$ is the X-ray photon energy (for Al K_α , $h\nu = 1486.6$ eV and

Mg K_{α} , $h\nu = 0 - 1200$ eV); E_k is the kinetic energy of photoelectron, which can be measured by the energy analyzer; and ϕ is the work function induced by the analyzer. Since the ϕ can be compensated artificially, it is eliminated, giving the binding energy (E_b) as follows:

$$E_b = h\nu - E_k \quad (3.20)$$

The photoemission process in 4 step (see figure 3.8): 1) the $h\nu$ energy radiation is absorbed by the electron transition from initial state to excited state (initial state effects), 2) atom response and makes photoelectron/relaxation (final state effects), 3) the photoemitted electron makes its way to the surface (extrinsic effects), 4) after overcoming the material's work function, the photoemitted electron is ejected into the vacuum. The majority of the photoemitted electrons that make their way to the surface undergo a series of inelastic scatterings, recombination, excitation of the sample, recapture or trapping in various excited states within the material, all of which results in a decrease in their kinetic energies.

In this work, the XPS results were measured at X-ray Photoelectron spectroscopy beam line (BL5.3) at synchrotron light research institute (SLRI, Public Organization, Thailand). The spectra were recorded at high pressure to measure C, N, O, I, Pb, Ba and Sn elements. All binding energies have been corrected for the charging effect with reference to the C 1s line at 284.6 eV.

3.2.6 X-ray absorption spectroscopy

XAS is a widely a widely used technique for the local structure and electronic structure study for materials. The experiment is performed by tuning the efficiency photon energy to reject a core electron from an atom. Samples can be in solution, gas-phase or condensed matter (solid). Structure can be determined from

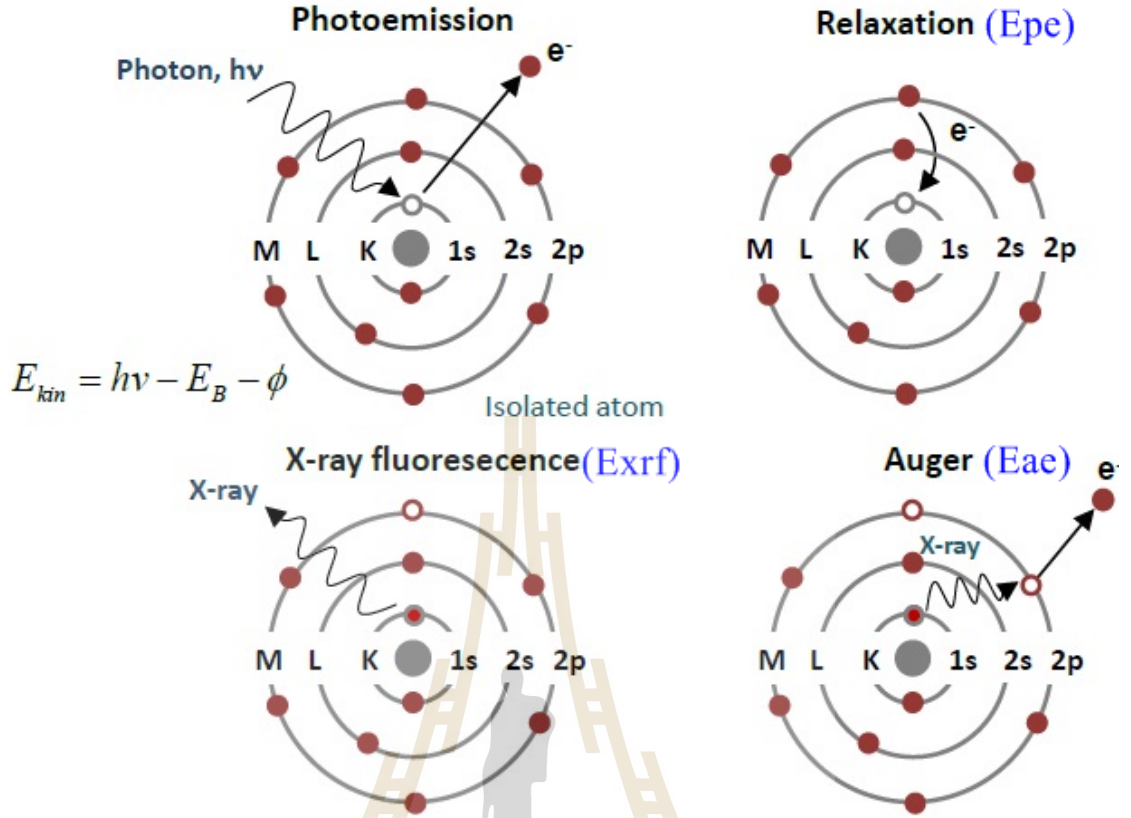


Figure 3.8 Schematic of X-ray processes which include photoemission, X-ray fluorescence and Auger electron emission where $h\nu$ is the incident photon, E_{ae} is the energy of the outgoing Auger electron ($E_{ae} = E_K - E_L - E_M$), E_p is the energy of the outgoing photoelectron or relaxation ($E_p = h\nu - E_K - E_M$), E_{erf} is the energy of the outgoing fluorescence photon ($E_{erf} = E_K - E_M$) and E_K , E_L and E_M are the energies of the K, L, and M orbitals respectively.

samples that are both heterogeneous and amorphous. A parallel monochromatic from samples that are that are both heterogeneous and amorphous. A parallel monochromatic X-ray beam of intensity I passing through a sample of thickness x will get a reduced intensity I following the equation.

$$I = I_0 e^{-\mu x} \quad (3.21)$$

where μ is the linear absorption coefficient which is the probability that it

will be absorbed, I_0 is the incident X-ray intensity.

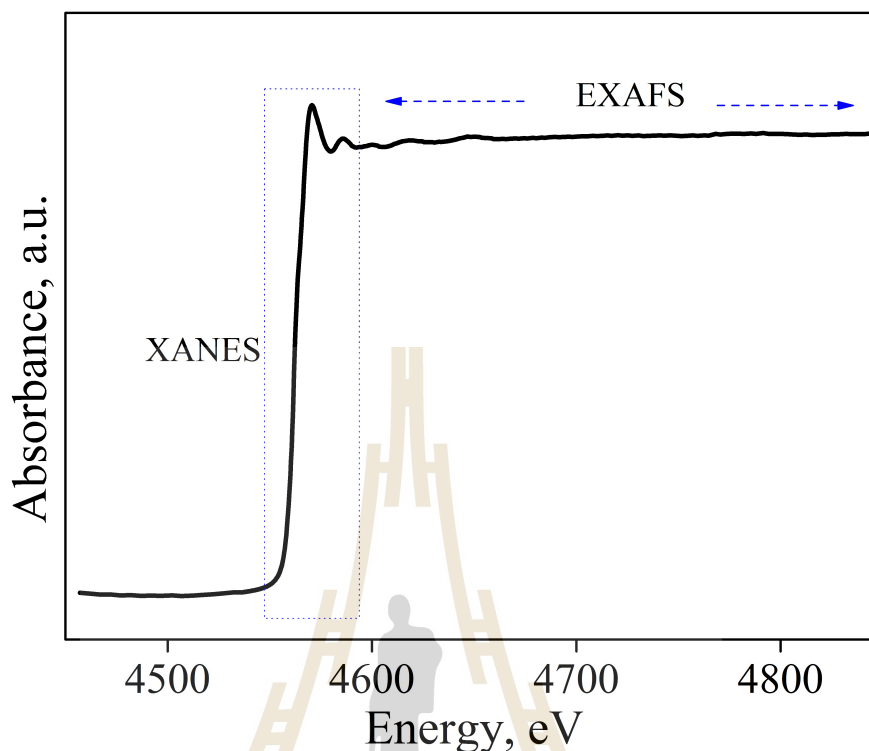


Figure 3.9 XAS spectrum of I L3-edge collected in transmission mode.

At certain energies the absorption of the X-ray increases dramatically when the energy matches well with the binding energy of the electrons. This is the reason for a decrease in the transmitted X-ray intensity of the absorption area. Normally, absorption edge occurs when the energy of the incident photon energy is sufficient to cause excitation of a core electron of the absorbing atom to a higher energy. Three main regions are commonly distinguished in the XAS spectra. First region at around 20-50 eV (shown in figure 3.9) below the absorption edge, namely pre-edge structure. The pre-edge peak caused by the electron transition (dipole allowed) to the lowest empty bound state near is the Fermi level. The strengths of the pre-edge peaks provide information about absorber local structure and electronic structure around absorber atom such as a number of neighbour atoms and valence state. The second region where the incident X-ray is sufficient to transfer an atomic core

of electrons to final states is in the energy region of about 40-100 eV above an absorbed atomic core level of ionization energy which X-ray absorption near edge structure (XANES). Analysis of the absorption edge feature of XANES spectra can be applied for understanding the oxidation state and the coordination number of the absorbing atoms. The final region of the oscillation above the edge, which can extend to 100-1000 eV or more is referred to as the Extended X-ray absorption fine structure (EXAFS) (see in figure 3.9). In this region, the incident photon is able to excite the core electron if its energy is equal or higher than the edge energy. Because there are many other atoms around the absorber atom and these become scattering centres of the photoelectrons wave. The final state of the photoelectrons can be explained by the sum of the original and single scattered waves from the nearest neighbouring atoms. The analysis of the EXAFS part contains information about the interatomic distance, coordination number and species of neighbouring atoms. The EXAFS signal is described as a function of the wave vector k as:

$$\chi(k) = \sum_j j \frac{S_0^2 N_j}{k R_j^2} |f_j(k, \pi)| \sin[2k R_j + \phi_j(k)] e^{-2\delta_j^2 k^2} e^{-2R_j/\lambda(k)} \quad (3.22)$$

where N_j is the number of neighbors in j shell of surrounding atoms, k is photoelectron wave vector, f_j is the scattering amplitude, $S_0^2(k)$ is the amplitude reduction term due to many-body effect, R_j is radial distance from absorbing atom to j shell, $S_0^2(k)$ is electron mean free path, σ_j is the Debye-Waller factor and $\phi(k)$ accounts for the total phase shift of the curve wave scattering amplitude along the scattering trajectory. Moreover, since the scattering amplitude and phase-shifts depend on the atomic number Z of the neighbouring atoms, EXAFS is also sensitive to the atomic number type of the neighbouring atoms. The absorption spectra were transposed to the wave vector k -space using the formula $k = (2m(E -$

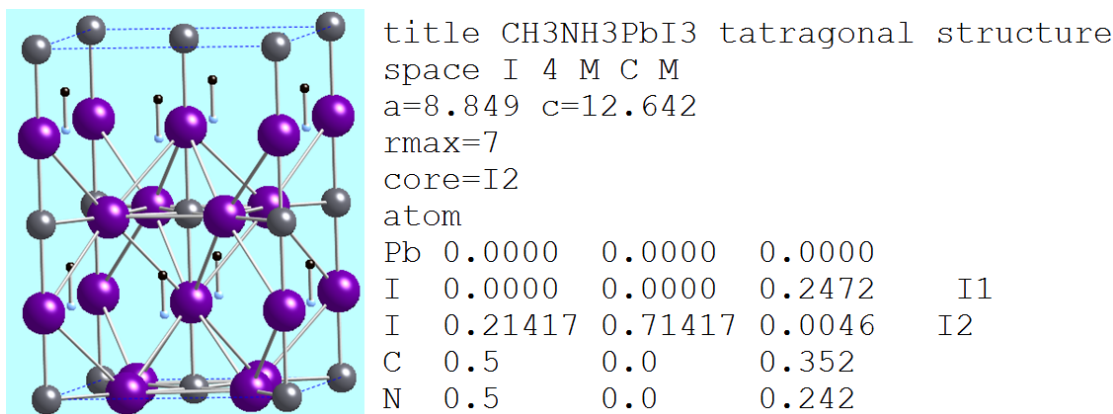


Figure 3.10 Detail an atoms.inp input file to generate “feff.inp” for FEFF calculation.

$E_0)/\hbar^2)^{1/2}$, and Fourier was transformed into the R-space with a k^3 -weight.

In this work, the XAS comprising of XANES and EXAFS were collected at the SUT-NANOTEC-SLRI XAS beamline (BL-5.2), Synchrotron Light Research Institute (SLRI) of Thailand. All spectra of I L3-edge, Pb M5-edge and Ba L3-edge were collected in transmission mode using a Ge (220) monochromator for I and fluorescent using InSb (111) for Pb and Ba edge. The EXAFS spectra were converted by Fourier transform from k space to real space using k^3 -weighting factor and a Hanning window.

The spectra from XANES and EXAFS from experiment and calculation are compared and analyzed in this study two programs in the package are used: 1) ATHENA, a program for basic XAS spectrum analysis, 2) ATHEMIS, a program for EXAFS analysis and fitting the experimental spectra with FEFF theoretical modeling. Which FEFF-XAS spectrum calculation can be edited within the input file name “feff.inp” (see figure 3.10 and 3.11). The file can be controlled with some details, for instance the generator of input file and number of atom which is contained in cluster.

3.2.7 Low-temperature phase transition

Measurement of dielectric properties can provide design parameter information, the loss of a cable insulator, the complex relative permittivity and the complex relative permittivity of the materials. A complex dielectric permittivity includes a dielectric permittivity and dielectric loss. The dielectric permittivity is the ability to store energy an external electrical field when it is applied to the material. The dielectric loss part represent how much energy is lost from the materials due to an external electric field.

The dielectric and specific heat capacities characterization were performed using an alpha Impedance Analyzer (Novacontrol, Germany) in conjunction with the physical property measurement system (see figure 3.12) (PPMS, Quantum Design, USA) at NIMS (National institute for materials science), Japan. This section was employed to measure the dielectric constant and loss tangent on a frequency of 10-10,000 Hz and temperature range from 2-300 K, to determine the phase transition temperature. In addition, still can do in the function of heat capacity in the range of 2-200 K.

```

* This feff.inp file generated by ATOMS, version 2.50
* ATOMS written by and copyright (c) Bruce Ravel, 1992-1999

* -- * -- * -- * -- * -- * -- * -- * -- * -- * -- * -- * --
* -- *
*      total mu =      123.3 cm^-1, delta mu =      75.1 cm^-1
*      specific gravity = 4.119, cluster contains 26 atoms.
* -- * -- * -- * -- * -- * -- * -- * -- * -- * -- * -- * --
* -- *
*      mcmaster corrections: 0.00014 ang^2 and 0.406E-07 ang^
4
* -- * -- * -- * -- * -- * -- * -- * -- * -- * -- * -- * --
* -- *

TITLE    CH3NH3PbI3 tatragonal structure

EDGE      L3
S02       1.0

*      pot      xsph   fms   paths  genfmt  ff2chi
CONTROL   1      1      1      1      1      1
PRINT     1      0      0      0      0      0
|
*      r_scf    [ l_scf  n_scf  ca ]
SCF        6.95441  0      15      0.1

*      ixc      [ Vr   Vi ]
EXCHANGE   0      0      0

*EXAFS
*RPATH     13.90883

*      kmax     [ delta_k  delta_e ]
XANES      4.0      0.07      0.5
*      r_fms     [ l_fms ]
FMS        6.95441  0

*
RPATH       0.10000
*      emin    emax    resolution
*LDOS       -20      20      0.1

POTENTIALS
*      ipot     z [ label  l_scm  l_fms  stoichiometry ]
          0    53   I      -1      -1      0

```

Figure 3.11 Detail of feff.inp input file of $\text{CH}_3\text{NH}_3\text{PbI}_3$ with Pb as center atom for FEFF calculation.

```

POTENTIALS
^  ipot  z  [ label  l_scm  l_fm  stoichiometry ]
    0   53   I    -1    -1      0
    1   82  Pb    -1    -1      1
    2    6   C    -1    -1      1
    3    7   N    -1    -1      1
    4   53   I    -1    -1      3

ATOMS
0.00000  0.00000  0.00000  0  I2
0.00000
-1.89519  2.52931  -0.05815  1  Pb
3.16110
2.52931  -1.89519  -0.05815  1  Pb
3.16110
-1.89519  -1.89519  -1.92917  2  C
3.30230
-1.89519  -1.89519  3.00121  3  N
4.02377
2.52931  2.52931  -1.92917  2  C
4.06405
-1.89519  -1.89519  -3.31979  3  N
4.26667
2.52931  -1.89519  3.06695  4  I1
4.40401
-1.89519  2.52931  3.06695  4  I1
4.40401
-4.42450  0.63412  0.00000  4  I2
4.46971
0.63412  -4.42450  0.00000  4  I2
4.46971
4.42450  0.63412  0.00000  4  I2
4.46971
0.63412  4.42450  0.00000  4  I2
4.46971
2.52931  -1.89519  -3.25405  4  I1
4.53630
-1.89519  2.52931  -3.25405  4  I1
4.53630
2.52931  2.52931  3.00121  3  N
4.66927
2.52931  2.52931  -3.31979  3  N
4.88015

```

Figure 3.11 (Continued) Detail of feff.inp input file of $\text{CH}_3\text{NH}_3\text{PbI}_3$ with Pb as center atom for FEFF calculation.

```

      2.52931      2.52931     -1.92917      2      C
4.06405
      -1.89519     -1.89519     -3.31979      3      N
4.26667
      2.52931     -1.89519      3.06695      4      I1
4.40401
      -1.89519      2.52931      3.06695      4      I1
4.40401
      -4.42450      0.63412      0.00000      4      I2
4.46971
      0.63412     -4.42450      0.00000      4      I2
4.46971
      4.42450      0.63412      0.00000      4      I2
4.46971
      0.63412      4.42450      0.00000      4      I2
4.46971
      2.52931     -1.89519     -3.25405      4      I1
4.53630
      -1.89519      2.52931     -3.25405      4      I1
4.53630
      2.52931      2.52931      3.00121      3      N
4.66927
      2.52931      2.52931     -3.31979      3      N
4.88015
      -1.89519     -1.89519      4.39183      2      C
5.14506
      -3.79038     -3.79038      0.00000      4      I2
5.36041
      2.52931      2.52931      4.39183      2      C
5.66419
      5.05862     -3.79038      0.00000      4      I2
6.32112
      -3.79038      5.05862      0.00000      4      I2
6.32113
      0.63412      0.63412      6.32100      4      I2
6.38430
      0.63412      0.63412     -6.32100      4      I2
6.38430
      -1.89519     -6.31969     -0.05815      1      Pb
6.59800
      -6.31969     -1.89519     -0.05815      1      Pb
6.59800
END

```

Figure 3.11 (Continued) Detail of feff.inp input file of $\text{CH}_3\text{NH}_3\text{PbI}_3$ with Pb as center atom for FEFF calculation.



Figure 3.12 The alpha Impedance Analyzer in conjunction with the physical property measurement system.

CHAPTER IV

RESULT AND DISCUSSION

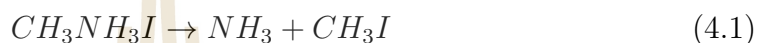
The experimental results and their discussion on the study of the Lead-free perovskites materials are reported in this chapter. This chapter is divided into four sections. The first section describes the $\text{CH}_3\text{NH}_3\text{I}$ pure phase formation. The second is devoted to explaining the phase formation of $\text{CH}_3\text{NH}_3\text{PbI}_3$. The other two sections describe the phase formation of Sn^{2+} and Ba^{2+} doped $\text{CH}_3\text{NH}_3\text{PbI}_3$. In part of characterization, the phase structure, crystal size of all samples are studied by XRD, FTIR and XPS. The optical bandgap are studied by UV-vis technique. The local structure that confirm the structure in materials, are studied by using XANES and EXAFS. These techniques can be employed to explain the low-temperature phase transition.

4.1 $\text{CH}_3\text{NH}_3\text{I}$ synthesis

$\text{CH}_3\text{NH}_3\text{I}$ powders were synthesized by sol-gel method. The $\text{CH}_3\text{NH}_3\text{I}$ showed a white color conversion from solvent yellow color. The global structure of $\text{CH}_3\text{NH}_3\text{I}$ was investigated by PXRD patterns which 2θ scans were obtained using a step size of 0.02° and time per step of 4 s was used. In addition, the $\text{CH}_3\text{NH}_3\text{I}$ powder were characterized by TGA and XPS to confirmed the organic compound in the sample.

4.1.1 TGA analysis

TGA is used here to determine the mass loss behaviour of individual organic component that make up the building block of $\text{CH}_3\text{NH}_3\text{I}$ as the function of temperature. The TGA spectra is presented in figure 4.1. The component, undergo 100% weight loss in the first step during the thermal degradation of $\text{CH}_3\text{NH}_3\text{I}$, which occurs at 271°C under an inert atmosphere proceeds as:



Therefore, the decomposition reactions of the methylammonium ions (CH_3NH_3^+) assisted by iodide proceed through the so-called reverse Menshutkin reaction (a bimolecular nucleophilic substitution $\text{S}_{\text{N}}2$ simultaneously breaking a C–N bond and forming a C–I bond) as it is well described for quaternary ammonium salts (Emilio J et al., 2016). The remaining residues may be some decomposition products or impurities present in the materials. For example, the HI is distilled 99.999% trace metal basis, thus contain 0.001% impurities that may or not undergo decomposition or evaporation up to 650°C .

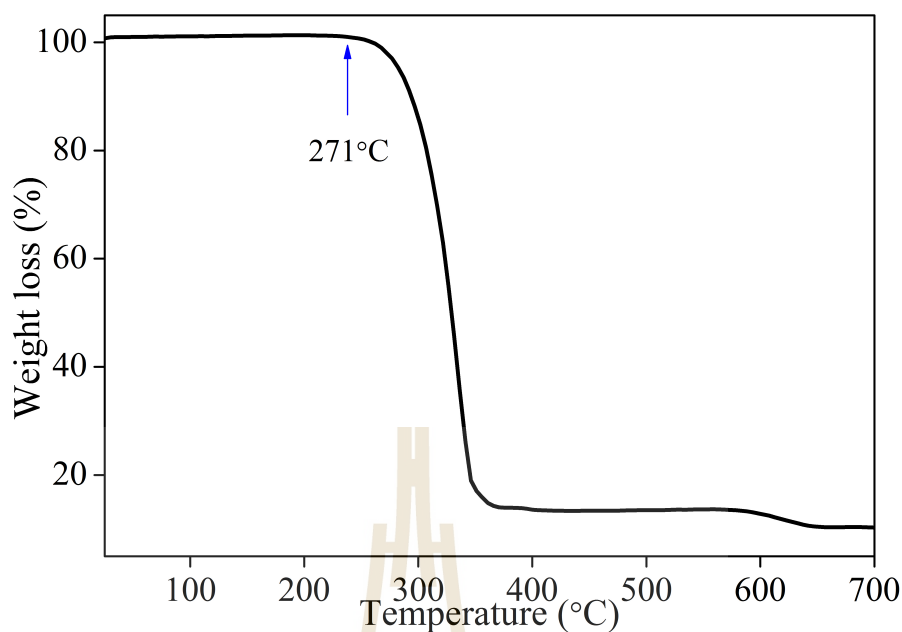


Figure 4.1 Weight loss curves of powder.

4.1.2 XRD spectra

XRD measurement was formed from HI and CH_3NH_2 are observed to show the peaks associated with the expected CH_3NH_3 (see figure 4.2). Clearly, the XRD peaks are good agreement with previous work (Emilio J et al., 2016) and exhibited single phase of orthorhombic (P22121) space group. In addition, the Rietveld refinement shown $W_{Rp} = 10.40\%$, $\text{GOF} = 1.92$, which confirm the good fitted with 100% orthorhombic (P22121) model.

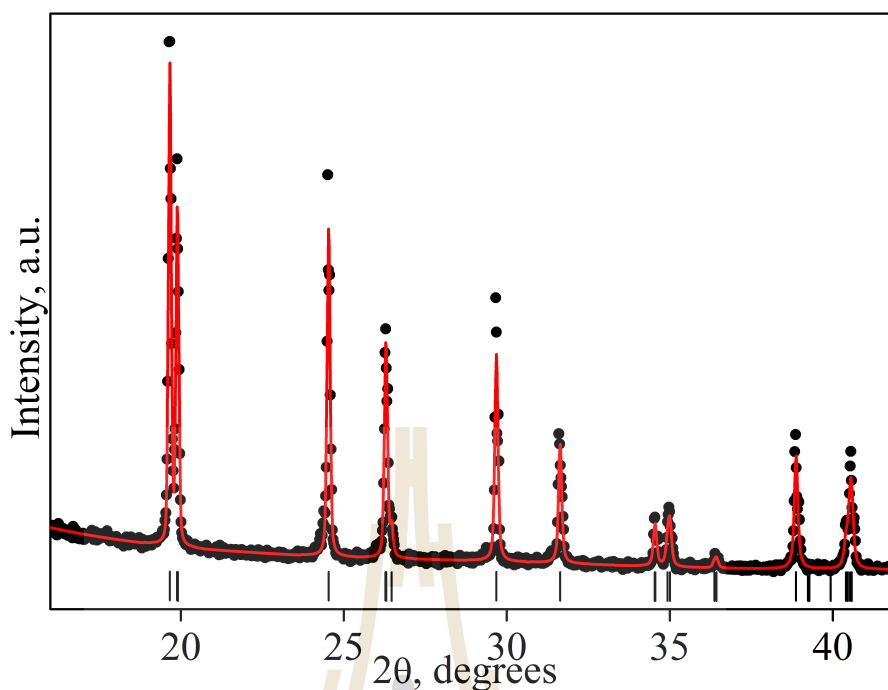


Figure 4.2 The XRD spectra of $\text{CH}_3\text{NH}_3\text{I}$ powders from mixed precursor solution of HI and CH_3NH_2 .

4.1.3 XPS spectra

The XPS spectra are shown figure 4.3, representation spectra for C 1s, N 1s, I 3d and O 1s are presented in figure 4.3, panels a-d, respectively. The C 1s spectrum attribute the appearance of a higher BE peak at 284.6 eV in the C 1s spectrum to NH_3 from $\text{CH}_3\text{NH}_3\text{I}$ sample. Moreover, we observed signal at 285.6, 287.2 and 288.3 eV, corresponding to C-N, C-I and CO_2 . The CO_2 signal was exposed to any carbon-/oxygen-containing contamination of the XPS preparation (see figure 4.3a and d). In addition, N 1s show strong and small peaks confirmed the N-H and C-N, respectively.

Additionally, I 3d is presented in figure 4.3c. The I 3d spectra show a strong peaks at 617.8 and 629.4 eV (I $3d_{5/2}$ and I $3d_{3/2}$), corresponding to C-I in the I 3d for CH_3I , which corresponding to chemical reaction as equation 4.1.

Based on the observations above, we can specify that synthesized $\text{CH}_3\text{NH}_3\text{I}$ has an outstandingly orthorhombic phase. First principles calculation support the experimental results, which molecular ionic pair (CH_3NH_2^+ and I^-) decomposes to energetically favoured thermal degradation products CH_3I and NH_3 in strong contrast to the decomposition pathway to CH_3NH_2 and HI (Emilio J et al., 2016).

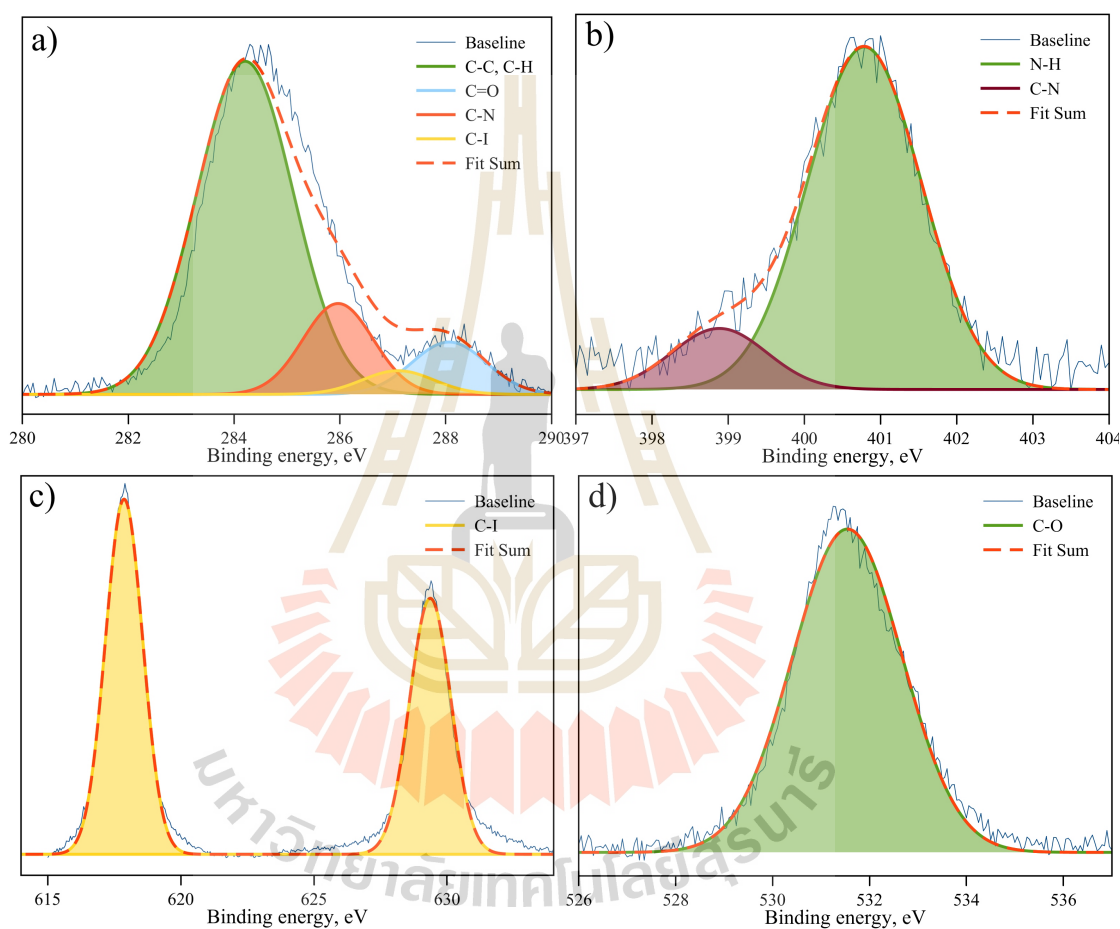


Figure 4.3 The XPS spectra of a) C 1s, b) N 1s, c) I 3d and O 1s for $\text{CH}_3\text{NH}_3\text{I}$.

4.2 $\text{CH}_3\text{NH}_3\text{PbI}_3$ perovskite

We synthesized $\text{CH}_3\text{NH}_3\text{PbI}_3$ compound from $\text{CH}_3\text{NH}_3\text{I}$ and PbI_2 by direct mixing method. The samples were analyzed using many techniques, including TGA, PXRD, UV-vis, FT-Raman, XPS technique and phase transition at low temperature.

4.2.1 TGA analysis

Thermal analysis was used to determine the mass loss behavior of the individual organic and inorganic components that make up the building blocks of MAPbI_3 as a function of temperature. The sublimation behavior of the isolated organic component was examined in depth and used to interpret the STA data of $\text{CH}_3\text{NH}_3\text{PbI}_3$ powder. STA curve is shown in figure 4.4. The weight loss occurs in several steps between 250 and 700°C corresponding to the total weight loss of 85% with the remaining 15% of the unidentified black residue. Our STA data show two main weight loss steps at 326 and 426°C corresponding to the weight loss of 28%, 57% (see figure 4.4), respectively. The high-temperature weight loss demonstrated several shoulders extending to 700°C. The STA data reported here are in qualitative agreement with the $\text{CH}_3\text{NH}_3\text{PbI}_3$ decomposition reported earlier by Amalie et al. (Amalie et al., 2014). While there are some quantitative differences between the two data sets (see figure 4.4), they may be explained by the different carrier gas used (e.g., Ar in our case and N_2 in the case of Ref. (Amalie et al., 2014)) and different heating rates.

The weight loss between 270 and 340°C is attributed to the thermal decomposition of the $\text{CH}_3\text{NH}_3\text{PbI}_3$ at which the organic components i.e., $\text{CH}_3\text{NH}_3\text{I}$, CH_3NH_2 and HI are removed from the material. Indeed, the decomposition reaction $\text{CH}_3\text{NH}_3\text{PbI}_3 \rightarrow \text{CH}_3\text{NH}_3\text{I} + \text{PbI}_2$ predicts the weight loss of 25.7% in good

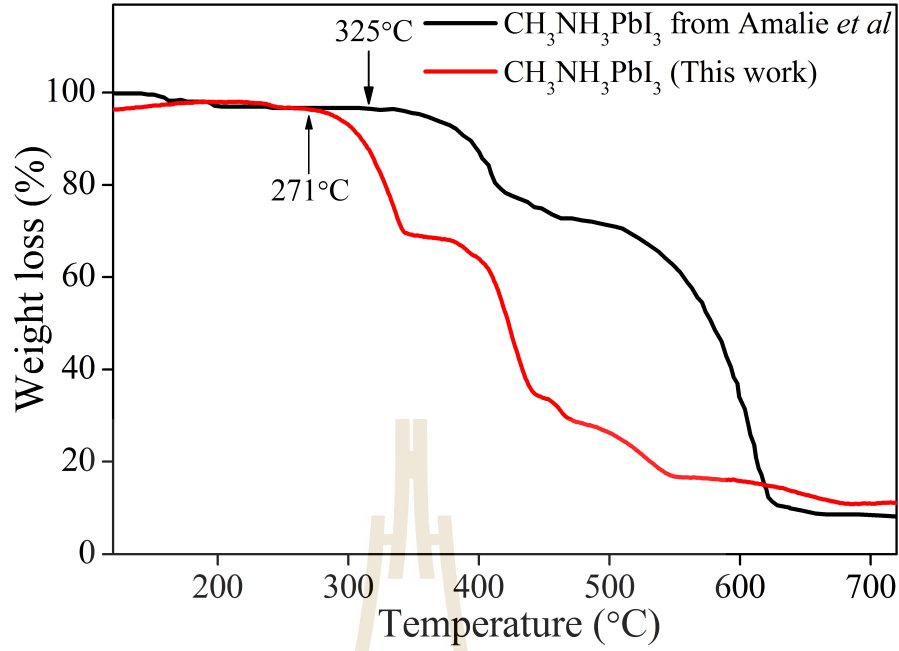


Figure 4.4 The weight loss curves of $\text{CH}_3\text{NH}_3\text{PbI}_3$ powder (red) and data from Amalie et al. (black).

agreement with the experimentally determined weight loss of 28%. A recent study on the $\text{CH}_3\text{NH}_3\text{PbI}_3$ perovskite thin film shows that $\text{CH}_3\text{NH}_3\text{PbI}_3$ begins to transform to PbI_2 at temperature as low as 140°C (Supasai et al., 2013). The next major weight loss occurs in the temperature interval of $400\text{--}690^\circ\text{C}$. We attribute this loss to the partial sublimation of the remaining PbI_2 inorganic component from the melt. While there is a noticeable difference in the onset temperature of the PbI_2 sublimation process detected in our data ($T = 425^\circ\text{C}$) and the data reported in Ref. (Amalie et al., 2014) ($T = 588^\circ\text{C}$), the temperature of the completion of the weight loss is almost the same, i.e. $650 \pm 20^\circ\text{C}$. At the moment we do not have a clear explanation as to why the onset temperatures of the PbI_2 sublimation in our data and Ref. (Amalie et al., 2014) differ so much. The possible reasons behind this discrepancy could be the different heating and gas flow rates as well as the morphology and purity of the sample.

4.2.2 XRD spectra

$\text{CH}_3\text{NH}_3\text{PbI}_3$ perovskite powders, all Bragg peaks were indexed as (hh0) Bragg reflections on a tetragonal I4/mcm cell with $a = b \simeq \sqrt{2}a_c$, $c \simeq 2a_c$ indicating a highly oriented growth.

The XRD patterns of MAPbI powders annealed at different temperatures are shown in figure 4.5. XRD patterns of sample show sharp diffraction peaks at 13.9° for (002), 14.1° for (110), 19.9° for (112), 28.4° for (220), 32.1° for (310), 40.5° for (224) and 41.1° for (400), as shown in Figure 4.5. Among them, (110) and (220) peaks are the strongest. The XRD results suggest that the crystal structure of MAPbI powders is a tetragonal phase (I4/mcm space group) with lattice parameters of $a = 8.8586 \text{ \AA}$ and $c = 12.6280 \text{ \AA}$ (Takeo, 2015). The XRD result also indicates that an increase in the annealing temperature causes a gradual shift in diffraction peaks toward lower angles, suggesting larger lattice parameters. Figure 4.5b shows the magnification of (002) and (110) peaks where both peaks shift to lower 2θ values as the temperature increases. An increase in the annealing temperature to 225 and 250°C results in materials with the cubic structure (Pmm space group), as indicated by the typical peak at 13.84° . The sharp diffraction peaks also indicate the high crystallinity of the powders. It is evidenced by the low-value shift of 2θ in figure 4.5b, the annealed tetragonal samples exhibit larger cell parameters than the as prepared MAPbI. This observation is confirmed by the results of the Rietveld refinement listed in Table 4.1. The particle size was estimated by the Scherrer equation $\tau = k\lambda/\text{FWHM} \cos \theta$; where τ is the crystallite size, k is the dimensionless shape factor (0.89), λ is the X-ray wavelength (1.5406 \AA), FWHM is the line broadening at half the maximum intensity and θ is the Bragg angle (in degrees) of the XRD pattern. The results for tetragonal samples are summarized in Table 4.1. The data for MAPbI-225 and MAPbI-250 samples

are not shown here because in this work we focus mainly on the materials with a tetragonal structure, while MAPbI-225 and MAPbI-250 samples exhibited the cubic structure, as shown in figure 4.5, with an increased portion of PbI₂ phase.

A clear correlation is observed between the annealing temperature and the perovskite formation behavior. The samples annealed at 200°C gave the higher proportion of the tetragonal structure (97.4%) with the lattice parameters a , c and τ ; $a = 8.8735, 12.6657 \text{ \AA}$ and 2.55 nm , respectively. At lower annealing temperatures, both the lattice parameters and the crystallinity decreased as a consequence of incomplete conversion of PbI₂ + CH₃NH₃I into the perovskite phase also resulting in appearance of the secondary phases. At higher temperature (200°C) a more complete phase formation was observed, as confirmed by Rietveld refinement. Unfortunately we could not achieve complete phase purity of the CH₃NH₃PbI₃ perovskite. In addition to the main phase, the peak at $2\theta = 12.6^\circ$ originating from PbI₂ was present in all the samples both annealed and as-prepared. This is consistent with the results reported in Ref. (Brenner et al., 2016). However, our results show that annealing at 200°C can significantly suppress the PbI₂ secondary phase in our powder down to 3.6%.

Table 4.1 Phase formation, lattice parameter and Crystallite size by Rietveld refinement of the XRD pattern. (when AT is annealed temperature, PF is phase formation, LP is lattice parameter and CS is crystallite size).

| Sample | AT (°C) | % PF | | LP (Å) | | CS | |
|-----------|------------|--|------------------|---------|---------|--------|--------|
| | | CH ₃ NH ₃ PbI ₃ | PbI ₂ | a | c | FWHM | D (nm) |
| MAPbI | - | 46.6 | 53.4 | 8.8743 | 12.6660 | 0.0905 | 2.30 |
| MAPbI-150 | 150 | 83.9 | 16.1 | 8.8769 | 12.6581 | 0.0790 | 2.49 |
| MAPbI-200 | 200 | 97.4 | 3.6 | 8.8735 | 12.6657 | 0.0870 | 2.55 |

4.2.3 UV-vis spectroscopy

The optical properties of MAPbI powders are shown in figure 4.7. In the absorption spectra of the samples at different annealing temperatures, the absorption edge is seen to shift to lower energy (longer wavelength) with increasing annealing temperature. The band gap was calculated by applying the Kubelka-Munk (K-M) equation to the measured diffused reflectance spectra (Kortüm, 1969; EL, 1975). By fitting the plots of the photon energy (eV) vs $[F(R)h\nu]^2$, the band gap energies of $E_g=1.53 (\pm 0.002)$, $1.52 (\pm 0.001)$ and $1.51 (\pm 0.004)$ eV were obtained for as-prepared sample and samples annealed at $T = 150^\circ\text{C}$ and 200°C , respectively; consistent with the previous reports (Oku, 2015). The position of the absorption peak corresponding to the band gap is determined by I (5p) orbitals and the Pb (6s) orbitals. The optical transitions in the methylammonium lead halide perovskite are similar to the transitions in PbI₂ (Oku, 2015; Brenner et al., 2016; Ishihara et al., 1990). The valence band of the PbI₂ is composed of

Pb (6s) orbitals and I (5p) orbitals while the conduction band is composed of Pb (6p) orbitals. Moreover, the energy level of I (5p) is lower than the energy level of Pb (6s) (Ishihara, 1994), the optical absorption peak position of MAPbI is thus shifted to lower energy with an increase in annealing temperature.



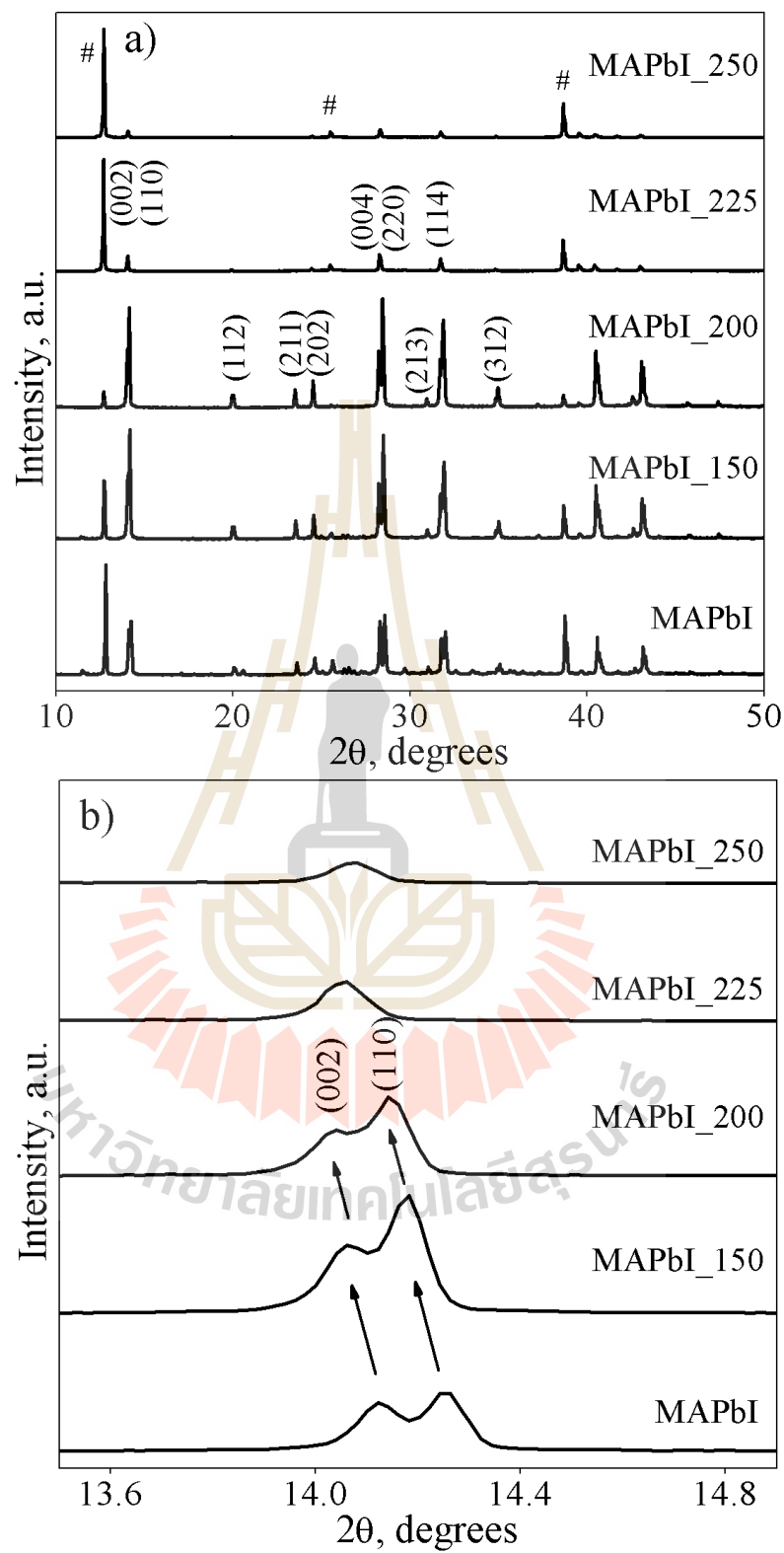


Figure 4.5 a) XRD patterns of $\text{CH}_3\text{NH}_3\text{PbI}_3$ annealed at different temperatures and b) the magnified XRD spectra of (002) and (110) peaks (# PbI_2).

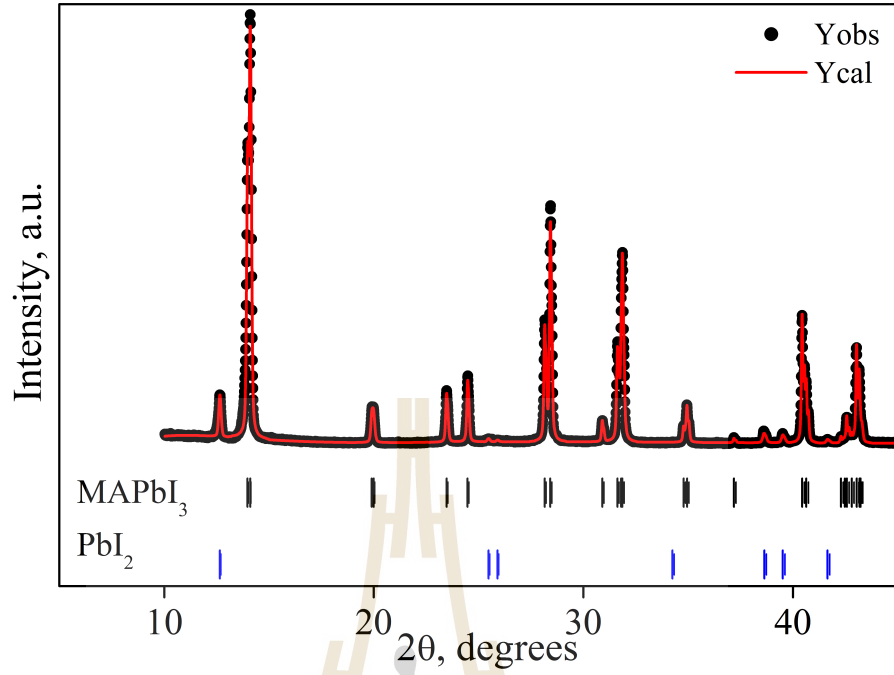


Figure 4.6 Rietveld refinement of the powder X-ray diffraction data of the $\text{CH}_3\text{NH}_3\text{PbI}_3$ materials with experimental data are show as \bullet symbols. The solid line is fit, the vertical bars are the expected Bragg reflection position.

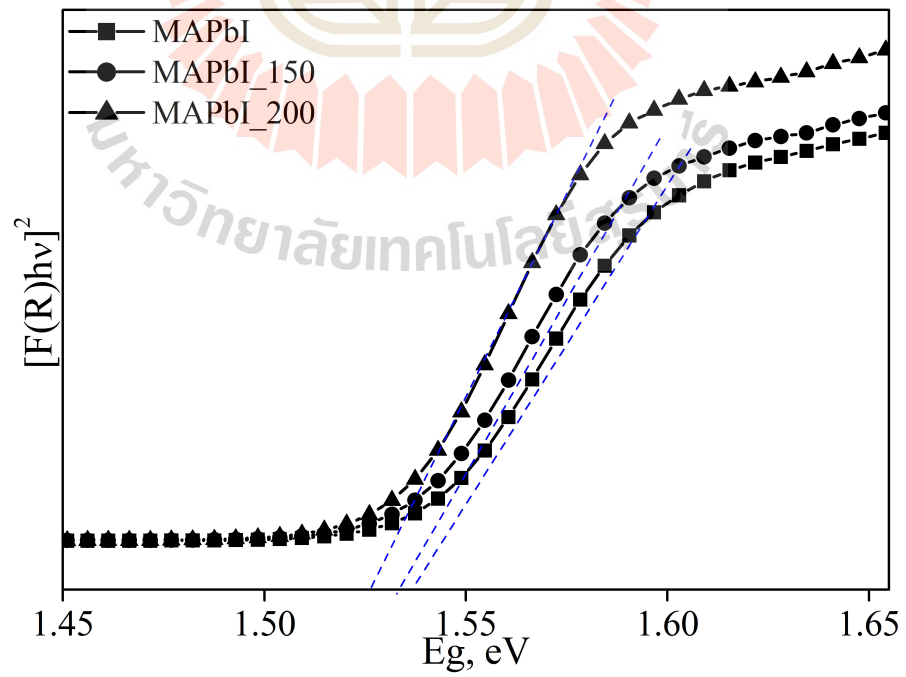


Figure 4.7 The absorption spectra of the $\text{CH}_3\text{NH}_3\text{PbI}_3$ samples.

4.2.4 FT-Raman measurements

The chemical structure of the synthesized perovskite samples can be examined and correlated by the FTIR measurements, as shown in figure 4.8, and Raman measurements presented in figure 4.9a, 4.9b. The FTIR spectra shown in figure 4.8 display the characteristic bands for organic groups detected in the powder samples with peaks at 905 cm^{-1} ($\text{CH}_3\text{-NH}_3^+$ rocking), 957 cm^{-1} (C-N stretch), 1472 cm^{-1} (N-H bending) and 3099 cm^{-1} (N-H stretch), which are attributed to C-H bending modes and N-H stretching modes with the NH_3^+ group of the $\text{CH}_3\text{NH}_3\text{I}$ cation (Müller et al., 2015). The details of the characteristic bands and peak positions are presented in Table 4.2. As seen in figure 4.8, only as-prepared MAPbI sample shows new broad peaks at around 3500 cm^{-1} , which is related to O-H stretching vibrations, as the measurements were carried out under ambient conditions. The O-H oscillations of water molecules are embedded in such a way that they affect the hydrogen bonds between the NH_3^+ group and the iodide because the N-H stretch vibrations are known for their sensitivity to the strength of the interaction between the methylammonium and the iodide (Müller et al., 2015; Glaser et al., 2015).

Figure 4.9a presents the Raman spectra, which offer complementary details on the characteristic bands for the inorganic group in MAPbI powders as a function of annealing temperature. Raman signals in the region from 50 to 300 cm^{-1} (excitation wavelength 532 nm) is present for all measurements and there was no visual change of the samples during the experiment. The spectra are quite similar to those of related hybrid perovskite (Pérez-Osorio et al., 2015) and are characterized by a broad Raman signal in the $50\text{-}150\text{ cm}^{-1}$ region, with two well-defined maxima at ~ 71 and 96 cm^{-1} and two less intense maxima at ~ 61 and 109 cm^{-1} . A broad signal between 166 and 215 cm^{-1} is also found. The ~ 61

and 96 cm^{-1} vibration peaks are in good agreement with density functional theory calculations (Quarti et al., 2014). The 62 and 94 cm^{-1} peaks were reported previously for MAPbI, where as in our samples 61 cm^{-1} peak is very weak, and stronger 71 cm^{-1} peak is more likely corresponding to the significant mode in this area. In addition, the Raman spectra of MAPbI in the region from 800 to 1700 cm^{-1} (excitation wavelength 1064 nm) show the features characteristic to organic species which are compared with the FTIR data, as shown in the figure 4.9b and summarized in Table 4.2. The Raman peaks in the 800 - 1700 cm^{-1} range well correspond to the FTIR features as shown in figure 4.9b. It is noted that some peaks cannot be found in the infrared spectra, but are present in the Raman spectra. This is because the vibration energy is Raman active if it causes a change in polarizability whereas it is IR active if there is a change in the dipole moment. It should be emphasized that the peaks at 905 , 957 , 980 , 1239 , 1423 , 1472 and 1579 cm^{-1} are related to the frequency of vibration mode of organic cation, $\text{CH}_3\text{-NH}_3^+$ rocking, C-N stretching, O-H bending, $\text{CH}_3\text{-NH}_3^+$ rocking, CH_3^+ bending and NH_3^+ bending, respectively (Idigoras et al., 2016). The displacement of the above peaks was found previously (Glaser et al., 2015) when different halides ($\text{X} = \text{Cl}$, Br and I) were used; this change is known as Lorentz-Lorenz shift caused by different interactions of the MA cation with the surrounding Pb-X cage (Lewis and McElhaney, 2000; Juana, 1960).

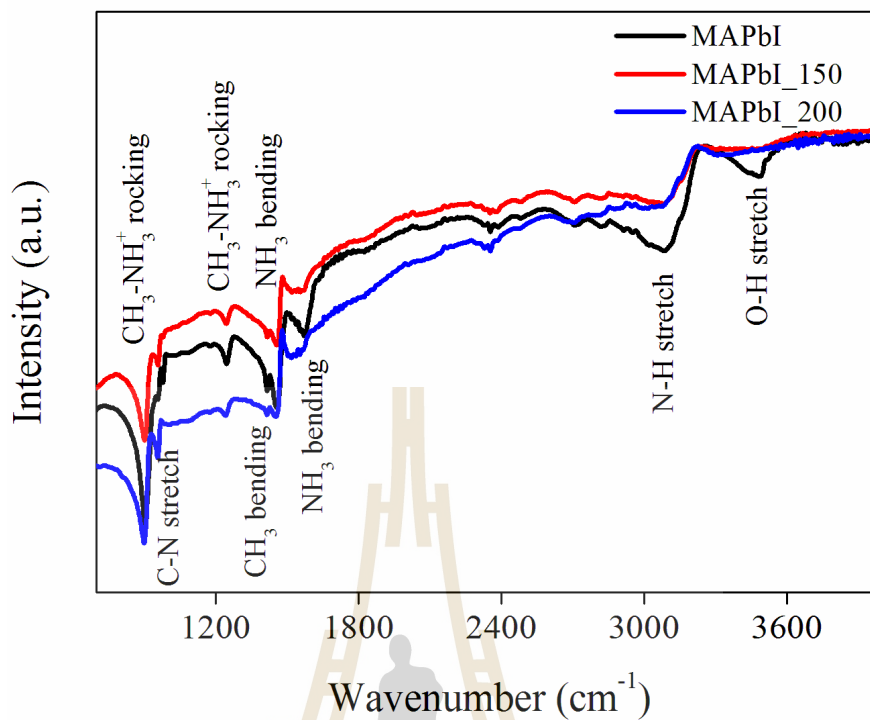


Figure 4.8 FTIR spectra of MAPbI powder in the range of 700-4400 cm^{-1} .

Table 4.2 Measured resonance frequencies of vibrational modes and peak Assignments for perovskites.

| ν | Position (cm^{-1}) | Peak assignment |
|---------|-------------------------------|-------------------------------------|
| ν_1 | 904.74 | $\text{CH}_3\text{-NH}_3^+$ rocking |
| ν_2 | 957.16 | C-N stretch |
| ν_3 | 979.74 | C-N bending |
| ν_4 | 1239.16 | $\text{CH}_3\text{-NH}_3^+$ rocking |
| ν_5 | 1422.64 | CH_3 bending |
| ν_6 | 1472.01 | NH_3 bending |
| ν_7 | 1581.13 | NH_3 bending |

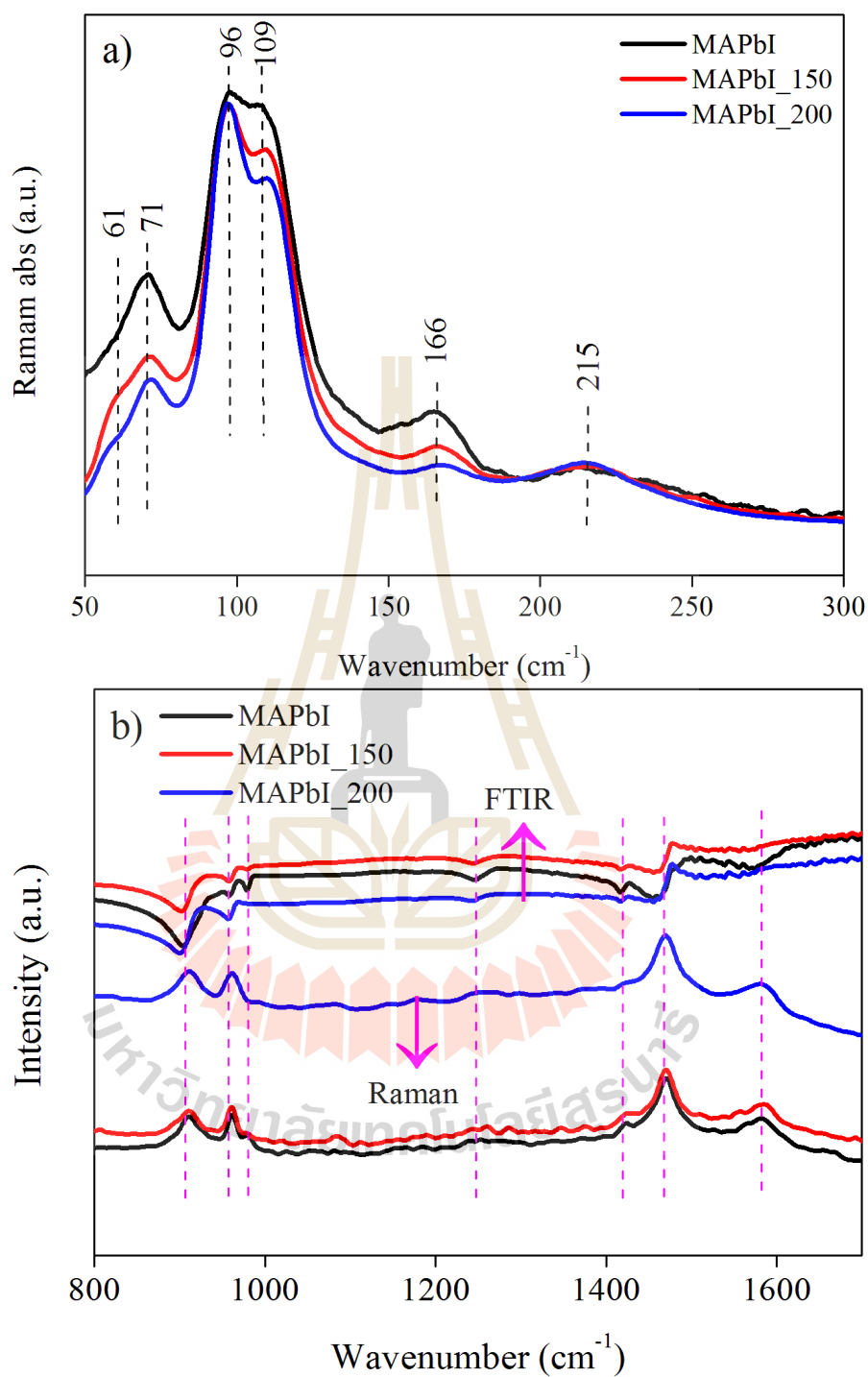


Figure 4.9 The Raman spectra of MAPbI powder in the range of 50-300 cm^{-1} a) and b) comparison between Raman and FTIR spectra in the range of 800-1700 cm^{-1} .

4.2.5 XPS measurement

The XPS spectra were recorded to confirm the oxidation state and chemical bonding states in the samples. The XPS data of C1s, N1s, I3d and Pb4f core levels with the different annealing temperatures. All spectra have been normalized to the same height for visual clarity. When carbon signal is substantially larger, an N1s signal from the organic cation appears. In the case of Pb shown the Figure 4.11, the main Pb4f peak is spin-orbit split into a $4f_{5/2}$ and $4f_{7/2}$ doublet located at ca. 138.4 eV and 143 eV in agreement with the literature data (Haining et al., 2015). The as-prepared sample shows a low-energy shoulder which completely disappears in the sample annealed at 200°C (Figure 4.11). We tentatively attribute this low-energy shoulder in the as-prepared sample to the PbI_2 second phase where the Pb^{2+} ion is located in the different crystal field environment. As the PbI_2 phase almost disappears in the sample annealed at 200°C so does the low-energy shoulder in the Pb4f peak. Figure 4.12 shows I signal ($\text{I}3d_{3/2}$ and $\text{I}3d_{5/2}$) spectra for all the samples at 619.3 eV and small signal at ~ 618.5 eV. The spectra indicate a well separated spin-orbit component, with a separation of around 11.5 eV being found in all the cases which is typical of the presence of I^- (NIST, 2000). In addition, the signals of I are shifted towards higher BE values, suggesting that small modifications are produced in the oxidation state of I^- after annealing (~ 0.2 eV), and the small signal at ~ 618.5 eV suggesting the presence of alkali iodides (Noh et al., 2013). The slight modifications of an interaction between PbI_2 and MAI can be observed in the chemical bonding. For example, the signals obtained for N are analyzed; both N1s and C1s core levels include a second peak, as shown in Figure 4.13 - 4.14 for both as-prepared and annealed samples. The N1s and C1s core signals of the annealed samples shifted slightly towards the higher BE, indicating that the N and C components undergo some complex chemical modifications occurring during the

annealing process. In addition, O-C was found (see figure 4.15), indicated that the samples contamination with air during preparing the sample for measurement.

The previous work by Calloni group reported XPS analysis of the organic-inorganic perovskite prepared from a solution of PbCl_2 and $\text{CH}_3\text{NH}_3\text{I}$ (Alberto et al., 2015). Through a thin-film characterization, it was found that the absence of the Cl peak and detection of the N1s peak in the XPS spectrum are related to methylamine molecules, a strong indication of the dissociation of $\text{CH}_3\text{NH}_3\text{Cl}$ species. Sadoughi et al (Sadoughi et al., 2015) studied the depth-dependent chemical composition of mixed-halide perovskite. Substantial amounts of metallic lead were found in the perovskite films. The post-annealing process in air can reduce the metallic lead content in the perovskite film, indicating that a simple annealing procedure could be employed to increase the performance of perovskite solar cells (Sadoughi et al., 2015). The study reported in Ref. (Sadoughi et al., 2015) clearly demonstrated the importance of the understanding of which type of impurities or defects play a key role in the photovoltaic performance of the perovskite material. In our present work, the optimum annealing condition appears to be approximately 30 min at 200°C in Ar-atmosphere, resulting in the highest proportion of the perovskite material, as confirmed by Rietveld refinement method. The Rietveld refinement was employed in this work to confirm the crystal structure and quantitative phase assemblage. The quantitative information of the $\text{CH}_3\text{NH}_3\text{PbI}_3$ phase listed in the Table 4.1. Annealing of the samples at the temperature higher than 200°C causes degradation of the perovskite material with the loss of the organic component and the PbI_2 formation (Alberto et al., 2015; Sadoughi et al., 2015; Haining et al., 2015; NIST, 2000; Noh et al., 2013), as shown in the Figure 4.5.

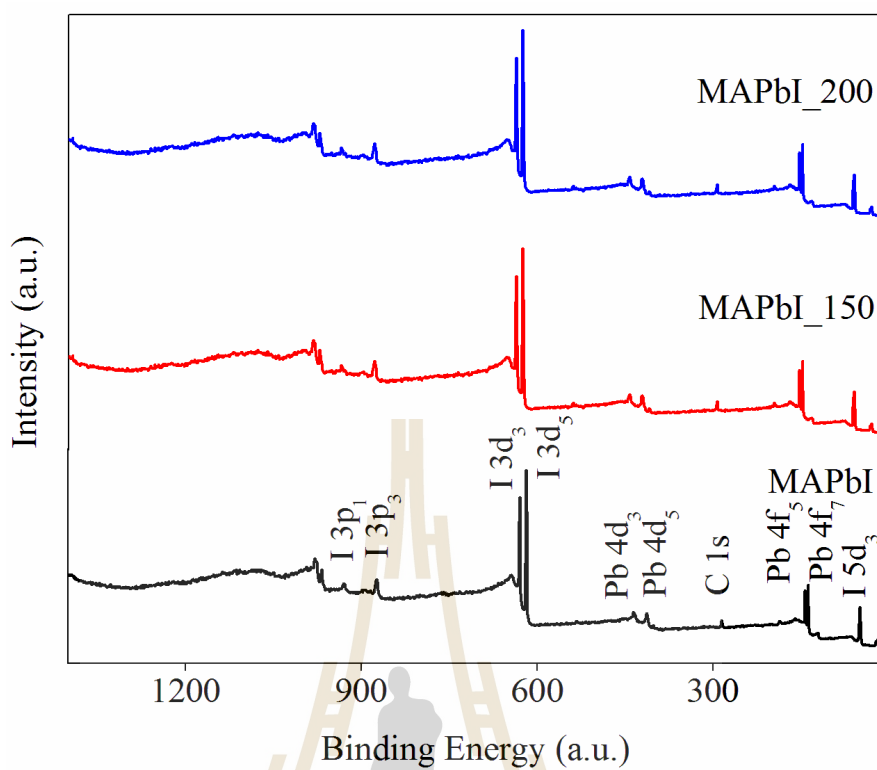


Figure 4.10 XPS survey scan of $\text{CH}_3\text{NH}_3\text{PbI}_3$ powders.

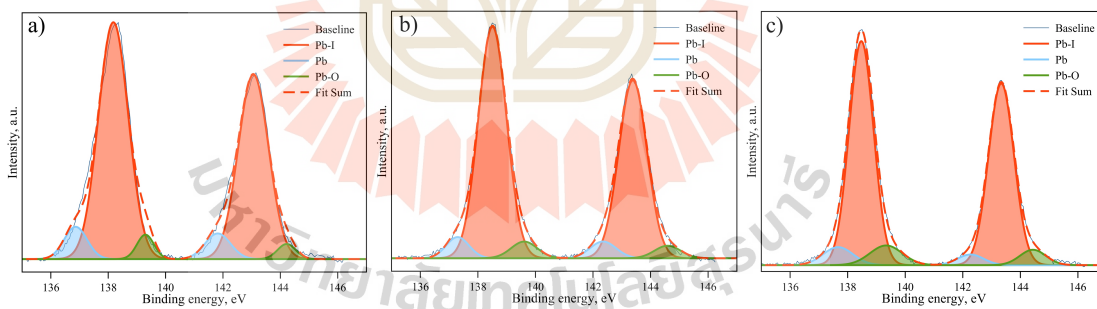


Figure 4.11 XPS spectra of $\text{CH}_3\text{NH}_3\text{PbI}_3$ samples and the Gaussian fitting for Pb 4f of a) MAPbI, b) MAPbI-150°C and c) MAPbI-200°C.

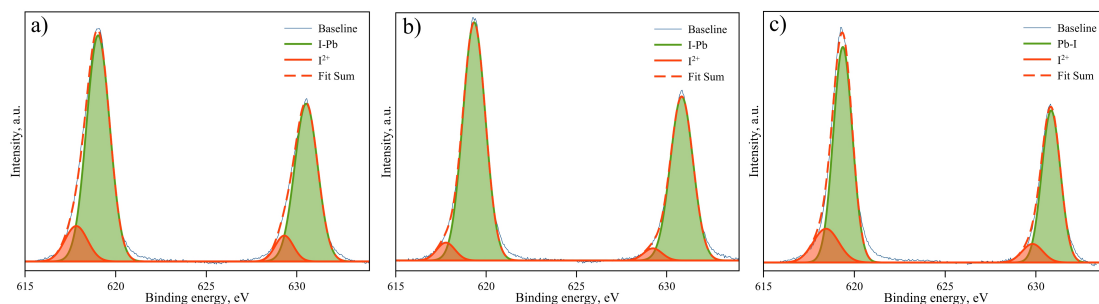


Figure 4.12 XPS spectra of $\text{CH}_3\text{NH}_3\text{PbI}_3$ samples and the Gaussian fitting for I 3d of a) MAPbI, b) MAPbI-150°C and c) MAPbI-200°C.

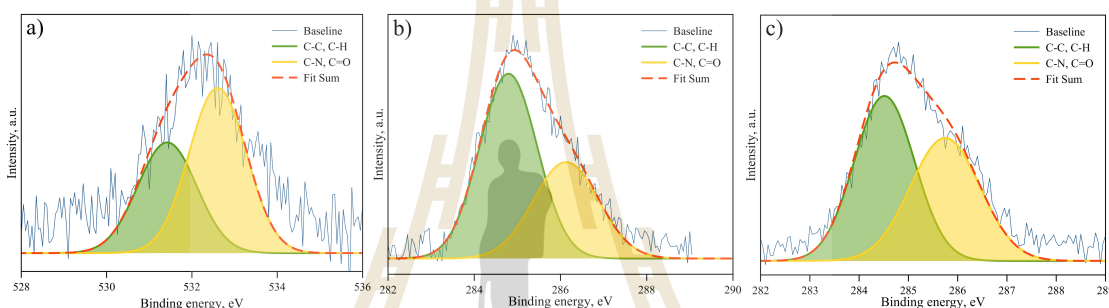


Figure 4.13 XPS spectra of $\text{CH}_3\text{NH}_3\text{PbI}_3$ samples and the Gaussian fitting for C 1s of a) MAPbI, b) MAPbI-150°C and c) MAPbI-200°C.

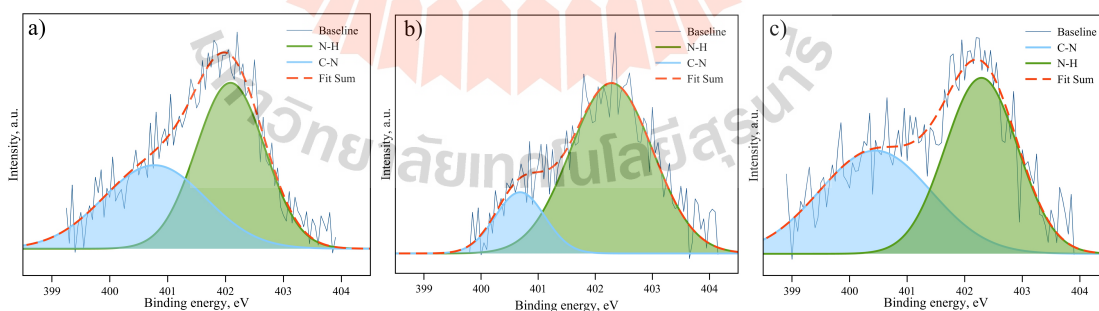


Figure 4.14 XPS spectra of $\text{CH}_3\text{NH}_3\text{PbI}_3$ samples and the Gaussian fitting for N 1s of a) MAPbI, b) MAPbI-150°C and c) MAPbI-200°C.

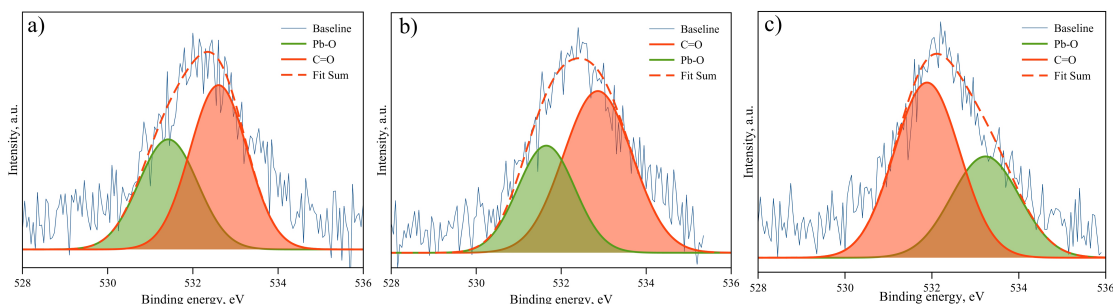


Figure 4.15 XPS spectra of $\text{CH}_3\text{NH}_3\text{PbI}_3$ samples and the Gaussian fitting for O 1s of a) MAPbI, b) MAPbI-150°C and c) MAPbI-200°C.

4.2.6 XANES analysis

The experimental Pb M5-edge (2484 eV) and I L3-edge (4557 eV) XANES spectra have been reported on Lead-halide perovskite materials by a few group. Indeed, up to present, there is no report on theoretical XANES spectrum. In this section, it is shown that XANES can provide the complementary information on local structure verification.

The XANES measurement was done in florescence mode (FL), InSb(111) for Pb M5-edge and transmission mode (TM) Ge(220) for I L3-edge double crystal monochromator were used for photon energy selection. The measurement Pb M5-edge and I L3-edge XANES of $\text{CH}_3\text{NH}_3\text{PbI}_3$ and PbI_2 do not have reference compound available in the database. However, there get supporting information from XRD (Weber, 1978). Therefore, the calculation XANES from candidate compounds must be generated and compared with the experiment results.

The FEFF 8.2 code is used to calculate the XANES spectra of $\text{CH}_3\text{NH}_3\text{PbI}_3$ and PbI_2 for ensuring all features of extrapolated XANES spectra. For calculation of $\text{CH}_3\text{NH}_3\text{PbI}_3$ tetragonal structure, the lattice parameters $a=8.849$ and $c=12.642$ Å (Weber, 1978) are used. For PbI_2 trigonal ($P3m1$) structure, the parameter $a=4.558$, $c=6.986$ Å is used. After the calculation XANES database

has been compiled, the spectra can be used to compared and fitted with the experiment spectra as shown in Figure 4.16 and 4.17. The features of Pb M5-edge experiment spectra (see figure 4.16a) look similar to calculation spectra (see figure 4.16b) of those materials. The calculated spectra are in good agreement with the corresponding measured spectra obtained from those samples. Therefore, from the XAS point of view, it can be concluded that the $\text{CH}_3\text{NH}_3\text{PbI}_3$ and PbI_2 materials used in this work are composed of $\text{CH}_3\text{NH}_3\text{PbI}_3$ and PbI_2 compound.

In addition, I L3-edge (4557 eV) XANES spectra of $\text{CH}_3\text{NH}_3\text{PbI}_3$ and PbI_2 samples also were measured at room temperature. The features of I L3-edge spectra of samples also look similar to calculation spectra. However, a small shift of the absorption edge to the higher energy as shown in figure 4.17. These can be attributed to the concentration of phase with $\text{CH}_3\text{NH}_3\text{PbI}_3$ and PbI_2 structure appeared in XRD pattern of samples.

4.2.7 EXAFE analysis

The experimental absorption result was performed using ATHENA software to get EXAFS spectra. The curve fitting was done for the k^2 -weighted spectrum over the k -range of $3\text{--}8 \text{ \AA}^{-1}$ using a window of Hanning type $W(k)$. The EXAFS spectra were processed, information on local structure of I atom via fitting with perovskite model of $\text{CH}_3\text{NH}_3\text{PbI}_3$ (Weber, 1978) in ARTEMIS program. This material, the I L3-edge EXAFS spectra can only be obtained up to photon of 200 eV above the absorption edge. Therefore, direct EXAFS fitting for sample, the structural parameters can be obtained. In the Figure 4.18a are two k^2 -weighted L3-edge EXAFS spectra; the experimental spectrum and the spectrum from direct fitting. Normally, it may be seen that the two spectra are good agreement over the region $3\text{--}8 \text{ \AA}^{-1}$. Therefore, the good overview of qualitatively and the reliable

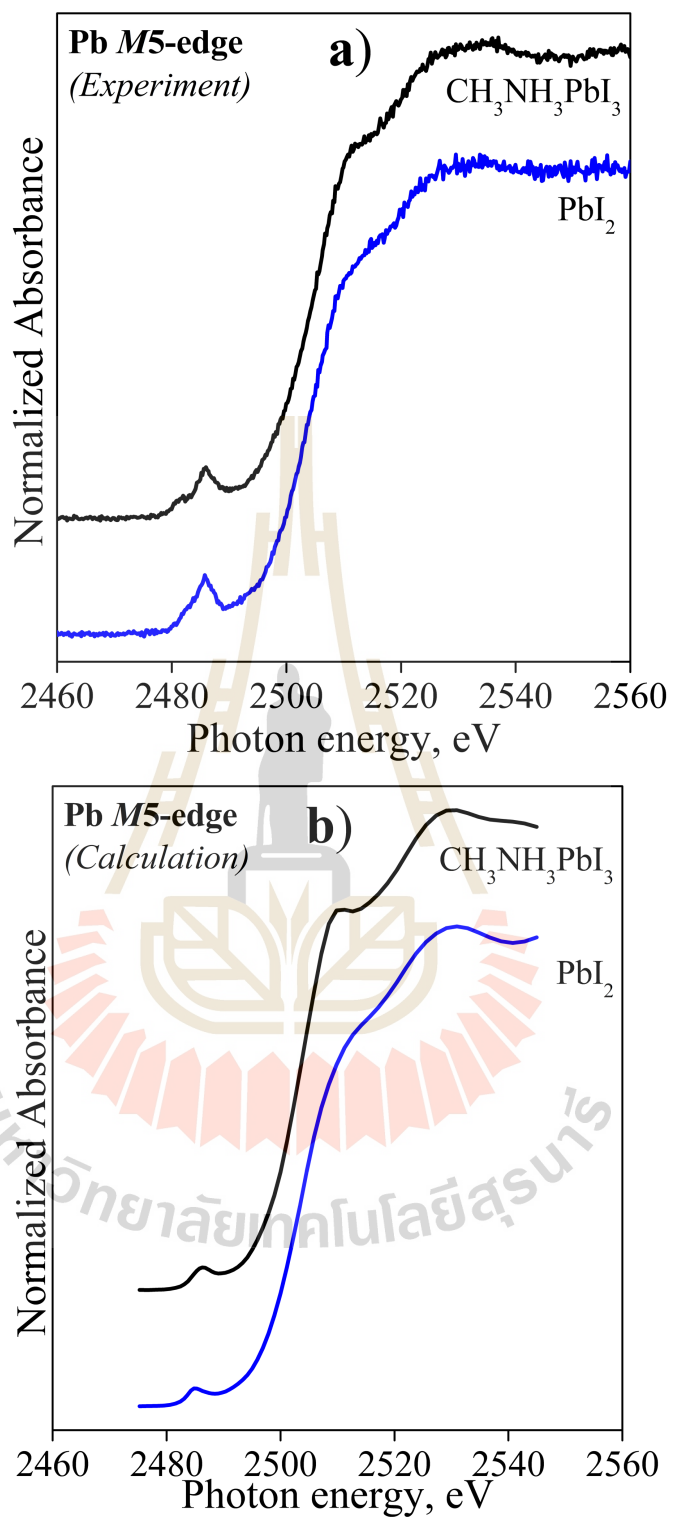


Figure 4.16 Measured Pb M5-edge XANES spectra (a) and calculated Pb M5-edge XANES spectra (b).

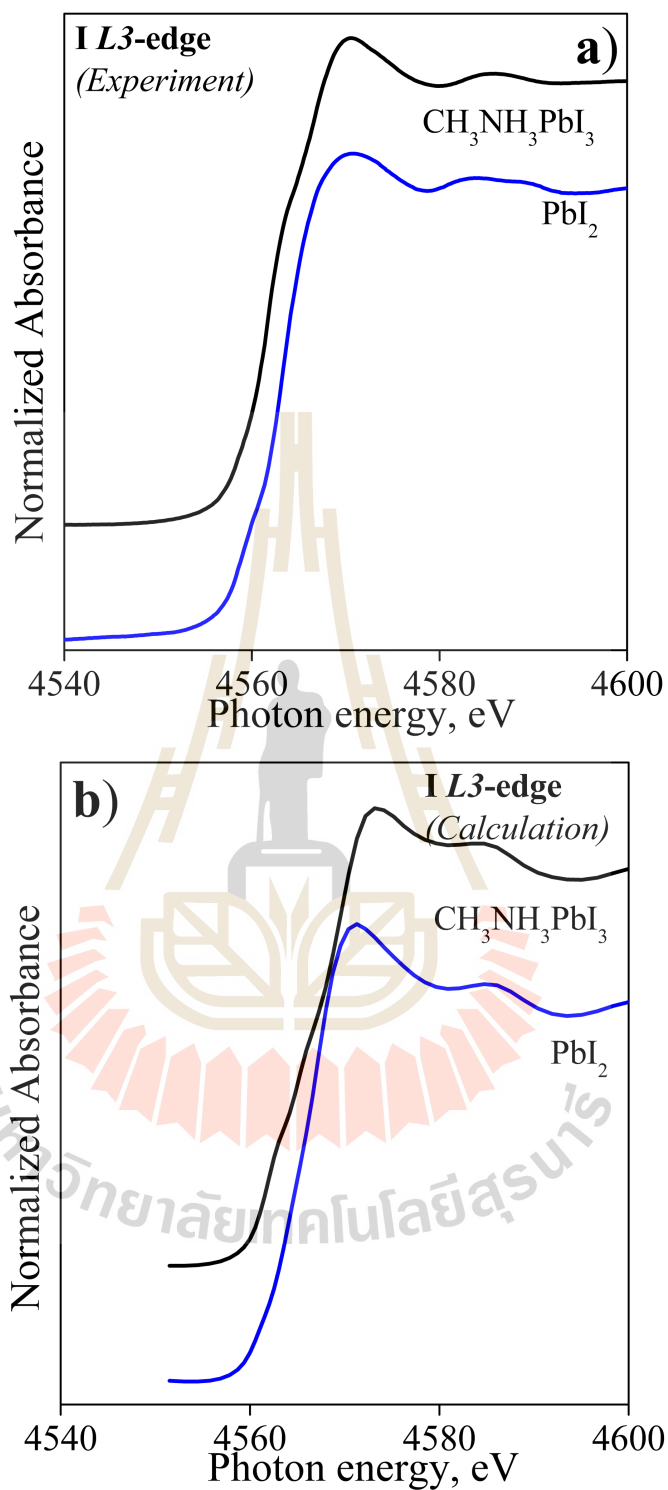


Figure 4.17 Measured I L3-edge XANES spectra (a) and calculated I L3-edge XANES spectra (b).

structural parameters would be obtained from fitting.

From curve fitting of experiment data to the EXAFS equation using FEFF-fit, important structure parameters were extracted. The consistent Fourier transform (FT) of the two spectra are shown in the real space in the figure 4.18b. It can be seen that the fitting spectra can reproduce the experimental data nicely. Indeed, all two spectra show quite good agreement. The first peak position in real space EXAFS can be converted into the radius of first I-Pb shell. The fitting parameters obtained from this sample for average bond length of I absorbing atoms within Pb, C and N atoms (R), Debye-Waller factors (σ^2) and coordination number (N) are shown in Table 4.3.

Table 4.3 The structure parameters coordination numbers N, interatomic distances R and DW factors σ^2 obtained by fitting the EXAFS data for the $\text{CH}_3\text{NH}_3\text{PbI}_3$.

| Shell | N | R [Å] | σ^2 |
|-------|---|-----------|------------|
| I-Pb1 | 1 | 2.9457(6) | 0.0013 |
| I-Pb2 | 1 | 3.0609(1) | 0.0110 |
| I-I1 | 4 | 3.9145(4) | 0.0131 |
| I-I2 | 4 | 4.1083(6) | 0.0180 |
| I-N | 4 | 3.9221(6) | 0.0030 |
| I-C | 4 | 4.1097(1) | 0.0030 |

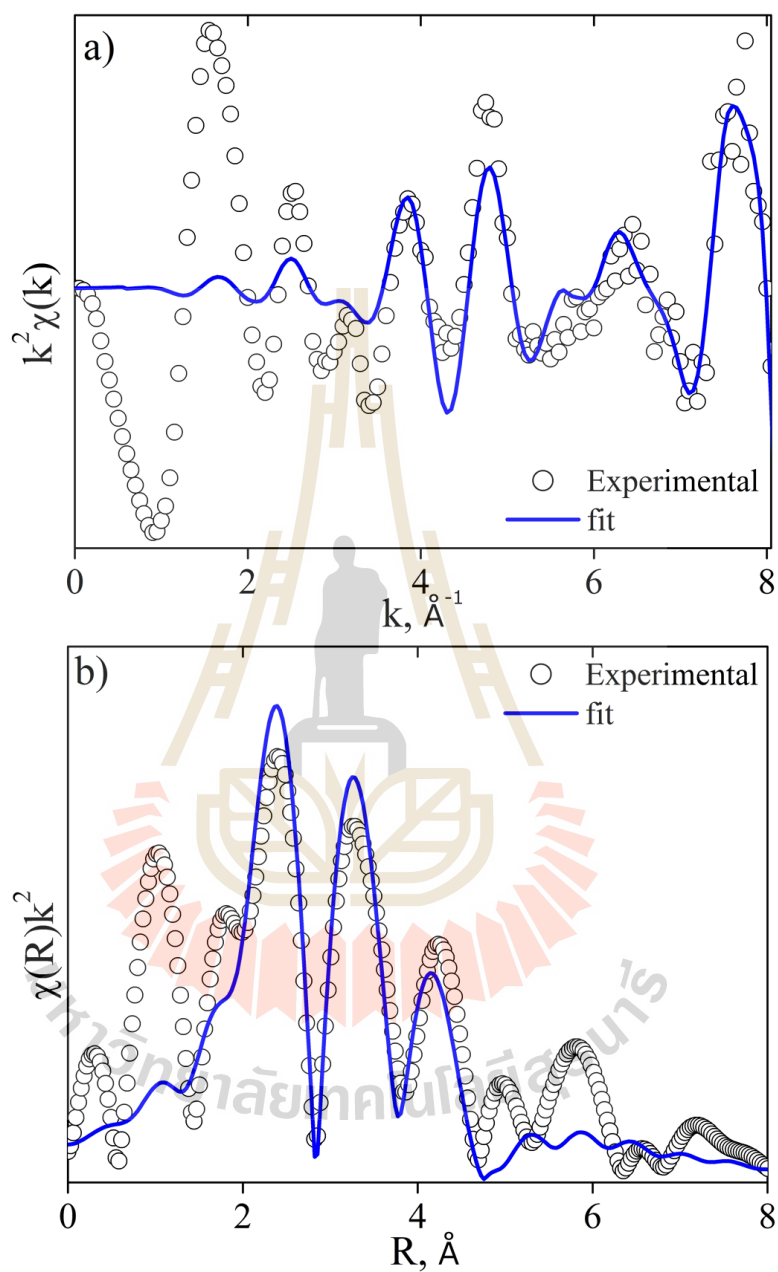


Figure 4.18 Comparison of Experiment and fitted magnitude of EXAFS Fourier transform (FT) (a) and (b) comparison of k^2 -weighted spectrum over the k -range of $\text{CH}_3\text{NH}_3\text{PbI}_3$. The k range used in the FT is from $3\text{--}8.7 \text{ \AA}^{-1}$ for data set.

4.2.8 Low temperature phase transition

Investigation of the low temperature heat capacity on a plot of C/T^3 versus T , shown in the inset of Figure 4.19 to supports the postulate of glassy static disorder in composition. The broader hump in the C/T^3 is similar with previous report. System with glassy disorder are well known to exhibit heat capacity in excess of that which can be attributed to acoustic phonon, although the exact origin of the corresponding 'Boson peak' in the vibrational density state is still an active area of research (Vassiliy and Peter, 2003; Safarik et al., 2006). Fabini et al reported the model curves of Debye temperature to assume a single phase A-site atom rather than a molecule (Fabini et al., 2016), a simplified model that nonetheless reflects the negligible occupancy of high-frequency intermolecular modes at low temperatures.

In addition, the temperature dependence of permittivity (ϵ_r) and dielectric loss ($\tan \delta$) in the range of 3-200 K measured at 1 kHz are presented in Figure 4.20. The $\text{CH}_3\text{NH}_3\text{PbI}_3$ data are quite similar to that reported earlier (Noriko et al., 1992). A sharp drop in dielectric permittivity upon cooling was found for all samples at around 160 K which corresponds to the transition from the high-temperature tetragonal to the low-temperature orthorhombic phase (Weber, 1978; Weller et al., 2015). At temperature of 3 K the dielectric permittivity is around 20-21 for $\text{CH}_3\text{NH}_3\text{PbI}_3$. The low-temperature $\epsilon_r \sim 20-21$ values of the orthorhombic $\text{CH}_3\text{NH}_3\text{PbI}_3$ are in agreement with the earlier reports on the dielectric data (Noriko et al., 1992). The ϵ_r maximum value ($\epsilon_r \sim 47$) at the orthorhombic-to-tetragonal phase transition observed in our studies is similar to the report of Fabini et al (Fabini et al., 2016).

Another important feature is a relatively weak dielectric dispersion at $T_m \sim 60-100$ K whose details are shown in Figure 4.21. Remarkably, similar type

low-temperature weak dielectric dispersion was also observed in the formamidinium lead iodide by Fabini et al. (Fabini et al., 2016). Although it is believed that the orientation (with respect to the inorganic cage) and rotational (around the C-N axis) degrees of freedom of methylammonium ions are frozen out in the orthorhombic phase, the weak dielectric dispersion may indicate some residual dipolar contribution originating from the incomplete frees out, random fields, defects and disorder. Better understanding of the low-temperature dielectric relaxation may lead to further optimization of the room temperature charge carrier transport and PV properties of the $\text{CH}_3\text{NH}_3\text{PbI}_3$ -related perovskites. The low-temperature dielectric dispersion in the title compounds is characterized by the frequency dependent dielectric permittivity anomaly and $\tan \delta$ peak that shifts to higher temperatures as frequency increases (see Figure 4.21).

Interpretation of the low- T dielectric dispersion in $\text{CH}_3\text{NH}_3\text{PbI}_3$ is not without controversy. Onoda-Yamamuro (Noriko et al., 1992) have fitted the dielectric relaxation with a simple Arrhenius-type temperature-activated behaviour, whereas Fabini et al. (Fabini et al., 2016) have attributed the low-temperature relaxation dynamics and specific heat in both $\text{CH}_3\text{NH}_3\text{PbI}_3$ and $\text{HC}(\text{NH}_2)_2\text{PbI}_3$ to the ‘glassy slowing’ which is expected to follow the Vogel-Fulcher-type spin glass dynamics. To better understand the nature of the low-temperature dielectric relaxation we have fitted the frequency dependence of the $\tan \delta(T)$ peak of our samples to both Arrhenius-type behavior.

The fit to Arrhenius and Vogel-Fulcher dielectric relaxation behaviour is shown in Figures 4.22a-b, respectively. The fitting parameters are summarized in Tables 4.4. According to the results, the dielectric relaxation can be described by Arrhenius-type thermally activated behaviour with $E_a \sim 123$ meV and attempt frequency of $f_0 \sim 2 \times 10^{12}$ Hz. Attempts to fit the data to the Volger-Fulcher-type

behaviour resulted in extremely large standard deviations and static dipolar freezing temperature $T_{VF} \approx 4$ (3) K within the standard deviation. However, support the Arrhenius-type thermally activated dynamics of the dipolar re-orientation and do not seem to agree well with the ‘glassy slowing’ of the dipolar relaxation, as proposed by Fabini et al. (Fabini et al., 2016).

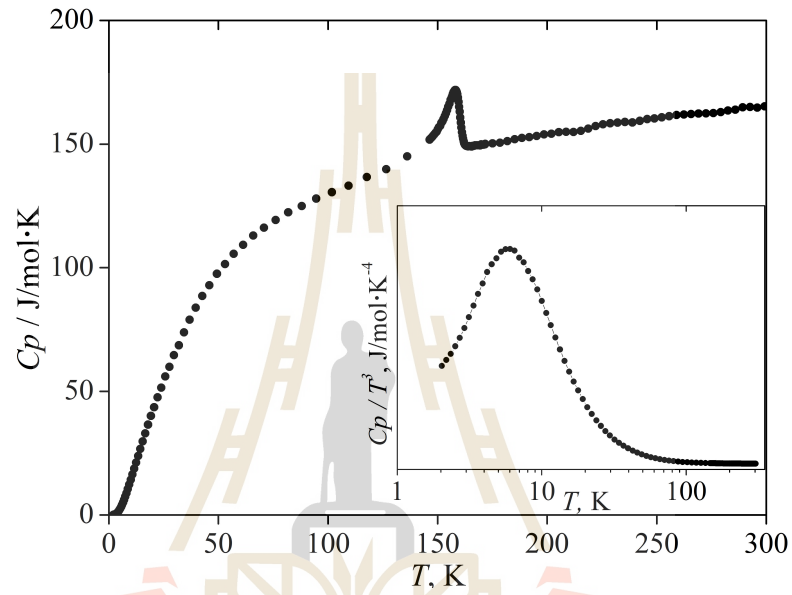


Figure 4.19 Low temperature heat capacity and inset show the C/T^3 of related $\text{CH}_3\text{NH}_3\text{PbI}_3$ material.

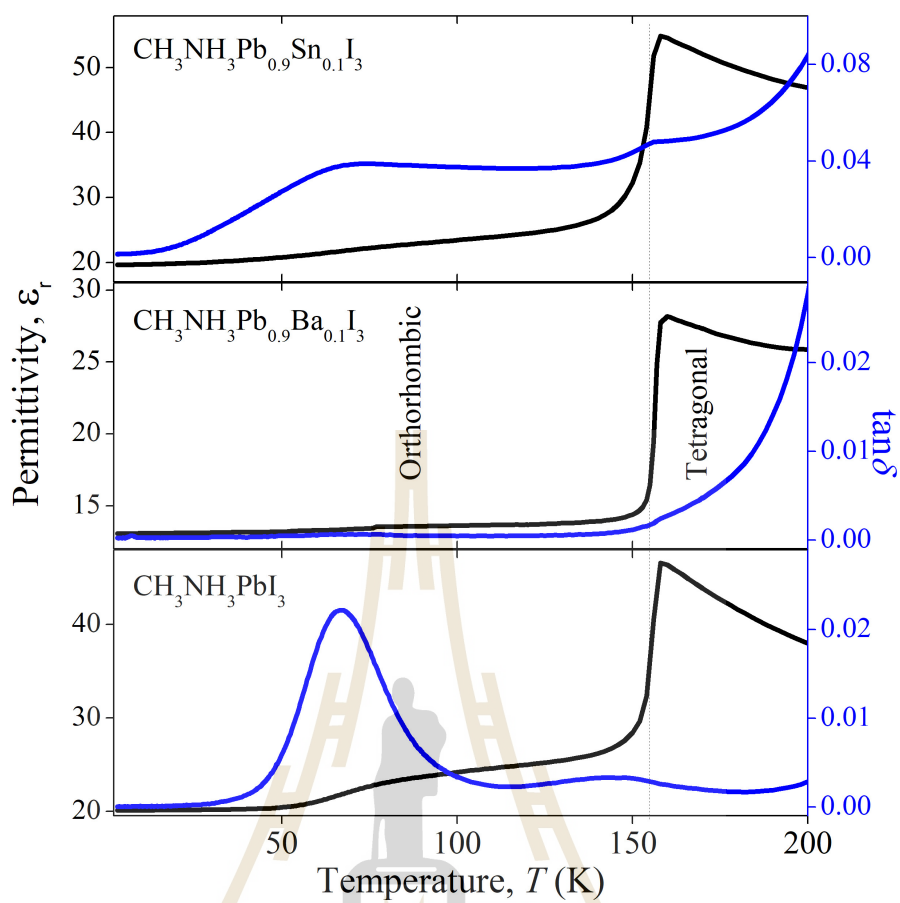


Figure 4.20 Temperature dependence of dielectric permittivity and dielectric loss of $\text{CH}_3\text{NH}_3\text{PbI}_3$, $\text{CH}_3\text{NH}_3\text{Pb}_{0.9}\text{Sn}_{0.1}\text{I}_3$ and $\text{CH}_3\text{NH}_3\text{Pb}_{0.9}\text{Ba}_{0.1}\text{I}_3$.

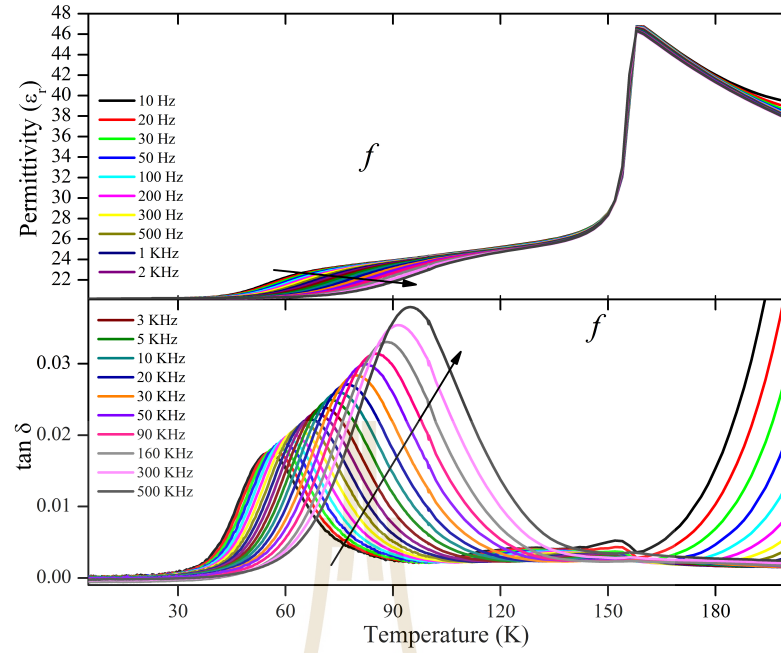


Figure 4.21 Low temperature of permittivity (ϵ_r) and loss tangent ($\tan \delta$) of $\text{CH}_3\text{NH}_3\text{PbI}_3$. Frequency dependent dielectric loss peaks indicating substantial slowing of relaxation dynamics are observed in the sample.

Table 4.4 Fitting parameters and goodness of fit (χ^2) for Arrhenius-type thermally-activated model and Vogel-Fulcher-type model of the dielectric relaxation of $\text{CH}_3\text{NH}_3\text{PbI}_3$ sample. The standard deviations of the fitting parameters are given in brackets.

| Type of fit | f_0 [Hz] | E_a [meV] | T_{VF} [K] | χ^2 |
|---------------|-------------------------|-------------|--------------|----------|
| Arrhenius | $1.8(3) \times 10^{12}$ | 123.0(8) | - | 0.999 |
| Vogel-Fulcher | $6(6) \times 10^{11}$ | 110(10) | 4(3) | 0.999 |

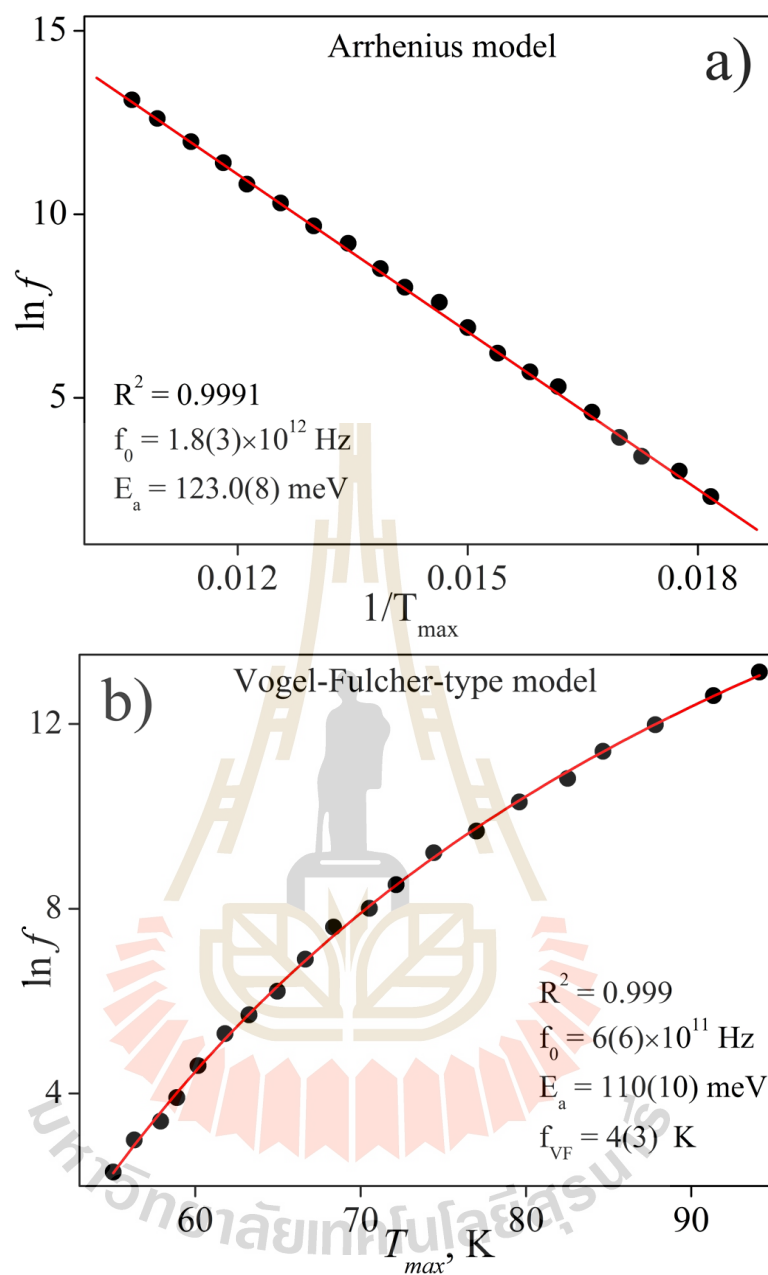


Figure 4.22 Natural logarithm of f as the function of $1/T$ by Arrhenius model a) and b) with the function of T_{\max} by Vogel-fulcher fit model for $\text{CH}_3\text{NH}_3\text{PbI}_3$.

4.3 Sn^{2+} doped on $\text{CH}_3\text{NH}_3\text{Pb}_{1-x}\text{Sn}_x\text{I}_3$ perovskite

We synthesized $\text{CH}_3\text{NH}_3\text{Pb}_{1-x}\text{Sn}_x\text{I}_3$ compound where $x = 0.02, 0.04, 0.06, 0.08, 0.1$ and 0.2 . To do this, synthesized samples were characterized using XRD, UV-vis, FTIR, XPS and phase transition at low temperature.

4.3.1 XRD spectra

The XRD patterns for Sn^{2+} substituted are shown in Figure 4.23. The pattern show the Rietveld refinement of XRD pattern for Sn^{2+} with the profile obtained from the rietveld analysis. It can be clearly seen that the diffraction peaks can be indexed to main phase of tetragonal structure $\text{CH}_3\text{NH}_3\text{PbI}_3$ with I4/mcm space group as reported in the literature (Jintara and Rattikorn, 2017). In addition, the XRD pattern reveals a small amount of impurity phases according to $\text{CH}_3\text{NH}_3\text{I}$ phases. The shape diffraction peaks also indicate that high crystallinity of the powders. It is evidenced by the high-values of shift of 2θ in Figure 4.24a, the Sn^{2+} substituted samples exhibit larger cell parameters than $\text{CH}_3\text{NH}_3\text{PbI}_3$ undoped. In addition, this observation are confirmed by the results of the Rietveld refinement listed in Table 4.5.

The crystallite size of samples calculated from diffraction peaks is about 15 nm. Clearly correlation is observed between the Sn^{2+} substitution and the perovskite formation behavior. The Sn^{2+} substituted in the $\text{CH}_3\text{NH}_3\text{PbI}_3$ gave the high fraction of the tetragonal structure (80-90%) with the enlarge lattice parameter. Unfortunately we could not achieve complete phase purity of $\text{CH}_3\text{NH}_3\text{PbI}_3$ material. The impurity phase originated from $\text{CH}_3\text{NH}_3\text{I}$ and PbI_2 were present in all the samples. This is contract results reported in ref (Javier et al., 2015). They are claimed that the 10% doping of Sn^{2+} on thin film shows single phase of tetragonal structure.

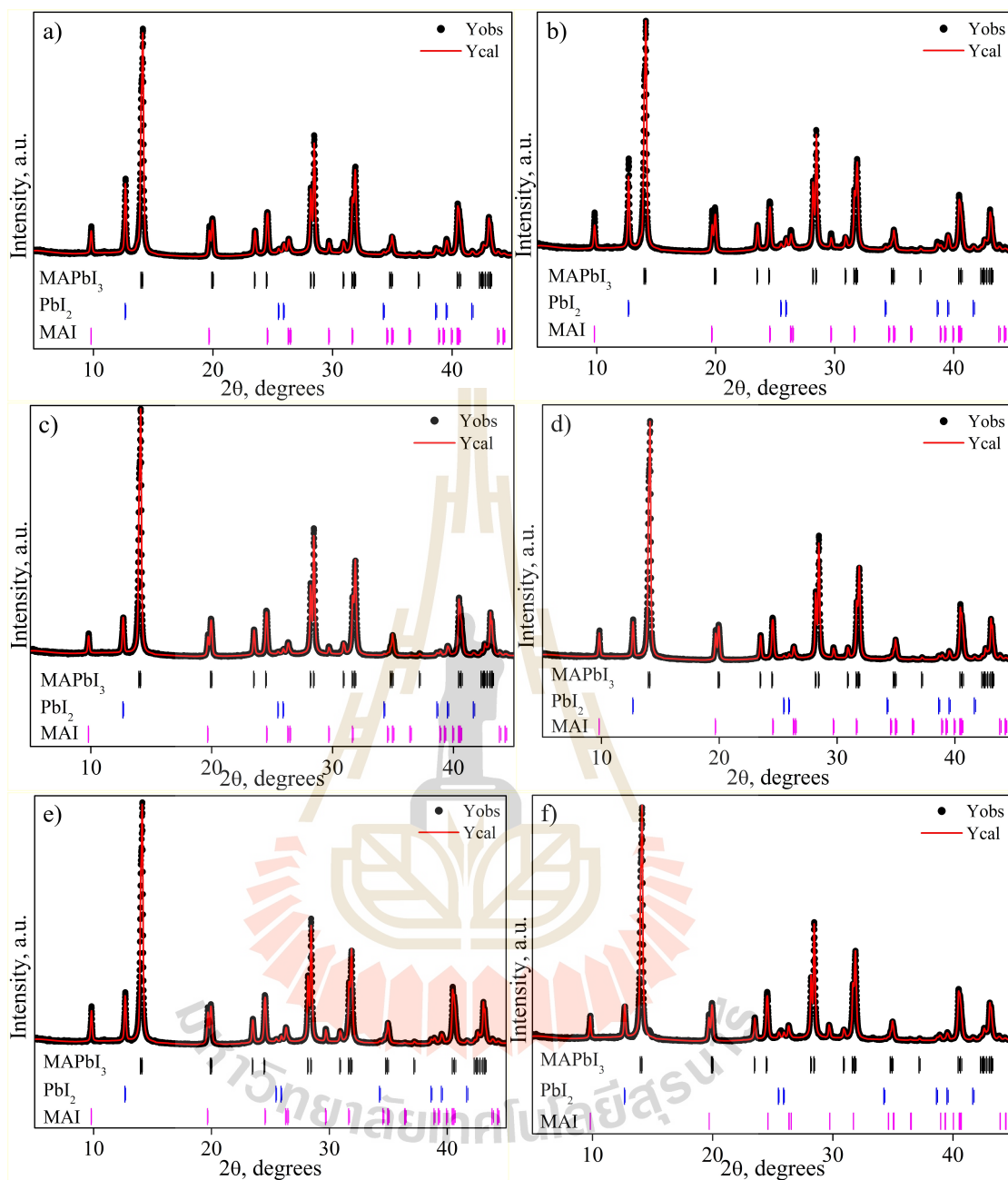


Figure 4.23 Rietveld refinement of the powder X-ray diffraction data of the Sn^{2+} doped $\text{CH}_3\text{NH}_3\text{Pb}_{1-x}\text{Sn}_x\text{I}_3$ materials with $x =$ a) 0.02, b) 0.04, c) 0.06, d) 0.08, e) 0.1 and f) 0.2. Experimental data are shown as \bullet symbols. The solid line is fit, the vertical bars are the expected Bragg reflection position.

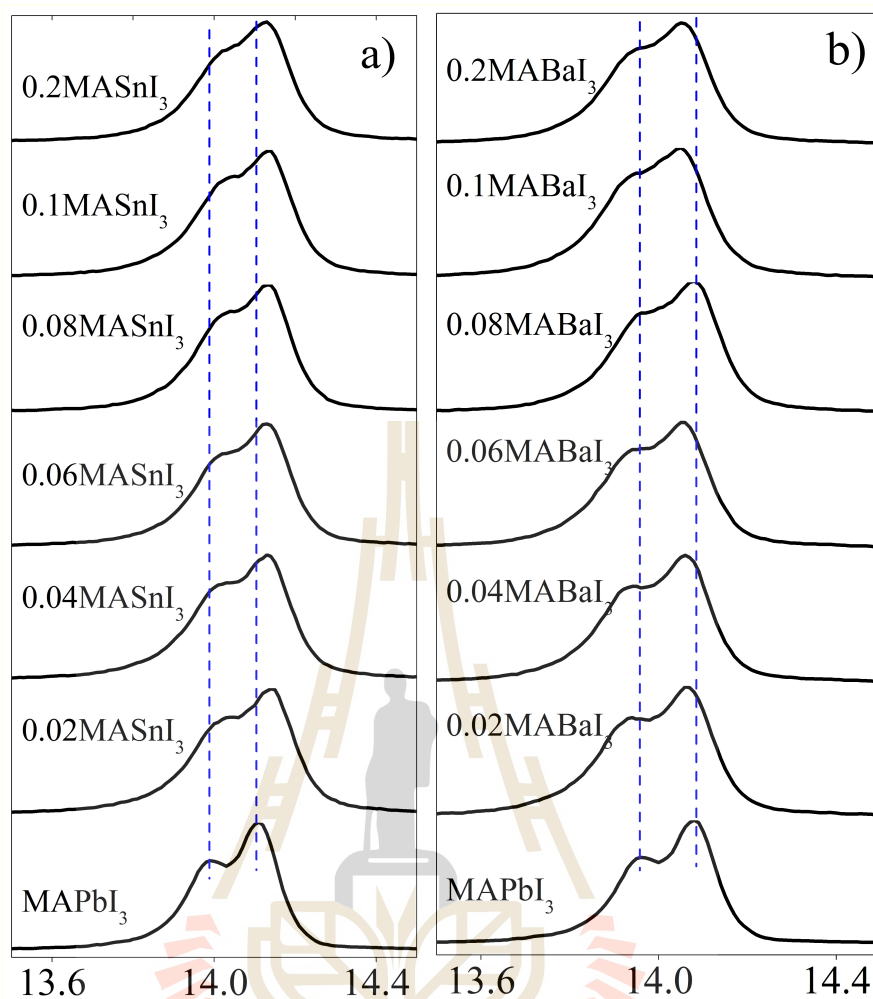


Figure 4.24 The XRD expanded peak at 2θ of around 13.5 - 14.5° , when a) Sn^{2+} substitution and b) Ba^{2+} substitution.

Table 4.5 Phase formation, lattice parameter by Rietveld refinement of Sn^{2+} substitution on $\text{MAPb}_{1-x}\text{Sn}_x\text{I}_3$ XRD pattern.

| x | | 0 | 0.02 | 0.04 | 0.06 | 0.08 | 0.1 | 0.2 |
|--------------------|-----------|------------|------------|------------|------------|------------|------------|------------|
| MAPbI ₃ | a = b (Å) | 8.8735(5) | 8.8626(2) | 8.8655(1) | 8.8683(1) | 8.8677(1) | 8.8675(1) | 8.86796(1) |
| | c (Å) | 12.6657(9) | 12.6618(3) | 12.6609(2) | 12.6624(2) | 12.6590(2) | 12.6585(2) | 12.6570(2) |
| | %wt | 97.35 | 91.72 | 91.62 | 91.30 | 92.63 | 92.17 | 90.65 |
| PbI ₂ | a = b (Å) | 4.5577(2) | 4.5546(2) | 4.5545(2) | 4.5566(2) | 4.5557(2) | 4.5554(2) | 4.5568(3) |
| | c (Å) | 6.9891(2) | 6.9841(3) | 6.9837(3) | 6.9845(4) | 6.9831(3) | 6.9831(3) | 6.9778(4) |
| | %wt | 2.65 | 5.83 | 5.88 | 6.01 | 5.14 | 5.50 | 6.22 |
| MAI | a (Å) | - | 9.0134(3) | 9.0135(3) | 9.0171(3) | 9.0166(3) | 9.0161(3) | 9.0183(3) |
| | b (Å) | - | 5.1327(3) | 5.1329(3) | 5.1381(2) | 5.1306(3) | 5.1318(3) | 5.1282(4) |
| | c (Å) | - | 5.1047(3) | 5.1049(3) | 5.1038(2) | 5.1074(3) | 5.1092(3) | 5.1089(4) |
| | %wt | - | 2.45 | 2.50 | 2.69 | 2.23 | 2.36 | 3.11 |
| wRp(%) | | 6.92 | 5.73 | 5.94 | 5.35 | 5.26 | 5.53 | 5.94 |
| GOF | | 1.71 | 1.65 | 1.71 | 1.49 | 1.53 | 1.61 | 1.65 |
| D (nm) | | 16.22±0.02 | 14.09±0.01 | 14.48±0.03 | 15.17±0.01 | 15.28±0.01 | 14.82±0.03 | 15.25±0.02 |

4.3.2 UV-vis spectroscopy

Diffuse reflectance UV vis spectroscopy were measured to determine the E_g . Figure 4.25 shows the region of spectra obtained for 0.02-0.2 Sn^{2+} substitutions in $\text{MAPb}_{1-x}\text{Sn}_x\text{I}_3$. According to the theory, the properties are related to their electronic structure and have an important rule in determining optical bandgap. The optical bandgap can be determined from the plot of the Kubelka-Munk function $[F(R)hv]^2$ vs photon energy. The E_g values are calculated by the linear extrapolation portion of the plots to $[F(R)hv]^2 = 0$. The figure 4.25a shows that the presence of Sn^{2+} substitutions increasing leads to a slight orange shift of the reflectance band, while presence of optical bandgap (see figure 4.25b) in the substitutions of 0.02-0.06 Sn^{2+} lead to increased bandgap and decreasing lead to stable values. As literature was reported to the formula $\text{MAPb}_{0.95}\text{Sn}_{0.05}\text{I}_3$ for optical bandgap values below 1.57 eV with tetragonal phase (Javier et al., 2015), as same as our works shows around 1.55-1.56 eV. However, The optical bandgap values for substitutions in $\text{CH}_3\text{NH}_3\text{PbI}_3$ were decreased gradually with increases in the substitution content of the ions from $x = 0.06$ to 0.2, which is in accordance with other reports (Javier et al., 2015). Generally, the bandgap is strongly dependent on the particle size and the existence of deficient levels induction between the conduction band and valence band, especially when energy levels are close to the conduction bend. Moreover, the change in the bandgap could be attributed to the distortion in the PbI_6 octahedral and higher forced symmetry to decrease the bandgap due to the doping of ions.

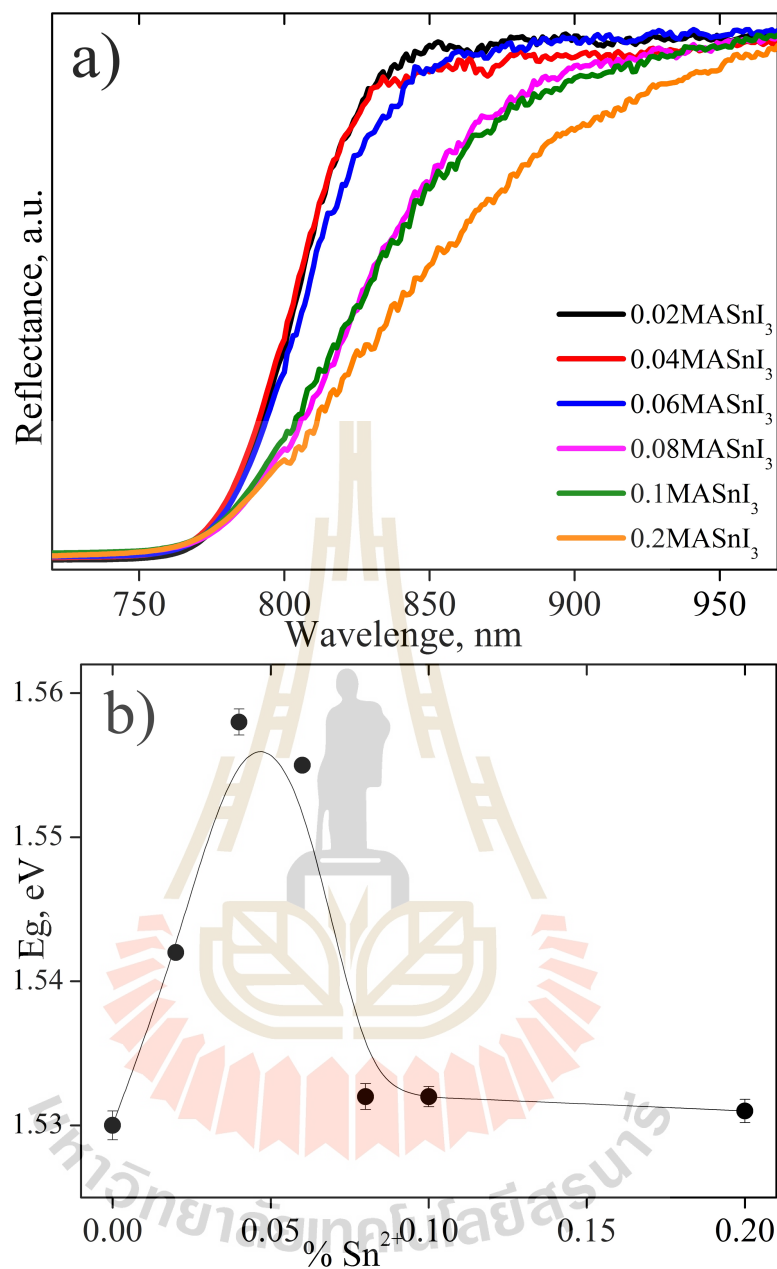


Figure 4.25 a) diffuse reflectance UV vis spectra for $\text{CH}_3\text{NH}_3\text{Pb}_{1-x}\text{Sn}_x\text{I}_3$ samples with 0.02-0.2 Sn^{2+} substitutions and b) the plot of the optical bandgap values for each samples.

4.3.3 FTIR measurement

To study the bonding in Sn-substituted material a FTIR was used. The room temperature FTIR spectra of Sn-substituted with different concentrations of substitution ions (0.02, 0.04, 0.06, 0.08, 0.1 and 0.2) sample have been shown in Figure 4.26 in wavenumber of 400-2000 cm^{-1} . Figure 4.26 shows characteristic vibration bands of Sn^{2+} substituted in $\text{CH}_3\text{NH}_3\text{PbI}_3$ (see table 4.2), whose main peaks are related to the frequency of vibrational modes of the organic cation (Pérez-Osorio et al., 2015; Jintara and Rattikorn, 2017). In the figure show the weaker vibrational mode of materials mainly related to the bending and rocking mode in the range of 600-1700 cm^{-1} . According ref. (Pérez-Osorio et al., 2015; Jintara and Rattikorn, 2017), we propose the summary attribution of these peaks to vibrational by Table 4.2. However, the perovskite Sn^{2+} substituted in $\text{CH}_3\text{NH}_3\text{PbI}_3$ have been used and no shift of all peaks. As it was mentioned above, N-H stretching, N-H bending, C-H bending, C-N rocking vibration modes of all materials. In particular, The spectra similar results were found for $\text{CH}_3\text{NH}_3\text{PbI}_3$ material, we infer that the interaction found are attributable to the chemical nature of organic compound. In addition, the broad low intensity band with the maximum around 3000-3400 cm^{-1} (do not show here) has been assigned to the antisymmetric stretching of water from ambient moisture due to contact of the sample with the environment.

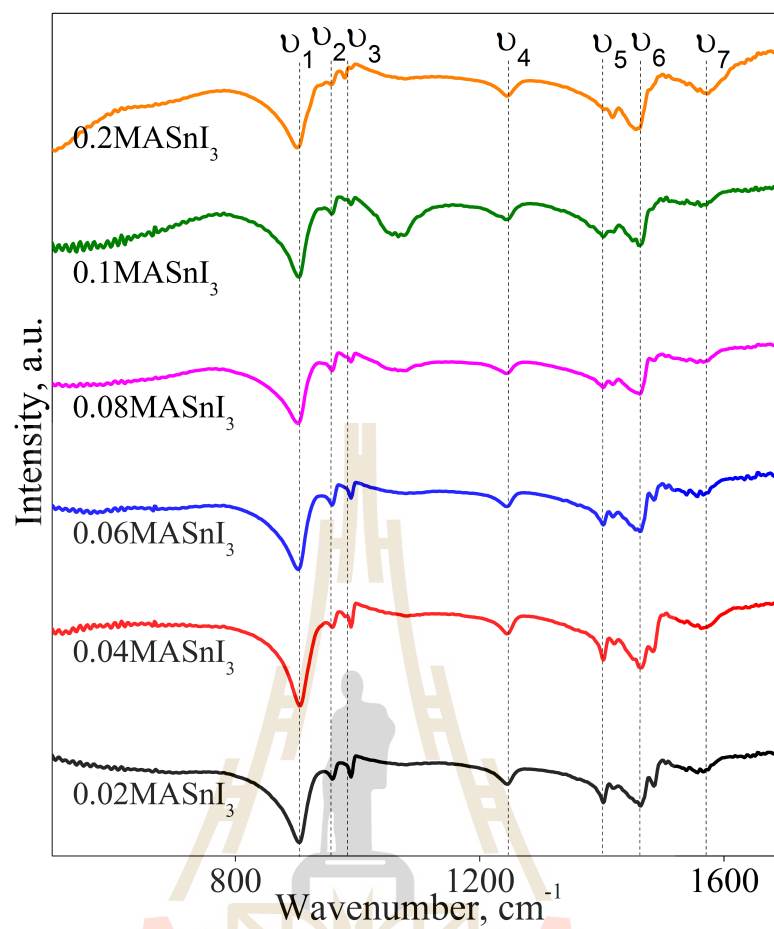


Figure 4.26 FTIR spectra of Sn^{2+} substituted in $\text{CH}_3\text{NH}_3\text{PbI}_3$ materials in the range of $500\text{-}1700\text{ cm}^{-1}$.

4.3.4 XPS measurement

The XPS spectra were recorded to confirmed chemical bonding states in the samples. The survey spectra were acquired and we observed the possible core level peaks that arise, we proceeded to measure the spectra for the individual peaks. Figure 4.27 shows the XPS data of C 1s, N 1s, I 3d, Pb 4f and Sn 3d core level with the Sn^{2+} substitution. We began our measurements with carbon, where the adventitious C 1s line would be used for charge referencing and calibration.

The all of data are the calibrated spectra for the C 1s for all samples. The spectra were analyzed using a Shirley function for background deduction and Gaussian function to fit the peaks. The FWHM of all samples fitted curves were constrained to be the very close/ similar. The main carbon peak and the most peak arises from the adventitious carbon found in the atmosphere and other impurities that may contaminate from the preparation XPS measurement (see figure 4.28). This C peak is conventionally set to 284.8 eV and indicate for the C-C/C-H chemical state for carbon. The other peaks at 285.8, 286.6, <287.5 and 283.2 eV correspond to the C-I, C-N, C=O and metal carbide chemical states. The N 1s spectra are shown in Figure 4.29 and the peaks was fitted using the same way with C 1s. The BE of N 1s was around 400-402 eV confirmed C-H and N-H chemical states at 400.1 and 402 eV.

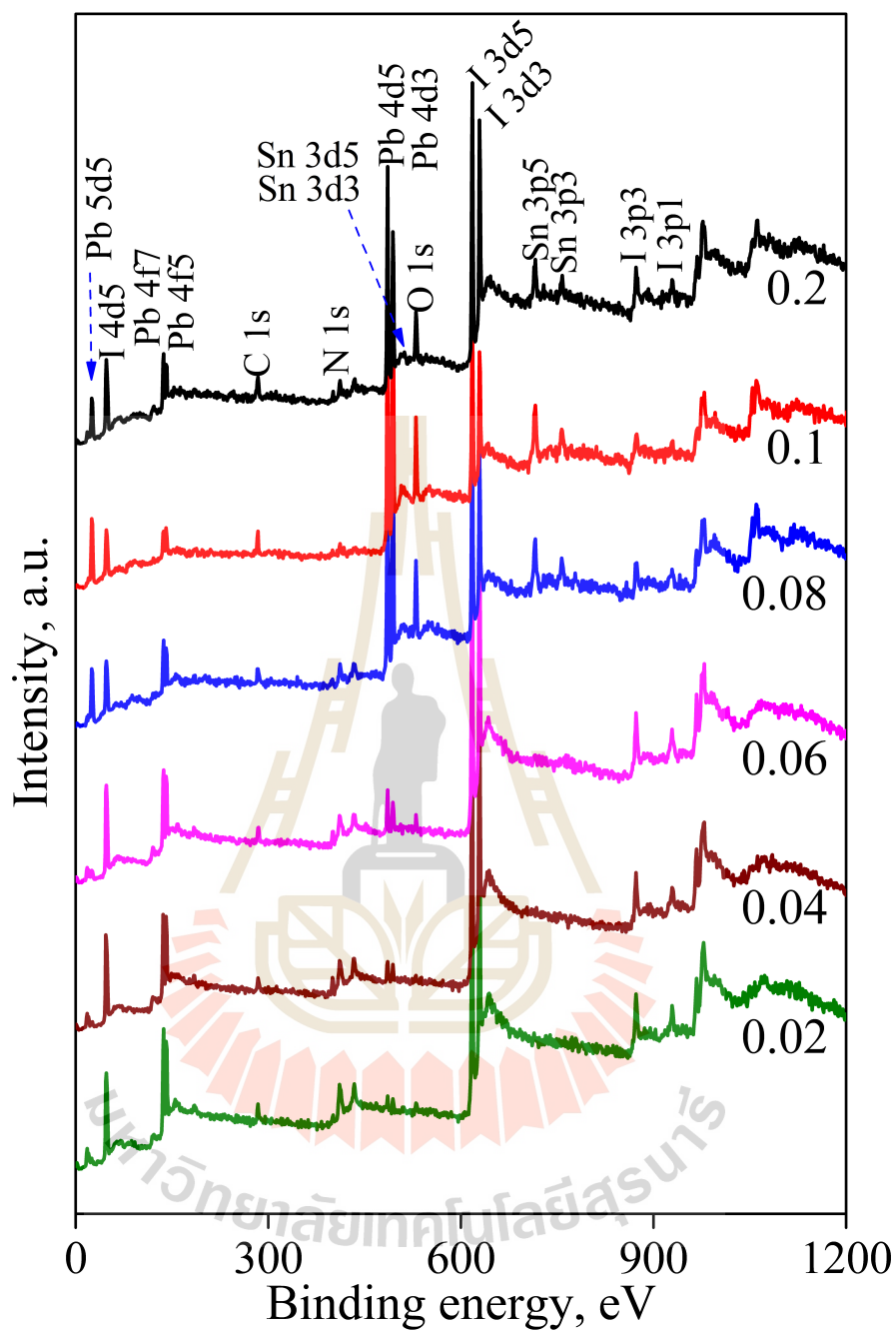


Figure 4.27 XPS survey scan of Sn^{2+} substituted in $\text{CH}_3\text{NH}_3\text{Pb}_{1-x}\text{Sn}_x\text{I}_3$ materials.

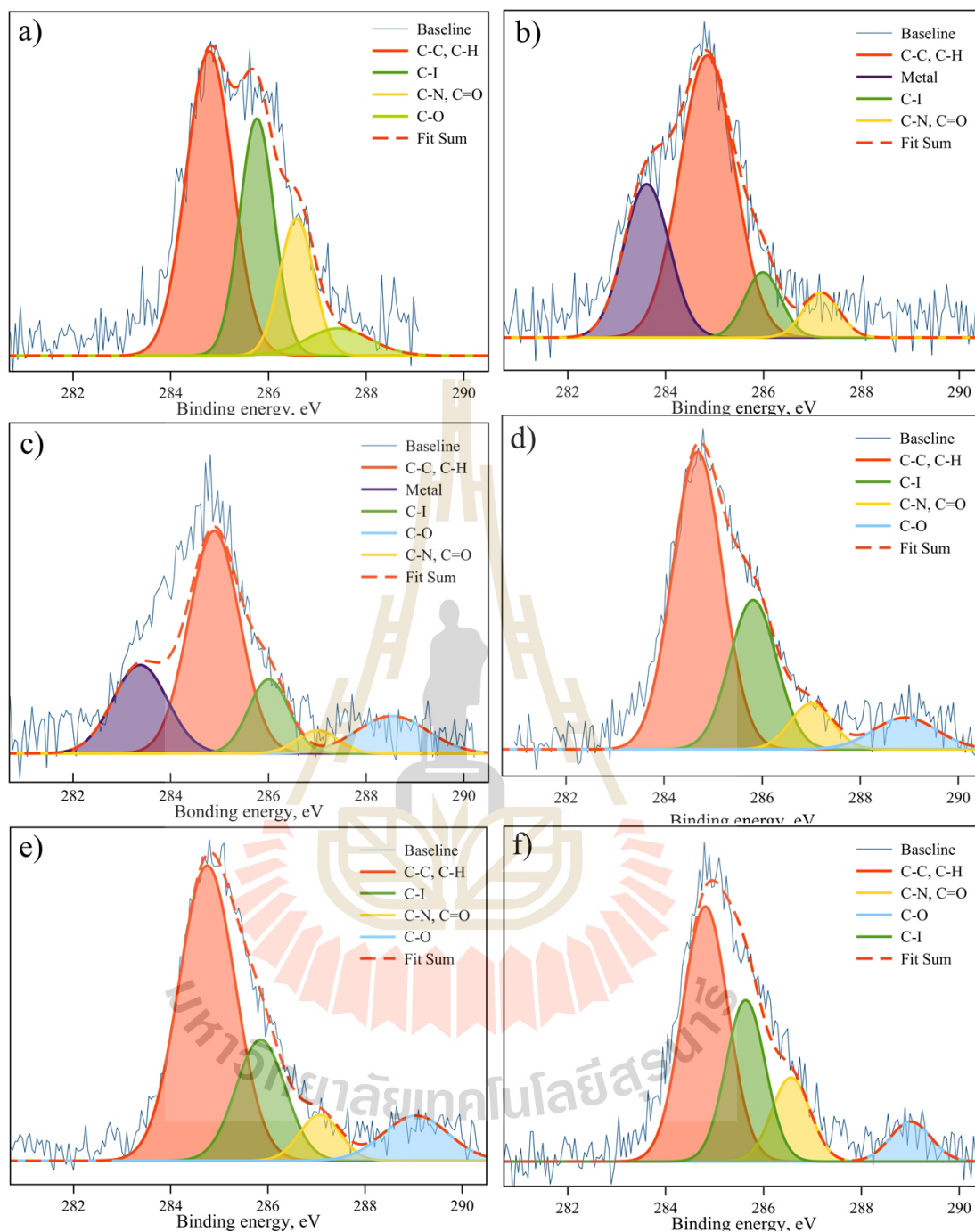


Figure 4.28 XPS spectra for C 1s of the samples and the Gaussian fitting, when a) 0.02, b) 0.04, c) 0.06, d) 0.08, e) 0.1 and f) 0.2 Sn^{2+} substituted in $\text{CH}_3\text{NH}_3\text{Pb}_{1-x}\text{Sn}_x\text{I}_3$ materials.

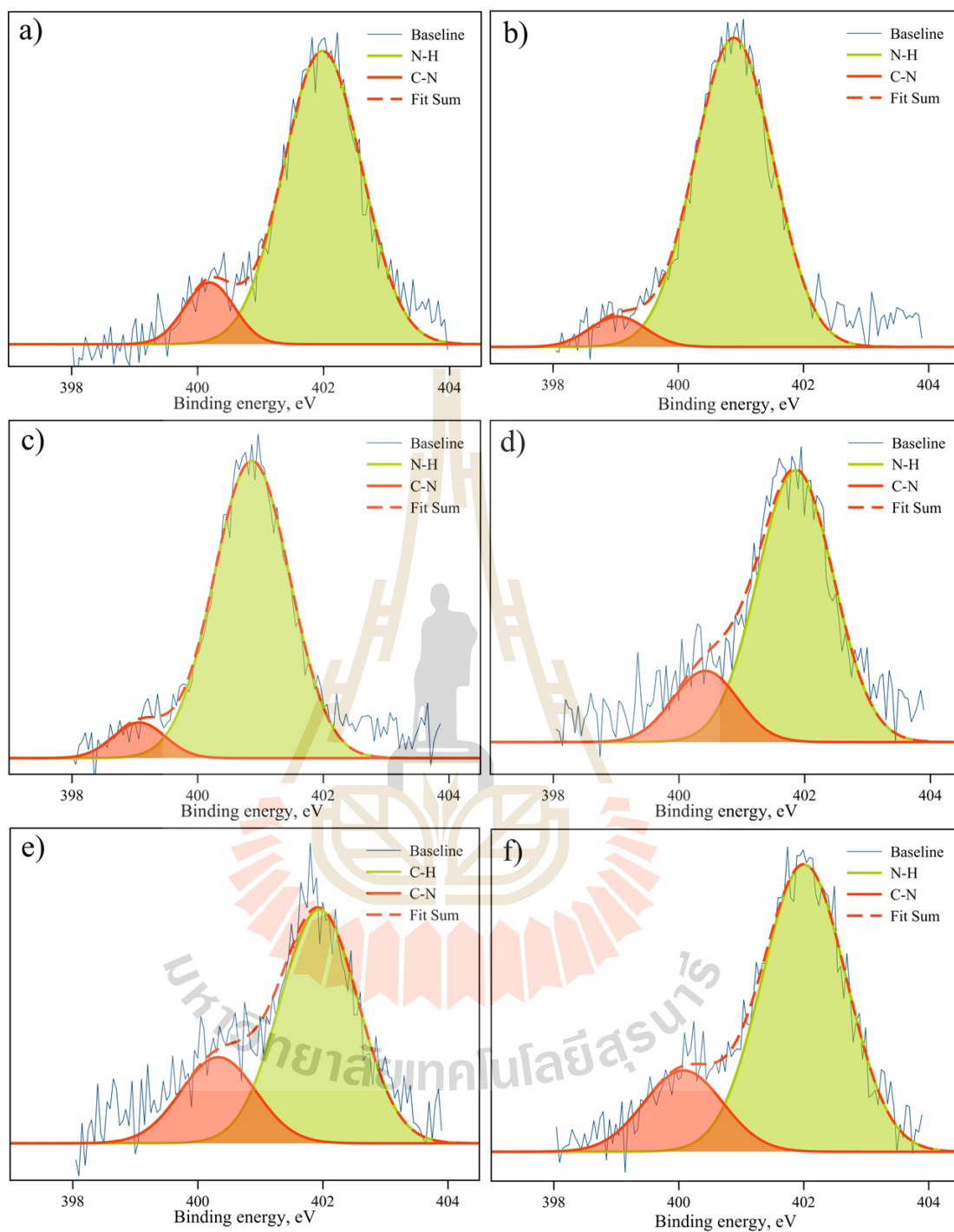


Figure 4.29 XPS spectra for N 1s of the samples and the Gaussian fitting, when a) 0.02, b) 0.04, c) 0.06, d) 0.08, e) 0.1 and f) 0.2 Sn^{2+} substituted in $\text{CH}_3\text{NH}_3\text{Pb}_{1-x}\text{Sn}_x\text{I}_3$ materials.

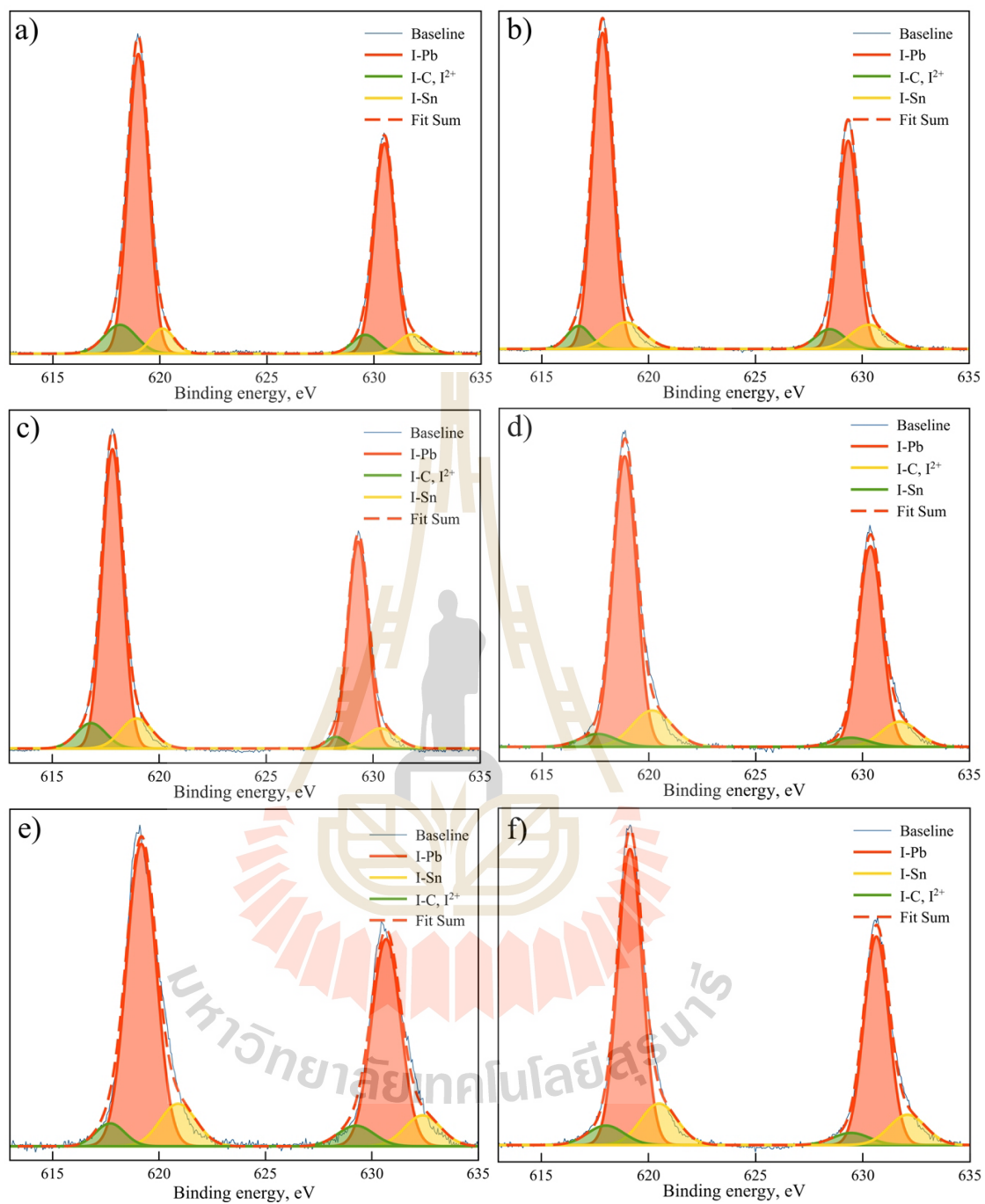


Figure 4.30 XPS spectra for I 3d of the samples and the Gaussian fitting, when a) 0.02, b) 0.04, c) 0.06, d) 0.08, e) 0.1 and f) 0.2 Sn^{2+} substituted in $\text{CH}_3\text{NH}_3\text{Pb}_{1-x}\text{Sn}_x\text{I}_3$ materials.

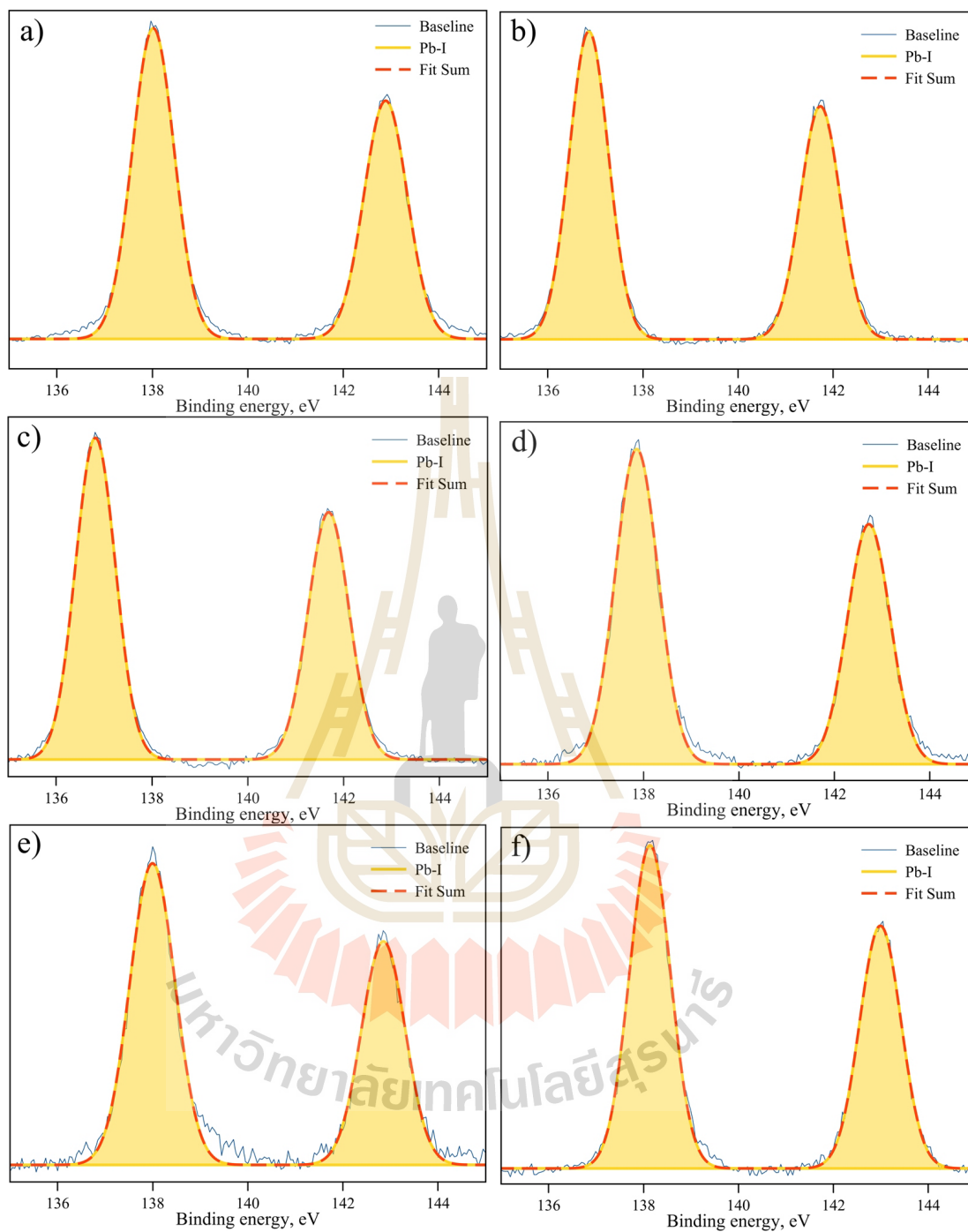


Figure 4.31 XPS spectra for Pb 4f of the samples and the Gaussian fitting, when a) 0.02, b) 0.04, c) 0.06, d) 0.08, e) 0.1 and f) 0.2 Sn^{2+} substituted in $\text{CH}_3\text{NH}_3\text{Pb}_{1-x}\text{Sn}_x\text{I}_3$ materials.

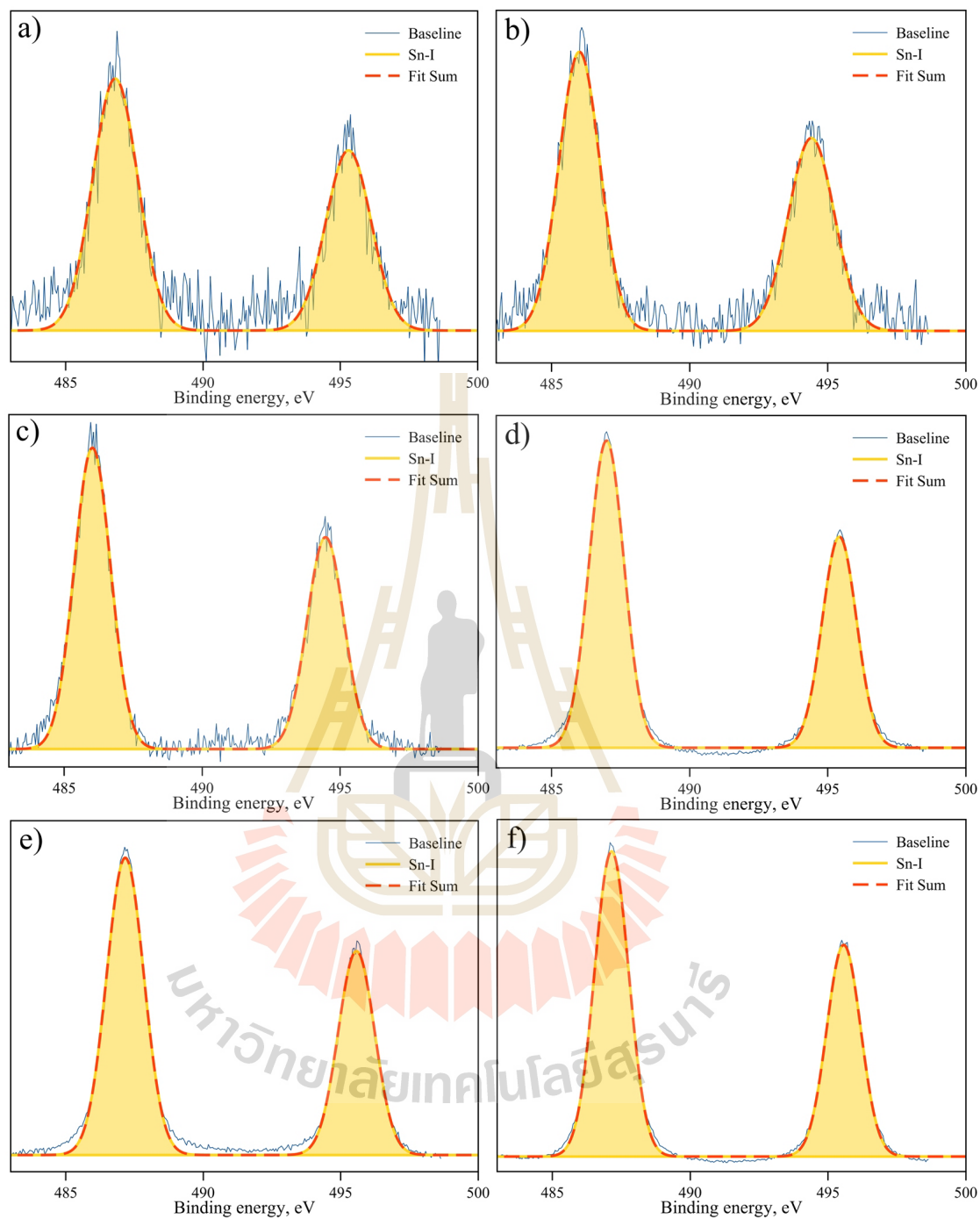


Figure 4.32 XPS spectra for Sn 3d of the samples and the Gaussian fitting, when a) 0.02, b) 0.04, c) 0.06, d) 0.08, e) 0.1 and f) 0.2 Sn^{2+} substituted in $\text{CH}_3\text{NH}_3\text{Pb}_{1-x}\text{Sn}_x\text{I}_3$ materials.

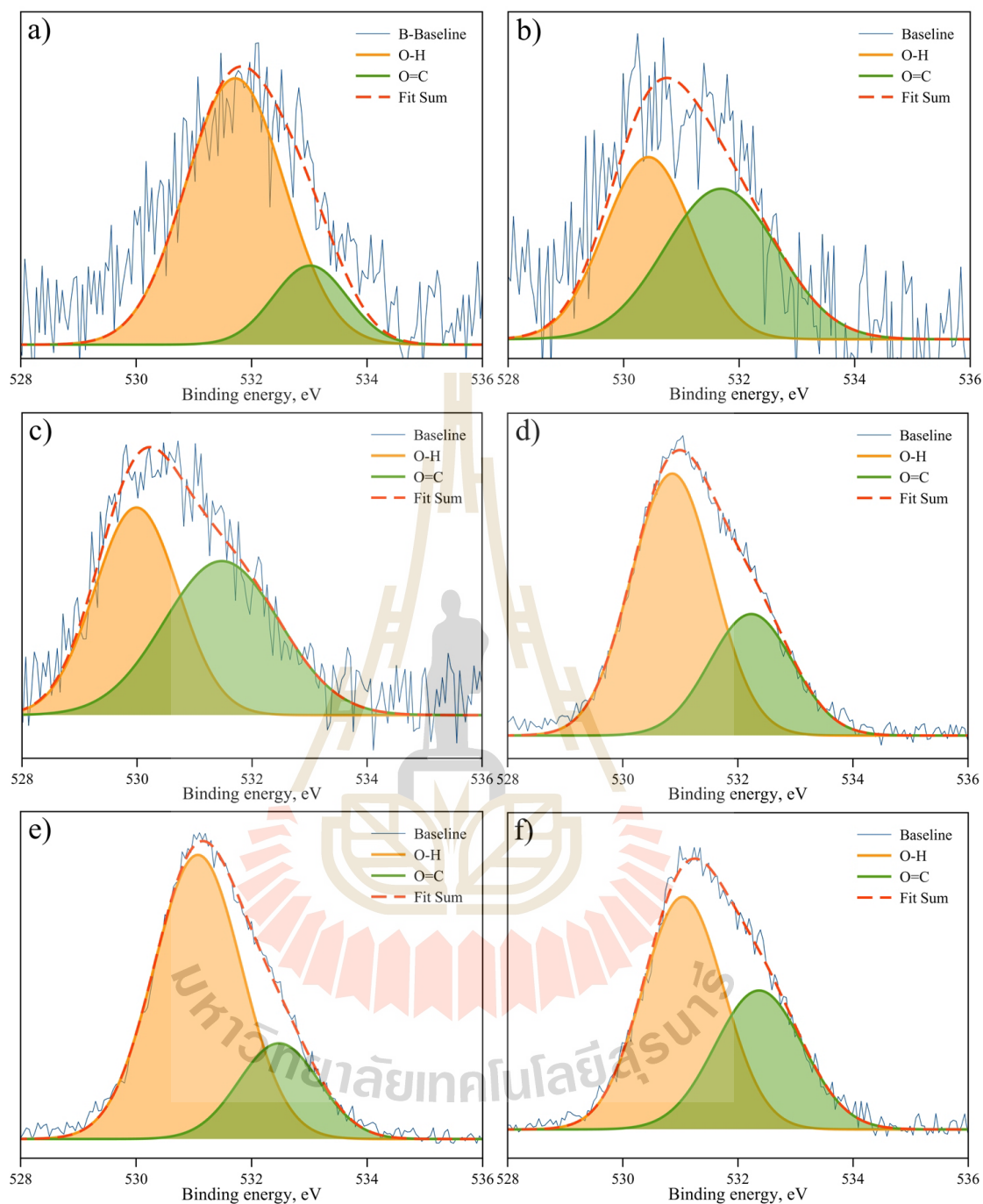


Figure 4.33 XPS spectra for O 1s of the samples and the Gaussian fitting, when a) 0.02, b) 0.04, c) 0.06, d) 0.08, e) 0.1 and f) 0.2 Sn^{2+} substituted in $\text{CH}_3\text{NH}_3\text{Pb}_{1-x}\text{Sn}_x\text{I}_3$ materials.

The core level spectra for I was acquired for the 3d for all samples. Similar to the C 1s spectra, the curves were fit using an asymmetric Gaussian function.

Figure 4.30 shows the well separated spin-orbit components, a separation of around 11.3-11.5 eV being found in all sample, which is typical of presence of I^- and no other chemical states of iodine are present. In turn, the signal of Sn^{2+} substituted perovskite coincide with those obtained in the oxidation state of I^- after substitution with Sn^{2+} consistent with previous work (Jintara and Rattikorn, 2017).

In addition, figure 4.31 shows the spectrum for the Pb 4f spectra at a BE of 139 eV. These BE are consistent with literature estimates for PbI_2 and indicate the presence of Pb^{2+} species. However, no chemical shift in the spectrum as well as the absence of other chemical states of Pb. Figure 4.30-4.31 shows the peaks I 3d and Pb 4f spectra are no significant change except some intensity reduction. It is confirmed the peaks corresponding the Pb-I bond in the Pb 4f spectra for PbI_2 and $CH_3NH_3PbI_3$ has the same BE. In turn, the BE of Sn 3d (see Figure 4.32) was around 486 and 495 eV ($3d_{5/2}$ and $3d_{3/2}$). It is the typical position and separation of spin-orbit component for Sn^{2+} . However, the sample of 0.04MASnI₃ and 0.06MASnI₃ were found to be a shift towards lower BE values, may be indicating that small modification is formed in metal carbide. The formation of metal carbide was confirmed by C 1s spectra (see Figure 4.28). We attribute the appearance of lower BE peak at 283.2 eV in C 1s spectrum to Sn_2C for the samples prepared under ambient. More core level of O 1s spectra are shown in the Figure 4.33. The spectra was fitted using the same way with C 1s. We can see clearly from the spectra of all samples. We have oxygen impurities corresponding to the O=C and O-H chemical state as well as the main O 1s peaks attributed to the C 1s.

4.3.5 XANES analysis

This section, the $\text{CH}_3\text{NH}_3\text{Pb}_{0.9}\text{Sn}_{0.1}\text{I}_3$ sample used study were obtained. The XANES measurement was done in TM mode for Pb M5-edge and TM for I L3-edge. At the same time with $\text{CH}_3\text{NH}_3\text{PbI}_3$, the measurement Pb M5-edge and I L3-edge XANES of $\text{CH}_3\text{NH}_3\text{PbI}_3$ and PbI_2 do not have reference compound available in the database. We get supporting information from XRD (Weber, 1978) and modified by substituted metal halide. Therefore, the calculation XANES from candidate compounds must be generated and compared with the experiment results.

The FEFF 8.2 code is used to calculate the XANES spectra of $\text{CH}_3\text{NH}_3\text{Pb}_{0.9}\text{Sn}_{0.1}\text{I}_3$ and PbI_2 for ensuring all features of extrapolated XANES spectra, same way with $\text{CH}_3\text{NH}_3\text{PbI}_3$ section. After the calculation XANES database has been compiled, the spectra can be used to compared and fitted with the experiment spectra as shown in Figure 4.34-4.35. The features of Pb M5-edge experiment spectra (see figure 4.34) look similar to calculation spectra (see figure 4.34b) of those materials, as well as that $\text{CH}_3\text{NH}_3\text{PbI}_3$ spectra. The calculated spectra are in good agreement with the corresponding measured spectra obtained from those samples. Therefore, from the XAS point of view, it can be concluded 10% substitution of Sn^{2+} into the structure of $\text{CH}_3\text{NH}_3\text{PbI}_3$, which corresponding with XRD. However, the XANES of $\text{CH}_3\text{NH}_3\text{Pb}_{0.9}\text{Sn}_{0.1}\text{I}_3$ and SnI_2 have been calculated in Sn L3-edge are shown in Figure 4.36 (Sn edge of experimental does not showed here).

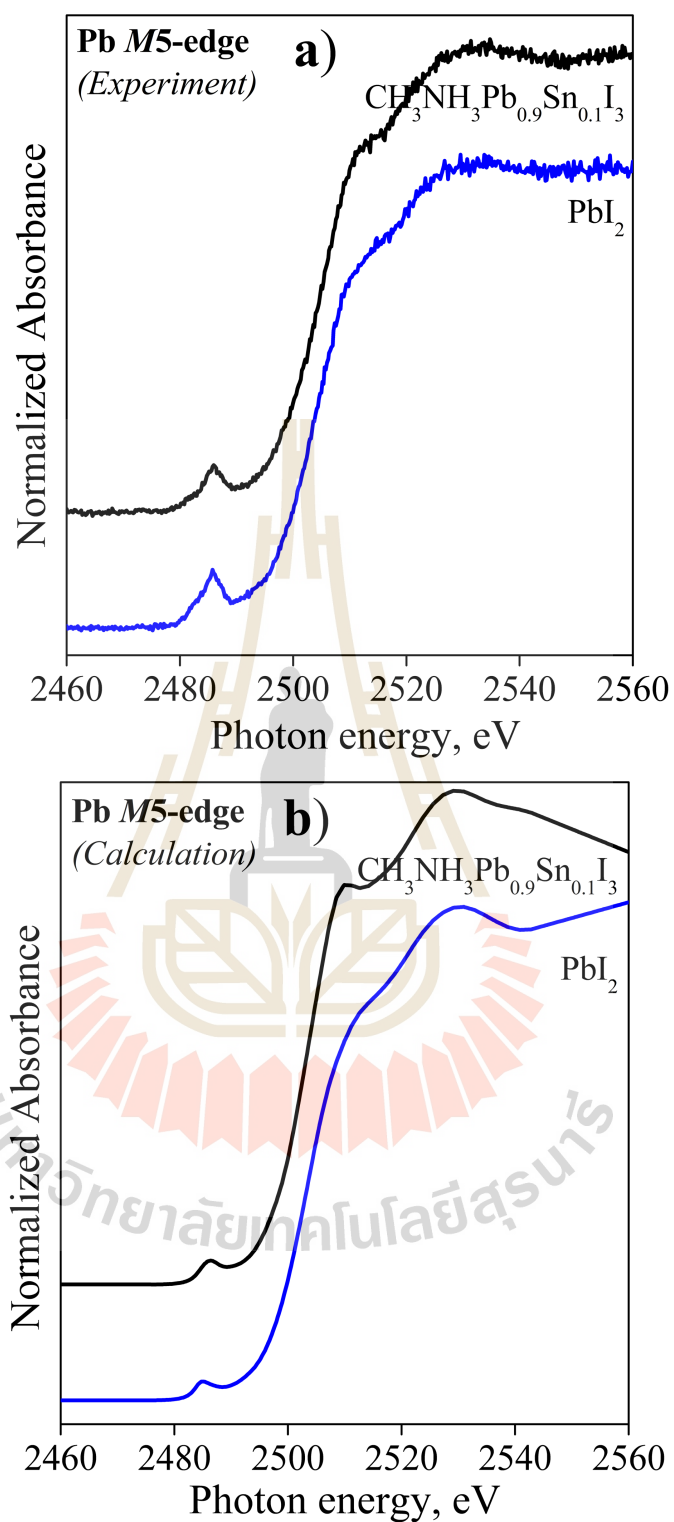


Figure 4.34 Measured Pb M5-edge XANES spectra (a) and calculated Pb M5-edge XANES spectra (b) of $\text{CH}_3\text{NH}_3\text{Pb}_{0.9}\text{Sn}_{0.1}\text{I}_3$ materials.

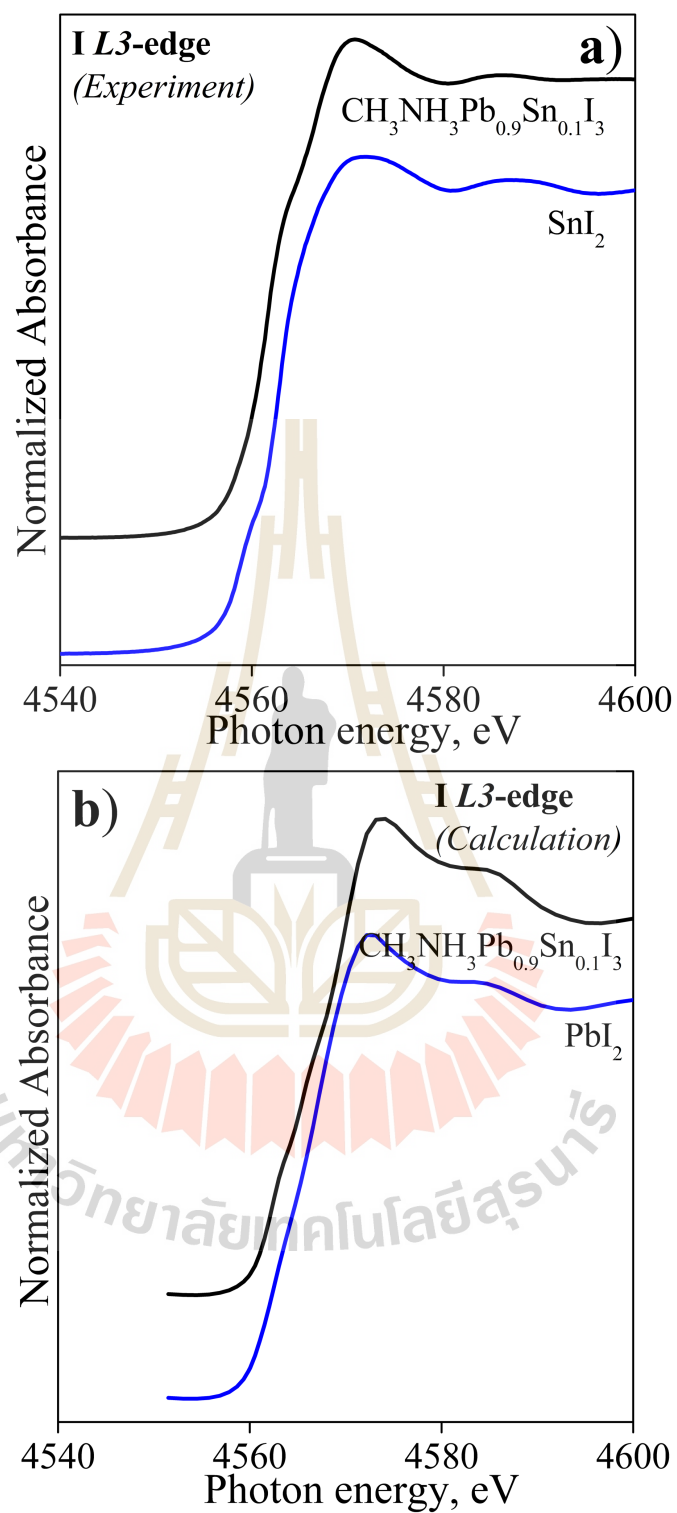


Figure 4.35 Measured I L3-edge XANES spectra (a) and calculated I L3-edge XANES spectra (b) of $\text{CH}_3\text{NH}_3\text{Pb}_{0.9}\text{Sn}_{0.1}\text{I}_3$ materials.

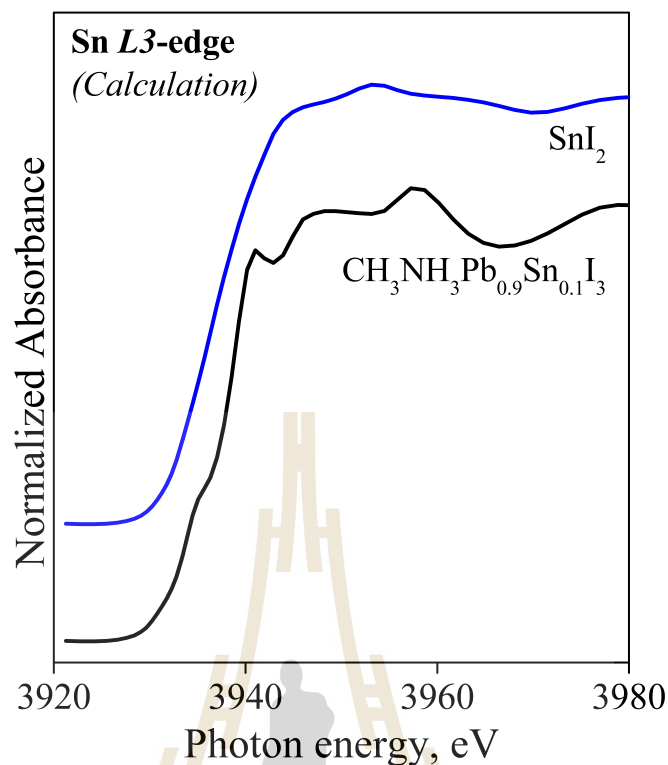


Figure 4.36 Calculated Sn L3-edge XANES spectra of $\text{CH}_3\text{NH}_3\text{Pb}_{0.9}\text{Sn}_{0.1}\text{I}_3$ materials.

4.3.6 EXAFS analysis

The result was performed using ATHENA software to get EXAFS spectra. The curve fitting was done for the k^2 -weighted spectrum of $3\text{--}6 \text{ \AA}^{-1}$. The EXAFS spectra were processed, information on local structure of I atom via fitting with perovskite model of $\text{CH}_3\text{NH}_3\text{PbI}_3$ with Sn^{2+} substituted in B-site in ARTEMIS program. This compound can direct EXAFS fitting for sample, the structural parameters can be obtained. In the Figure 4.37a are two k^2 -weighted L3-edge EXAFS spectra. Normally, it seen that the two spectra are good agreement over the region $2\text{--}5 \text{ \AA}^{-1}$. Therefore, the good overview of qualitatively and the reliable structural parameters would be obtained from fitting. However, the important structure parameters were extracted and consistent FT are shown in

the Figure4.37b. It can be seen that the fitting spectra can reproduce the experimental data. The fitting parameters obtained from this sample for average bond length of I absorbing atoms within Pb, C and N atoms (R), Debye-Waller factors (σ^2) and coordination number (N) are shown in Table 4.6. The results can be confirmed the local structure consistent with XANES and XRD result.

Table 4.6 The structure parameters coordination numbers N, interatomic distances R and DW factors σ^2 obtained by fitting the EXAFS data for the $\text{CH}_3\text{NH}_3\text{Pb}_{0.9}\text{Sn}_{0.1}\text{I}_3$.

| Shell | N | R [Å] | σ^2 |
|-------|---|-----------|------------|
| I-Sn | 1 | 3.2052(1) | 0.1974 |
| I-Pb | 1 | 3.2052(1) | 0.0172 |
| I-I1 | 4 | 4.4654(6) | 0.7442 |
| I-I2 | 4 | 4.5320(7) | 0.7452 |
| I-N | 4 | 4.0799(5) | 0.0844 |
| I-C | 4 | 3.3483(8) | 0.5013 |

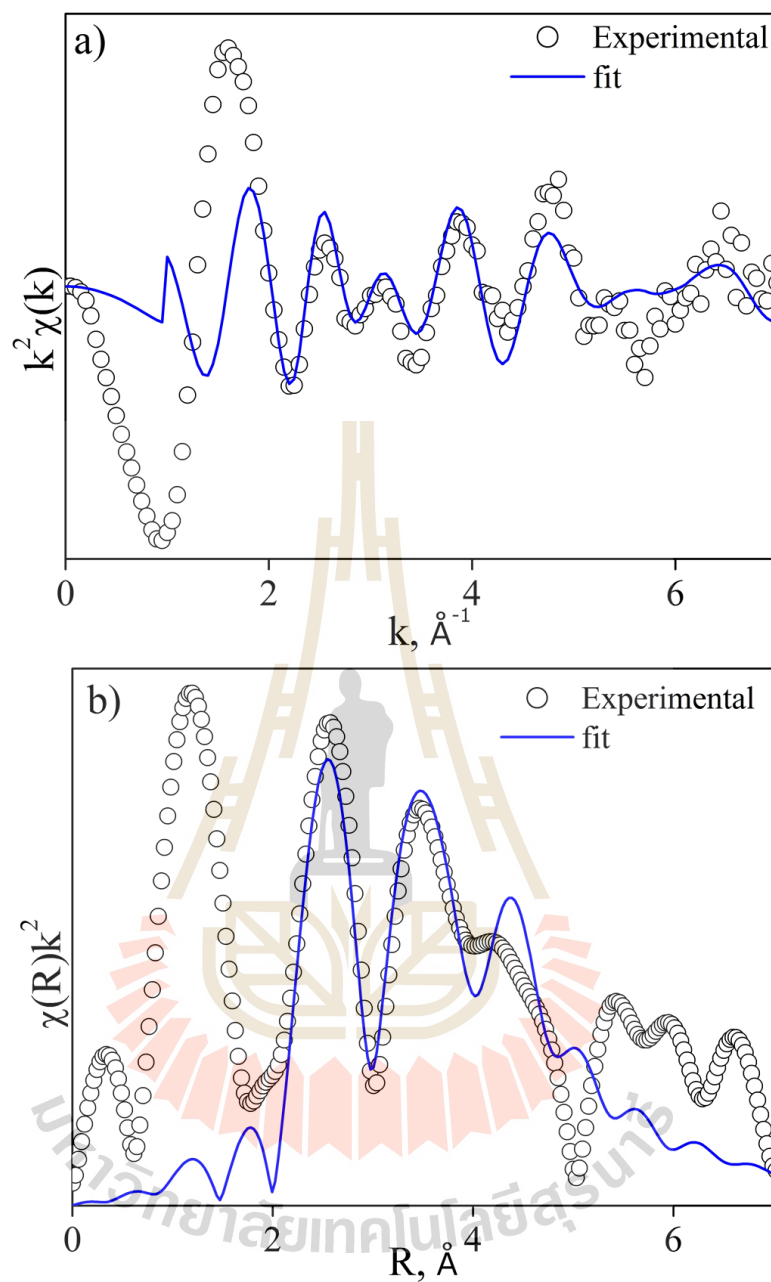


Figure 4.37 Comparison of Experiment and fitted magnitude of EXAFS Fourier transform (FT) (a) and (b) comparison of k^2 -weighted spectrum over the k -range of $\text{CH}_3\text{NH}_3\text{Pb}_{0.9}\text{Sn}_{0.1}\text{I}_3$. The k range used in the FT is from 3-8.7 \AA^{-1} for data set

4.3.7 Low temperature phase transition

The temperature dependence variations of permittivity (ϵ_r) and dielectric loss ($\tan \delta$) in the range of 3-200 K measured at 1 kHz are also presented in Figure 4.20. The $\text{CH}_3\text{NH}_3\text{Pb}_{0.9}\text{Sn}_{0.1}\text{I}_3$ data are quite similar to that reported earlier (Noriko et al., 1992) and also our reported in section of $\text{CH}_3\text{NH}_3\text{PbI}_3$. At temperature of 3 K the dielectric permittivity is around 20-21 are quite similar to $\text{CH}_3\text{NH}_3\text{PbI}_3$. The important feature is a relatively weak dielectric dispersion at $T_m \sim 60\text{-}100$ K whose details are shown in Figure 4.38. Similar type low-temperature weak dielectric dispersion was also observed in the formamidinium lead iodide by Fabini et al. (Fabini et al., 2016) and our $\text{CH}_3\text{NH}_3\text{PbI}_3$. The low-temperature dielectric dispersion in the title compounds is characterized by the frequency dependent dielectric permittivity anomaly and $\tan \delta$ peak that shifts to higher temperatures as frequency increases (see Figure 4.38).

$\text{CH}_3\text{NH}_3\text{Pb}_{0.9}\text{Sn}_{0.1}\text{I}_3$ shows much broader (two-component) $\tan \delta$ peak whose components show a different frequency dependence: the lower-frequency part of the $\tan \delta(T)$ peak gradually increases with temperature whereas the higher-frequency part of the $\tan \delta(T)$ peak show a gradual decrease with T . We have fitted the frequency dependence of the $\tan \delta(T)$ peak of our samples to both Arrhenius and Vogel-Fulcher dielectric relaxation behaviour is shown in Figures 4.39a-b, respectively. The fitting parameters are summarized in Table 4.7. $\text{CH}_3\text{NH}_3\text{Pb}_{0.9}\text{Sn}_{0.1}\text{I}_3$ specimen shows an additional low-temperature relaxation with $E_a \sim 70$ meV and $f_0 \sim 9 \times 10^7$ Hz (see Table 4.7). According to Table 4.7, attempts to fit the data to the Volger Fulcher-type behaviour resulted in extremely large standard deviations and static dipolar freezing temperature $T_{VF} \approx 0$ K within the standard deviation. Our results, therefore, support the Arrhenius-type thermally activated dynamics of the dipolar re-orientation and also do not

seem to agree well with the ‘glassy slowing’ of the dipolar relaxation, as proposed by Fabini et al. (Fabini et al., 2016) similarly to $\text{CH}_3\text{NH}_3\text{PbI}_3$ materials.

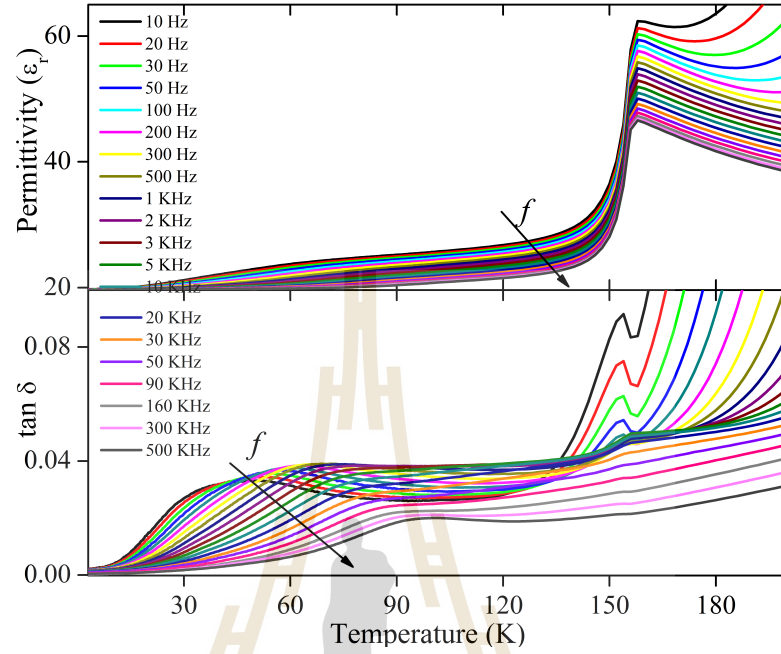


Figure 4.38 Low temperature of permittivity (ϵ_r) and loss tangent ($\tan \delta$) of $\text{CH}_3\text{NH}_3\text{Pb}_{0.9}\text{Sn}_{0.1}\text{I}_3$ perovskite. Frequency dependent dielectric loss peaks indicating substantial slowing of relaxation dynamics are observed in the sample.

Table 4.7 Fitting parameters and goodness of fit (χ^2) for Arrhenius-type thermally-activated model and Vogel-Fulcher-type model (marked by the asterisk) of the dielectric relaxation of $\text{CH}_3\text{NH}_3\text{Pb}_{0.9}\text{Sn}_{0.1}\text{I}_3$ at low-temperature fit (LT) and high-temperature fit (HT). The standard deviations of the fitting parameters are given in brackets.

| Compound | f_0 [Hz] | E_a [meV] | T_{VF} [K] | χ^2 |
|---|------------------------|-------------|--------------|----------|
| $\text{CH}_3\text{NH}_3\text{Pb}_{0.9}\text{Sn}_{0.1}\text{I}_3$ LT | $9(3) \times 10^7$ | 70(2) | - | 0.995 |
| $\text{CH}_3\text{NH}_3\text{Pb}_{0.9}\text{Sn}_{0.1}\text{I}_3$ HT | $4(4) \times 10^{14}$ | 171(7) | - | 0.984 |
| $\text{CH}_3\text{NH}_3\text{Pb}_{0.9}\text{Sn}_{0.1}\text{I}_3^*$ LT | $9(23) \times 10^7$ | 70(28) | 0(12) | 0.995 |
| $\text{CH}_3\text{NH}_3\text{Pb}_{0.9}\text{Sn}_{0.1}\text{I}_3^*$ HT | $1(16) \times 10^{14}$ | 151(221) | 5(60) | 0.981 |

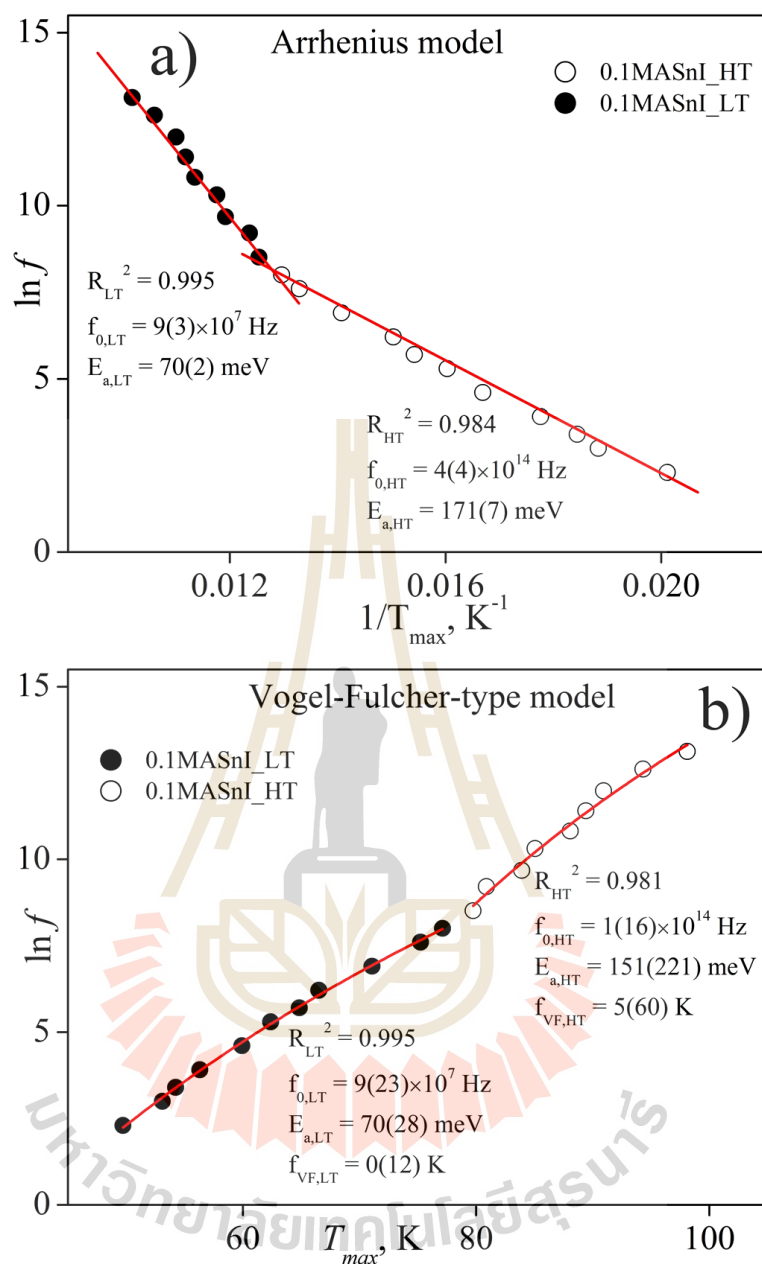


Figure 4.39 Natural logarithm of f as the function of $1/T$ by Arrhenius model a) and b) with the function of T_{max} by Vogel-fulcher fit model for $\text{CH}_3\text{NH}_3\text{Pb}_{0.09}\text{Sn}_{0.1}\text{I}_3$.

4.4 Ba^{2+} doped on $\text{CH}_3\text{NH}_3\text{Pb}_{1-x}\text{Ba}_x\text{I}_3$ perovskite

This section were reported using Ba^{2+} substitutes in Pb-site of $\text{CH}_3\text{NH}_3\text{PbI}_3$ perovskite materials. We synthesized $\text{CH}_3\text{NH}_3\text{Pb}_{1-x}\text{Ba}_x\text{I}_3$ compound where $x = 0.02, 0.04, 0.06, 0.08, 0.1$ and 0.2 . To do this, synthesized samples were characterized using XRD, UV-vis, FTIR, XPS and phase transition at low temperature.

4.4.1 XRD spectra

Figure 4.40 illustrates the XRD patterns for Ba^{2+} substituted in $\text{CH}_3\text{NH}_3\text{PbI}_3$ perovskite at room temperature. The pattern show diffraction that can be assigned to planes of the tetragonal (I4/mcm) phase with similarly as $\text{CH}_3\text{NH}_3\text{PbI}_3$ material. In turn, $\text{CH}_3\text{NH}_3\text{I}$ is also present. Several diffraction peak, which can be identification to tetragonal phase (Jintara and Rattikorn, 2017).

The shape diffraction peaks also indicate that high crystallinity of the powders. The Ba^{2+} substituted results confirm that a solid solution was achieved by Ba substitution at the Pb-site of perovskite structure. In addition, this observation are confirmed by the results of the Rietveld refinement listed in Table 4.40. Clearly correlation is observed between the Ba^{2+} substitution and the perovskite formation behavior. The Ba^{2+} substituted in the $\text{CH}_3\text{NH}_3\text{Pb}_{1-x}\text{Ba}_x\text{I}_3$ gave the high fraction of the tetragonal structure ($< 91\%$) with the enlarge lattice parameter. Unfortunately we could not achieve complete phase purity of $\text{CH}_3\text{NH}_3\text{PbI}_3$ material. The impurity phase originated from $\text{CH}_3\text{NH}_3\text{I}$ and PbI_2 were also present in all the samples. However, our results still show high main phase of $\text{CH}_3\text{NH}_3\text{PbI}_3$ about 91%.

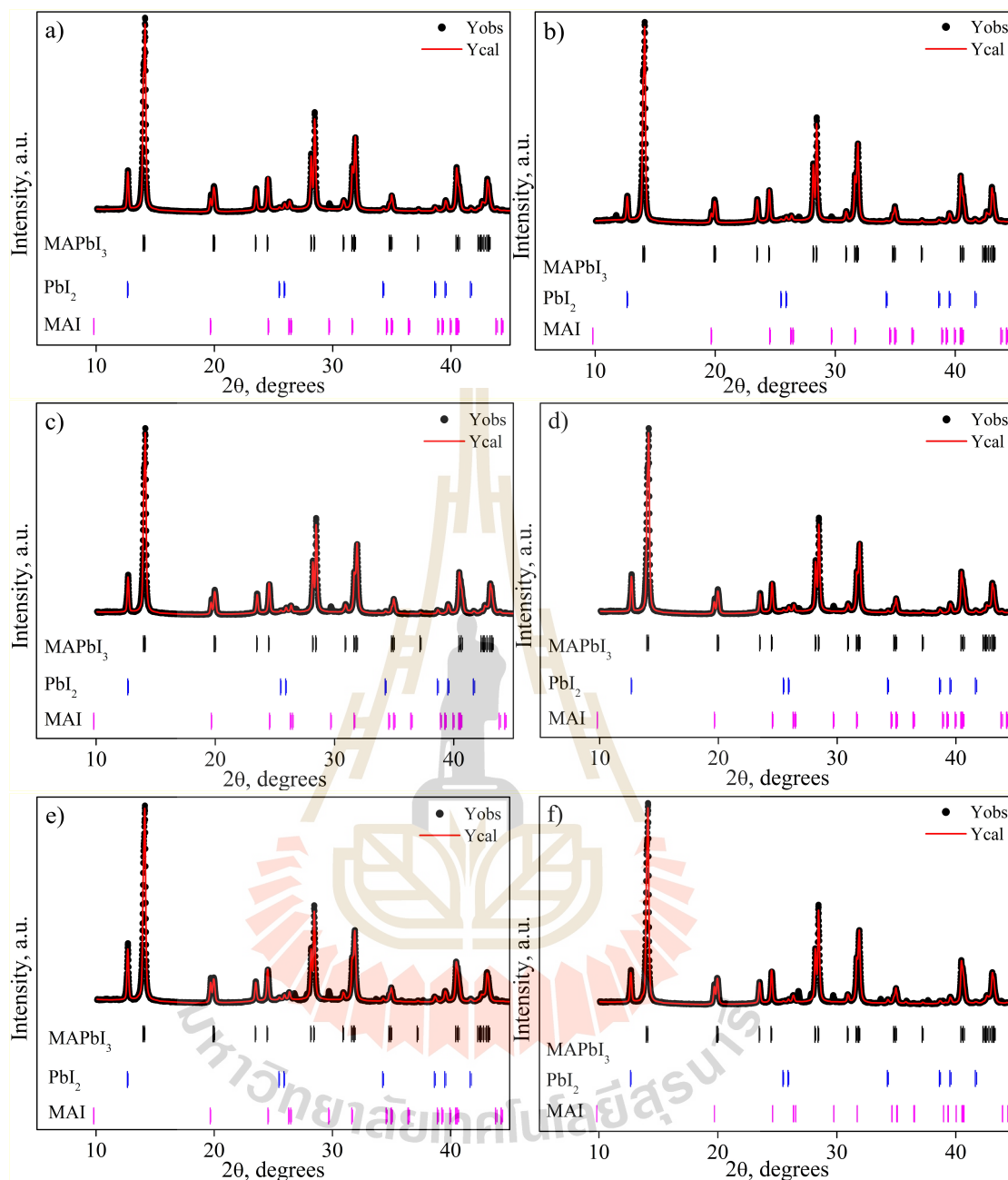


Figure 4.40 Rietveld refinement of the powder X-ray diffraction data of the Ba^{2+} doped $\text{CH}_3\text{NH}_3\text{Pb}_{1-x}\text{Ba}_x\text{I}_3$ materials with $x =$ a) 0.02, b) 0.04, c) 0.06, d) 0.08, e) 0.1 and f) 0.2. Experimental data are shown as \bullet symbols. The solid line is fit, the vertical bars are the expected Bragg reflection position.

Table 4.8 Phase formation, lattice parameter by Rietveld refinement of of Ba²⁺ substitution on CH₃NH₃Pb_{1-x}Ba_xI₃ XRD pattern.

| x | | 0 | 0.02 | 0.04 | 0.06 | 0.08 | 0.1 | 0.2 |
|--------------------|-----------|------------|------------|------------|------------|------------|------------|------------|
| MAPbI ₃ | a = b (Å) | 8.8735(5) | 8.8592(2) | 8.8638(2) | 8.8643(2) | 8.8655(2) | 8.8648(2) | 8.8655(2) |
| | c (Å) | 12.6657(9) | 12.6635(3) | 12.6638(2) | 12.6598(3) | 12.6604(3) | 12.6558(3) | 12.6573(3) |
| | %wt | 97.35 | 92.33 | 91.69 | 92.30 | 91.81 | 91.39 | 91.49 |
| PbI ₂ | a = b (Å) | 4.5577(2) | 4.5538(2) | 4.5555(2) | 4.5546(2) | 4.5551(2) | 4.5542(2) | 4.5548(3) |
| | c (Å) | 6.9891(2) | 6.9814(4) | 6.9844(5) | 6.9824(4) | 6.9851(3) | 6.9802(4) | 6.9806(5) |
| | %wt | 2.65 | 4.91 | 5.82 | 5.00 | 5.44 | 5.92 | 5.89 |
| MAI | a (Å) | - | 9.0183(4) | 9.0201(5) | 9.0195(4) | 9.0206(4) | 9.0188(4) | 9.0177(5) |
| | b (Å) | - | 5.1342(4) | 5.1344(4) | 5.1340(4) | 5.1338(4) | 5.1339(4) | 5.1329(4) |
| | c (Å) | - | 5.0970(4) | 5.0963(4) | 5.0968(4) | 5.0968(4) | 5.0972(4) | 5.0982(5) |
| | %wt | - | 2.87 | 2.49 | 2.70 | 2.75 | 2.69 | 2.62 |
| wRp(%) | | 6.92 | 6.20 | 6.52 | 6.19 | 6.32 | 6.69 | 7.77 |
| GOF | | 1.71 | 1.78 | 1.86 | 1.79 | 1.84 | 1.97 | 2.26 |
| D (nm) | | 16.22±0.02 | 14.13±0.01 | 14.76±0.03 | 15.03±0.02 | 15.26±0.04 | 15.27±0.01 | 15.52±0.01 |

4.4.2 UV-vis spectroscopy

The diffuse reflectance UV vis spectroscopy were measured to determine the Optical bandgap. The optical bandgap is an important factor in understanding the PV properties of semiconductors. Figure 4.41 shows the region of reflectance spectra obtained for 0.02-0.2 Ba²⁺ substitutions in CH₃NH₃PbI₃. The figure 4.25a shows that the presence of Ba²⁺ substitutions increasing leads to a slight shift of 0.02MABaI to other substituted.

According to the theory of optical absorption, properties are related to their electronic structure and important role in determining optical bandgap. The optical bandgap can be determined from the plot of the Kubelka-Munk function $[F(R)hv]^2$ vs photon energy (E_g) where $F(R)$, h , v and E_g are the absorption coefficient, planck constant, the light frequency and bandgap, respectively. Thus, E_g values are calculated by the linear extrapolation portion of the plots to $[F(R)hv]^2 = 0$. The optical bandgap are determined by extrapolating the linear approach as illustrated in figure 4.25b. From the figure, it can be seen that the optical bandgap of the parent of Ba-substitution are estimated to 1.55-1.57 eV in 20% substitutes. As literature was calculated to the formula MABaI₃ for optical bandgap values around 3.30 eV with tetragonal phase (Pazoki et al., 2016), while our works shows around 1.55-1.57 eV for increasing the Sn²⁺ substitutions. It is too difficult with theoretical maybe from second phase and low-density of samples.

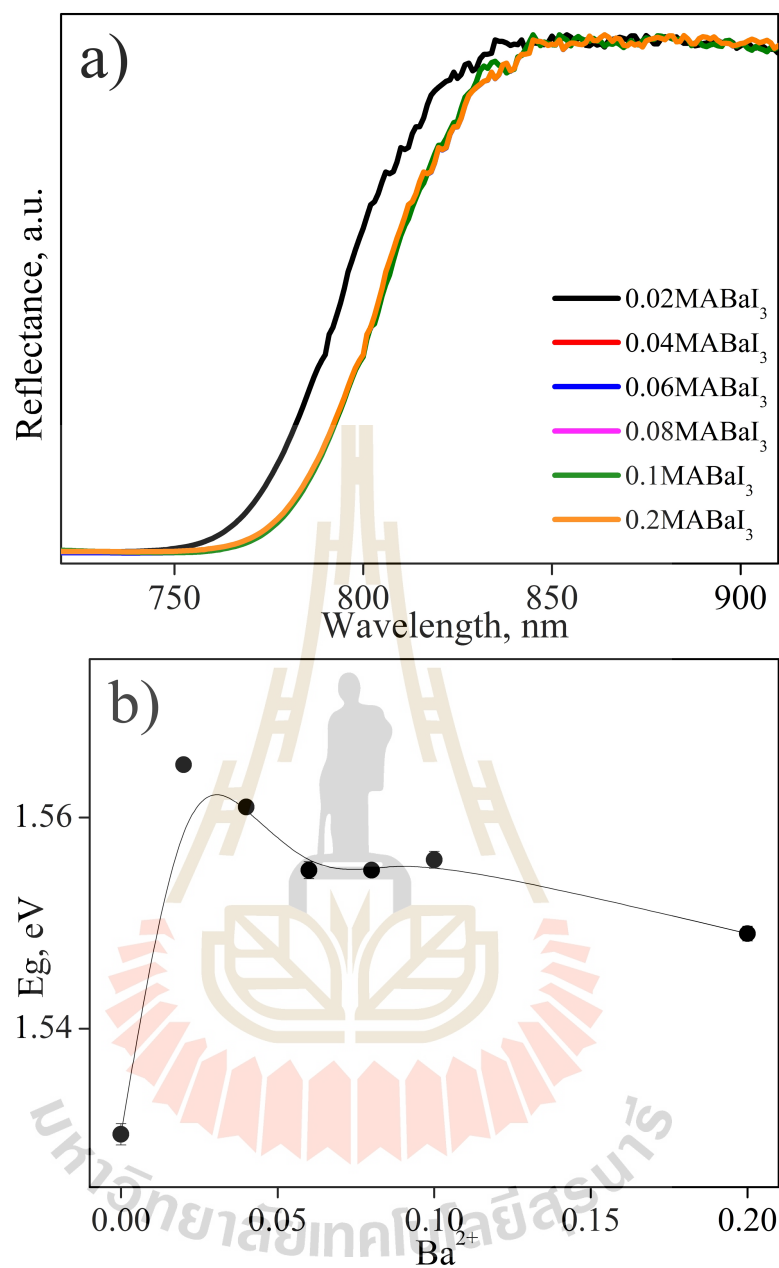


Figure 4.41 a) diffuse reflectance UV vis spectra for $\text{CH}_3\text{NH}_3\text{Pb}_{1-x}\text{Ba}_x\text{I}_3$ samples with 0.02-0.2 Ba^{2+} substitutions and b) the plot of the optical bandgap values for each samples.

4.4.3 FTIR measurement

To study the bonds in the substitution a FTIR spectrometer was used. The room temperature FTIR spectra of Ba-substituted with different concentrations of substitution ions samples have been show in Figure4.42 in wavenumber of 400-2000 cm^{-1} . The figure show room temperature FTIR spectra and characteristic vibration bands with Ba^{2+} substituted in $\text{CH}_3\text{NH}_3\text{Pb}_{1-x}\text{Ba}_x\text{I}_3$ (see table 4.2). The main peaks are related to the frequency of vibrational modes of the organics cation (Pérez-Osorio et al., 2015; Jintara and Rattikorn, 2017). In the spectra show the weaker vibrational mode of materials mainly related to the bending and rocking mode in the range of 600-1700 cm^{-1} . According ref. (Pérez-Osorio et al., 2015; Jintara and Rattikorn, 2017), we propose the summary attribution of these peaks to vibrational by Table 4.2. However, the perovskite Ba^{2+} substituted in $\text{CH}_3\text{NH}_3\text{Pb}_{1-x}\text{Ba}_x\text{I}_3$ have been used and no shift of all peaks. As it was mentioned above, N-H stretching, N-H bending, C-H bending, C-N rocking vibration modes of all materials. In particular, The spectra similar results were found for $\text{CH}_3\text{NH}_3\text{PbI}_3$ and Sn^{2+} substituted in $\text{CH}_3\text{NH}_3\text{PbI}_3$ material. We infer that the interaction found are attributable to the chemical nature of organic compound in perovskite materials.

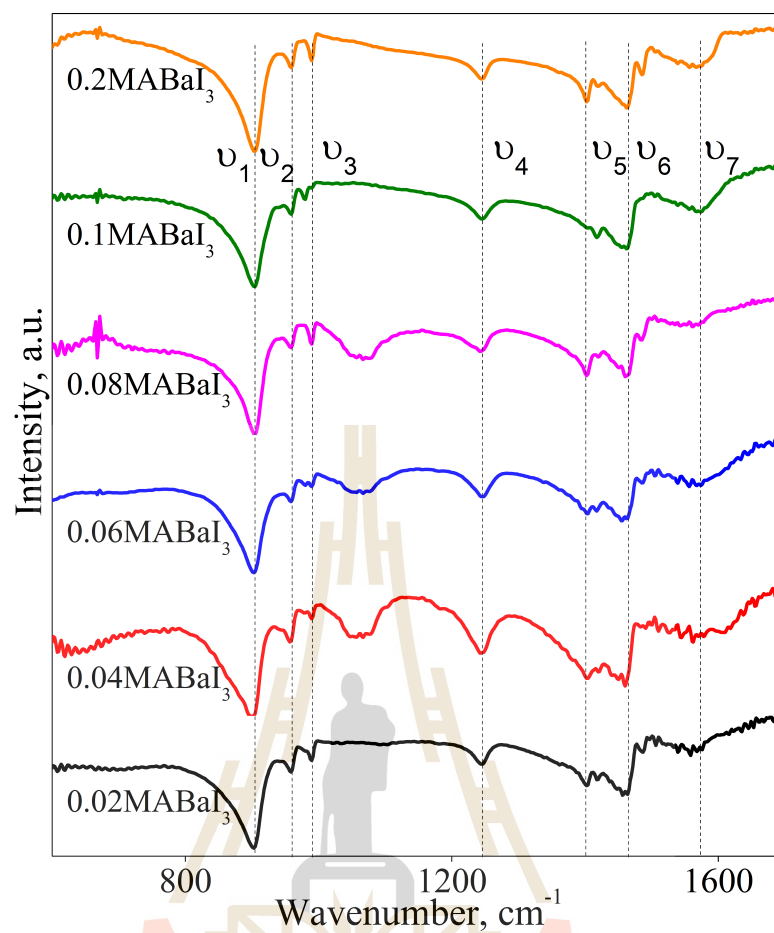


Figure 4.42 FTIR spectra of Ba^{2+} substituted in $\text{CH}_3\text{NH}_3\text{Pb}_{1-x}\text{Ba}_x\text{I}_3$ materials in the range of $500\text{-}1700\text{ cm}^{-1}$.

มหาวิทยาลัยเทคโนโลยีสุรนารี

4.4.4 XPS measurement

Figure 4.43 shows the XPS data of C 1s, N 1s, I 3d, Pb 4f and Sn 3d core level with the Sn^{2+} substitution. We began our measurements with carbon, where the adventitious C 1s line would be used for charge referencing and calibration.

The C 1s spectrum (Figure 4.44) is the calibrated spectra for the C 1s for all samples. The spectra were analyzed using a Shirley function for background deduction and Gaussian function to fit the peaks. The FWHM of all samples fitted curves were constrained to be the very close/ similar. The main carbon peak and the most peak arises from the adventitious carbon found in the atmosphere and other impurities that may contaminate from the preparation XPS measurement. This C peak is conventionally set to 284.8 eV and indicate for the C-C/C-H chemical state for carbon. The other peaks at 285.6 and 286.3 eV correspond to the C-I and C-N states. The N 1s spectra (see Figure 4.45) are remarkably similar and two features BE at 401.8 and 400.2 eV are detected. A good agreement with the $\text{CH}_3\text{NH}_3\text{PbI}_3$ result and ref. data (NIST, 2000) are confirmed N-H and C-H chemical states.

The I 3d, Pb 4f and Ba 3d spectra (see Figure 4.46, 4.47 and 4.48) are characterized by a orbit-split doublet, with I $3d_{5/2}$, Pb $4f_{7/2}$ and Ba $3d_{5/2}$ peaks at a BE of 618.9, 137.9 and 780.5 eV, respectively. These BE are consistent with literature for bulk PbI_2 and BaI_2 (Qingbiao et al., 2004; NIST, 2000). It is indicate the presence of I^- , Pb^{2+} and Ba^{2+} species. The spectra appeared I^2 and C-I (617.6 and 620.1 eV) for I spectra, which consistent C spectra (Figure 4.44). As the same time, Pb spectra detected the Pb-metal and Pb-O at 136.5 and 138.9 eV, respectively. However, figure 4.49 confirmed the O-Pb around 531.6 eV and detected O-H chemical state. This contamination detect could be explained during to the preparation of XPS technique.

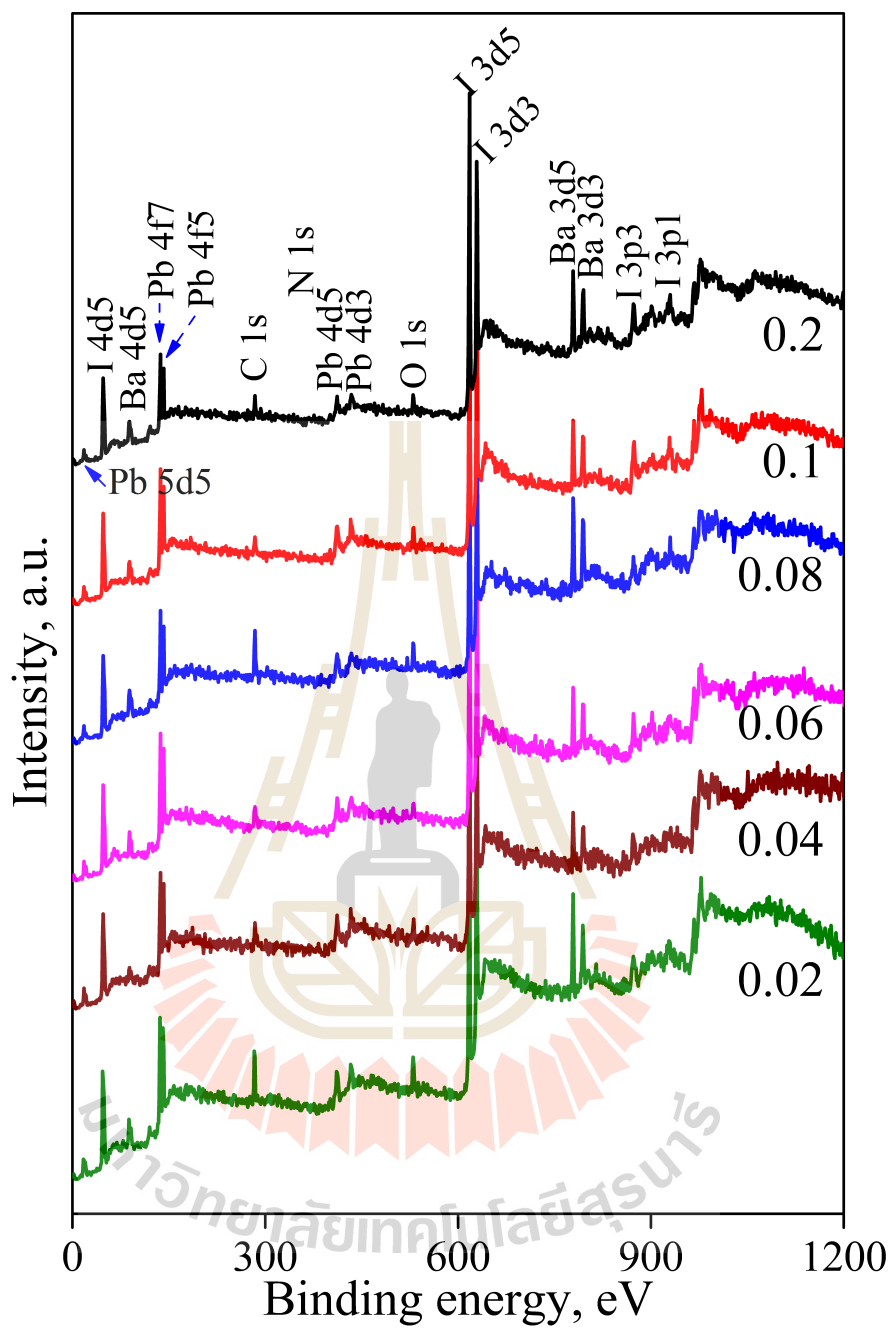


Figure 4.43 XPS survey scan of Ba^{2+} substituted in $\text{CH}_3\text{NH}_3\text{Pb}_{1-x}\text{Ba}_x\text{I}_3$ materials.

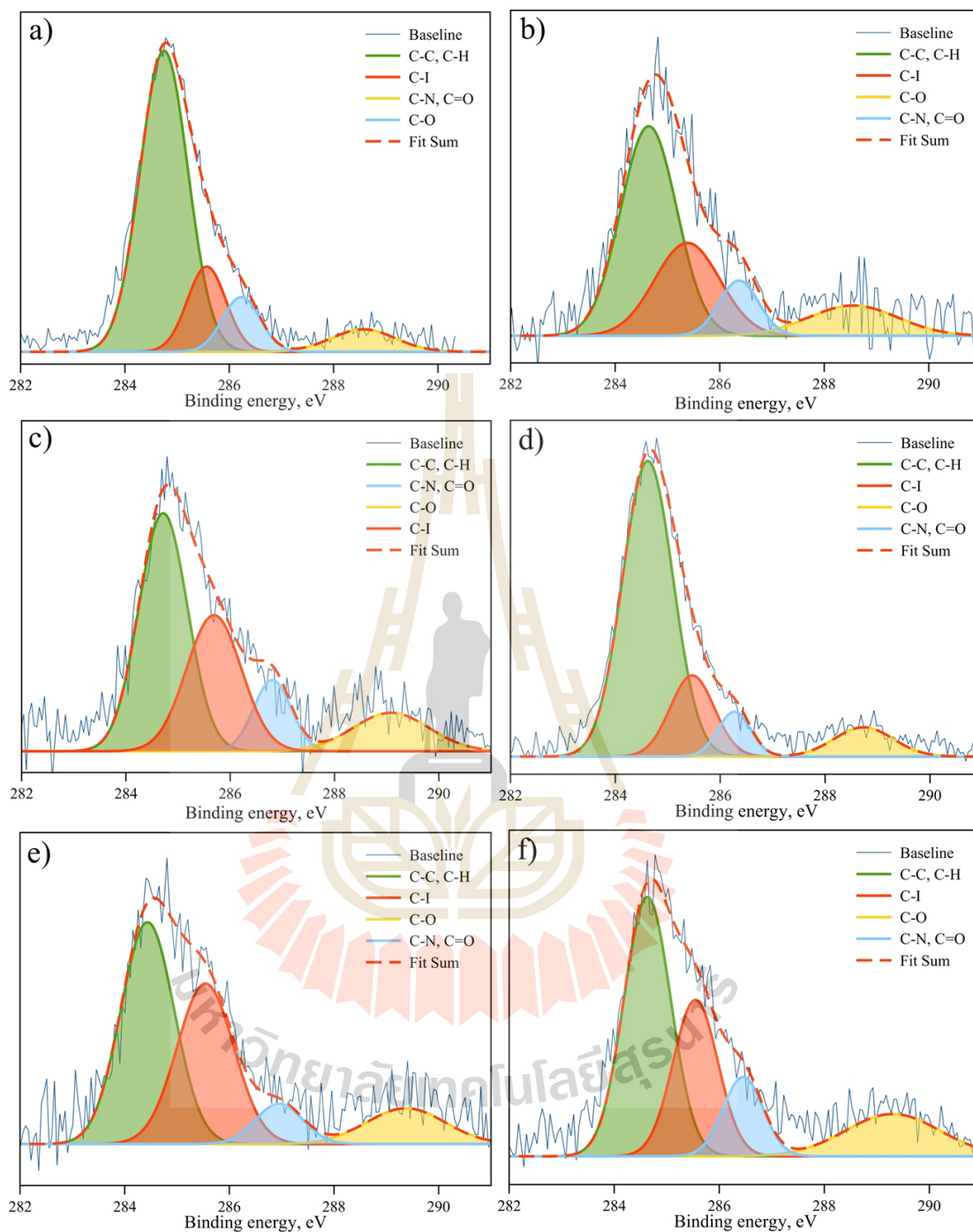


Figure 4.44 XPS spectra for C 1s of the samples and the Gaussian fitting, when a) 0.02, b) 0.04, c) 0.06, d) 0.08, e) 0.1 and f) 0.2 Ba^{2+} substituted in $\text{CH}_3\text{NH}_3\text{Pb}_{1-x}\text{Ba}_x\text{I}_3$ materials.

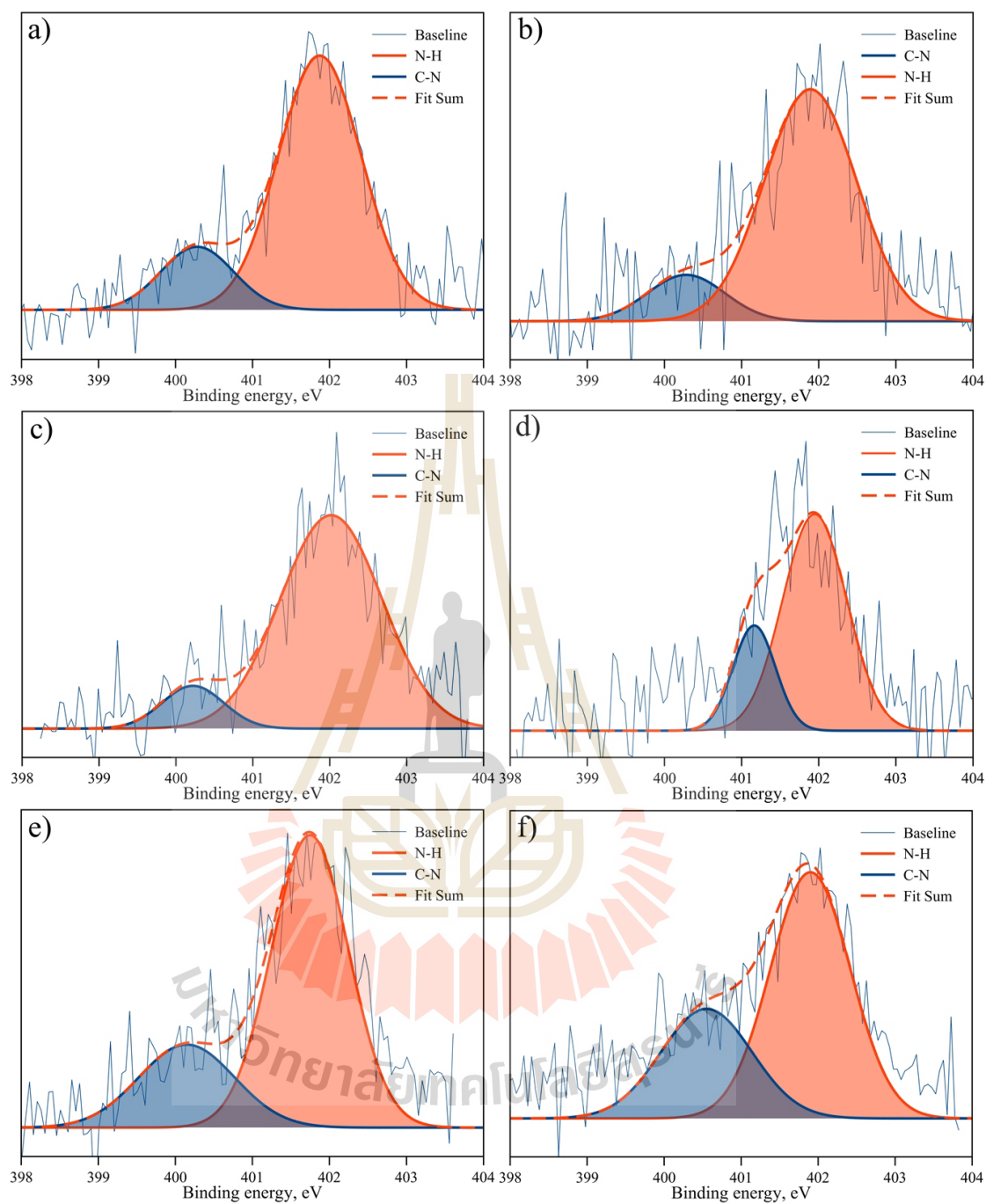


Figure 4.45 XPS spectra for N 1s of the samples and the Gaussian fitting, when a) 0.02, b) 0.04, c) 0.06, d) 0.08, e) 0.1 and f) 0.2 Ba^{2+} substituted in $\text{CH}_3\text{NH}_3\text{Pb}_{1-x}\text{Ba}_x\text{I}_3$ materials.

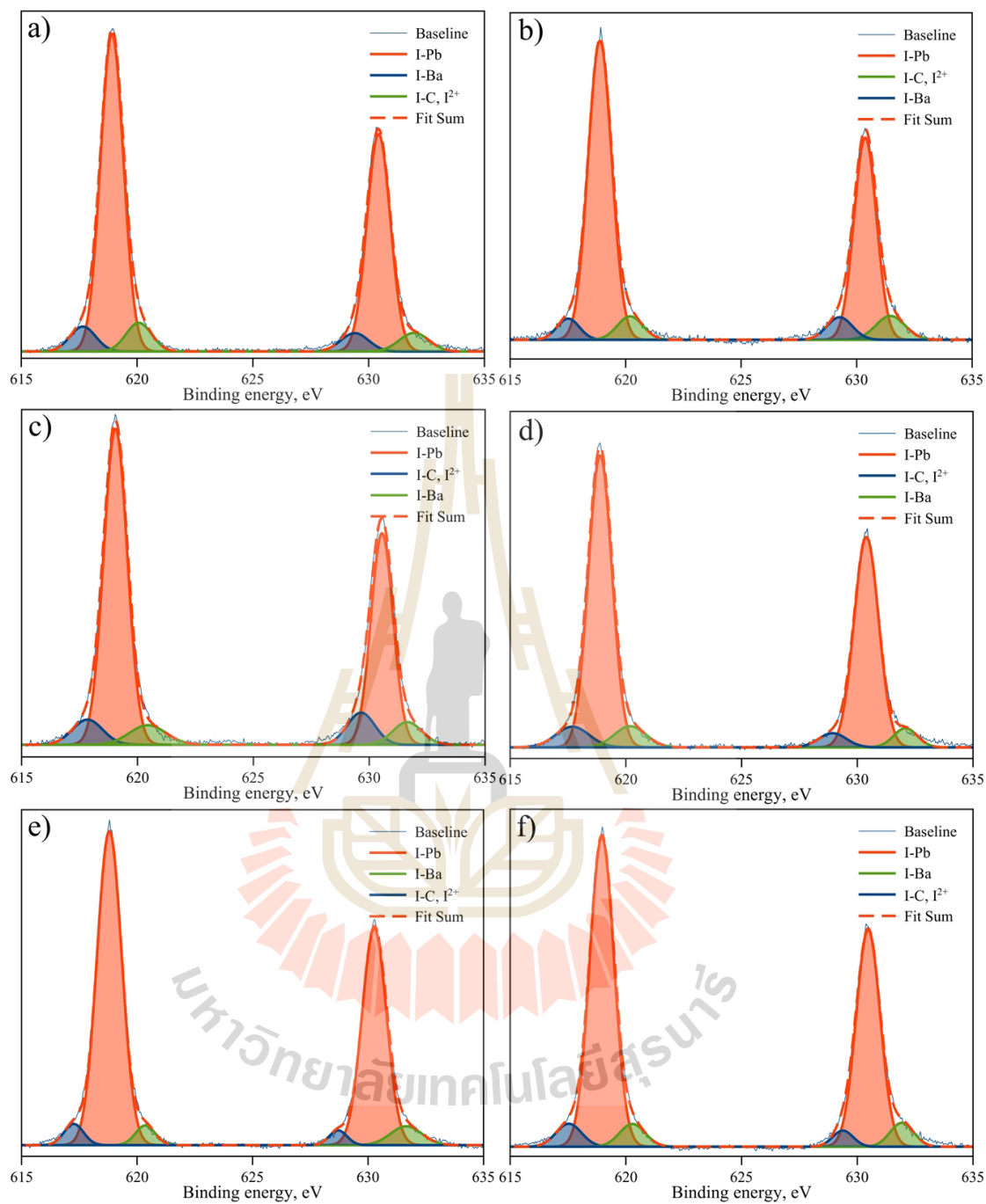


Figure 4.46 XPS spectra for I 3d of the samples and the Gaussian fitting, when a) 0.02, b) 0.04, c) 0.06, d) 0.08, e) 0.1 and f) 0.2 Ba^{2+} substituted in $\text{CH}_3\text{NH}_3\text{Pb}_{1-x}\text{Ba}_x\text{I}_3$ materials.

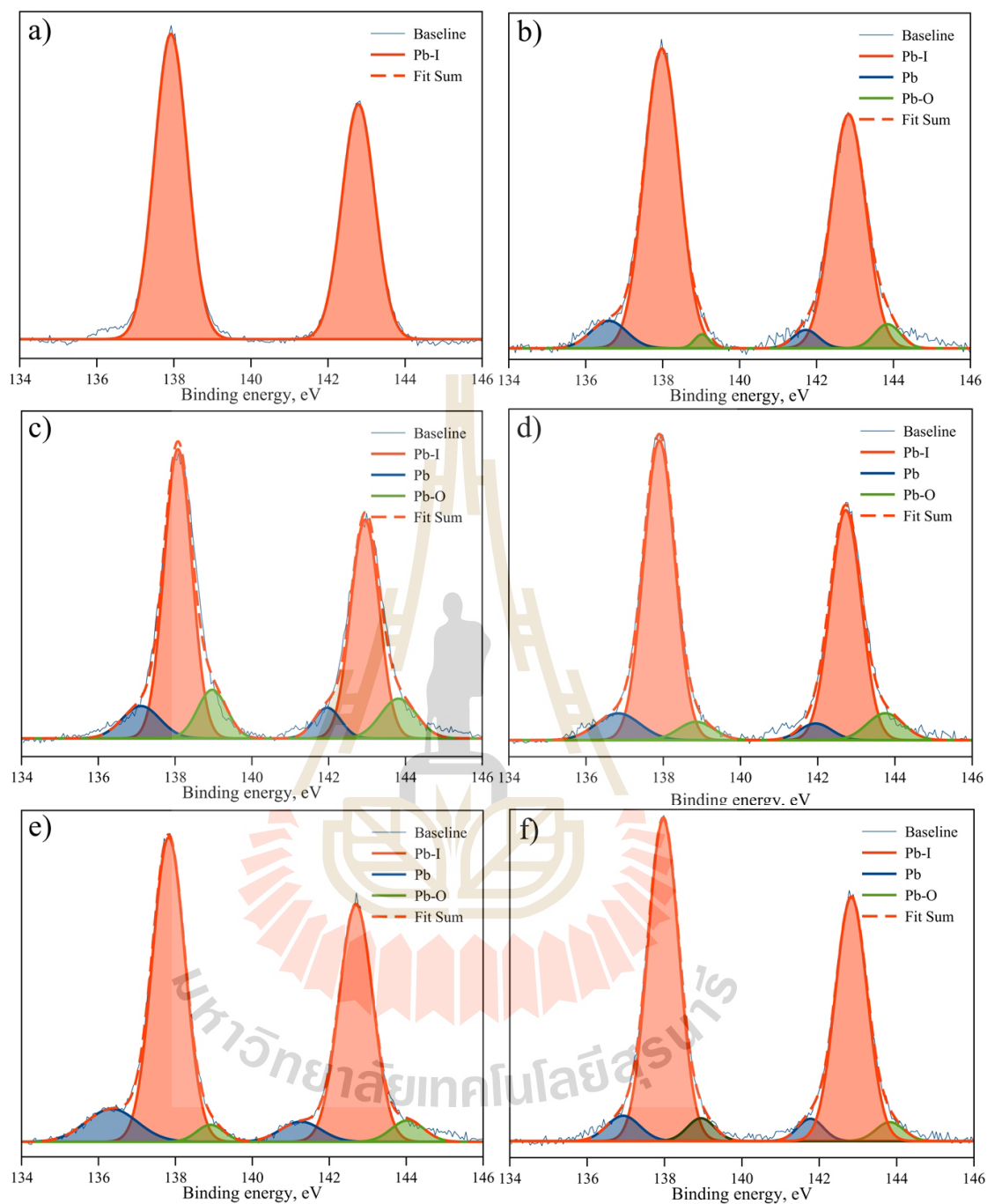


Figure 4.47 XPS spectra for Pb 4f of the samples and the Gaussian fitting, when a) 0.02, b) 0.04, c) 0.06, d) 0.08, e) 0.1 and f) 0.2 Ba^{2+} substituted in $\text{CH}_3\text{NH}_3\text{Pb}_{1-x}\text{Ba}_x\text{I}_3$ materials.

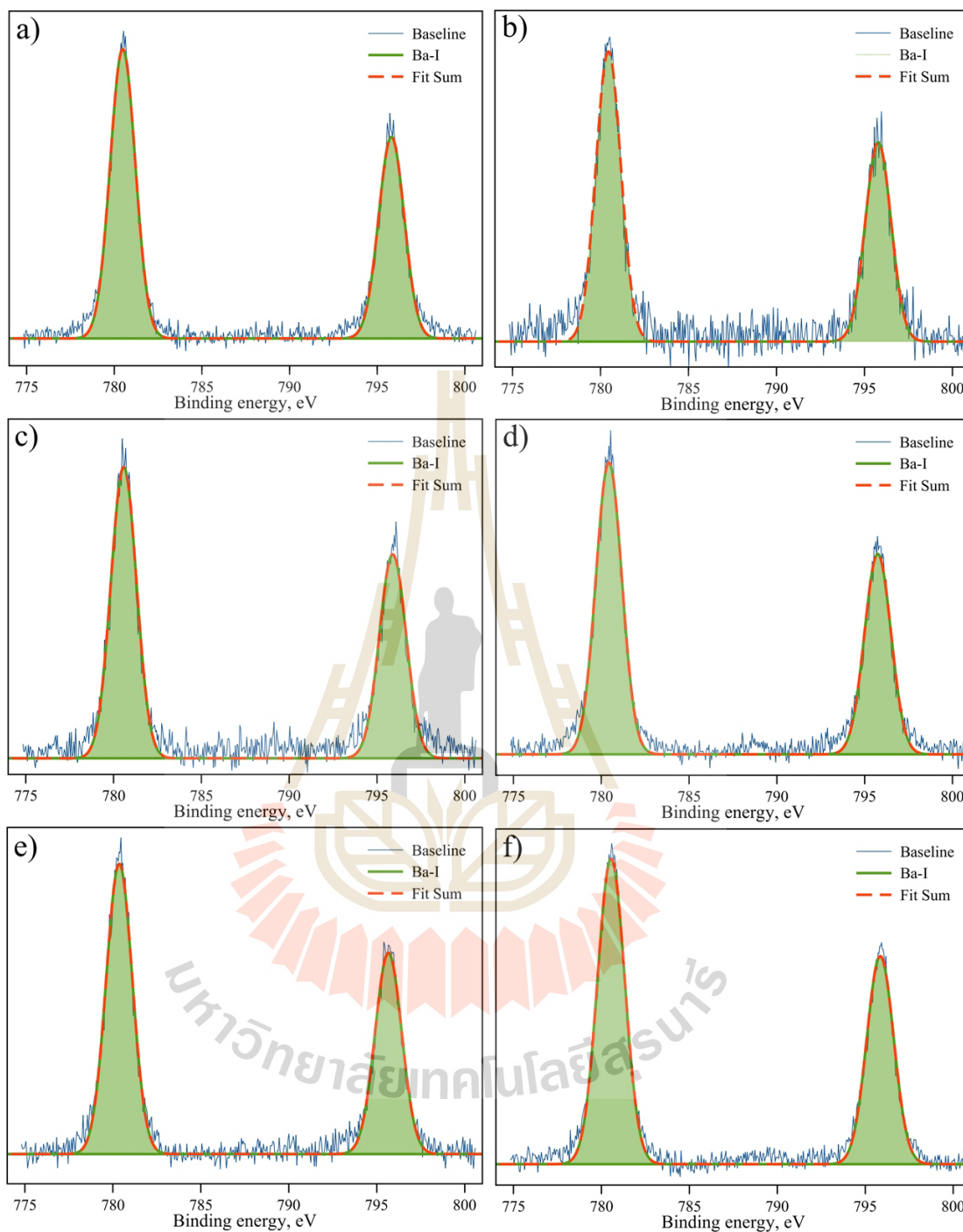


Figure 4.48 XPS spectra for Ba 3d of the samples and the Gaussian fitting, when a) 0.02, b) 0.04, c) 0.06, d) 0.08, e) 0.1 and f) 0.2 Ba²⁺ substituted in CH₃NH₃Pb_{1-x}Ba_xI₃ materials.

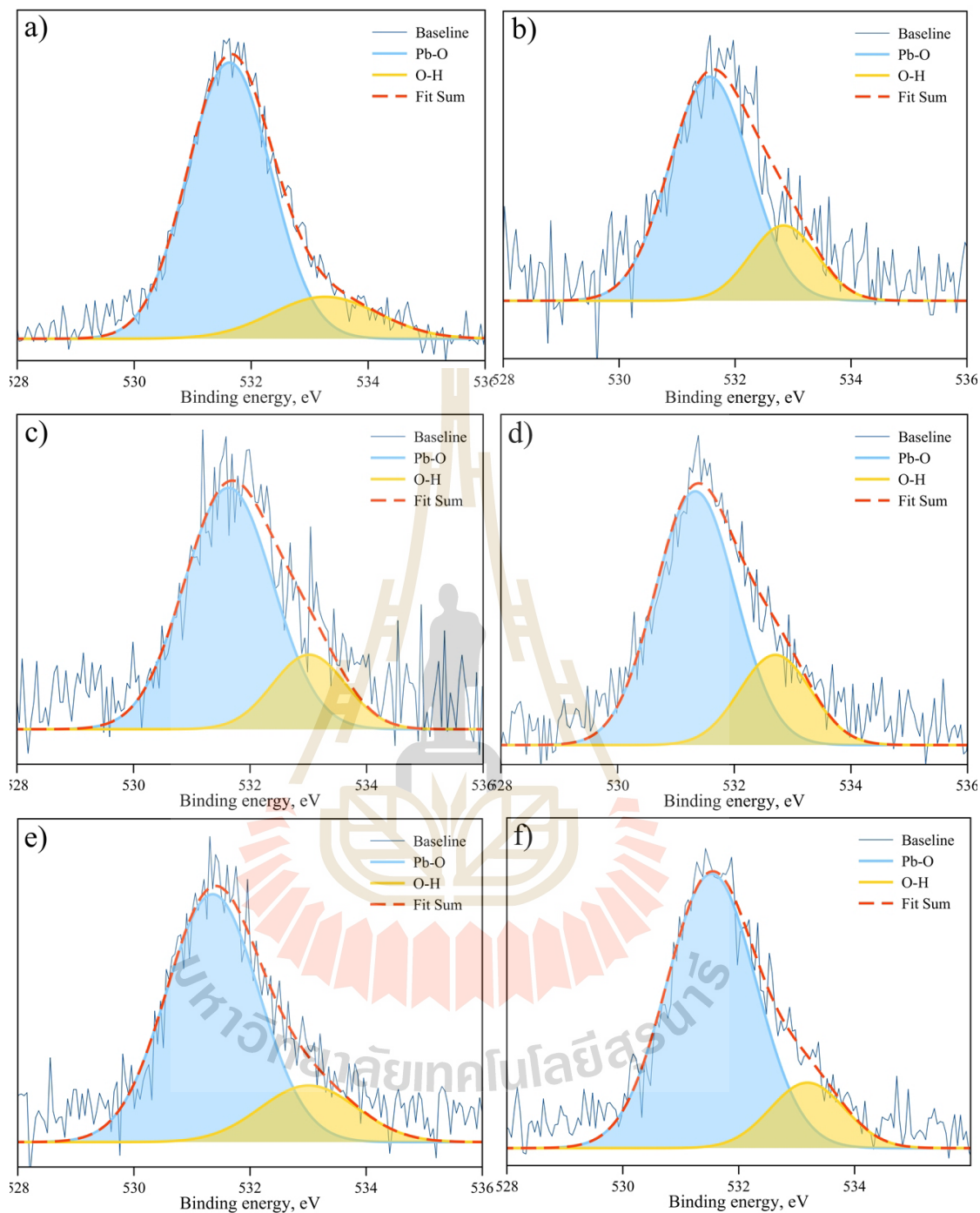


Figure 4.49 XPS spectra for O 1s of the samples and the Gaussian fitting, when a) 0.02, b) 0.04, c) 0.06, d) 0.08, e) 0.1 and f) 0.2 Ba^{2+} substituted in $\text{CH}_3\text{NH}_3\text{Pb}_{1-x}\text{Ba}_x\text{I}_3$ materials.

4.4.5 XANES analysis

The $\text{CH}_3\text{NH}_3\text{Pb}_{0.9}\text{Ba}_{0.1}\text{I}_3$ sample used study were obtained. The XANES measurement was done in FL mode for Pb M5-edge, TM for I L3-edge and Ba L3-edge for FL mode. At the same time, the measurement Pb M5-edge, I L3-edge and Ba L3-edge XANES of $\text{CH}_3\text{NH}_3\text{PbI}_3$, Pb^{2+} and substituted of some metal on B-site do not have reference compound available in the database. We get supporting information from XRD (Weber, 1978, 1979) and modified by substituted metal halide. Therefore, the calculation XANES from candidate compounds must be generated and compared with the experiment results.

To calculate the XANES spectra of $\text{CH}_3\text{NH}_3\text{Pb}_{0.9}\text{Ba}_{0.1}\text{I}_3$ and Pb^{2+} for ensuring all features of extrapolated XANES spectra, same way with $\text{CH}_3\text{NH}_3\text{PbI}_3$ and $\text{CH}_3\text{NH}_3\text{Pb}_{0.9}\text{Sn}_{0.1}\text{I}_3$ section. After the calculation XANES database has been compiled, the spectra can be used to compared and fitted with the experiment spectra as shown in Figure 4.50, 4.51 and 4.52. The features of Pb M5-edge and I L3-edge experiments spectra (see figure 4.50a-4.51a) look similar to calculation spectra (see figure 4.50b-4.51b) of those materials, as well as that $\text{CH}_3\text{NH}_3\text{PbI}_3$ and $\text{CH}_3\text{NH}_3\text{Pb}_{0.9}\text{Sn}_{0.1}\text{I}_3$ spectra. In addition, 10% substitution into the structure can be confirmed by Ba L3-edge XANES spectra. The spectra look a bit different with calculation spectra, but still would be confirmed the Ba existed in the structure (see figure 4.52). Therefore, from the XAS point of view, it can be concluded 10% substitution of Ba^{2+} and Sn^{2+} into the structure of $\text{CH}_3\text{NH}_3\text{PbI}_3$, which corresponding with XRD.

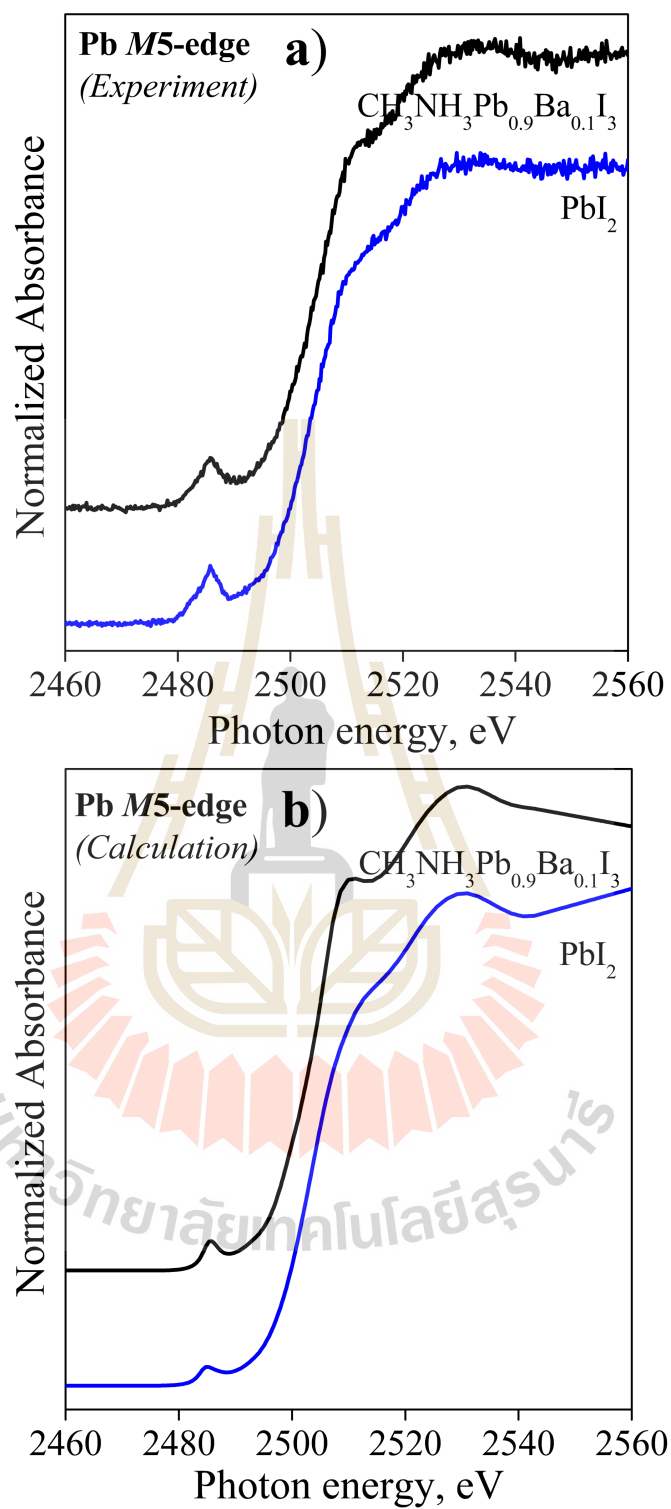


Figure 4.50 Measured Pb M5-edge XANES spectra (a) and calculated Pb M5-edge XANES spectra (b) of $\text{CH}_3\text{NH}_3\text{Pb}_{0.9}\text{Ba}_{0.1}\text{I}_3$ materials.

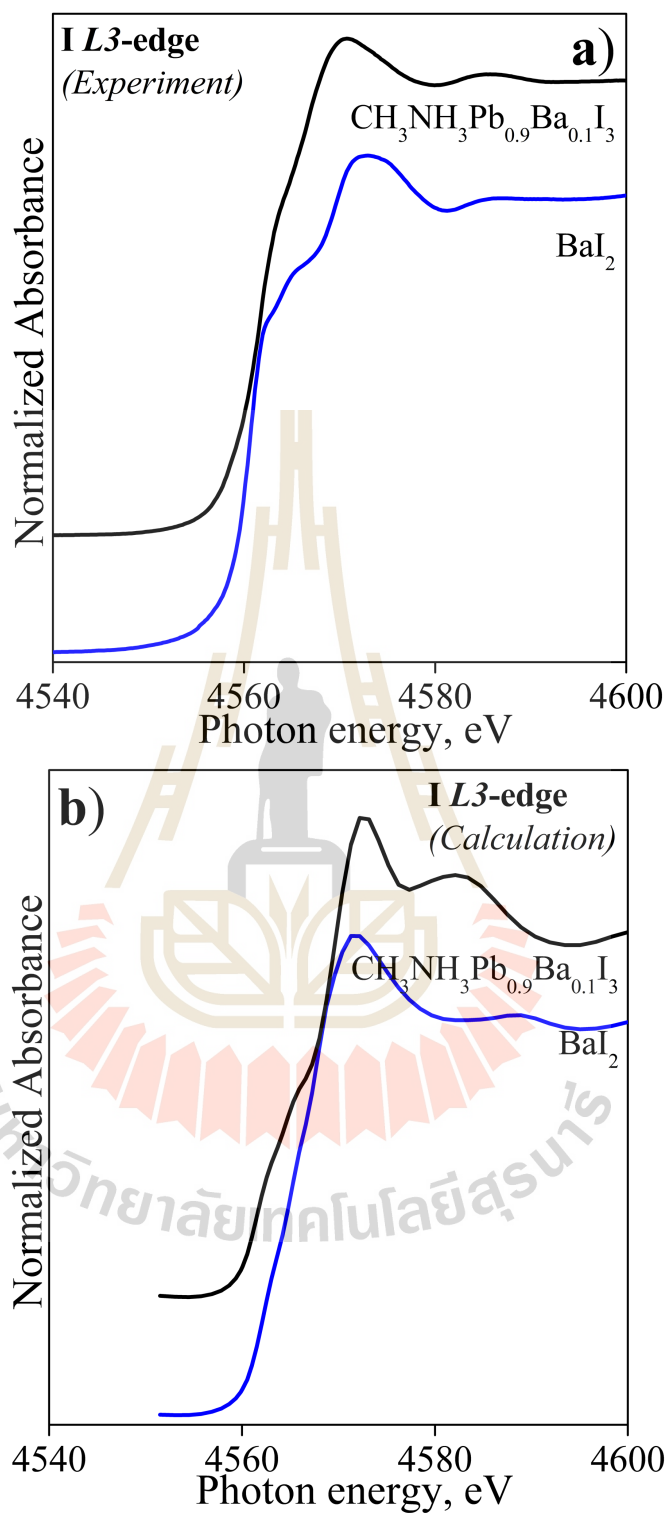


Figure 4.51 Measured I L3-edge XANES spectra (a) and calculated I L3-edge XANES spectra (b) of $\text{CH}_3\text{NH}_3\text{Pb}_{0.9}\text{Ba}_{0.1}\text{I}_3$ materials.

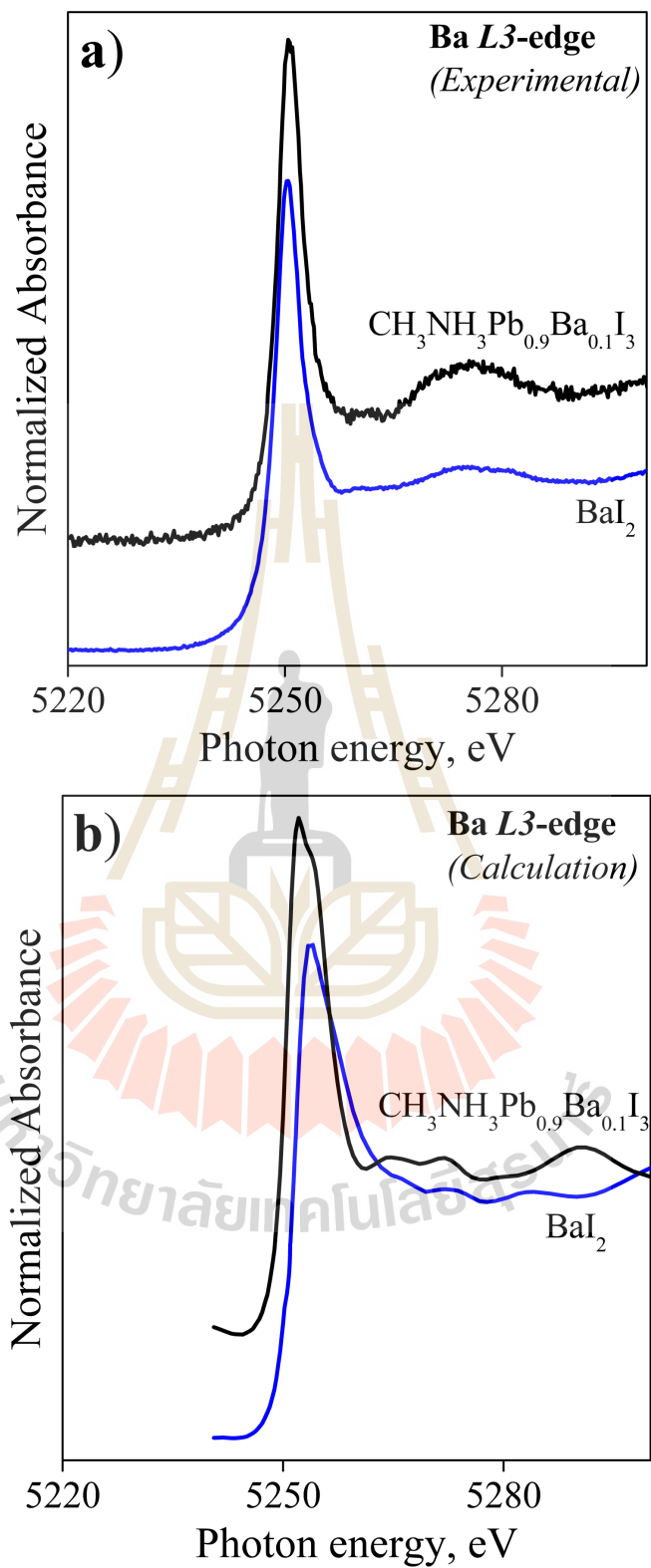


Figure 4.52 Measured Ba L3-edge XANES spectra (a) and calculated Ba L3-edge XANES spectra (b) of $\text{CH}_3\text{NH}_3\text{Pb}_{0.9}\text{Ba}_{0.1}\text{I}_3$ materials.

4.4.6 EXAFS analysis

The raw data was produced using ATHENA program to get EXAFS spectra. The curve fitting was done for the k^2 -weighted spectrum of 3-8.7 \AA^{-1} . The EXAFS spectra were processed, information on local structure of I atom via fitting with perovskite model of $\text{CH}_3\text{NH}_3\text{PbI}_3$ with Ba^{2+} substituted in B-site in ARTEMIS program. In the Figure 4.53a are two k^2 -weighted L3-edge EXAFS spectra. Normally, it seen that the two spectra are good agreement over the region 2-5 \AA^{-1} . However, the important structure parameters were extracted and consistent FT are shown in the Figure 4.53b. It can be seen that the fitting spectra can reproduce the experimental data. The fitting parameters obtained from this sample for average bond length of I absorbing atoms (R), Debye-Waller factors (σ^2) and coordination number (N) are shown in Table 4.9. The results can be confirmed the local structure consistent with XANES and XRD result.

Table 4.9 The structure parameters coordination numbers N, interatomic distances R and DW factors σ^2 obtained by fitting the EXAFS data for the $\text{CH}_3\text{NH}_3\text{Pb}_{0.9}\text{Ba}_{0.1}\text{I}_3$.

| Shell | N | R [\AA] | σ^2 |
|-------|---|--------------------|------------|
| I-Ba | 1 | 3.1060(6) | 0.0176 |
| I-Pb | 1 | 3.1060(6) | 0.0036 |
| I-I1 | 4 | 4.3273(1) | 0.0524 |
| I-I2 | 4 | 4.3918(7) | 0.0624 |
| I-N | 4 | 3.9537(3) | 0.0624 |
| I-C | 4 | 3.2448(1) | 0.0078 |

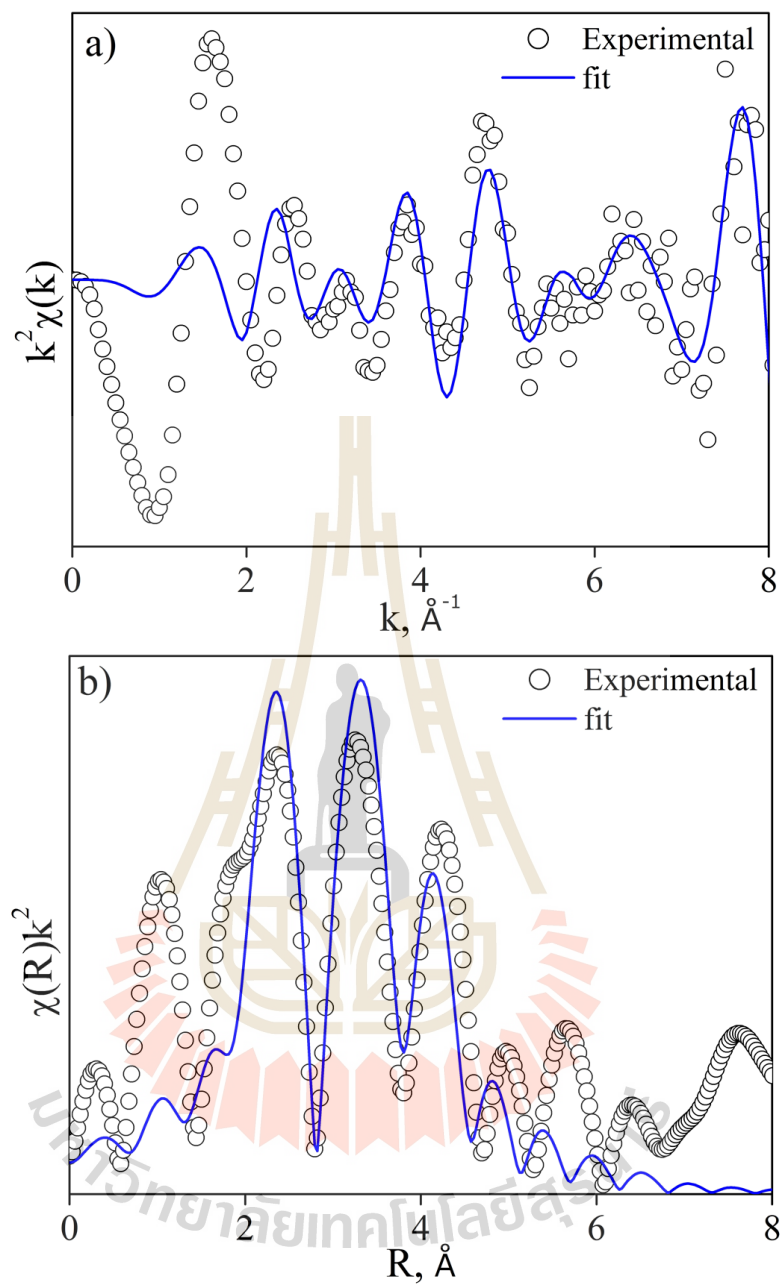


Figure 4.53 Comparison of Experiment and fitted magnitude of EXAFS Fourier transform (FT) (a) and (b) comparison of k^2 -weighted spectrum over the k -range of $\text{CH}_3\text{NH}_3\text{Pb}_{0.9}\text{Ba}_{0.1}\text{I}_3$. The k range used in the FT is from 3-8 \AA^{-1} for data set.

4.4.7 Low temperature phase transition

The heat capacities of $\text{CH}_3\text{NH}_3\text{Pb}_{0.9}\text{Ba}_{0.1}\text{I}_3$ are presented in Figure 4.54. The figure represent the normal heat capacity of $\text{CH}_3\text{NH}_3\text{Pb}_{0.9}\text{Ba}_{0.1}\text{I}_3$ samples determined as described below. For $T < 140$ K where the heat capacities were can not measured because Ba substituted material are attributed to the lower density of the pressed pellets. Thus, anomalies was found at 160 K, which this temperature consistent with previous reported (O et al., 1986). The phase transition in $\text{CH}_3\text{NH}_3\text{Pb}_{0.9}\text{Ba}_{0.1}\text{I}_3$ occur at close to temperature with $\text{CH}_3\text{NH}_3\text{PbI}_3$ (see figure 4.19) sample.

In addition, the temperature dependence of the complex permittivity (ϵ_r) and dielectric loss dispersion ($\tan \delta$) are shown in the Figure 4.20. The future data quite similar to $\text{CH}_3\text{NH}_3\text{PbI}_3$, $\text{CH}_3\text{NH}_3\text{Pb}_{0.9}\text{Sn}_{0.1}\text{I}_3$ and reported earlier (Fabini et al., 2016). A sharp drop in dielectric permittivity was found around 160 K, which corresponding to the heat capacities of the transition from the high-temperature tetragonal to the low temperature orthorhombic phase (Weber, 1978; Fabini et al., 2016). At first temperature of 3 K the dielectric permittivity is around ~ 14 . The dielectric permittivity of $\text{CH}_3\text{NH}_3\text{Pb}_{0.9}\text{Ba}_{0.1}\text{I}_3$ shows qualitatively similar trend to that found in $\text{CH}_3\text{NH}_3\text{PbI}_3$ and $\text{CH}_3\text{NH}_3\text{Pb}_{0.9}\text{Sn}_{0.1}\text{I}_3$ perovskites, the lower dielectric constant values for Ba substituted material are most likely attributed to the rather low density ($\sim 75\%$) of the polycrystalline sample. At higher temperatures ($T > 200$ K) the electrode polarization (Maxwell-Wagner effect) due to the itinerant charge carriers dominates the low-frequency dielectric permittivity and $\tan \delta$.

However, important feature is a relatively weak dielectric dispersion at $T_m \sim 60\text{-}100$ K whose details are shown in Figure 4.55a-b. The same way with $\text{CH}_3\text{NH}_3\text{PbI}_3$ and $\text{CH}_3\text{NH}_3\text{Pb}_{0.9}\text{Sn}_{0.1}\text{I}_3$, we have fitted the frequency dependence of

the $\tan \delta$ peak of the sample by Arrhenius and Vogel-Fulcher dielectric relaxation behaviour are shown in Figures 4.56 and fitting parameters are summarized in Tables 4.10. The results can be described by Arrhenius-type thermally activated behaviour with $E_a \sim 156$ meV and attempt frequency of $f_0 \sim 2 \times 10^{14}$ Hz. According to fitting by the Volger-Fulcher-type behaviour resulted in extremely large standard deviations and static dipolar freezing temperature $T_{VF} \approx 0$ K within the standard deviation similarly to $\text{CH}_3\text{NH}_3\text{Pb}_{0.9}\text{Sn}_{0.1}\text{I}_3$ data. Our results, Thus, support the Arrhenius-type thermally activated dynamics of the dipolar re-orientation and do not seem to agree well with the ‘glassy slowing’ of the dipolar relaxation, as proposed by previous reported (Fabini et al., 2016).

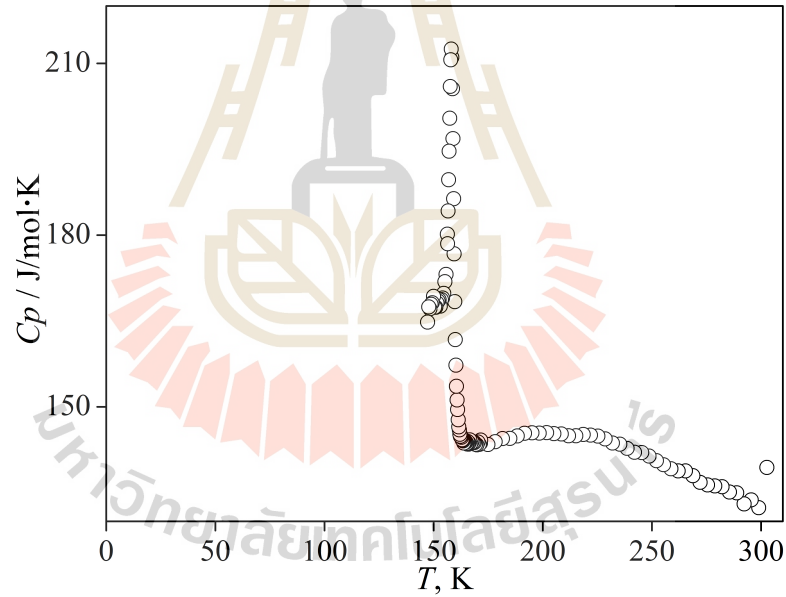


Figure 4.54 Low temperature heat capacity of related $\text{CH}_3\text{NH}_3\text{Pb}_{0.9}\text{Ba}_{0.1}\text{I}_3$ material.

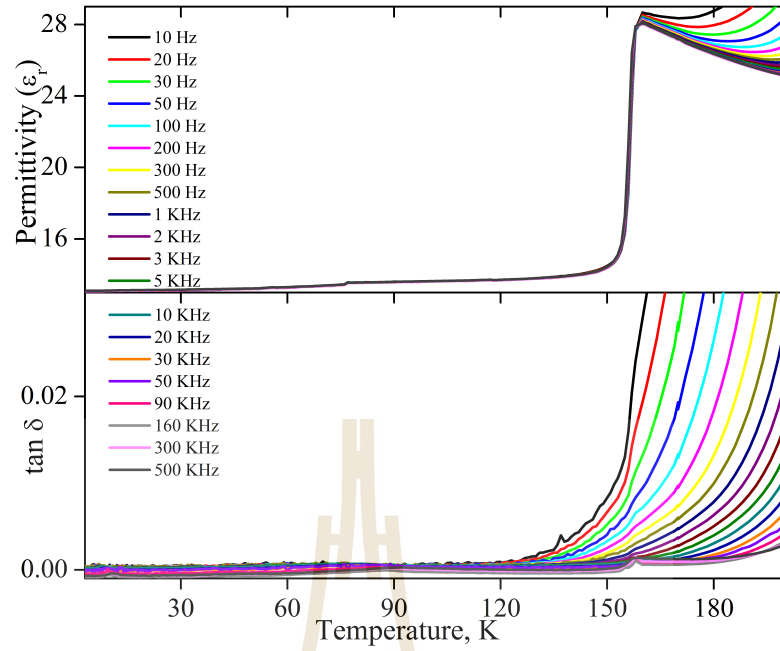


Figure 4.55 Low temperature of permittivity (ϵ_r) and loss tangent ($\tan \delta$) of $\text{CH}_3\text{NH}_3\text{Pb}_{0.9}\text{Ba}_{0.1}\text{I}_3$. Frequency dependent dielectric loss peaks indicating substantial slowing of relaxation dynamics are observed in the sample.

Table 4.10 Fitting parameters and goodness of fit (χ^2) for Arrhenius-type thermally-activated model and Vogel-Fulcher-type model of the dielectric relaxation of $\text{CH}_3\text{NH}_3\text{Pb}_{0.9}\text{Ba}_{0.1}\text{I}_3$ materials. The standard deviations of the fitting parameters are given in brackets.

| Type of fit | f_0 [Hz] | E_a [meV] | T_{VF} [K] | χ^2 |
|---------------|-------------------------|-------------|--------------|----------|
| Arrhenius | $1.8(9) \times 10^{14}$ | 156(3) | - | 0.994 |
| Vogel-Fulcher | $2(11) \times 10^{14}$ | 157(78) | 0(19) | 0.994 |

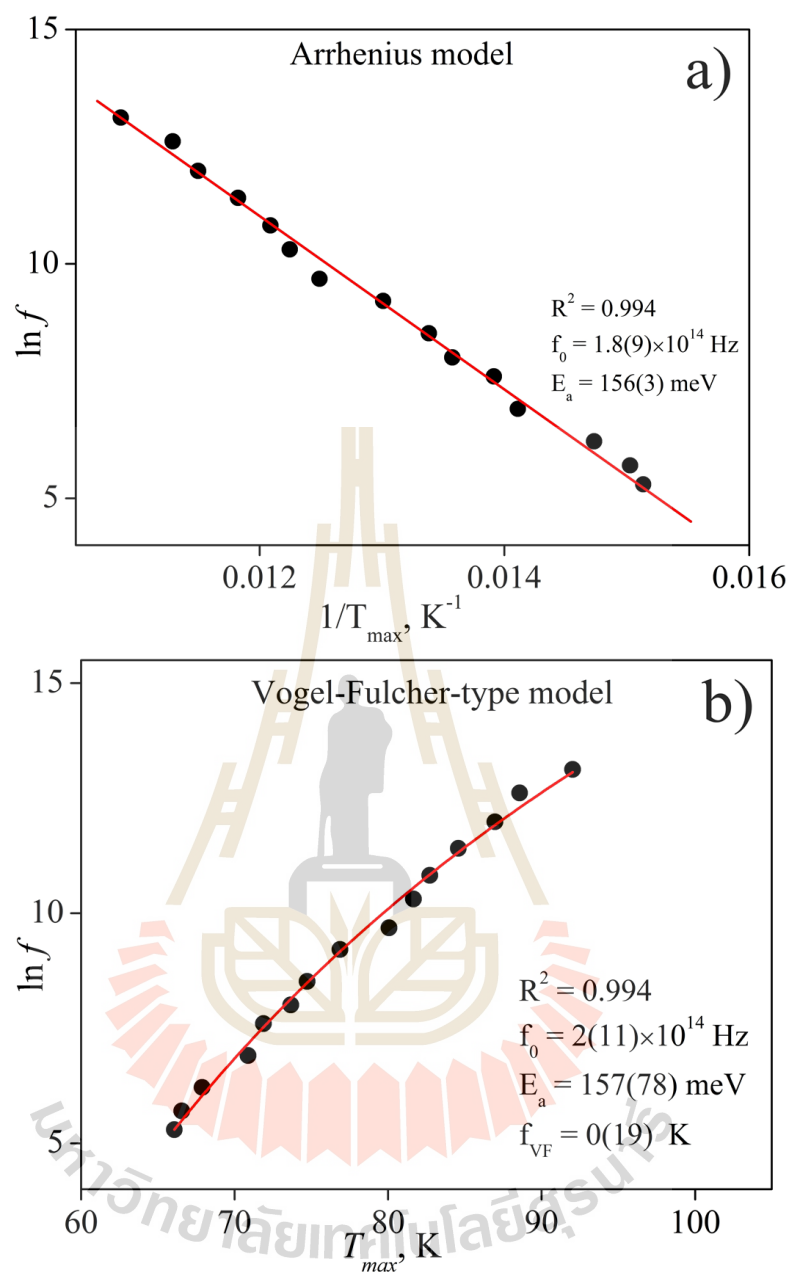


Figure 4.56 Natural logarithm of f as the function of $1/T$ by Arrhenius model a) and b) with the function of T_{\max} by Vogel-fulcher fit model for $\text{CH}_3\text{NH}_3\text{Pb}_{0.09}\text{Ba}_{0.1}\text{I}_3$.

CHAPTER V

CONCLUSIONS

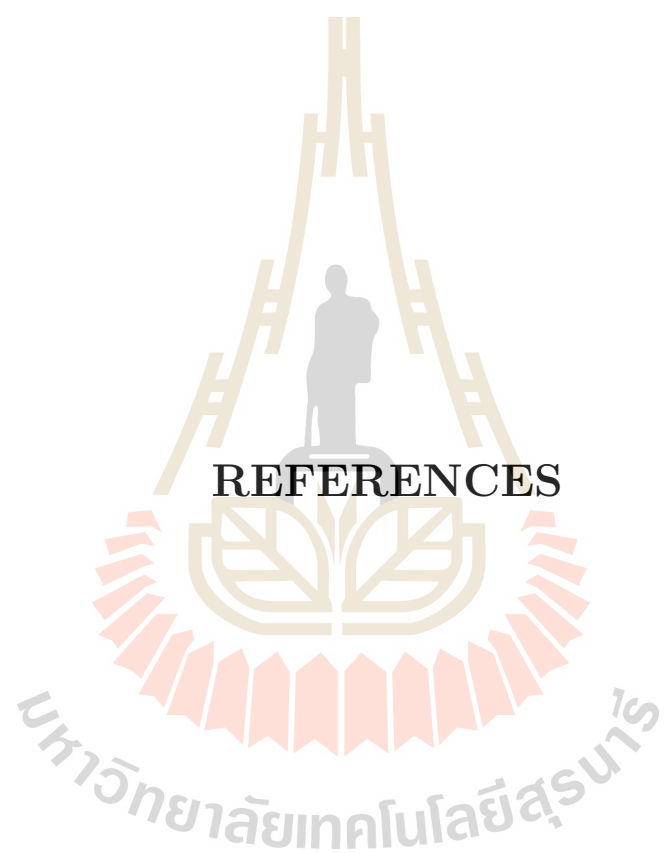
From the all above results, The XRD pattern shown $\text{CH}_3\text{NH}_3\text{PbI}_3$ samples exhibited a tetragonal I4/mcm space group. The XRD pattern of Sn^{2+} and Ba^{2+} modified $\text{CH}_3\text{NH}_3\text{PbI}_3$ show the reflections pattern that can be assigned to tetragonal phase with the space group I4/mcm , which is similar to that of the undoped sample. On the other hand, traces of the $\text{CH}_3\text{NH}_3\text{I}$ second phase are also detected in the Sn^{2+} and Ba^{2+} substituted materials.

The fit powder diffraction profiles was refined based on tetragonal (I4/mcm) space group of $\text{CH}_3\text{NH}_3\text{PbI}_3$, PbI_2 , and $\text{CH}_3\text{NH}_3\text{I}$ second phases were also included in refinement. The results of the Rietveld refinement, including the lattice parameter of the main phase, $\text{wRp}\%$ and GOF are evident that the substituted of Sn^{2+} and Ba^{2+} did not cause the phase transition from tetragonal to cubic in our samples. The optical bandgap energy presented of Ba and Sn substitution leads to a slight shift of the reflectance edge, following the trend that the $\text{CH}_3\text{NH}_3\text{PbI}_3 > \text{CH}_3\text{NH}_3\text{Pb}_{1-x}\text{Ba}_x\text{I}_3 > \text{CH}_3\text{NH}_3\text{Pb}_{1-x}\text{Sn}_x\text{I}_3$.

The FTIR spectra confirmed characteristic bands for organic group with many peaks, which are attributed to MA cation. More evident of chemical bonding and oxidation state in the samples are record by XPS spectra. The XPS results also confirmed the core levels of C 1s, N 1s, I 3d, Pb 4f, Sn 3d and Ba 3d. In addition, the experimental XAS results, both in XANES and EXAFS region showed the local structure around I atom from tetragonal structure in $\text{CH}_3\text{NH}_3\text{PbI}_3$. Moreover, XANES calculation spectra can fit nicely to the experiment spectra using

$\text{CH}_3\text{NH}_3\text{PbI}_3$, $\text{CH}_3\text{NH}_3\text{Pb}_{0.9}\text{Ba}_{0.1}\text{I}_3$, and $\text{CH}_3\text{NH}_3\text{Pb}_{0.9}\text{Sn}_{0.1}\text{I}_3$ as basis compound consists XRD results.

Another important, the temperature dependence of permittivity (ε_r) and dielectric loss ($\tan\delta$) in the range of 3-200 K measured at 1 kHz are presented in Figure 4.21. A sharp drop in dielectric permittivity upon cooling was found for all samples at around 160 K which corresponds to the transition from the high-temperature tetragonal to the low-temperature orthorhombic phase. The important feature is a relatively weak dielectric dispersion at $T_m \approx 60\text{-}100$ K whose detail was shown. Although it is believed that the orientational (with inorganic cage) and rotational (around the C-N axis) degrees of freedom of methylammonium ions are frozen out in the orthorhombic phase, the weak dielectric dispersion may indicate some residual dipolar contribution originating from the incomplete frees out, random fields, defects and disorder. To better understand the nature of the low-temperature dielectric relaxation we have fitted the frequency dependence of the $\tan\delta$ peak of our samples to both Arrhenius-type and Vogel-Fulcher. According to the results, the dielectric relaxation can be described by Arrhenius-type thermally activated behaviour with $E_a \approx 123\text{-}171$ meV and attempt frequency of $f_0 \approx 2 \times 10^{12} - 4 \times 10^{14}$ Hz. Furthermore, Sn-substituted specimen shows an additional low-temperature relaxation with $E_a \approx 70$ meV and $f_0 \approx 9 \times 10^7$ Hz. Attempts to fit the data to the Volger-Fulcher-type behavior resulted in extremely large standard deviations and static dipolar freezing temperature $T_{VF} \approx 0$ K within the standard deviation. Our results, therefore, support the Arrhenius-type thermally activated dynamics of the dipolar re-orientation of the dipolar relaxation.



REFERENCES

REFERENCES

- Alberto, C., Antonio, A., Gianlorenzo, B., Giulia, B., Rossella, Y., Franco, C., and Lamberto, D. (2015). Stability of organic cations in solution-processed $\text{CH}_3\text{NH}_3\text{PbI}_3$ perovskites: formation of modified surface layers. **J. Phys. Chem. C**. 119: 21329–21335.
- Amalie, D., Peng, G., Sang Il, S., Mohammad Khaja, N., and Michael, G. (2014). Thermal Behavior of Methylammonium Lead-Trihalide Perovskite Photovoltaic Light Harvesters. **Chem. Mater.** 26: 6160–6164.
- BA, B. (2003). Fuel cells: The amazing perovskite anode. **Nat. Mater.** 5: 294–296.
- Ball, J. M., Lee, M. M., Hey, A., and Snaith, H. J. (2013). Low-temperature processed meso-superstructured to thin-film perovskite solar cells. **Energy Environ. Sci.** 6: 1739–1743.
- Bhadeshia, H. K. D. H. (2002). Thermal Analyses Techniques. Differential Thermal Analysis. **Mater. Sci. Metal.**
- Brenner, T. M., Rakita, Y., Orr, Y., Klein, E., Feldman, I., Elbaum, M., Cahen, D., and Hodes, G. (2016). Conversion of Single Crystalline PbI_2 to $\text{CH}_3\text{NH}_3\text{PbI}_3$: Structural Relations and Transformation Dynamics. **Chem. Mater.** 28: 6501–6510.
- Brivio, F., Frost, J. M., Skelton, J. M., Jackson, A. J., Weber, O. J., Weller, M. T., Goni, A. R., Leguy, A. M. A., Barnes, P. R. F., and Walsh, A. (2015). Lattice dynamics and vibrational spectra of the orthorhombic,

- tetragonal and cubic phases of methylammonium lead iodide. **Phys. Rev. B.**92: 144308.
- Burschka, J., Pellet, N., Moon, S.-J., Humphry-Baker, R., Gao, P., Nazeeruddin, M. K., and Grätzel, M. (2013). Sequential deposition as a route to high-performance perovskite-sensitized solar cells. **Nature.** 499: 316–319.
- Coats, A. W. and Redfern, J. P. (1963). Thermogravimetric analysis. A review. **Analyst.** 88: 906–924.
- D B, M., C A, F., Z, S., and R B, L. (1995). Transport, Optical, and Magnetic Properties of the Conducting Halide Perovskite $\text{CH}_3\text{NH}_3\text{SnI}_3$. **J. Solid. State. Chem.** 114: 159–163.
- Eamesl, C., Frost, J. M., Barnes, P. R. F., ORegan, B. C., Walshl, A., and Islam, M. S. (2015). Ionic transport in hybrid lead iodide perovskite solar cells. **Nat. Commun.** 6: 7497.
- EL, S. (1975). Diffuse reflectance spectroscopy:a comparison of the theories. **Appl. Opt.** 14: 1380–1386.
- Emilio J, J.-P., Zafer, H., Sonia R, R., Luis K, O., and Yabing, Q. (2016). Thermal degradation of $\text{CH}_3\text{NH}_3\text{PbI}_3$ perovskite into NH_3 and CH_3I gases observed by coupled thermogravimetry-mass spectrometry analysis. **Energy Environ. Sci.** 9: 3406–3410.
- Eperon, G. E., Stranks, S. D., Menelaou, C., Johnston, M. B., Herz, L. M., and Snaith, H. J. (2014). Formamidinium lead trihalide: a broadly tunable perovskite for efficient planar heterojunction solar cells. **Energy Environ. Sci.**7: 982–988.

- Fabini, D. H., Hogan, T., Evans, H. A., Stoumpos, C. C., Kanatzidis, M. G., and Seshadri, R. (2016). Dielectric and Thermodynamic Signatures of Low-Temperature Glassy Dynamics in the Hybrid Perovskites $\text{CH}_3\text{NH}_3\text{PbI}_3$ and $\text{HC}(\text{NH}_2)_2\text{PbI}_3$. **J. Phys. Chem. Lett.** 7: 376–381.
- Fatih, D., Hong, L., Maryline, G.-V., and Octavio, P. (2015). Focus on properties and applications of perovskites. **Sci. Technol. Adv. Mater.** 16: 020301.
- Filip, M. R., Eperon, G. E., Snaith, H. J., and Giustino, F. (2014). Steric engineering of metal-halide perovskites with tunable optical band gaps. **Nat. Commun.** 5: 5757.
- Glaser, T., Müller, C., Sendner, M., Krekeler, C., Semonin, O. E., Hull, T. D., Yaffe, O., Owen, J. S., Kowalsky, W., Pucci, A., and Lovrinčić, R. (2015). Infrared Spectroscopic Study of Vibrational Modes in Methylammonium Lead Halide Perovskites. **J. Phys. Chem. Lett.** 6: 2913–2918.
- Haining, C., Zhanhua, W., Xiaoli, Z., and Shihe, Y. (2015). A Scalable electro deposition route to the low-cost, versatile and controllable fabrication of perovskite solar cells. **Nano Energy.** 15: 216–226.
- Idigoras, J., Todinova, A., Sanchez-Valencia, J. R., Barranco, A., Borras, A., and Anta, J. A. (2016). The interaction between hybrid organic–inorganic halide perovskite and selective contacts in perovskite solar cells: an infrared spectroscopy study. **Phys. Chem. Chem. Phys.** 18: 13583–13590.
- Ishihara, T. (1994). Optical properties of PbI-based perovskite structures. **J. Lumin.** 60: 269–274.

- Ishihara, T., Takahashi, J., and Goto, T. (1990). Optical properties due to electronic transitions in two-dimensional semiconductors $(C_nH_{2n+1}NH_3)PbI_4$. **Phys. Rev. B.** 42: 11099.
- Jacobsson, T. J., Pazoki, M., Hagfeldt, A., and Edvinsson, T. (2015). Goldschmidt's Rules and Strontium Replacement in Lead Halogen Perovskite Solar Cells: Theory and Preliminary Experiments on $CH_3NH_3SrI_3$. **J. Phys. Chem. C.** 119: 25673–25683.
- Javier, N., Antonio, S.-C., Juan, J. G., Norge, C. H., Jose, C. P., Rodrigo, A., Concha, F.-L., Desirée, M. D. I. S., Teresa, A., and Joaquín, M.-C. (2015). New insights into organic–inorganic hybrid perovskite $CH_3NH_3PbI_3$ nanoparticles. An experimental and theoretical study of doping in Pb^{2+} sites with Sn^{2+} , Sr^{2+} , Cd^{2+} and Ca^{2+} . **Nanoscale.** 7: 6216–6229.
- Jeong-Hyeok, I., Hui-Seon, K., and Nam-Gyu, P. (2014). Morphology-photovoltaic property correlation in perovskite solar cells: One-step versus two-step deposition of $CH_3NH_3PbI_3$. **American Institute of Physics Materials** 2: 081510.
- Jin Hyuck, H., Dae Ho, S., and Sang Hyuk, I. (2014). Planar $CH_3NH_3PbBr_3$ Hybrid Solar Cells with 10.4% Efficiency, Fabricated by Controlled Crystallization in the Spin-Coating Process. **Adv. Mater.** 26: 8179–8183.
- Jintara, P. and Rattikorn, Y. (2017). Effects of Annealing Temperature on Stability of Methylammonium Lead Iodide Perovskite Powders. **J. Alloy. Comp.** 720: 63–69.
- Juana, B. (1960). Infra-red spectra of ethylene diamine dihydrochloride and

- other amine hydrochlorides in alkali halide disks. **Spectrochim. Acta.** 16: 1344–1357.
- Jung, H. S. and Park, N. (2014). Perovskite Solar Cells: From Materials to Devices. **Materials Views** 11: 10–25.
- Kagan, C. R., Mitzi, D. B., and Dimitrakopoulos, C. D. (1999). Organic-Inorganic Hybrid Materials as Semiconducting Channels in Thin-Film Field-Effect Transistors. **American Association for the Advancement of Science** 286: 945–947.
- Kieslich, G., Suna, S., and Cheetham, A. K. (2015). An extended Tolerance Factor approach for organic–inorganic perovskites. **Chem. Sci.** 6: 3430–3433.
- Kim, H.-S., Lee, C.-R., Im, J.-H., Lee, K.-B., Moehl, T., Marchioro, A., Moon, S.-J., Humphry-Baker, R., Yum, J.-H., Moser, J. E., Grätzel, M., and Park, N.-G. (2012). Lead Iodide Perovskite Sensitized All-Solid-State Submicron Thin Film Mesoscopic Solar Cell with Efficiency Exceeding 9 **Sci. Rep.** 2: 591.
- Kitazawa, N., Watanabe, Y., and Nakamura, Y. (2002). Optical properties of $\text{CH}_3\text{NH}_3\text{PbX}_3$ (X = halogen) and their mixed-halide crystals. **J. Mater. Sci.**, 37: 3585–3587.
- Knop, O., Wasylishen, R. E., White, M. A., Cameron, T. S., and Van Oort, M. J. M. (1990). Alkylammonium lead halides. Part 2. $\text{CH}_3\text{NH}_3\text{PbX}_3$ (X = Cl, Br, I) perovskites: cuboctahedral halide cages with isotropic cation reorientation. **Can. J. Chem.** 68: 412–422.
- Kojima, A., Teshima, K., Shirai, Y., and Miyasaka, T. (2009). Organometal Halide

- Perovskites as Visible-Light Sensitizers for Photovoltaic Cells. **J. Am. Chem. Soc.**131: 6050–6051.
- Kollek, T., Gruber, D., Gehring, J., Zimmermann, E., Mende, L. S., and Polarz, S. (2014). Porous and Shape-Anisotropic Single Crystals of the Semiconductor Perovskite $\text{CH}_3\text{NH}_3\text{PbI}_3$ from a Single-Source Precursor. **Angew. Chem.** 54: 1341–1346.
- Kortüm, G. (1969). Reflectance Spectroscopy Principles, Methods, Applications, Springer, New York.
- Lewis, R. N. and McElhaney, R. N. (2000). Calorimetric and IR spectroscopic studies of phase transitions in Methylammonium Trihalogen oplumbates (II). **Biophys. J.**79: 2043–2055.
- Liu, M., Johnston, M. B., and Snaith, H. J. (2013). Efficient planar heterojunction perovskite solar cells by vapour deposition. **Nature** 501: 395–398.
- Müller, C., Glaser, T., Plogmeyer, M., Sendner, M., Döring, S., Bakulin, A. A., Brzuska, C., Scheer, R., Pshenichnikov, M. S., Kowalsky, W., Pucci, A., and Lovrinčić, R. (2015). Water Infiltration in Methylammonium Lead Iodide Perovskite: Fast and Inconspicuous. **Chem. Mater.** 27: 7835–7841.
- Nguyen, M.-T., Phan Vu, T.-V., and Bui, B.-T. (2016). Optical and Structural Study of Organometal Halide Materials for Applications in Perovskite-Based Solar Cells. **J. Electron. Mater.** 45: 2322–2327.
- NIST (2000). X-ray Photoelectron Spectroscopy Database, Standard Reference Database Number 20.

- Noh, J. H., Im, S. H., Heo, J. H., Mandal, T. N., and Seok, S. I. (2013). Chemical management for colorful, efficient, and stable inorganic-organic hybrid nanostructured solar cells. **Nano Lett.** 4: 1764–1769.
- Noriko, O.-Y., Takasuke, M., and Hiroshi, S. (1992). Dielectric study of $\text{CH}_3\text{NH}_3\text{PbX}_3$ ($X = \text{Cl}, \text{Br}, \text{I}$). **J. Phys. Chem. Solids.** 53: 935–939.
- NREL (2018). Research Cell Efficiency Records. Retrieved from <https://www.nrel.gov/pv/>.
- O, Y., M, O., T, M., and H, S. (1986). Calorimetric and dilatometric studies on the phase transitions of crystalline $\text{CH}_3\text{NH}_3\text{I}$. **J. Chem. Thermodyn.** 18: 939–954.
- Oku, T. (2015). Crystal Structures of $\text{CH}_3\text{NH}_3\text{PbI}_3$ and Related Perovskite Compounds Used for Solar Cells. In: Kosyachenko, L.A., Ed., Solar Cells—New Approaches and Reviews. **IntechOpen.** 3: 77–101.
- Onoda-Yamamuro, N., Yamamuro, O., Matsuo, T., and Suga, H. (1996). Heat Capacities and Phase Transitions of Protonated and Deuterated Methylammonium Tetrafluoroborates. **J. Phys. Chem. A** 100: 19647–19652.
- Pazoki, M., Jacobsson, T. J., Hagfeldt, A., Boschloo, G., and Edvinsson, T. (2016). Effect of metal cation replacement on the electronic structure of metal-organic halide perovskites: Replacement of lead with alkaline-earth metals. **Phys. Rev. B.** 93: 144105.
- Piskunov, S., Heifets, E., Eglitis, R. I., and Borstel, G. (2004). Bulk properties and electronic structure of SrTiO_3 , BaTiO_3 , PbTiO_3 perovskites: an ab initio HF/DFT study. **Comput. Mater. Sci.** 29: 165–178.

- Pérez-Osorio, M. A., Milot, R. L., Filip, M. R., Patel, J. B., Herz, L. M., Johnston, M. B., and Giustino, F. (2015). Vibrational properties of the organic-inorganic halide perovskite $\text{CH}_3\text{NH}_3\text{PbI}_3$ from theory and experiment: factor group analysis, first-principles calculations, and low-temperature infrared spectra. **J. Phys. Chem. C.** 119: 25703–25718.
- Qidong, T., Peng, Y., Hongqian, S., Zhike, L., Chenglong, H., Helen, L. W. C., and Feng, Y. (2016). Efficient and stable perovskite solar cells prepared in ambient air irrespective of the humidity. **Nat. Commun.** 7: 11105.
- Qingbiao, Y., Zhenyu, L., Youliang, H., Yiyang, Z., Shilun, Q., Ce, W., and Yen, W. (2004). Influence of solvents on the formation of ultrathin uniform poly(vinyl pyrrolidone) nanofibers with electrospinning. **J. Polym. Sci. B. Polym. Phys.** 42: 3721–3726.
- Quarti, C., Grancini, G., Mosconi, E., Bruno, P., Ball, J. M., Lee, M. M., Snaith, H. J., Petrozza, A., and De Angelis, F. (2014). The raman spectrum of the $\text{CH}_3\text{NH}_3\text{PbI}_3$ hybrid perovskite: interplay of theory and experiment. **J. Phys. Chem. Lett.** 5: 1948–7185.
- Richard, J. D. T. (2006). Crystals and Crystal Structures, John WileySons Ltd,Chepter 6,Diffracton and crystal structures.
- Sadoughi, G., Starr, D., Handick, E., Stranks, S., Gorgoi, M., Wilks, R., Bär, M., and Snaith, H. (2015). Observation and mediation of the presence of metallic lead in organic-inorganic perovskite films. **ACS Appl. Mater. Interfaces.** 7: 13440–13444.
- Safarik, D. J., Schwarz, R. B., and Hundley, M. F. (2006). Similarities in the

- C_p/T^3 Peaks in Amorphous and Crystalline Metals. **Phys. Rev. Lett.** 96: 195902.
- Saliba, M., Matsui, T., Seo, J.-Y., Domanski, K., Correa-Baena, J.-P., Nazeeruddin, M. K., Zakeeruddin, S. M., Tress, W., Abate, A., Hagfeldt, A., and Gratzel, M. (2016). Cesium-containing triple cation perovskite solar cells: improved stability, reproducibility and high efficiency. **Energy Environ. Sci.** 9: 1989–1997.
- Supasai, T., Rujisamphan, N., Ullrich, K., Chemseddine, a., and Dittrich, T. (2013). Formation of a passivating $\text{CH}_3\text{NH}_3\text{PbI}_3/\text{PbI}_2$ interface during moderate heating of $\text{CH}_3\text{NH}_3\text{PbI}_3$ layers. **Appl. Phys. Lett.** 103: 183906.
- Takeo, O. (2015). Crystal Structures of $\text{CH}_3\text{NH}_3\text{PbI}_3$ and Related Perovskite Compounds Used for Solar Cells, chapter 3.
- Vassiliy, L. and Peter, G. W. (2003). The origin of the boson peak and thermal conductivity plateau in low-temperature glasses. **Natl. Acad. Sci.** 100: 1515–1518.
- Wang, F., Grinberg, I., and Rappe, A. M. (2014). Common envelope evolution. **Appl. Phys. Lett.** 104: 152903.
- Wang, Z. Z., Otsuka, B., Inoue, T., Kobayashi, H., and Kurmood, M. (2004). Anionic NaCl-type frameworks of $[\text{Mn}^{II}(\text{HCOO})_3^-]$, templated by alkylammonium, exhibit weak ferromagnetism. **Dalton. Trans.** 0: 2209–2216.
- Weber, D. (1978). $\text{CH}_3\text{NH}_3\text{PbX}_3$, a Pb(II)- System with Cubic Perovskite Structure. **Z. Naturforsch. B Chem. Sci.** 33: 1443–1445.

Weber, D. (1979). The Perovskite System $\text{CH}_3\text{NH}_3[\text{PbnSn}_{1-n}\text{X}_3]$ ($\text{X} = \text{Cl}, \text{Br}, \text{I}$).

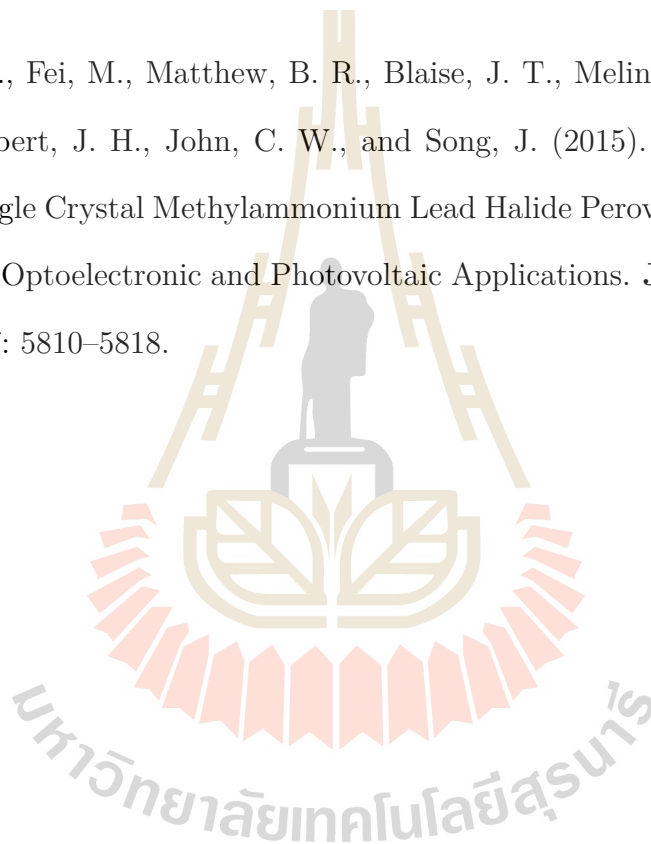
Z. Naturforsch. B Chem. Sci. 34: 939–941.

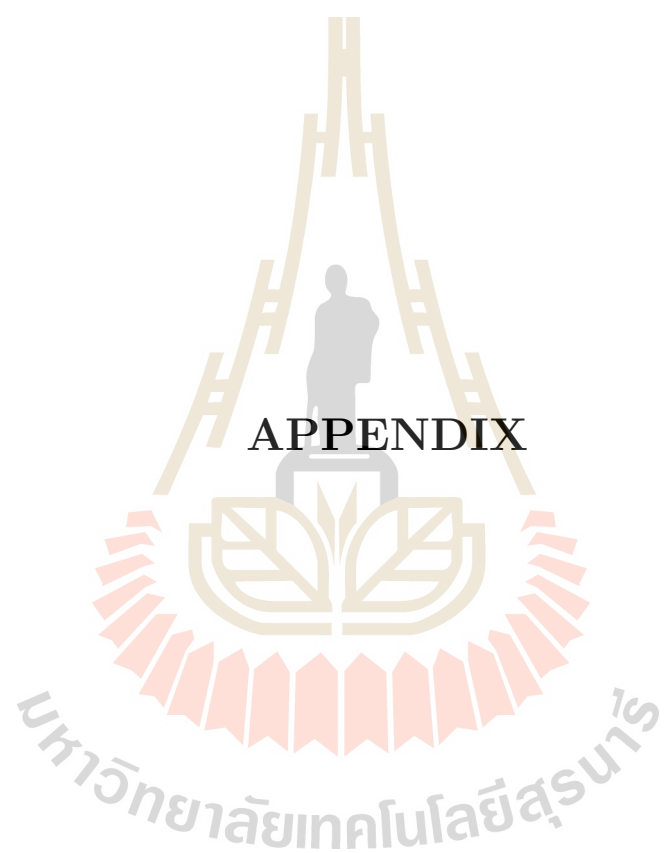
Weller, M. T., Weber, O. J., Henry, P. F., Di Pumpo, A. M., and Hansen, T. C.

(2015). Complete structure and cation orientation in the perovskite photovoltaic methylammonium lead iodide between 100 and 352 K. **Chem-Comm.** 51: 4180–4183.

Yongping, F., Fei, M., Matthew, B. R., Blaise, J. T., Melinda, J. S., Dewei, M.,

Robert, J. H., John, C. W., and Song, J. (2015). Solution Growth of Single Crystal Methylammonium Lead Halide Perovskite Nanostructures for Optoelectronic and Photovoltaic Applications. **J. Am. Chem. Soc.** 137: 5810–5818.





APPENDIX

APPENDIX

Abstract submitted for the 10th Asian Meeting on Electroceramics
(AMEC-2016) Dec. 04-07, 2016, Taipei, Taiwan.

AMEC-2016
The 10th Asian Meeting on Electroceramics
Dec. 04-07, 2016, Taipei, Taiwan

Preparation and Phase Formation Behavior of Methylammonium Lead Iodide Perovskite Materials

Jintara Padchasri^{1,*}, Rattikorn Yimnirun¹

¹*School of Physics, Institute of Science, and NANOTEC-SUT COE on Advanced Functional
Nanomaterials, Suranaree University of Technology, Nakhon Ratchasima, Thailand 30000*

The methylammonium lead iodide material is currently investigated as active material in perovskite solar cells. In this work, the methylammonium lead iodide ($\text{CH}_3\text{NH}_3\text{PbI}_3$ or MAPbI) perovskite materials were synthesized by a direct mixing method. The starting materials of methylammonium (CH_3NH_2) and hydroiodic acid (HI) were first mixed to form $\text{CH}_3\text{NH}_3\text{I}$ solid powders. Lead iodide (PbI_2) was then added to form $\text{CH}_3\text{NH}_3\text{PbI}_3$. The preparation process and the phase formation behavior were investigated in details via several techniques, including thermal analysis, X-Ray Diffraction (XRD), Scanning Electron Microscopy (SEM) and X-ray Photoelectron Spectroscopy (XPS). The thermal analysis revealed that the formation reaction of MAPbI reached a completion below 300°C , and further heating led to highly endothermic crystallization. The chemical composition and phase formation behavior of the prepared powders were analyzed by XPS and XRD, respectively. The results will be presented and discussed in details.

Keywords: methylammonium lead iodide, perovskite, X-ray Photoelectron Spectroscopy

Abstract submitted for The Fourteenth International Meeting on Ferroelectricity
(IMF2017) September 4-8 2017, Texas, USA.

**Electronic Structure of Lead-Free Organic-Inorganic Hybrid $\text{CH}_3\text{NH}_3\text{XI}_3$
Perovskite Materials**

Jintara Padchasri^{1,*} and Rattikorn Yimnirun¹

*¹School of Physics, Institute of Science, and NANOTEC-SUT COE on Advanced
Functional Nanomaterials, Suranaree University of Technology, NakhonRatchasima,
Thailand*

The importance of $\text{CH}_3\text{NH}_3\text{XI}_3$ or MAXI_3 (X=Pb and Ba) organic-inorganic hybrid materials has increased dramatically because of their potential use in solar cells. However, the basic structural characterization of these interesting materials remains sparse. In particular, advanced techniques, such as X-ray photoemission (XPS) and photoelectron emission spectroscopy (PES), could be employed to examine electronic structure and formation mechanism of these important perovskite materials. Here, systematic XPS and PES studies are employed to determine the electronic structure and chemical compositions of MAXI_3 powders. The results from this study help in explaining the possible electronic structure of the materials. The finding also leads to an awareness of the reactions, which in turn allow us to perform post synthetic reactions to form the organic-inorganic metal iodide perovskites.

Keywords: hybrid materials; electronic structure; X-ray photoemission; photoelectron emission spectroscopy

Abstract submitted for International Conference on Science and Technology of Emerging Materials 2018 (STEMa2018) 18-20 July 2018, Pattaya, Thailand.

Dielectric behavior of lead-free perovskite materials

Jintara Padchasri^{1,*}, Saroj Rujirawat¹, Taras Kolodiazhnyi²
and Rattikorn Yimnirun³

¹*School of Physics, Institute of Science and NANOTEC-SUT COE on Advanced Functional Nanomaterials, Suranaree University of Technology, Nakhon Ratchasima 30000, Thailand*

²*National Institute for Materials Science, 1-1 Namiki, Tsukuba, Ibaraki 305-0044, Japan*

³*School of Energy Science and Engineering, Vidyasirimedhi Institute of Science and Technology, Wangchan, Rayong 21210, Thailand*

**corresponding author, E-mail: jintara_liwliw@hotmail.com*

Abstract

We report dielectric behavior of Pb-free perovskite materials based on a non-toxic metal earth of $\text{MAPb}_{0.9}\text{X}_{0.1}\text{I}_3$ ($\text{X} = \text{Pb}, \text{Sn}, \text{Ba}$). The Rietveld refinements analysis indicated that 10%doped of Sn and Ba compositions are tetragonal phase. Clear evidence of phase transitions was found in dielectric permittivity results. As a result, show outstanding of anomalous dielectric relaxation is far below the orthorhombic to tetragonal phase transition at $T \approx 40\text{-}150\text{ K}$. The dielectric relaxation fitted well to the Arrhenius thermally an activated process with activation energy of $E_a \approx 70\text{-}180\text{ meV}$.

Keywords: dielectric behavior, lead-free, rietveld refinement, activation energy



Contents lists available at ScienceDirect

Journal of Alloys and Compounds

journal homepage: <http://www.elsevier.com/locate/jalcom>

Effects of annealing temperature on stability of methylammonium lead iodide perovskite powders

Jintara Padchasri*, Rattikorn Yimnirun

School of Physics, Institute of Science, and NANOTEC-SUT COE on Advanced Functional Nanomaterials, Suranaree University of Technology, Nakhon Ratchasima, Thailand



ARTICLE INFO

Article history:

Received 14 February 2017

Received in revised form

4 May 2017

Accepted 16 May 2017

Available online 17 May 2017

Keywords:

Methylammonium lead iodide
Perovskite
XPS

ABSTRACT

The methylammonium lead iodide ($\text{CH}_3\text{NH}_3\text{PbI}_3$ or MAPbI) material is currently investigated as active material in perovskite solar cells. Its stability, high optical band gap, low processing temperature and abundant elemental constituents provide numerous advantages over most powder absorber materials. In this work, the stability of MAPbI perovskite powders under different annealing temperature conditions was examined. X-ray diffraction (XRD) measurement demonstrated that the direct mixing synthesis method was able to produce a highly crystalline MAPbI material in a tetragonal phase structure. Thermal stability measurement based on the Simultaneous Thermal Analyzer (STA) indicated that the MAPbI was stable below 275 °C. The optical properties were characterized by employing refraction spectroscopy, which confirmed a direct bandgap of 1.53 eV in MAPbI perovskite powders. FT-Raman and XPS spectra confirmed the existence of organic groups. The annealing affected significantly the phase formation and stability of MAPbI. A small amount of lead iodide (PbI_2), a product of the degradation, was observed with increasing annealing temperature. Therefore, a suitable annealing temperature should be chosen to produce MAPbI powders, which in turn will result in a high performance perovskite solar cell.

© 2017 Elsevier B.V. All rights reserved.

1. Introduction

In recent years, there has been a great deal of interest in organic-inorganic perovskites for their applications as photovoltaic (PV) materials [1–3]. The activity of the organic-inorganic perovskite materials is strongly influenced by the physical and chemical processes, and more studies on these materials can help in developing the device performance progress [4]. Hence, in order to understand these materials better and to control their properties, it is very important that good structure of the material is obtained.

Several techniques have been employed to obtain phase formation and structural information of the organic-inorganic perovskite materials. These include the simplest method of deposition requiring only annealing to convert the deposited precursor solution to the perovskite in crystalline form [5]. The new reports have demonstrated the power conversion efficiency (PCEs) of over 20% from a thin-film perovskite solar cell [6]. However, the PCE is very sensitive to phase transformation behavior of the perovskite materials while the influence of moisture on a variation of

optoelectronic properties of $\text{CH}_3\text{NH}_3\text{PbI}_3$ prepared by the simple deposition method has been highlighted very recently. An alternative approach to the problem is to use solid state method to produce the perovskite material that can be compared with the thin-film perovskite data from Sadoughi and Calloni group [7,8].

The most investigated organic-inorganic perovskites are $\text{CH}_3\text{NH}_3\text{PbX}_3$ ($\text{X} = \text{Cl}, \text{Br}$ and I), which could be synthesized by mixing methylammonium and lead halide salts. Mixed halide perovskites are prepared by a solution of lead halide and methylammonium iodide. The relative simplicity of formation of $\text{CH}_3\text{NH}_3\text{PbX}_3$ enabled preparation of the perovskite films which have been used to make photovoltaic devices with efficiency similar to the best established organic-inorganic technologies [7]. In addition, the performance of device could be improved by controlling crystallization process and annealing conditions [9]. However, annealing at high temperature for short durations or low-temperature thermal annealing for longer periods have been reported to bring the decomposition of the film causing the decrease in the device efficiency [10,11] and deterioration in PV performance [12]. In other relevant works, Cu_2O films synthesized by radical oxidation with nitrogen plasma treatment and different RF powers at low temperature were studied by Zang et al. [13,14]. Although the

* Corresponding author.

E-mail address: jintara_liwliw@hotmail.com (J. Padchasri).

optical bandgap energy and hole density are increased, the resistivity is decreased after N_2 treatment time from 0 to 40 min, the performance of CuO_2 films is poorer compared to that of Cu_2O using RF power which shows a good rectifying behavior.

In this paper we report the phase formation behavior and electronic structure of MAPbI perovskite powders. The prepared perovskite powders were analyzed using various techniques, including Simultaneous Thermal Analyzer (STA), powder X-ray Diffraction (XRD), Ultraviolet Visible Spectroscopy (UV–Vis), Fourier Transform-Raman Spectroscopy (FT-Raman) and X-ray Photoelectron Spectroscopy (XPS). The study of perovskite formation under various annealing conditions is reported and discussed in this work.

2. Materials and methods

Methylammonium lead iodide ($CH_3NH_3PbI_3$ or MAPbI) was prepared by first synthesizing methylammonium iodide (CH_3NH_3I or MAI). Then, CH_3NH_3I was reacted with PbI_2 in the stoichiometric ratio of 1:1. MAI was synthesized by equimolar reaction between methylammonium (CH_3NH_2 , 24 mL, 33 wt% in ethanol, Sigma Aldrich) and hydroiodic acid (HI, 12 mL, 57 wt% in water, Aldrich). The mixture was stirred in an ice bath for 2 h, controlling the temperature continuously. Then, the solution was stirred at 50 °C for 24 h and MAI was obtained. The precipitate was washed three times with diethyl ether (purity $\geq 99.8\%$, Sigma Aldrich) and vacuum dried. The MAPbI was synthesized by homogenizing the 1:1 (m/m) MAI and PbI_2 (purity 99%, Sigma Aldrich) mixture in a mortar according to (1).



The as-prepared MAPbI was subsequently annealed in Ar for 30 min at a temperature of 150–250 °C. The samples were denoted as follows; as-prepared MAPbI (MAPbI), MAPbI annealed at 150, 200, 225 and 250 °C (MAPbI_150, MAPbI_200, MAPbI_225 and MAPbI_250), respectively. It is noted that the selection of the annealing temperatures was based on the STA results (as will be discussed later). As we did not want the material to completely transform to a new compound during the annealing process, the range of the annealing temperature should thus lie in the region where no strong thermal reaction occurs.

Thermal analysis was performed on as-prepared MAPbI to examine the thermal reaction of the material by Simultaneous Thermal Analyzer (STA, NETZCH/STA449F3). The phase formation, quality and crystalline phase were determined by powder X-ray diffraction (XRD) with Bruker D2 diffractometer (with $Cu-K_\alpha$ radiation). The diffraction patterns were refined using the Rietveld method. The Rietveld method refines user-selected parameters to minimize the difference between an experimental pattern (observed data) and a model based on the hypothesized crystal structure and instrumental parameters (calculated pattern) by using crystallographic constraints of lattice parameters, space group to constrain the peak positions and crystal structure to constrain the peak intensities. The optical band gap values (E_g) were obtained from diffuse reflectance measurements by Ultraviolet Visible spectroscopy (UV–VIS, Perkin Elmer/LAMBDA950). In addition, the Fourier transform-Raman (FT-Raman, Bruker/Vertex70 + RamII) and Raman spectrometer (Raman, JOBIN YVON HORIBA/T64000 triple monochromator) were employed to examine the absorption bands of organic groups. X-ray photoelectron spectroscopy (XPS, PHI5000 Versa ProbelI; Al- K_α radiation) experiment was conducted at Beamline 5.1, SLRI (Synchrotron Light Research Institute) to analyze the chemical bonding states and the chemical composition of the samples.

3. Results and discussion

Thermal analysis was used to determine the mass loss behavior of the individual organic and inorganic components that make up the building blocks of MAPbI as a function of temperature. The sublimation behavior of the isolated organic component was examined in depth and used to interpret the STA data of MAPbI powder. STA curve is shown in Fig. 1. The weight loss occurs in several steps between 250 and 700 °C corresponding to the total weight loss of 85% with the remaining 15% of the unidentified black residue. Our STA data show two main weight loss steps at 326 and 426 °C corresponding to the weight loss of 28%, 57% (Fig. 1), respectively. The high-temperature weight loss demonstrated several shoulders extending to 700 °C. The STA data reported here are in qualitative agreement with the $CH_3NH_3PbI_3$ decomposition reported earlier by Amalie et al. [11]. While there are some quantitative differences between the two data sets (see Fig. 1), they may be explained by the different carrier gas used (e.g., Ar in our case and N_2 in the case of Ref. [11]) and different heating rates.

The weight loss between 270 and 340 °C is attributed to the thermal decomposition of the $CH_3NH_3PbI_3$ at which the organic components i.e., CH_3NH_3I , CH_3NH_2 and HI are removed from the material. Indeed, the decomposition reaction $CH_3NH_3PbI_3 \rightarrow CH_3NH_3I + PbI_2$ predicts the weight loss of 25.7% in good agreement with the experimentally determined weight loss of 28%. A recent study on the $CH_3NH_3PbI_3$ perovskite thin film shows that $CH_3NH_3PbI_3$ begins to transform to PbI_2 at temperature as low as 140 °C [15]. The next major weight loss occurs in the temperature interval of 400–690 °C. We attribute this loss to the partial sublimation of the remaining PbI_2 inorganic component from the melt. While there is a noticeable difference in the onset temperature of the PbI_2 sublimation process detected in our data ($T = 425$ °C) and the data reported in Ref. [11] ($T = 588$ °C), the temperature of the completion of the weight loss is almost the same, i.e. $\approx 650 \pm 20$ °C. At the moment we do not have a clear explanation as to why the onset temperatures of the PbI_2 sublimation in our data and Ref. [11] differ so much. The possible reasons behind this discrepancy could be the different heating and gas flow rates as well as the morphology and purity of the sample.

The powder XRD measurements were carried out in air. The XRD

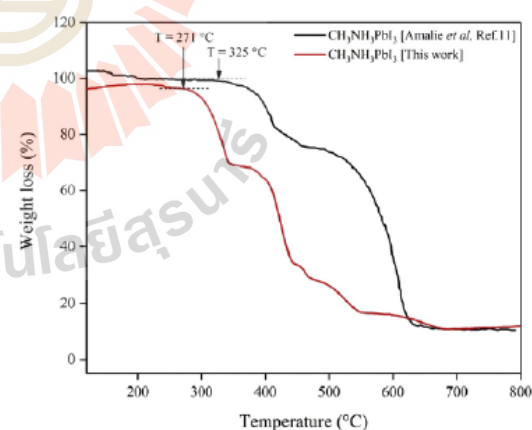


Fig. 1. The weight loss curves of MAPbI powder (red) and data from Amalie et al. [11] (black). (For interpretation of the references to colour in this figure legend, the reader is referred to the web version of this article.)

patterns of MAPbI₃ powders annealed at different temperatures are shown in Fig. 2. XRD patterns of all samples show sharp diffraction peaks at 13.9° for (002), 14.1° for (110), 19.9° for (112), 28.4° for (220), 32.1° for (310), 40.5° for (224) and 41.1° for (400), as shown in Fig. 2a. Among them, (110) and (220) peaks are the strongest. The XRD results suggest that the crystal structure of MAPbI₃ powders is a tetragonal phase (*I4/mcm* space group) with lattice parameters of $a = 8.8586 \text{ \AA}$ and $c = 12.6280 \text{ \AA}$ [16]. The XRD result also indicates that an increase in the annealing temperature causes a gradual shift in diffraction peaks toward lower angles, suggesting larger lattice parameters. Fig. 2b shows the magnification of (002) and (110) peaks where both peaks shift to lower 2θ values as the temperature increases. An increase in the annealing temperature to 225 and 250 °C results in materials with the cubic structure (*Pmm* space group), as indicated by the typical peak at 13.84°. The sharp diffraction peaks also indicate the high crystallinity of the powders. It is evidenced by the low-value shift of 2θ in Fig. 2b, the annealed tetragonal samples exhibit larger cell parameters than the as-prepared MAPbI₃. This observation is confirmed by the results of the Rietveld refinement listed in Table 1. The particle size was estimated by the Scherrer equation $\tau = \frac{k\lambda}{FWHM \cos \theta}$, where τ is the crystallite size, k is the dimensionless shape factor (0.89), λ is the X-ray wavelength (1.5406 Å), $FWHM$ is the line broadening at half the

maximum intensity and θ is the Bragg angle (in degrees) of the XRD pattern. The results for tetragonal samples are summarized in Table 1. The data for MAPbI₃_225 and MAPbI₃_250 samples are not shown here because in this work we focus mainly on the materials with a tetragonal structure, while MAPbI₃_225 and MAPbI₃_250 samples exhibited the cubic structure, as shown in Fig. 2b, with an increased portion of PbI₂ phase.

A clear correlation is observed between the annealing temperature and the perovskite formation behavior. The samples annealed at 200 °C gave the higher proportion of the tetragonal structure (99.6%) with the lattice parameters (a , c) and r ; $a = 8.8798$, $c = 12.6490 \text{ \AA}$ and 2.55 nm, respectively. At lower annealing temperatures, both the lattice parameters and the crystallinity decreased as a consequence of incomplete conversion of PbI₂ + CH₃NH₃I into the perovskite phase also resulting in appearance of the secondary phases. At higher temperature (200 °C) a more complete phase formation was observed, as confirmed by Rietveld refinement. Unfortunately we could not achieve complete phase purity of the CH₃NH₃PbI₃ perovskite. In addition to the main phase, the peak at $2\theta = 12.6^\circ$ originating from PbI₂ was present in all the samples both annealed and as-prepared. This is consistent with the results reported in Ref. [17]. However, our results show that annealing at 200 °C can significantly suppress the PbI₂ secondary phase in our powder down to 0.4%.

The optical properties of MAPbI₃ powders are shown in Fig. 3. In the absorption spectra of the samples at different annealing temperatures, the absorption edge is seen to shift to lower energy (longer wavelength) with increasing annealing temperature. The band gap was calculated by applying the Kubelka-Munk (K-M) equation to the measured diffused reflectance spectra [18,19]. By fitting the plots of the photon energy (eV) vs $[F(R)/h\nu]^2$, the band gap energies of $E_g = 1.53 (\pm 0.002)$, $1.52 (\pm 0.001)$ and $1.51 (\pm 0.004) \text{ eV}$ were obtained for as-prepared sample and samples annealed at $T = 150^\circ\text{C}$ and 200°C , respectively; consistent with the previous reports [16]. The position of the absorption peak corresponding to the band gap is determined by I (5p) orbitals and the Pb (6s) orbitals. The optical transitions in the methylammonium lead halide perovskite are similar to the transitions in PbI₂ [16,17,20]. The valence band of the PbI₂ is composed of Pb (6s) orbitals and I (5p) orbitals while the conduction band is composed of Pb (6p) orbitals. Moreover, the energy level of I (5p) is lower than the energy level of Pb (6s) [21], the optical absorption peak position of MAPbI₃ is thus shifted to lower energy with an increase in annealing temperature.

The chemical structure of the synthesized perovskite samples can be examined and correlated by the FTIR measurements, as shown in Fig. 4, and Raman measurements presented in Fig. 5. The FTIR spectra shown in Fig. 4 display the characteristic bands for organic groups detected in the powder samples with peaks at 905 cm^{-1} (CH₃-NH₃⁺ rocking), 957 cm^{-1} (C-N stretch), 1472 cm^{-1} (N-H bending) and 3099 cm^{-1} (N-H stretch), which are attributed to C-H bending modes and N-H stretching modes with the NH₃⁺ group of the MA cation [22]. The details of the characteristic bands and peak positions are presented in Table 2. As seen in Fig. 4, only as-prepared MAPbI₃ sample shows new broad peaks at around 3500 cm^{-1} , which is related to O-H stretching vibrations, as the measurements were carried out under ambient conditions. The OH oscillations of water molecules are embedded in such a way that they affect the hydrogen bonds between the NH₃⁺ group and the iodide because the N-H stretch vibrations are known for their sensitivity to the strength of the interaction between the methylammonium and the iodide [22,23].

Fig. 5a presents the Raman spectra, which offer complementary details on the characteristic bands for the inorganic group in MAPbI₃ powders as a function of annealing temperature. Raman signals in the region from 50 to 300 cm^{-1} (excitation wavelength 532 nm) is

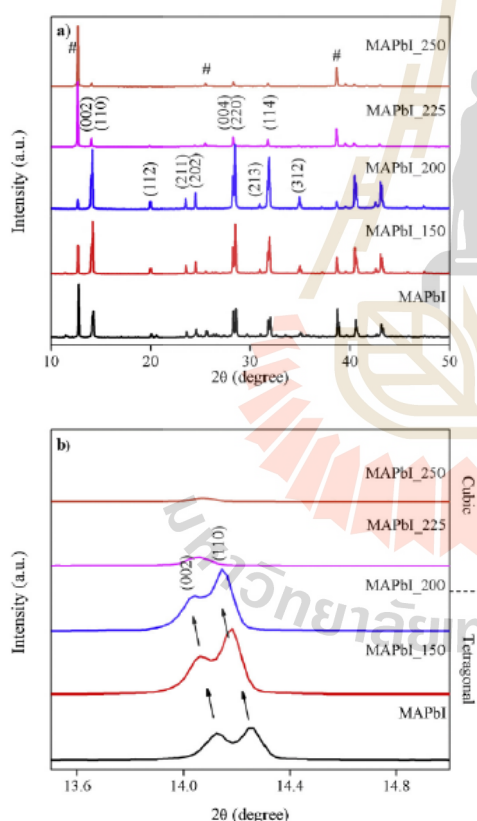


Fig. 2. a) XRD patterns of MAPbI₃ annealed at different temperatures and b) the magnified XRD spectra of (002) and (110) peaks (# PbI₂).

Table 1
Phase formation, lattice parameter and Crystallite size by Rietveld refinement of the XRD pattern.

| Sample | Annealed temp. (°C) | % Phase formation | | Lattice parameter | | Crystallite size | |
|-----------|---------------------|--|------------------|-------------------|---------|------------------|-------------|
| | | CH ₃ NH ₃ PbI ₃ | PbI ₂ | a | c | FWHM | τ (nm) |
| MAPbI | — | 46.6 | 53.4 | 8.8743 | 12.6660 | 0.0905 | 2.30 |
| MAPbI_150 | 150 | 83.9 | 16.1 | 8.8769 | 12.6581 | 0.0790 | 2.49 |
| MAPbI_200 | 200 | 99.6 | 0.4 | 8.8798 | 12.6490 | 0.0770 | 2.55 |

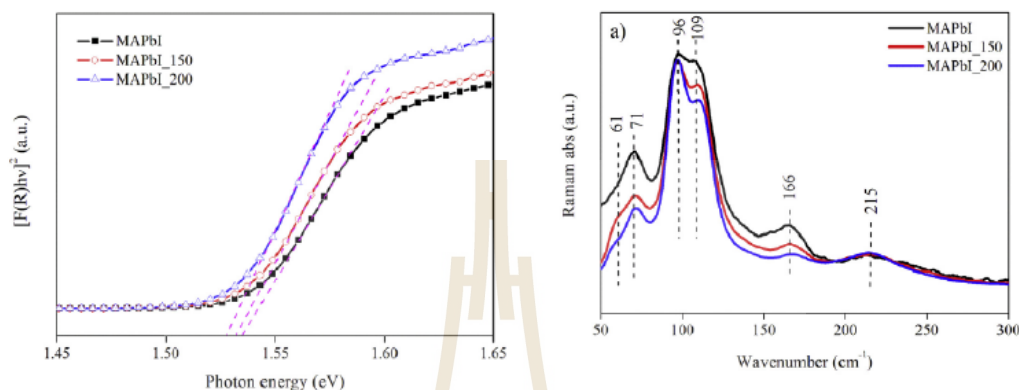


Fig. 3. The absorption spectra of the MAPbI samples.

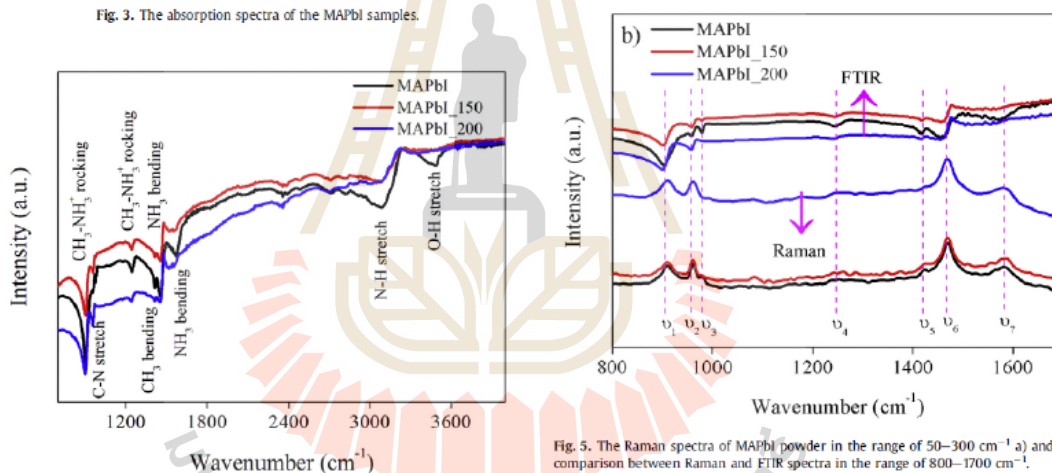


Fig. 4. FTIR spectra of MAPbI powder in the range of 700–4400 cm⁻¹.

present for all measurements and there was no visual change of the samples during the experiment. The spectra are quite similar to those of related hybrid perovskite [24] and are characterized by a broad Raman signal in the 50–150 cm⁻¹ region, with two well-defined maxima at ~71 and 96 cm⁻¹ and two less intense maxima at ~61 and 109 cm⁻¹. A broad signal between 166 and 215 cm⁻¹ is also found. The ~61 and 96 cm⁻¹ vibration peaks are in good agreement with density functional theory calculations [25]. The 62 and 94 cm⁻¹ peaks were reported previously for MAPbI, where as in our samples 61 cm⁻¹ peak is very weak, and stronger 71 cm⁻¹ peak is more likely corresponding to the significant mode in this area. In

Fig. 5. The Raman spectra of MAPbI powder in the range of 50–300 cm⁻¹ a) and b) comparison between Raman and FTIR spectra in the range of 800–1700 cm⁻¹.

addition, the Raman spectra of MAPbI in the region from 800 to 1700 cm⁻¹ (excitation wavelength 1064 nm) show the features characteristic to organic species which are compared with the FTIR data, as shown in Fig. 5b and summarized in Table 2. The Raman peaks in the 800–1700 cm⁻¹ range well correspond to the FTIR features as shown in Fig. 5b. It is noted that some peaks cannot be found in the infrared spectra, but are present in the Raman spectra. This is because the vibration energy is Raman active if it causes a change in polarizability whereas it is IR active if there is a change in the dipole moment [26]. It should be emphasized that the peaks at 905, 957, 980, 1239, 1423, 1472 and 1579 cm⁻¹ are related to the frequency of vibration mode of organic cation, CH₃-NH₃⁺ rocking, C-N stretching, O-H bending, CH₃-NH₃⁺ rocking, CH₃ bending and

Table 2
Measured resonance frequencies of vibrational modes and peak Assignments for perovskites.

| ν | Position (cm^{-1}) | Peak assignment |
|---------|-------------------------------|-----------------------------------|
| ν_1 | 904.74 | $\text{CH}_3\text{-NH}_3$ rocking |
| ν_2 | 957.16 | C–N stretch |
| ν_3 | 979.74 | O–H bending |
| ν_4 | 1239.16 | $\text{CH}_3\text{-NH}_3$ rocking |
| ν_6 | 1422.64 | CH_3 bending |
| ν_7 | 1472.01 | NH_3 bending |
| ν_8 | 1581.13 | NH_3 bending |

NH_3 bending, respectively [27]. The displacement of the above peaks was found previously [23] when different halides ($\text{X} = \text{Cl}$, Br and I) were used; this change is known as Lorentz-Lorenz shift caused by different interactions of the MA cation with the surrounding Pb-X cage [28,29].

The XPS spectra were recorded to confirm the oxidation state and chemical bonding states in the samples. Fig. 6 shows the XPS data of C1s, N1s, I3d and Pb4f core levels with the different annealing temperatures. All spectra have been normalized to the same height for visual clarity. When carbon signal is substantially larger, an N1s signal from the organic cation appears. In the case of Pb shown Fig. 7a, the main Pb4f peak is spin-orbit split into a $4f_{5/2}$ and $4f_{7/2}$ doublet located at ca. 138.4 eV and 143 eV in agreement with the literature data [30,31]. The as-prepared sample shows a low-energy shoulder which completely disappears in the sample annealed at 200 °C (Fig. 7a). We tentatively attribute this low-energy shoulder in the as-prepared sample to the PbI_2 second phase where the Pb^{2+} ion is located in the different crystal field environment. As the PbI_2 phase almost disappears in the sample annealed at 200 °C so does the low-energy shoulder in the Pb 4f peak. Fig. 7b shows I signal ($3d_{3/2}$ and $3d_{5/2}$) spectra for all the samples at 619.3 eV and small signal at ~618.5 eV. The spectra indicate a well separated spin-orbit component, with a separation of around 11.5 eV being found in all the cases which is typical of the presence of I^- [31]. In addition, the signals of I are shifted towards higher BE values, suggesting that small modifications are produced in the oxidation state of I^- after annealing (~0.2 eV), and the small signal at ~618.5 eV suggesting the presence of alkali iodides [32]. The slight modifications of an interaction between PbI_2 and MAI

can be observed in the chemical bonding. For example, the signals obtained for N are analyzed; both N1s and C1s core levels include a second peak, as shown in Fig. 7c–d for both as-prepared and annealed samples. The N1s and C1s core signals of the annealed samples shifted slightly towards the higher BE, indicating that the N and C components undergo some complex chemical modifications occurring during the annealing process.

The previous work by Calloni group reported XPS analysis of the organic-inorganic perovskite prepared from a solution of PbCl_2 and $\text{CH}_3\text{NH}_3\text{I}$ [7]. Through a thin-film characterization, it was found that the absence of the Cl peak and detection of the N1s peak in the XPS spectrum are related to methylamine molecules, a strong indication of the dissociation of $\text{CH}_3\text{NH}_3\text{Cl}$ species. Sadoughi et al. [8] studied the depth-dependent chemical composition of mixed-halide perovskite. Substantial amounts of metallic lead were found in the perovskite films. The post-annealing process in air can reduce the metallic lead content in the perovskite film, indicating that a simple annealing procedure could be employed to increase the performance of perovskite solar cells [8]. The study reported in Ref. [8] clearly demonstrated the importance of the understanding of which type of impurities or defects play a key role in the photovoltaic performance of the perovskite material. In our present work, the optimum annealing condition appears to be approximately 30 min at 200 °C in Ar-atmosphere, resulting in the highest proportion of the perovskite material, as confirmed by Rietveld refinement method. The Rietveld refinement was employed in this work to confirm the crystal structure and quantitative phase assemblage. The quantitative information of the $\text{CH}_3\text{NH}_3\text{PbI}_3$ phase listed in Table 1. Annealing of the samples at the temperature higher than 200 °C causes degradation of the perovskite material with the loss of the organic component and the PbI_2 formation [7,8,30–33], as shown in Fig. 2.

From the above results, it is possible to deduce that the annealing temperature of perovskite precursors could play a crucial role in fabricating high performance solar cell devices. The phase degradation mechanism as a result of annealing process in MAPbI is evidenced. Through a chemical degradation, the stability of MAPbI powders decreases with increasing annealing temperature, resulting in an increasing proportion of PbI_2 formed when annealing temperature >200 °C, as confirmed by XRD and STA measurements. In addition, FTIR, Raman and XPS spectra reveal the existence of organic groups and indicate that the PbI_2 and $\text{CH}_3\text{NH}_3\text{I}$ are also present in the prepared MAPbI perovskite materials.

4. Conclusion

MAPbI was prepared by a direct mixing process. The annealing temperature was found to have significant impact on the perovskite phase formed. The XRD results indicate that annealing temperature up to 200 °C in Ar is required to form the almost phase-pure $\text{CH}_3\text{NH}_3\text{PbI}_3$ perovskite. Thermal stability measurement based on the STA analysis indicates that the MAPbI is stable below 275 °C with no detectable material loss at low temperature. The optical properties were characterized by applying reflection spectroscopy, which confirms a direct bandgap of 1.53 eV. FTIR and Raman spectra reveal the existence of organic groups and we can conclude that the annealing process affects the phase formation and stability of MAPbI. A small amount of PbI_2 , a product of the degradation, is observed with increasing annealing temperature. Therefore, a suitable annealing temperature should be chosen to produce active material to be used in high performance perovskite solar cell. These findings offer useful insights in studying phase formation and stability of the perovskite solar cells at ambient condition.

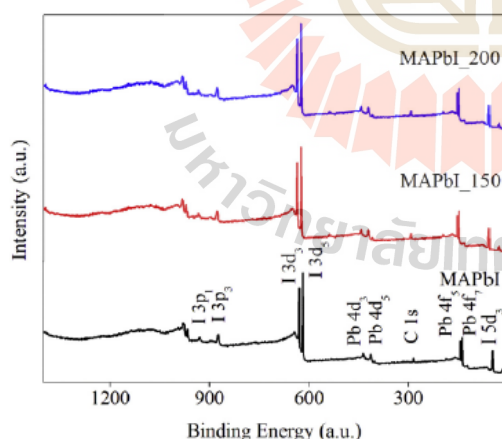


Fig. 6. XPS survey scan of MAPbI powders.

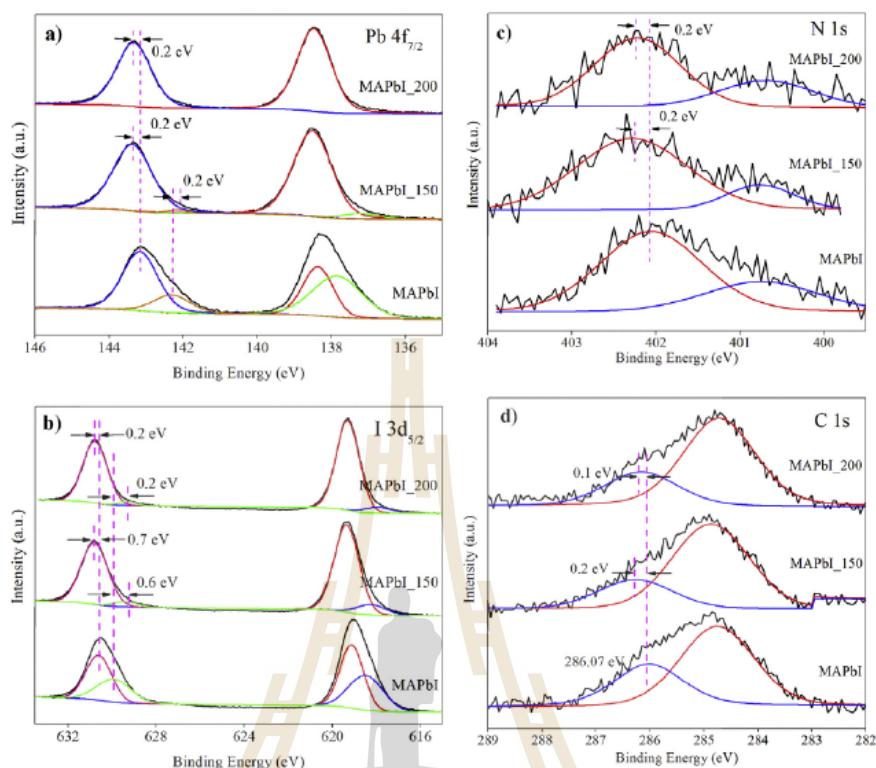


Fig. 7. XPS core level peaks of the samples and the Gaussian fitting for a) Pb 4f_{7/2}, b) I 3d_{5/2}, c) N 1s and d) C 1s.

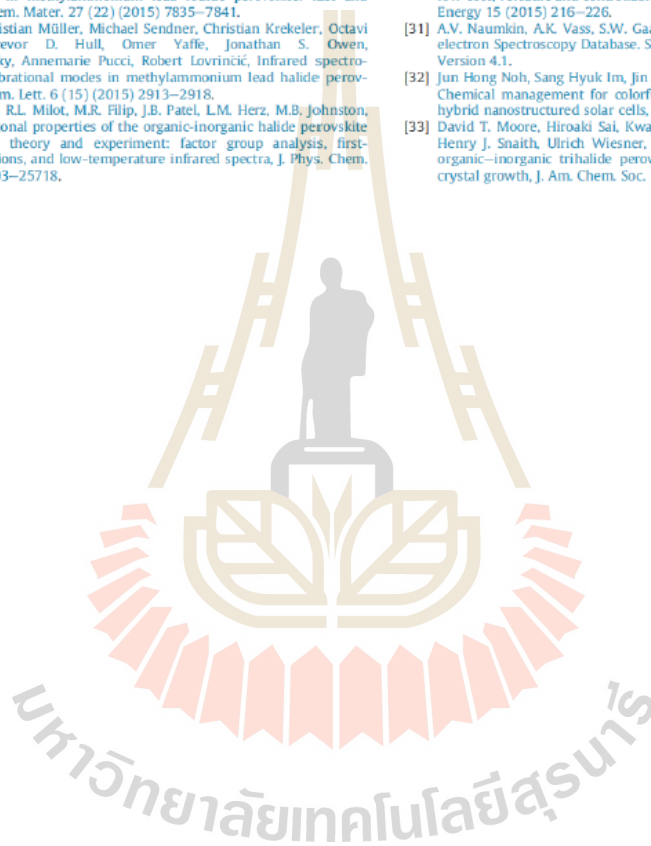
Acknowledgements

JP is financially supported by Science Achievement Scholarship of Thailand (SAST) for her PhD Scholarship. Authors acknowledge SUT Research and Development Fund, Suranaree University of Technology for financial support. Technical help and discussion on XPS measurement by Dr.Narong Chanlek of Synchrotron Light Research Institute (SLRI) is greatly appreciated. Our heartfelt thanks are also to Dr.Taras Kolodiaznyy of National Institute for Materials Science (NIMS) Japan for his helping during manuscript preparation.

References

- [1] D.B. Mitzi, Synthesis, structure, and properties of organic-inorganic perovskites and related materials, *Prog. Inorg. Chem.* 48 (1999) 1–121.
- [2] D. Weber, CH₃NH₃PbX₃ a Pb(II)-system with cubic perovskite structure, *Z. Naturforsch. 33b* (1978) 1443–1445.
- [3] H. Gory, Perovskite-based solar cells, *Science* 342 (2013) 317–318.
- [4] Joseph Berry, Tonio Buonassisi, David A. Egger, Gary Hodes, Leon Kronik, Yueh-Lin Loo, Igor Lubomirsky, Seth R. Marder, Yitzhak Mastai, Joel S. Miller, David B. Mitzi, Yaron Paz, Andrew M. Rappe, Ilan Riess, Boris Rybtchinski, Oscar Stafsudd, Václav Števanović, Michael F. Toney, David Zitoun, Antoine Kahn, David Ginley, David Cahen, Hybrid organic-inorganic perovskites (HOIPs): opportunities and challenges, *Adv. Mater.* 27 (35) (2015) 5102–5112.
- [5] Y. Kumar, E. Regalado-Pérez, Arturo Martínez Ayala, N.R. Mathews, Xavier Mathew, Effect of heat treatment on the electrical properties of perovskite solar cells, *Sol. Energy Mater. Sol. Cells* 157 (2016) 10–17.
- [6] EPFL, Perovskite solar cells surpass 20 percent efficiency, <http://actu.epfl.ch/news/perovskite-solar-cells-surpass-20-efficiency>, 2016 (Accessed 16 September 2016).
- [7] A. Caloni, A. Abate, G. Bussetti, G. Berti, R. Yvliatin, F. Ciccarelli, L. Duo, Stability of organic cations in solution-processed CH₃NH₃PbI₃ perovskites: formation of modified surface layers, *J. Phys. Chem. C* 119 (2015) 21329–21335.
- [8] Golnaz Sadoughi, David E. Starr, Evelyn Handick, Samuel D. Stranks, Mihaela Gorgoi, Regan G. Wilks, Marcus Bär, Henry J. Snaith, Observation and mediation of the presence of metallic lead in organic-inorganic perovskite films, *ACS Appl. Mater. Interfaces* 7 (24) (2015) 13440–13444.
- [9] P. Sandeep, S. Alessandro, S. Aditya, D. Felix, H. Amir, S. Nobuya, C.G. Karl, D.S. Samuel, N. Nakita, P. Michael, H. Sven, A.H. Nicholas, H.F. Richard, S. Ullrich, J.S. Henry, Atmospheric influence upon crystallization and electronic disorder and its impact on the photophysical properties of organic-inorganic perovskite solar cells, *ACS Nano* 9 (2015) 2311–2320.
- [10] D. Amalie, T. Nicolas, M. Thomas, G. Peng, K.N. Mohammad, G. Michael, Effect of annealing temperature on film morphology of organic-inorganic hybrid perovskite solid-state solar cells, *Adv. Funct. Mater.* 24 (2014) 3250–3258.
- [11] D. Amalie, G. Peng, S. Sang Il, K.N. Mohammad, G. Michael, Thermal behavior of methylammonium lead-trihalide perovskite photovoltaic light harvesters, *Chem. Mater.* 26 (2014) 6160–6164.
- [12] Zhengguo Xiao, Qingfeng Dong, Cheng Bi, Yuchuan Shao, Yongbo Yuan, Jinsong Huang, Solvent annealing of perovskite-induced crystal growth for photovoltaic device efficiency enhancement, *Adv. Mater.* 26 (37) (2014) 6503–6509.
- [13] Zhigang Zang, Atsushi Nakamura, Jiro Temmyo, Single cuprous oxide films synthesized by radical oxidation at low temperature for PV application, *Opt. Express* 21 (9) (2013) 11448.
- [14] Zhigang Zang, Atsushi Nakamura, Jiro Temmyo, Nitrogen doping in cuprous oxide films synthesized by radical oxidation at low temperature, *Mater. Lett.* 92 (2013) 188–191.
- [15] T. Supasai, N. Rujsamphan, K. Ullrich, A. Chemseddine, T. Dittrich, Formation of a passivating CH₃NH₃PbI₂/PbI₂ interface during moderate heating of

- CH₃NH₃PbI₃ layers, *Appl. Phys. Lett.* 103 (2013) 183906.
- [16] T. Oku, Crystal structures of CH₃NH₃PbI₃ and related perovskite compounds used for solar cells, in: L.A. Kosyachenko (Ed.), *Solar Cells-new Approaches and Reviews Publisher: InTech*, 2015, pp. 77–101.
- [17] M.B. Thomas, R. Yevgeny, O. Yonatan, K. Eugenia, F. Ishay, E. Michael, C. David, H. Gary, Conversion of single crystalline PbI₂ to CH₃NH₃PbI₃: structural relations and transformation dynamics, *Chem. Mater.* 28 (2016) 6501–6510.
- [18] G. Kortum, *Reflectance Spectroscopy: Principles, Methods, Applications*, first ed., Springer, New York, 1969.
- [19] E.L. Simmons, Diffuse reflectance spectroscopy: a comparison of the theories, *Appl. Opt.* 14 (1975) 1380–1386.
- [20] T. Ishihara, J. Takahashi, T. Goto, Optical properties due to electronic transitions in two-dimensional semiconductors (CnH_{2n+1}NH₃)PbI₄, *Phys. Rev. B* 42 (1990) 11099.
- [21] Teruya Ishihara, Optical properties of PbI₂-based perovskite structures, *J. Luminescence* 60–61 (1994) 269–274.
- [22] Christian Müller, Tobias Glaser, Marcel Plogmeyer, Michael Sendner, Sebastian Döring, Artem A. Bakulin, Carlo Brzuska, Roland Scheer, Maxim S. Pshenichnikov, Wolfgang Kowalsky, Annemarie Pucci, Robert Lovrincić, Water infiltration in methylammonium lead iodide perovskite: fast and inconspicuous, *Chem. Mater.* 27 (22) (2015) 7835–7841.
- [23] Tobias Glaser, Christian Müller, Michael Sendner, Christian Krekeler, Octavi E. Semonin, Trevor D. Hull, Omer Yaffe, Jonathan S. Owen, Wolfgang Kowalsky, Annemarie Pucci, Robert Lovrincić, Infrared spectroscopic study of vibrational modes in methylammonium lead halide perovskites, *J. Phys. Chem. Lett.* 6 (15) (2015) 2913–2918.
- [24] M.A. Perez-Osorio, R.L. Milot, M.R. Filip, J.B. Patel, L.M. Herz, M.B. Johnston, F. Giustino, Vibrational properties of the organic-inorganic halide perovskite CH₃NH₃PbI₃ from theory and experiment: factor group analysis, first-principles calculations, and low-temperature infrared spectra, *J. Phys. Chem. C* 119 (2015) 25703–25718.
- [25] C. Quarti, G. Grancini, E. Mosconi, P. Bruno, J.M. Ball, M.M. Lee, H.J. Snaith, A. Petrozza, F.D. Angelis, The raman spectrum of the CH₃NH₃PbI₃ hybrid perovskite: interplay of theory and experiment, *J. Phys. Chem. Lett.* 5 (2014) 279–284.
- [26] Gateway Analytical A chemImage Company, Comparison of Raman and FTIR Spectroscopy: Advantages and Limitations. <http://www.gatewayanalytical.com/blog/of-raman-and-ftir-spectroscopy-advantages-and-limitations/>, (Accessed 16 September 2016).
- [27] J. Idigoras, A. Todinova, J.R. Sánchez-Valencia, A. Barranco, A. Borrás, J.A. Anta, The interaction between hybrid organic–inorganic halide perovskite and selective contacts in perovskite solar cells: an infrared spectroscopy study, *Phys. Chem. Chem. Phys.* 18 (19) (2016) 13583–13590.
- [28] N.O. Yamamuro, T. Matsuo, H. Suga, Calorimetric and IR spectroscopic studies of phase transitions in Methylammonium Trihalogen oplumbates (II), *J. Phys. Chem. Solids* 51 (1990) 1383–1395.
- [29] Juana Bellanato, Infra-red spectra of ethylenediamine dihydrochloride and other amine hydrochlorides in alkali halide disks, *Spectrochim. Acta* 16 (11–12) (1960) 1344–1357.
- [30] H. Chen, Z. Wei, X. Zheng, S. Yang, A Scalable electro deposition route to the low-cost, versatile and controllable fabrication of perovskite solar cells, *Nano. Energy* 15 (2015) 216–226.
- [31] A.V. Naumkin, A.K. Vass, S.W. Gaarenstroom, C.J. Powell, NIST X-ray Photoelectron Spectroscopy Database, Standard Reference Database, vol. 20, 2012, Version 4.1.
- [32] Jun Hong Noh, Sang Hyuk Im, Jin Hyuck Heo, Tarak N. Mandal, Sang Il Seok, Chemical management for colorful, efficient, and stable inorganic–organic hybrid nanostructured solar cells, *Nano Lett.* 13 (4) (2013) 1764–1769.
- [33] David T. Moore, Hiroaki Sai, Kwan W. Tan, Detlef-M. Smilgies, Wei Zhang, Henry J. Snaith, Ulrich Wiesner, Lara A. Estroff, Crystallization kinetics of organic–inorganic trihalide perovskites and the role of the lead anion in crystal growth, *J. Am. Chem. Soc.* 137 (6) (2015) 2350–2358.



CURRICULUM VITAE

NAME: Jintara Padchasri **DATE OF BIRTH:** March 1, 1989

EDUCATIONS:

2014-present PhD. in Physics. School of Physics, SUT

2012-2014 M.Sc.in Physics. Department of Physics, UBU

2008-2012 B.Sc. in Physics. Department of Physics, UBU

PUBLICATIONS:

J.Padchasri and R.Yimnirun : J.Alloys and comps, 720(2017)63-69.

J.Padchasri, R.Yimnirun, T.Kolodiazhnyi: J. Eur. Ceram. Soc, 38 (2018) 3412–3415.

T.Kolodiazhnyi, J.Padchasri, R.Yimnirun: J. Eur. Ceram. Soc, 38(2018)1517–1523.

J.Padchasri, T.Kolodiazhnyi, S.Rujirawat and R.Yimnirun: J. App. Phys. (submitted)

AWARDS:

2012-2017 Science Achievement Scholarship of Thailand (SAST)

Professional Experience:

03/2017-03/2018 Visiting researcher (trainee) at National Institute for Materials Science (NIMS, Tsukuba, Japan)

08/2015-02/2017 Research Assistant: Synchrotron light research Institute, 5.2 beamline staff